



HAL
open science

Experimental and theoretical charge density analysis of functionalized polyoxovanadates: toward a better understanding of chemical bonding and chemical reactivity

Xiao Xu

► **To cite this version:**

Xiao Xu. Experimental and theoretical charge density analysis of functionalized polyoxovanadates: toward a better understanding of chemical bonding and chemical reactivity. Other. Ecole Centrale Paris, 2015. English. NNT: 2015ECAP0026 . tel-01181264

HAL Id: tel-01181264

<https://theses.hal.science/tel-01181264v1>

Submitted on 29 Jul 2015

HAL is a multi-disciplinary open access archive for the deposit and dissemination of scientific research documents, whether they are published or not. The documents may come from teaching and research institutions in France or abroad, or from public or private research centers.

L'archive ouverte pluridisciplinaire **HAL**, est destinée au dépôt et à la diffusion de documents scientifiques de niveau recherche, publiés ou non, émanant des établissements d'enseignement et de recherche français ou étrangers, des laboratoires publics ou privés.

THESIS

presented by

Xiao XU

in order to obtain the

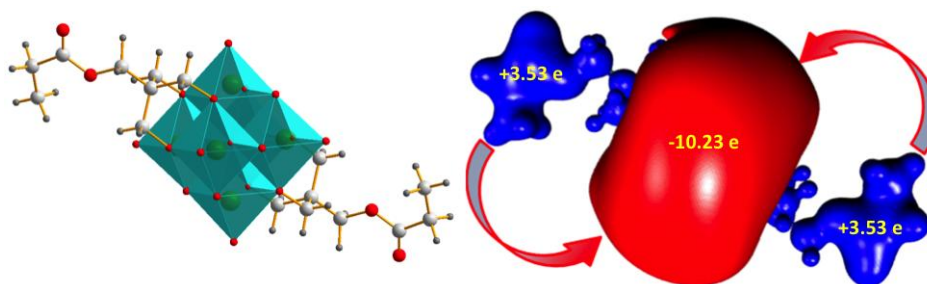
GRADE DE DOCTEUR

Speciality : Physical Chemistry

Laboratory:

Structure Propriétés Modélisations des Solides (UMR 8580 CNRS)

**Experimental and theoretical charge density analysis of
functionalized polyoxovanadates: toward a better
understanding of chemical bonding and chemical reactivity**



Oral defense to be held 30th March 2015

14h30, Bâtiment Dumas, C211

Jury:

Pr. Jean-Pierre DJUKIC
Pr. Christian JELSCH

Université de Strasbourg, Strasbourg, France, referee
Université de Lorraine, Nancy, France, referee

Pr. Françoise DUMAS
Pr. Carlo GATTI
Pr. Jean-Michel GILLET
Dr. Nada BOSNJAKOVIC-PAVLOVIC

Université Paris Sud, Châtenay-Malabry, France, examiner
Université di Milano, Milano, Italy, examiner
Centrale Supélec, Châtenay-Malabry, France, examiner
University of Belgrade, Belgrade, Serbia, examiner

Pr. Anne SPASOJEVIC – de BIRE
Pr. Nour-Eddine GHERMANI

Centrale Supélec, Châtenay-Malabry, France, Supervisor
Université Paris Sud, Châtenay-Malabry, France, Co-Supervisor

ABSTRACT

The functionalized polyoxovanadates (POVs) exhibit nanoscale superoctahedral cluster-core structures, fascinating electronic and magnetic properties, various thermodynamically stable redox isomers, and potential catalytic capabilities. Among of the various properties, we are interested in the charge transfer and fluorescent properties. However, understanding such a charge transfer behavior and fluorescence mechanism of these functionalized hexavanadates is still a formidable challenge.

High resolution X-ray crystallography allows the analysis of the electronic and topological properties, and provides a method to study the chemical bonding and chemical reactivity based on charge density and the electrostatic properties determination. Experimental and theoretical charge density analysis of functionalized polyoxovanadates has been carried out and the related properties have been discussed at the atomic level.

In this manuscript, we present the results of: i) experimental charge density and related electronic and topological properties of two functionalized hexavanadates (V6), $[(C_4H_9)_4N]_2[V_6O_{13}\{(OCH_2)_3CCH_2OCCH_2CH_3\}_2]$ (V6-C3) and $Na_2[V_6O_{13}\{(OCH_2)_3CCH_2OH\}_2] \cdot 3.5H_2O$ (V6OH); ii) theoretical calculations on a series of functionalized V6 compounds, and decavanadate (V10). The chemical information from charge density analysis is used for a better understanding of the charge density distribution, charge transfer, fluorescent properties, functionalization behavior, and biological activities.

Key words: Crystallography, charge density, functionalized hexavanadate, chemical bonding, chemical reactivity

ACKNOWLEDGMENTS

I would like to thank all the people who made this thesis possible and an unforgettable experience for me.

First of all, it is my great pleasure to express my sincere thanks and deepest sense of gratitude to my supervisor, **Prof. Anne Spasojević – de Biré**, *SPMS, UMR 8580, CNRS, Centrale Supélec*. She offered her sustained enthusiasm, creative suggestions, and continuous encouragement during my PhD period. I thank her for the careful guidance and great effort she put into training me in the charge density field. Without her, I think I can not finish my PhD thesis.

I would like to thank to **Prof. Nour Eddine Ghermani**, *Faculty of Pharmacy, Institut Galien Paris Sud, UMR 8612, CNRS*, for his exemplary guidance with a lot of advices and scientific discussions, and for his help during the period of my research. I thank him for teaching me how to perform charge density refinement at the beginning, which is really important to me, and for helping me to collect the X-ray diffraction data.

I would like to thank to **Prof. Jean-Michel Gillet**, *SPMS, UMR 8580, CNRS, Centrale Supélec*, for introducing me to the theoretical charge density field, extending my knowledge, and explaining me the various questions in charge density analysis. I also thank him for his supporting of Gaussian calculations.

I am thankful to **Prof. Pingfan Wu**, my teacher in undergraduate course, *Hubei University of Technology*, in China. I thank to her for introducing me to the POM/POV field, teaching me full of chemical knowledge, and training my logical thinking.

I am thankful to **Prof. Yongge Wei**, *Tsinghua University*, in China. I thank to him for providing me all the compounds in my research and meaningful advices for POM/POV chemistry.

I also thank to **Dr. Sladjana Novakovic**, *Vinča Institute of Nuclear Sciences*, in Serbia. I thank to her for helping me to perform the charge density refinement and generate the charge density properties.

I would like to thank to **Dr. Nada Bošnjaković-Pavlović**, *University of Belgrade*, in Serbia, to share her research experience in charge density analysis of decavanadate and CSD searching for non-covalent interaction.

I would like to thank to **Dr. Danjela Krstić and Dr. Mirjana Colovic**, *University of Belgrade*, in Serbia, for testing the biological activities of functionalized V6 compounds.

I am very thankful to my colleagues, **Xiaoxuan Shi (Sophie)** and **Wenjing Li (Sabrina)** to support me selflessly. I am very happy to work with them.

I would like to thank to **Dr. Nouha El Hassan, Dr. Aziza Ikni, Dr. Bertrand Clair** to help me during my PhD period.

I sincerely thank all the members, former and present, post-docs, PhD students, secretaries and technical staff at SPMS lab, for the discussions, encouragement, kindness and supporting atmosphere during the PhD period.

I sincerely thank all the friends in France. I really enjoyed myself being with them.

For financial support I thank **CSC** (China Scholarship Council).

Finally, I take this opportunity to express the profound gratitude from my deep heart to my parents, my sister, and the other members of the big family for their love and continuous support – both spiritually and materially.

CONTENTS

Introduction.....	1
1. State of art	6
1.1 Introduction	7
1.2 Charge density methodology	7
1.2.1 Experimental charge density analysis from X-ray diffraction.....	7
1.2.2 Charge density analysis steps.....	10
1.2.3 Crystallographic refinement.....	13
1.2.4 Charge density models.....	15
1.2.5 Residual electron density	18
1.2.6 Deformation electron density.....	19
1.2.7 Electrostatic potential.....	20
1.2.8 AIM theory and topological analysis.....	22
1.2.9 <i>d</i> -orbital calculation	26
1.2.10 Source function	28
1.2.11 Programs for charge density refinement and analysis	29
1.2.12 Charge density from theory	29
1.3 Polyoxometalates	30
1.3.1 POM chemistry	30
1.3.2 POM structure.....	31
1.3.3 Functionalized POMs.....	33
1.3.4 Applications of POMs.....	35
1.4 Polyoxovanadates	36
1.4.1 POVs' structures	36
1.4.2 Generality of functionalized hexavanadates	37
1.4.3 Previous X-ray structure of functionalized hexavanadates.....	39
1.4.4 Structure description of functionalized hexavanadates.....	45
1.5 Experimental and theoretical charge density analysis of POMs and POVs.....	47

1.6	Conclusion	51
2.	Experimental charge density analysis of functionalized hexavanadate V6-C3	53
2.1	Introduction	54
2.2	Experiment and refinement	54
2.2.1	Synthesis of functionalized hexavanadates.....	54
2.2.2	Crystallization of V6-C3.....	56
2.2.3	Data collection and data reduction.....	56
2.2.4	IAM refinement	56
2.2.5	Charge density refinement	57
2.3	Results	59
2.3.1	Crystal structure description	59
2.3.1.1	<i>V6 core of functionalized [V6-C3]²⁻</i>	60
2.3.1.2	<i>Organic ligands of functionalized [V6-C3]²⁻</i>	62
2.3.1.3	<i>The TBA cation</i>	63
2.3.2	Crystal packing	64
2.3.3	Electron density	69
2.3.3.1	<i>Plane definitions of the 2D electron density</i>	69
2.3.3.2	<i>Residual density maps</i>	73
2.3.3.3	<i>Experimental deformation density</i>	74
2.3.3.4	<i>Dynamic deformation density</i>	75
2.3.3.5	<i>Static deformation density</i>	76
2.3.3.6	<i>Laplacian of total electron density</i>	77
2.3.3.7	<i>Static deformation density of non covalent bonds</i>	78
2.3.4	Topological analysis of total electron density	79
2.3.4.1	<i>Topological analysis of total electron density of V6 core</i>	79
2.3.4.2	<i>Topological analysis of total electron density of organic ligand</i>	79
2.3.4.3	<i>Topological analysis of total electron density of TBA cation</i>	79
2.3.4.4	<i>Topological analysis of total electron density of non covalent bonds</i>	79
2.3.5	Atomic net charges	85
2.3.5.1	<i>Atomic net charges of V6 core</i>	85
2.3.5.2	<i>Atomic net charges of the organic ligand</i>	85
2.3.5.3	<i>Atomic net charge of TBA cation</i>	86
2.3.6	<i>d orbital populations of the vanadium atoms</i>	88

2.3.7	Electrostatic potential.....	90
2.3.7.1	<i>Electrostatic potential of functionalized V6-C3 anion</i>	90
2.3.7.2	<i>Electrostatic potential of TBA cation</i>	93
2.3.8	Source function analysis	94
2.4	Discussion	96
2.4.1	From geometrical analysis to charge density analysis.....	96
2.4.2	Chemical bonding in functionalized V6-C3 anion	97
2.4.2.1	<i>V-O bonding</i>	97
2.4.2.2	<i>Atomic net charges for V and O atoms in V6 core</i>	109
2.4.2.3	<i>d orbital population of vanadium atoms</i>	111
2.4.3	Chemical bonding in functionalized linkage and organic ligand.....	111
2.4.3.1	<i>Electron density maps</i>	112
2.4.3.2	<i>Topological analysis</i>	115
2.4.4	Chemical bonding in TBA cation	117
2.4.5	Non covalent bonding	117
2.4.6	Chemical reactivity and charge transfer	119
2.4.6.1	<i>Electrostatic potential</i>	119
2.4.6.2	<i>AIM charge distribution</i>	122
2.4.6.3	<i>Integrated source function analysis</i>	123
2.5	Conclusion	125
3.	Preliminary experimental charge density analysis of functionalized hexavanadate V6OH	126
3.1	Introduction	127
3.2	Experiment and refinement.....	127
3.2.1	Synthesis and crystallization.....	127
3.2.2	Crystallographic refinement.....	128
3.3	Results.....	130
3.3.1	Crystal structure description	130
3.3.1.1	<i>Functionalized [V6OH]²⁻ anion</i>	131
3.3.1.2	<i>Sodium cation</i>	132
3.3.2	Crystal packing	132
3.3.3	Electron density maps	134
3.3.4	Topological analysis of the total electron density.....	134

3.3.5	Atomic net charge	139
3.3.6	Electrostatic potential.....	139
3.4	Discussion and conclusion	141
4.	Theoretical charge density analysis of functionalized hexavanadates and decavanadate	142
4.1	Introduction	143
4.2	Computational methods.....	143
4.2.1	Model structures.....	143
4.2.1.1	<i>Functionalized V6-C3.....</i>	<i>143</i>
4.2.1.2	<i>List of the model structures for computational study</i>	<i>144</i>
4.2.2	Computational details	147
4.3	Results.....	149
4.3.1	Theoretical electron density maps	149
4.3.1.1	<i>Electron density maps of V-O bonding in functionalized V6-C3 anion.....</i>	<i>149</i>
4.3.1.2	<i>Electron density maps of organic ligand and TBA cation.....</i>	<i>150</i>
4.3.1.3	<i>Electron density maps of V10 anion.....</i>	<i>152</i>
4.3.2	Theoretical topological analysis	152
4.3.2.1	<i>Theoretical topological parameters of functionalized V6 series.....</i>	<i>152</i>
4.3.2.2	<i>Theoretical topological parameters of V10 anion.....</i>	<i>152</i>
4.3.2.3	<i>Theoretical topological parameters of TBA cation</i>	<i>152</i>
4.3.2.4	<i>Theoretical topological analysis of V-O bonds at BCP.....</i>	<i>161</i>
4.3.2	Theoretical AIM charges	162
4.3.2.1	<i>Theoretical AIM charges for functionalized V6 series and V10 anion.....</i>	<i>162</i>
4.3.2.2	<i>Theoretical AIM charges for TBA cation</i>	<i>162</i>
4.3.3	Theoretical <i>d</i> -orbital population of vanadium atoms.....	164
4.3.4	Theoretical electrostatic potential	165
4.3.4.1	<i>Theoretical EP of Isolated V6 and V10.....</i>	<i>165</i>
4.3.4.2	<i>Theoretical electrostatic potential of functionalized V6-C3.....</i>	<i>166</i>
4.3.4.3	<i>Theoretical electrostatic potentials of short functionalized V6 series.....</i>	<i>167</i>
4.3.4.4	<i>Theoretical electrostatic potentials of long functionalized V6 series.....</i>	<i>168</i>
4.3.4.5	<i>Theoretical electrostatic potential of TBA cation.....</i>	<i>169</i>
4.4	Discussion and conclusion.....	169
5.	General discussion	171

5.1	Introduction	172
5.2	Similarities and differences in experimental and theoretical charge density of three POV compounds	173
5.2.1	Functionalized V6-C3 anion	174
5.2.2	Functionalized V6OH anion	183
5.2.3	V10 anion.....	189
5.2.4	Conclusion	194
5.3	A summary of charge density application in functionalized V6 compounds and decavanadate	194
5.4	Electronic and topological properties of POV compounds	198
5.4.1	Charge density feature of V atom in POV structure	198
5.4.1.1	<i>Atomic net charges</i>	<i>198</i>
5.4.1.2	<i>d orbital population.....</i>	<i>200</i>
5.4.2	Charge density features of O atoms in POV structure.....	204
5.4.3	Chemical bonding in POV compounds.....	207
5.4.4	Classification of V-O bonds based on topological parameters.....	207
5.5	A better understanding of functionalization behavior by charge density analysis.....	224
5.5.1	Functionalized hexavanadate	225
5.5.2	Functionalized hexamolybdate	226
5.6	Charge density analysis of charge transfer behavior and fluorescence in POM/POV-based material.....	233
5.6.1	POM/POV-based charge transfer material	233
5.6.2	POV-based fluorescent material	238
5.7	Toward a better understanding of biological activity.....	242
5.7.1	Biological activity of functionalized V6 and V10 compounds.....	242
5.7.1.1	<i>Biological activity of V10 – A state of arts.....</i>	<i>242</i>
5.7.1.2	<i>Biological activities of functionalized V6 series – new tests.....</i>	<i>244</i>
5.7.2	CSD statistical research on non-covalent interactions of functionalized V6 anion	252
5.7.3	A combined approach to predict the interaction sites of functionalized V6 compounds: experimental/theoretical electrostatic potential, crystallographic statistical analysis, molecular interaction field determination	254

Conclusion and perspectives.....	263
List of abbreviations	266
Reference	267
Appendix.....	283
Poster and oral presentation.....	312

INTRODUCTION

Charge transfer materials have attracted increasing attentions in recent years due to their roles in the fields of semiconductors [Zhu, 2009], solar cells [Zhao, 2012], metal organic frameworks (MOFs) [Miyasaka, 2013], fluorescent materials [Grabowski, 2003], and catalysts [Akimov, 2013], [Sadakane, 1998]. According to Mulliken's theory [Mulliken, 1952; Orgel, 1957; Mulliken, 1962; Mulliken, 1964], charge transfer (CT) system is formed by an electron donor (D) and an electron acceptor (A), D and A could be two different molecules or ions, leading to intermolecular CT, or separate moieties within a large molecule, leading to intramolecular charge transfer (ICT) [Grabowski, 2003]. Polyoxometalates (POMs), a large group of early transition metal oxide clusters, are extensively studied due to their diversified structures and wide-ranging properties [Dolbecq, 2010]. POMs are well-known electron acceptors in CT materials prepared with organic donors, which is based on the ability of POMs to act as electron reservoirs [Yamase, 1998; Coronado, 2005]. The synergistic combination of POM acceptors and organic donors gives to the CT materials some important potential properties. For example, the CT materials containing the spherical POM acceptors (Lindqvist-type $[\text{Mo}_6\text{O}_{19}]^{2-}$, Keggin-type $[\text{SiMo}_{12}\text{O}_{40}]^{4-}$) and planar arene donors exhibit unique structures, potential nonlinear optical and ferromagnetic properties [Maguerès, 2000]. Different POMs acceptors connecting with ferrocenyl donors have exhibited various spectroscopic properties and broad CT bands [Veya, 1995; Stark, 1995; Kang, 2004; Xu, 2010; Niu, 2010]. TTF-POMs CT materials show semiconductor properties and have potential application in semiconductor devices [Coronado, 2005; Tsunashima, 2012; Li, 2011].

Among the various synthesized polyoxovanadates (POVs), functionalized hexavanadates (V6) in which the inorganic V6 core is covalently bonded to organic ligands, form one of the most interesting subgroups. The functionalized V6 also presents nanoscale superoctahedral cluster-core structures, fascinating electronic and magnetic properties, various thermodynamically stable redox isomers, and potential catalytic capabilities [Spandl, 2003; Daniel, 2005; Aronica, 2008; Daniel, 2009]. Recently, Prof. Yongge Wei (Department of Chemistry, University of Tsinghua, Beijing, China) firstly found that the functionalized V6 with hydrophobic groups

shows unexpected fluorescent properties, probably due to the ligand-to-metal charge transfer (LMCT), which might inspire a new mechanism for fluorescence emission [Yin, 2011; Wu, 2011; Li, 2011]. However, understanding such a CT behavior and fluorescence mechanism of these functionalized hexavanadates is still a formidable challenge.

Experimental charge density, determined from high resolution single crystal X-ray diffraction, has been becoming a useful tool used to investigate the charge density distribution, topological properties, AIM (Atoms in Molecule) charges, electrostatic potential, source function, etc. within the crystalline states [Hansen, 1978; Bader, 1991; Koritsanszky, 2001; Lecomte, 2003; Gatti, 2004]. Enlighten by the reported works of POV-based fluorescent materials involving oxide-to-vanadium charge transfer and intervalence charge transfer transitions [Yamase, 1994; Chen, 2005; Chen, 2009; Ma, 2011], the investigations on the CT behavior between POM/POV acceptor and organic donor could provide a new insight into fluorescence mechanism of the functionalized V6. Up to now, the most widely methods used for the experimental CT behavior description are various spectroscopic characterizations [Re, 2003; Benson-Smith, 2007], which only give indirect experimental evidences. A better knowledge of the experimental atomic charge distribution is needed for a more precise description of CT compounds. These results would be used as a direct evidence of CT behavior. It has been established that accurate charge density and electrostatic properties can give precise information on the CT behavior especially in the following aspects: i) the regions where the electrostatic potential are negative/positive give an idea of the D and A groups; ii) the AIM charges of the different groups determine the amount of the charge transferred between D and A [Ortmann, 1992; Gikas, 2005; Meindl, 2009; Jiang, 2011; Kotova, 2011]. Therefore, charge density analysis of functionalized V6 would be a promising approach to understand their CT behavior. The experimental electron density of decavanadate anion co-crystallized with cytosine/cytosinium molecules, $\text{Na}_3[\text{V}_{10}\text{O}_{28}](\text{C}_4\text{N}_3\text{OH}_5)_3(\text{C}_4\text{N}_3\text{OH}_6)_3 \cdot 10\text{H}_2\text{O}$ leads to a precise description of the chemical bonding inside the V10 cage as well as the atomic net charges of the oxygen atoms [Bošnjaković-Pavlović, 2008; Bošnjaković-Pavlović, 2009; Bošnjaković-Pavlović, 2010]. According to a statistical study of the non-covalent interactions and the experimental electrostatic properties of the V10 anion, our group has established the preferential relationship between an organic ligand and the V10

anion [Bošnjaković-Pavlović, 2011].

In order to give some insight to the charge transfer in some functionalized hexavanadate synthesized by Pr Yongge Wei, we have studied the experimental electronic and electrostatic properties of two functionalized V6 compounds, $[(C_4H_9)_4N]_2[V_6O_{13}\{(OCH_2)_3CCH_2OCCH_2CH_3\}_2]$ (V6-C3) and $Na_2[V_6O_{13}\{(OCH_2)_3CCH_2OH\}_2] \cdot 3.5H_2O$ (V6OH). A careful treatment of these experiments will give us access to different properties such as static deformation density, Laplacian of the total density, topology analysis of the total density, AIM charges, d orbital population, local and integrated source function and electrostatic potential. In the same time, we have performed theoretical calculations on a series of functionalized V6: $[V_6CH_3]^{2-}$, $[V_6NH_2]^{2-}$, $[V_6OH]^{2-}$, $[V_6NO_2]^{2-}$, $[V_6-C3]^{2-}$, $[V_6-C6]^{2-}$, $[V_6-C18]^{2-}$, $[V_6-TPY]^{2-}$ in order to determine the static deformation density, Laplacian of the total density, topology analysis of the total density, AIM charges and electrostatic potential. In addition, some calculations have been done on the unstable V6 ($[V_6O_{19}]^{8-}$) and the decavanadate anion $[V_{10}O_{28}]^{6-}$. Hence, the experimental and theoretical charge density analysis could provide us a detail picture of the chemical bonding and chemical reactivity of functionalized V6 compounds.

Then we would be able to give some insight to the understanding of the charge transfer property of this series and to the influence of the functionalized moiety on different properties. Finally, a precise study of the non-covalent interactions belonging to the V6 core of functionalized hexavanadate, the determination of the Hirshfeld surface [Spackman, 2009] and the study of the molecular interaction field [Artese, 2013] will be correlated to biological properties of these compounds determined by Dr. Danjela Krstić, Faculty of Medicine, University of Belgrade, Serbia.

The compounds studied in this manuscript are summarized in Table I-1.

The manuscript is organized as following:

In **chapter 1**, “*State of art*”, the basis of charge density methodology is exposed. Some general chemical informations and properties of polyoxovanadates are also given.

The “*Experimental charge density analysis of functionalized V6-C3*” is presented in detail in **chapter 2**. The discussion in this chapter deals with the chemical bonding in V6 core, the linkage, the organic moiety, and in the TBA (Tetrabutylammonium) cation, which have crystallized with the hexavanadate anion and some conclusion of the reactivity and charge transfer of V6-C3.

Chapter 3 contains “*Preliminary experimental charge density analysis of functionalized Hexavanadate V6OH*”, preliminary, due to the fact that some density centered on vanadium remains non taken into account by the multipole model. The comparison with the V6-C3 results is treated in chapter 5.

The results of “*Theoretical charge density analysis of functionalized hexavanadates and decavanadate*” are summarized in **chapter 4**. A discussion on the different methods of calculation is given in this chapter, while the chemical bonding description is done in chapter 5.

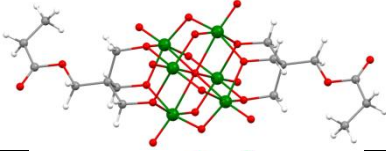
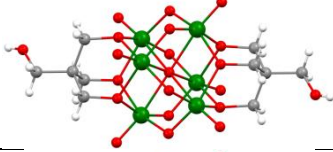
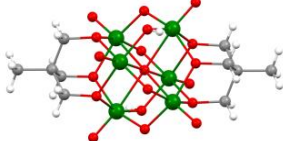
The similarities and differences on the experimental and theoretical of V6-C3, V6-OH and V10 are presented in the “*General discussion*”, **chapter 5**. From this comparison, we would be able to use all the results obtained in chapter 2, 3 and 4 to give a detailed description of the V-O bonds and classified it according to the topological parameters. We will give some insight in the understanding of the properties of the functionalized hexavanadate such as charge transfer, fluorescence, and functionalization. The non-covalent interactions study, the determination of the Hirshfeld surface and the study of the molecular interaction field will be correlated to biological properties of these compounds.

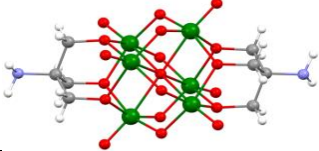
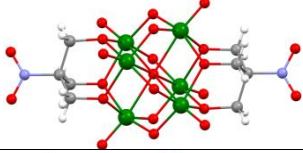
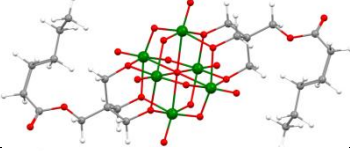
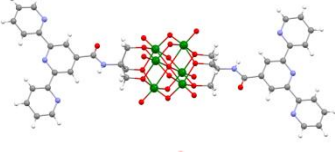
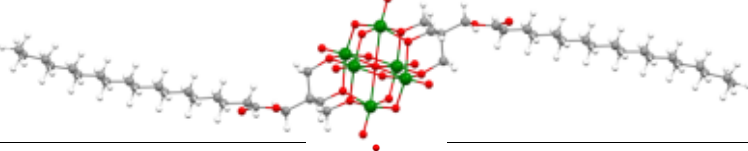
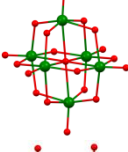
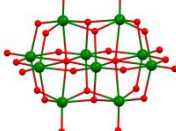
Finally, some “*Conclusion and perspectives*” are drawn.

References and appendix are presented at the end of the manuscript.

The experimental charge density have been done with the help of Prof. Nour Eddine Ghermani, Faculty of Pharmacy, Institut Galien Paris Sud, UMR 8612, CNRS, while the theoretical calculation have been performed with the help of Prof. Jean-Michel Gillet, SPMS, UMR 8580, CNRS, CentraleSupélec.

Table I.1. *Molecular structure of the compound used in the manuscript*

V6-C3	
V6-OH	
V6-CH3	

V6-NH2	 <p>A ball-and-stick model of a V6-NH2 complex. It features a central vanadium (V) cluster with six vanadium atoms (green) and twelve oxygen atoms (red) in a distorted octahedral arrangement. Two amine groups (-NH2) are coordinated to the cluster, with nitrogen atoms (blue) and hydrogen atoms (white) visible.</p>
V6-NO2	 <p>A ball-and-stick model of a V6-NO2 complex. It features a central vanadium (V) cluster with six vanadium atoms (green) and twelve oxygen atoms (red) in a distorted octahedral arrangement. Two nitro groups (-NO2) are coordinated to the cluster, with nitrogen atoms (blue) and oxygen atoms (red) visible.</p>
V6-C6	 <p>A ball-and-stick model of a V6-C6 complex. It features a central vanadium (V) cluster with six vanadium atoms (green) and twelve oxygen atoms (red) in a distorted octahedral arrangement. Two cyclohexane rings are coordinated to the cluster, with carbon atoms (grey) and oxygen atoms (red) visible.</p>
V6-TPY	 <p>A ball-and-stick model of a V6-TPY complex. It features a central vanadium (V) cluster with six vanadium atoms (green) and twelve oxygen atoms (red) in a distorted octahedral arrangement. Two terpyridine (TPY) ligands are coordinated to the cluster, with nitrogen atoms (blue) and carbon atoms (grey) visible.</p>
V6-C18	 <p>A ball-and-stick model of a V6-C18 complex. It features a central vanadium (V) cluster with six vanadium atoms (green) and twelve oxygen atoms (red) in a distorted octahedral arrangement. Two long-chain aliphatic ligands are coordinated to the cluster, with carbon atoms (grey) and oxygen atoms (red) visible.</p>
V6	 <p>A ball-and-stick model of a V6 cluster. It features six vanadium atoms (green) and twelve oxygen atoms (red) in a distorted octahedral arrangement.</p>
V10	 <p>A ball-and-stick model of a V10 cluster. It features ten vanadium atoms (green) and twenty oxygen atoms (red) in a distorted octahedral arrangement.</p>

1. STATE OF ART

1.1 Introduction

In this chapter, we will present the state of art necessary to illustrate the work done in this PhD. We will first state the basis of the experimental and theoretical charge density study. In the second and third part we will give some insight in the POM and POV compounds. Finally, in the last subsection the experimental and theoretical charge density studies will be described.

1.2 Charge density methodology

1.2.1 Experimental charge density analysis from X-ray diffraction

In 1912, the German physicist Max Von Laue published the first paper demonstrating the X-ray diffraction from a crystal. He was awarded the Nobel Prize in 1914. In 1913, William Lawrence Bragg and his father, William Henry Bragg presented the principle of diffraction, known as Bragg's Law illustrated by the Equation 1.1.

$$n\lambda = 2d_{hkl}\sin\theta \quad (1.1)$$

Where,

n the an order of the reflection,

λ is the wavelength,

d_{hkl} is the spacing between the planes in the atomic lattice, and

θ is the angle between the incident ray and the scattering planes, as shown in Figure 1.1.

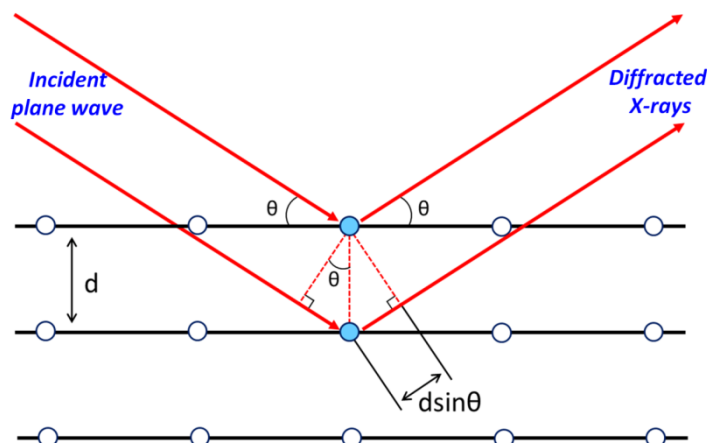


Figure 1.1. Diagram of the Bragg law

The possibility to probe the electronic structure of atoms by means of X-ray was recognized quite soon after the first diffraction experiments. In 1915, P. Debye wrote: *“It seems to me that experimental study of the scattered radiation, in particular from light atoms, should get more attention, since along this way it should be possible to determine the arrangement of the electrons in the atoms”* [Debye, 1915]. However, at that time measurements were not accurate enough to precisely detail the electron density distribution.

Technical developments that started in the 1960s and are still continuing have made X-ray diffraction a powerful tool for mapping the charge distribution in crystals [Koritsanszky & Coppens, 2001; Gatti, 2012]. These developments include:

1) improvements of the data quality, provided by semi-automatic diffractometers coupled with scintillation detectors;

2) availability of high power sources, like synchrotron radiation storage rings, and of neutron diffraction (for an independent assessment of thermal motion and atomic positions);

3) developments of models of electron density from measured Bragg intensities.

The main purpose of understanding a charge density analysis (either experimental or theoretical) is to shed some light on the combined information of physical properties, chemical bonding, and topological parameters. As Philip Coppens said, *“new theoretical methods and in particular Bader’s development of the density based “Theory of Atoms in Molecules”, combined with the exponential increase in computing power have created a link between theory and experiment which opened a new phase in electron density research in which the emphasis is very much on interpretation of the results and their application in the understanding of chemical, physical and biological phenomena.”* in the preface of book “Modern Charge-Density Analysis” [Gatti, 2012]. The applications of charge density are focused on the following fields:

Materials Science. Use of the charge density (CD) analysis in materials science has become increasingly pursued in the last decade, since this tool has a special ability to unveil, at an atomistic level, features that are notably important for material design and performance, while being difficult or often even impossible to be revealed with other approaches. Their analysis has then involved the study of thermally smeared densities, deformation densities, orbital populations and the exploitation of interpretive tools like QTAIM [Bader, 1985; Bader, 1990], Electron Localization

Indicator (ELI) [Kohout, 2004; Kohout, 2007], Hirshfeld Surfaces (HS) [Spackman, 2008; Spackman, 2009.] and electrostatic properties [Overgaard, 2002].

Bio-macromolecules. One of the major outcomes of research in electron density analysis has been the ability to model macro-molecules, especially those of interest in Biology and Biochemistry. Pioneering work was carried out by Claude Lecomte and co-workers, who exploited one of the most attractive feature of the pseudoatom multipolar expansion, namely the exportability of atomic parameters. Lecomte and co-workers have systematically investigated peptides using experimental methods (X-ray diffraction) and constructed two libraries of multipolar atom model refinement, ELMAM (Experimental Library of Multipolar Atom Model) [Pichon-Pesme, 1995; Zarychta, 2007] and ELMAM2 [Domagała, 2008]. This atomic level of description can provide a novel of electrostatic interactions to understand inhibitor-protein recognition and specificity in docking studies.

Electron density in compounds under perturbation. The progresses of the experimental techniques make nowadays available data collections on compounds under conditions often called “extreme”, that means under some kind of stress or excitation (mechanical, magnetic, electric, photonic etc.). “Extreme” indicates that the materials are far from their normal operative conditions. The aim of these studies is analyzing the response upon the perturbation.

Crystal Engineering. As mentioned by Desiraju, crystal engineering concerns *the understanding of intermolecular interactions in the context of crystal packing and in the utilization of such understanding in the design of new solids with desired physical and chemical properties* [Desiraju, 1989]. The tools and approaches of charge density analysis will play an increasing important role in addressing issues of concern in crystal engineering. This domain has quite deliberately interpreted the term “charge density analysis” quite broadly, with the aim of demonstrating the wealth of complementary information that can be obtained from *ab initio* calculations (on molecules and on the crystal) and X-ray diffraction measurements on single crystals, especially when the capabilities of modern graphics are exploited. It is important to recognize that this definition involves two important goals: (i) understanding the nature of intermolecular interactions; and (ii) building on that knowledge through rational design of new crystalline solids.

Stereochemistry. Stereochemistry remains extremely important in the modern chemistry, especially when the nature of chemical bonds in a molecule is somewhat

ambiguous and the localization or delocalization of electron pairs is such that a simple Lewis type model does not hold. The use of many mathematical and geometrical analyses of the charge density, especially within QTAIM framework [Tiana, 2010], sometimes has encouraged this tendency. Stereochemical problems, existing in transition metal complexes [Macchi, 2007], and compounds with hypervalent atoms [Leusser, 2004; Kocher, 2004], are illustrated by using the information from the electron density for the purposes of retrieving chemical concepts or chemical environment, not limited to bonded or non-bonded electron pairs [Farrugia, 2006].

Chemical reactivity. Frontier Molecular Orbital (FMO) theory has provided a very powerful basis for explaining, and often predicting, many aspects of chemical reactivity. Though FMO theory is useful and largely exploited, the molecular orbitals being unobservable experimentally. The approaches based on charge density analysis and related properties bring us a new insight to a better understanding of chemical reactivity on quantum observables. The widely-used reactivity indicator is molecular electrostatic potential (EP), mapped on molecular surfaces (e.g. the isodensity surface or the Hirshfeld surface), which is used for exploring molecular recognition and describing reactivity. The analysis of EP topography enables us to know the probable chemical reaction pathways and the predictable interaction sites or regions by the EP value determination. The other reactivity indicators, such as Laplacian of electron density, atomic net charge, ELI/ELF, can also reveal important chemical information about chemical reactivity.

1.2.2 Charge density analysis steps

Charge density analysis based on X-ray diffraction can be summarized in the steps given in Figure 1.2.

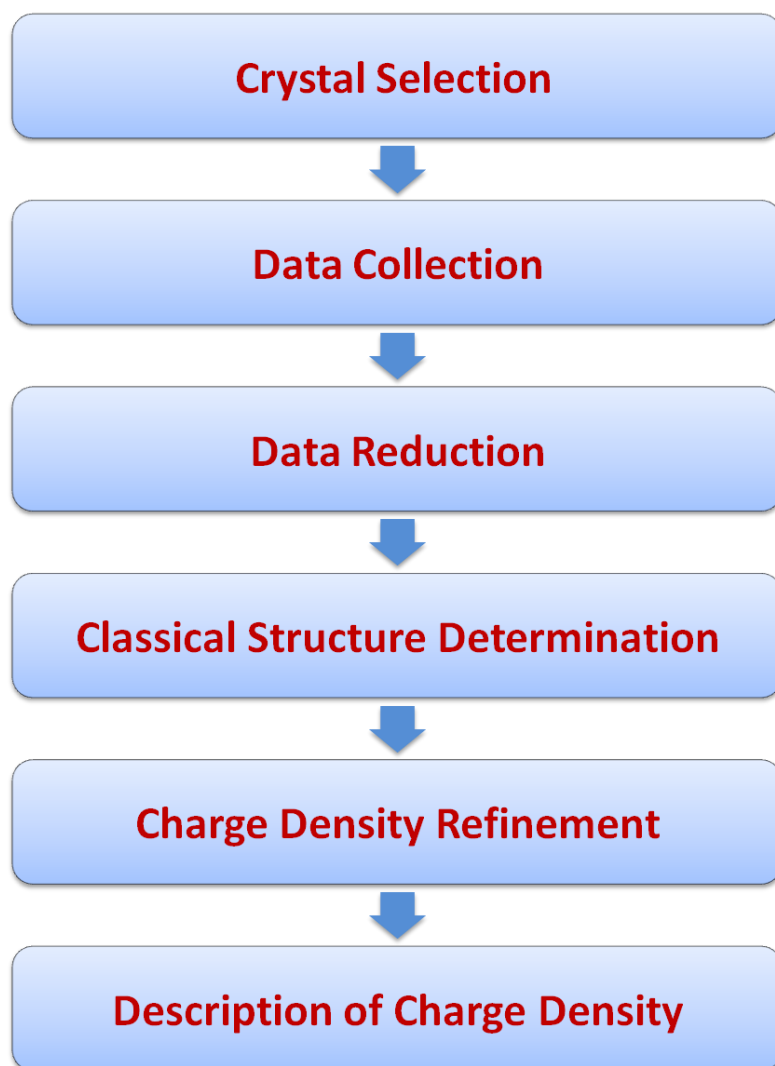


Figure 1.2. The process of charge density analysis

Crystal Selection. There are various methods to get single crystals such as evaporating a supersaturated solution, solvent liquid-liquid diffusion, solvent vapour-liquid diffusion (Figure 1.3). To obtain good quality high resolution data, a well diffracting crystal of a reasonable size and shape without fractures and twinning is necessary. The crystal should be not too small or too large, and the size of a good crystal is just smaller than the X-ray beam size. If the crystal is too small, its scattering power is very limited and the diffraction intensity is weak; if a crystal is too large that the size extends beyond the X-ray beam size, the resulted problems of scale factor, and large absorption might cause the molecular modeling too difficult even impossible. The diffraction resolution for a crystal of small organic molecules in charge density measurement should be at least $\sin\theta/\lambda = 1.0 \text{ \AA}^{-1}$.

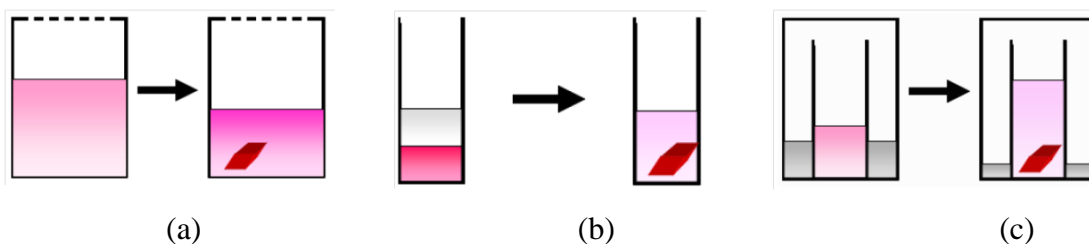


Figure 1.3. Methods of single crystal growth. (a) Slow Evaporation in supersaturated solution; (b) solvent liquid-liquid diffusion; (c) solvent vapour-liquid diffusion.

Data collection. The diffraction data is usually collected on the automatic four-circles diffractometer, which gives access to four different angular orientations (Figure 1.4).

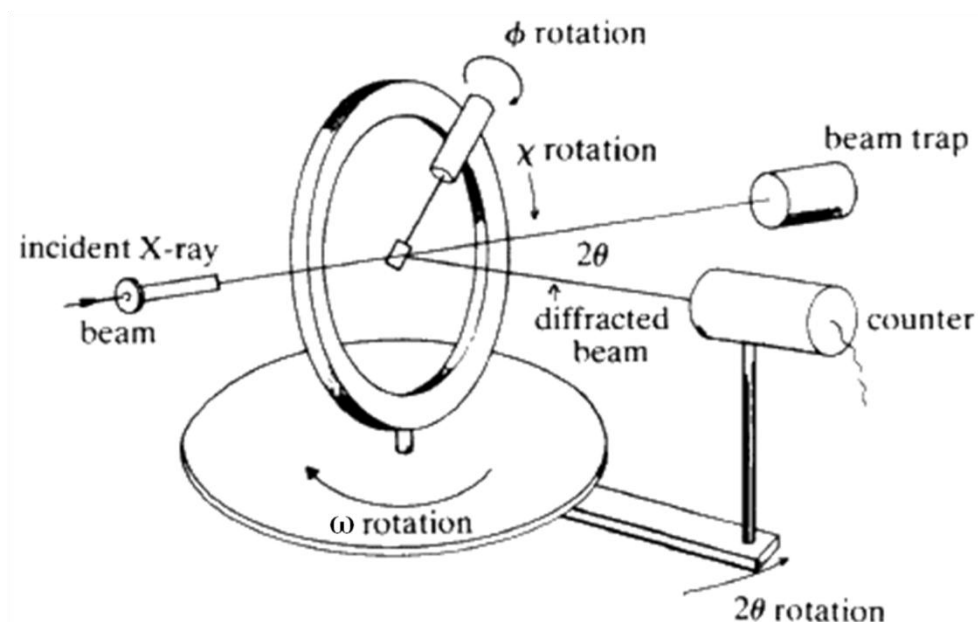


Figure 1.4. Principle of a four-circles diffractometer. The diffractometer can rotate around four axes: (1) ω around the axis of goniometer head; (2) ϕ around the vertical axis; (3) χ around the axis which form a variable angle with respect to the vertical ω ; (4) 2θ , the detector can be rotated around a vertical by an angle of 2θ .

Strategy for the high resolution charge density measurement differs from that for standard resolution spherical IAM (Independent Atom Model). The precision of the data set is governed by multiple measurements of the same reflection, leading to satisfactory redundancy and completeness up to high resolution angles. Low temperature measurement is necessary to minimize atomic thermal motions. A mathematical measure of the data quality is the internal R_{int} factor defined as:

$$R_{int} = \frac{\sum |I_{obs} - \langle I_{obs} \rangle|}{\sum I_{obs}} \quad (1.2)$$

where F_{obs} is the observed intensity. It should be < 0.05 for a good measurement.

Data Reduction. The reduction of integrated intensity to structure factor amplitudes is a well-developed procedure that can lead to accurate and reproducible data [Blessing, 1997].

Classical structure determination. In crystallography, the classically accepted and widely used model to refine a crystal structure is the Independent Atom Model (IAM). IAM is commonly used in standard resolution crystallography (0.8 \AA^{-1}) and suitable for determining the 3D structure/geometrical parameters of molecule, which is called “classic structure determination”. This model is used as the initial one in all further charge density determinations.

Charge density refinement. Charge density refinement is based on the pseudo-atomic multipolar model.

1.2.3 Crystallographic refinement

The main task of a crystallographic refinement is to optimize the electron density model using a least-squares procedure to manipulate the diffraction data [Tronrud, 2004].

Electron density. For a molecular system of N electrons and M nuclei, the stationary state function (ψ) is a function of the electronic spin and space coordinates ($\tau_i = (s_i, \mathbf{r}_i)$; $i = 1, 2, \dots, N$) and, within the Born-Oppenheimer approximation, the fixed nuclear space coordinates (\mathbf{R}_k ; $k = 1, 2, \dots, M$). The probability of finding any of the electrons in the volume element $d\mathbf{r}$ is given by

$$\rho(\mathbf{r}) d\mathbf{r} = N \{ \int |\psi|^2 d\tau' \} d\mathbf{r} \quad (1.3)$$

where $d\tau'$ denotes integration over all spin coordinates and the space coordinates of all electrons but one [Koritsanszky, 2001]. In the literature, the terms “charge density” and “electron density” are often used interchangeably even when talking about “charge density distribution” or “electron density distribution” [Spackman, 1997].

Structure factor. The intensities obtained by measurement of X-ray diffraction, are the square of the structure factor. The structure factor is a mathematical function

describing the diffraction by a unit cell [Born, 1926]. It plays a central role in the refinement of crystal structures and independent of the method and condition of the observation of the reflection [Stewart, 1980]. The structure factor is expressed by:

$$F(\mathbf{H}) = \sum_{j=1}^N f_j(\mathbf{H}) e^{2\pi i \mathbf{H} \mathbf{r}_j} \quad (1.4)$$

Where \mathbf{H} represents a vector in the reciprocal space, $\mathbf{H} = h\mathbf{a}^* + k\mathbf{b}^* + l\mathbf{c}^*$; \mathbf{r}_j is the position vector of j atom in the unit cell, and f_j is the dynamic scattering factor of it [Coppens, 1997]. In X-ray diffraction, f_j is a measure of the scattering amplitude of a wave by an isolated atom, and is the Fourier transform of the electron density:

$$f_j(\mathbf{H}) = \int_V \rho_j(\mathbf{r}) e^{2i\pi \mathbf{H} \mathbf{r}} dV \quad (1.5)$$

The integration extends over the whole atomic volume V . So, the relation between $F(\mathbf{H})$ and the electron density within the crystal is expressed by:

$$F(\mathbf{H}) = \int_V \rho(\mathbf{r}) e^{2i\pi \mathbf{H} \mathbf{r}} dV \quad (1.6)$$

The structure factors are defined only at the discrete set of reciprocal lattice points therefore the electron density in the unit cell may then be obtained through an inverse Fourier transform summation of an infinite number of \mathbf{H} .

$$\rho(\mathbf{r}) = \frac{1}{V} \sum_{\mathbf{H}} F(\mathbf{H}) e^{-2\pi i \mathbf{H} \mathbf{r}} = \frac{1}{V} \sum_{\mathbf{H}} |F(\mathbf{H})| \cos [2\pi \mathbf{H} \mathbf{r}_j - \varphi(\mathbf{H})] \quad (1.7)$$

φ is the phase angle of the structure factor (equal 0 or π for the centrosymmetric structures).

Least squares refinement. R factor is a measure of the agreement between the structure factor amplitudes calculated from a crystallographic model and those from experimental X-ray diffraction data:

$$R = \frac{\sum_{\mathbf{H}} ||F_{obs}(\mathbf{H})| - k|F_{calc}(\mathbf{H})||}{\sum_{\mathbf{H}} |F_{obs}(\mathbf{H})|} \quad (1.8)$$

where $(\mathbf{H} = h, k, l)$ are the indices of the reciprocal lattice points, and k , the scale factor:

$$k = \frac{\sum_{\mathbf{H}} F_{calc}(\mathbf{H})}{\sum_{\mathbf{H}} F_{obs}(\mathbf{H})} \quad (1.9)$$

F_{obs} and F_{calc} are the observed and calculated structure factors. The R factor is

calculated to evaluate the structure refinement progress and finally to assess the structure quality. The commonly used method for the refinement process is the least squares (LS) method, in which the residual function to be minimized, is

$$\Delta^2 = \sum_{\mathbf{H}} w_{\mathbf{H}} \left[\frac{1}{k} |F_{\text{obs}}(\mathbf{H})| - |F_{\text{calc}}(\mathbf{H})| \right]^2 \quad (1.10)$$

where k and $w_{\mathbf{H}}$ are the scale and weighting factors, respectively, and the F_{obs} and F_{calc} are observed structure factor and calculated structure factor. In other words, the aim of the refinement is to optimize the structural parameters for reducing the difference between F_{obs} and F_{calc} .

Independent atom model. The crystal structure reconstruction in the standard X-ray crystallography relies on the assumption that the core scattering dominates the total scattering of an atom; therefore the negative charge is mostly localized around the nuclei, which means that each atom is a neutral spherical entity. In this case, the molecule built of atoms is actually considered as a superposition of isolated, spherical atomic densities, forming the promolecule. This simple assumption is called Independent Atom Model (IAM) and the molecular Electron Density (ED) is described by equation:

$$\rho_{IAM}(\mathbf{r}) = \sum_k \rho_k^0(\mathbf{r} - \mathbf{R}_k) \quad (1.11)$$

where R_k is the position of the atom k . IAM is commonly used in standard resolution crystallography (0.8 \AA^{-1}) and is efficient for heavier atoms, where $e_{\text{valence}} / e_{\text{total}}$ ratio (e_{valence} and e_{ratio} are the number of valence and total electrons, respectively) is rather low; however it has many disadvantages especially for the hydrogen atoms which have only one electron - as a result the X-H distances are shortened with respect to internuclear distances. IAM neglects the inter- and intra-molecular charge transfer (*e.g.* between atoms or to the lone pairs) and imposes the electroneutrality and spherical form of atoms. Programs used for the IAM structure solution and refinement are SIR92 [Altomare, 1993] and SHELXL97 [Sheldrick, 2008], respectively.

1.2.4 Charge density models

X-ray diffraction gives information on electron distribution in the crystal. Conventional structure determination relies on the strong attraction between the electrons and the nuclei, which can locate the nuclear positions of heavy atoms but

not the lightest atoms, like H atom, which lack a core shell of electrons. The aim of the charge density analysis is to map the electron distribution in crystals and analyze all the detail that carries the information on chemical bonding. Several models used in X-ray crystallography are designed for the best fitting of the experimental and theoretical diffraction data for better description of the atomic density, from the spherical to aspherical one, has evolved during last few decades.

Kappa Formalism. IAM reproduces the structural results of a conventional least squares (LS) refinement, but is clearly unable to describe any electron redistribution due to bonding. The next step is to distinguish the atomic core density, kept fixed with respect to the neutral atom, from the atomic valence density which is instead allowed to be non neutral and to expand or contract, reflecting the bonding environment, and the whole electroneutrality being maintained for the crystal. P. Coppens *et al* [Coppens, 1997] proposed a radial kappa formalism to improve IAM to allow the charge transfer between atoms. In Kappa formalism, the contributions from the core shell electrons and those from the valence are separated, which are still considered to be spherical [Coppens, 1997]. The total density of an atom is defined by the sum of core and valence densities:

$$\rho_{tot}(r) = \rho_{core}(r) + P_{val}\kappa^3\rho_{val}(\kappa r) \quad (1.12)$$

where P_{val} is the valence population and κ , the spherical expansion/contraction coefficient. If κ is larger than unity, the atom is contracted with respect to a free atom and when κ is smaller than unity the atom is expanded. In general the electronegative atoms, such as oxygen or nitrogen, tend to expand, as they accept the electrons in the bond formation process. In kappa model the charge q of an atom can be estimated from the difference of valence population of the free atoms and valence population after kappa model refinement (*i.e.* $q = N_{val} - P_{val}$).

However, the κ -refinement allows a crude representation of the charge density and it is no longer used in modern CD analysis, despite the fact that it represents a possible useful intermediate step in the course of a multi-step least squares refinement procedure.

Hansen-Coppens Multipolar Model. Most of the recent charge density (CD) studies adopt a more flexible model, where each “atomic” unit is described by multipole expansion (MM), composed by a set of monopole terms, yielding the

population of the atom, and a number of higher poles allowing for deformation with respect to spherical symmetry. The main progresses occurred during the 1970s when, among many other approaches, the method of multipolar expansion of the electron density was recognized as the most applicable and accurate, hereinafter called the multipole model (MM). Several MM formulations were proposed by [Stewart, 1975; Kurki-Suonio, 1977], but the intuitive notation introduced by Hansen and Coppens [Hansen & Coppens, 1978], became afterwards the most popular. Within this method, the electron density of a crystal is expanded in atomic contributions, or better in terms of rigid pseudoatoms, i.e. atoms that behave structurally according to their electron charge distribution and rigidly follow the nuclear motion.

In the Hansen-Coppens Multipolar Model, the total atomic electron density is treated as aspherical and is divided in three parts:

$$\begin{aligned} \rho_{tot}(r) = & \rho_{core}(r) + P_{val}\kappa^3\rho_{val}(\kappa r) \\ & + \sum_{l=0}^{l_{max}} \kappa'^3 R_l(\kappa' r) \sum_{m=0}^{+l} P_{lm} d_{lm\pm}(\theta, \varphi) \end{aligned} \quad (1.13)$$

where P_{val} is the valence population, P_{lm} 's are the multipole populations and κ and κ' are the contraction/expansion coefficients for spherical and aspherical valence density, respectively. The two first terms are the spherically averaged core and valence electron densities of an atom. The third term is a sum of angular functions $d_{lm\pm}$ modulated by a Slater-type function which are density-normalized real spherical harmonic functions, and describes the multipolar electron density. The core and spherical valence densities are calculated from Hartree-Fock (HF) wave functions, and the radial function R_l is expressed as:

$$R_l(r) = \frac{\xi_l^{n_l+3}}{(n_l+2)!} r^{n_l} e^{-\xi_l r}, n_l \geq 1 \quad (1.14)$$

Each number l corresponds to different multipolar level (for visualization see Figure 2.13 and Table 1.1) – there are three dipoles, five quadrupoles, seven octapoles and nine hexadecapoles, in the current versions of MoPro [Jelsch, 2005] and XD [Koritsanszky, 1995].

Table 1.1. Multipoles list in Cartesian coordinates (from MoPro manual).

Multipolar level, (l,m)	Angular Function not normalized
Monopole (0, 0)	1
Dipoles (1, 1), (1,-1), (1, 0)	x y z
Quadrupoles (2, 0), (2, 1), (2,-1), (2, 2), (2,-2)	$2z^2 - (x^2 + y^2)$ zx zy $(x^2 - y^2)/2$ xy
Octapoles (3, 0), (3, 1), (3,-1), (3, 2), (3,-2), (3, 3), (3,-3)	$2z^3 - 3z(x^2 + y^2)$ x [4z^2 - (x^2 + y^2)] y [4z^2 - (x^2 + y^2)] z (x - y) (x + y) 2xyz x^3 - 3xy^2 y^3 - 3yx^2
Hexadecapoles (4, 0), (4, 1), (4,-1), (4, 2), (4,-2), (4, 3), (4,-3) (4, 4), (4,-4)	$8z^4 - 24z^2(x^2 + y^2) + 3(x^2 + y^2)^2$ x [4z^3 - 3z(x^2 + y^2)] y [4z^3 - 3z(x^2 + y^2)] $(x^2 - y^2) [6z^2 - (x^2 + y^2)]$ 2xy [6z^2 - (x^2 + y^2)] z (x^3 - 3xy^2) z (y^3 - 3yx^2) $x^4 - 6x^2y^2 + y^4$ 4x^3y - 4xy^3

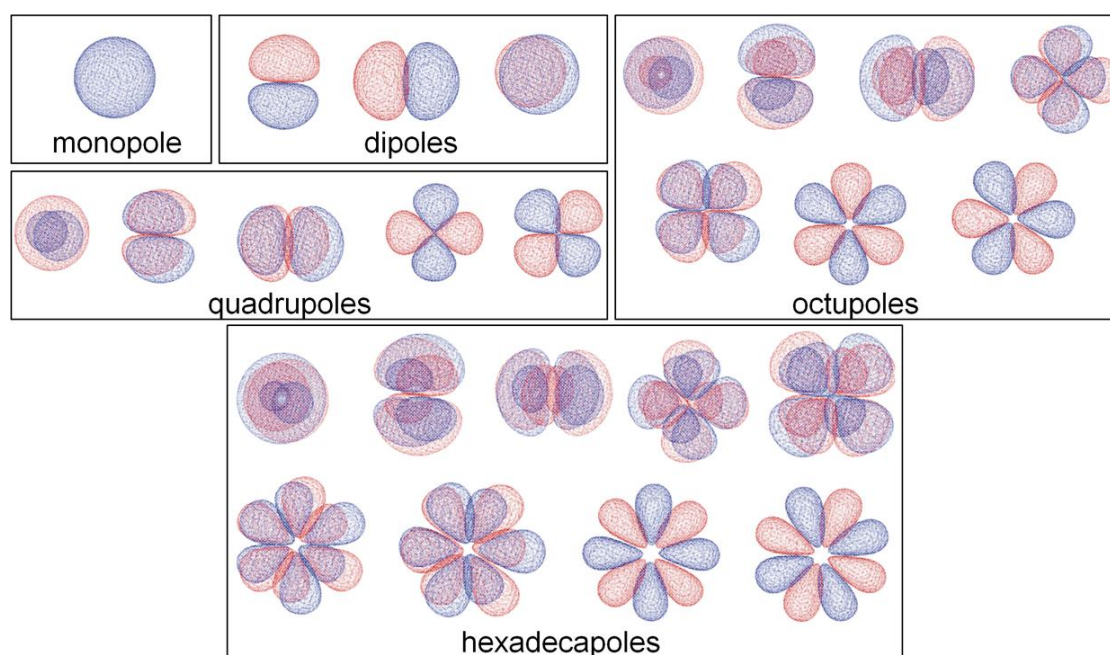


Figure 1.5. Visual representation of spherical harmonic functions (from monopole to hexadecapoles). Orthogonal axis system identical for all pictures. Blue regions – positive, red regions – negative. Pictures prepared with MoProViewer [Guillot, 2011].

1.2.5 Residual electron density

As mentioned above, the electron density, $\rho(\mathbf{r})$, is the Fourier transform of the structure factors $F(\mathbf{H})$. The residual electron density, $\Delta\rho_{\text{res}}(\mathbf{r})$, is defined as the

difference between the observed and the calculated electron density.

$$\Delta\rho_{res}(\mathbf{r}) = \rho_{obs}(\mathbf{r}) - \rho_{calc}(\mathbf{r}) \quad (1.15)$$

It can be interpreted as a measure of the error in electron density and due to the combination of an inadequate model and the errors in the observed structure factors. The residual density map should be featureless and for an ideal agreement between model and data - completely clear. If the model is unsatisfied, the least-squares parameters will be biased such as to minimize the residual density. The analysis of the residual density can help identify anharmonic sites and can reveal crystal-field effects directly.

1.2.6 Deformation electron density

The difference between the total electron density and that based on the promolecule density (IAM) is called the deformation density. It is in fact a representation of the electron density in the bonding regions of the molecule and can be described as following:

$$\Delta\rho_{def}(\mathbf{r}) = \rho(\mathbf{r}) - \rho_{pro}(\mathbf{r}) = \frac{1}{V_{cell}} \sum_{\mathbf{H}} [F_{obs}(\mathbf{H}) - F_{IAM}(\mathbf{H})] e^{-2\pi i \mathbf{H} \mathbf{r}_j} \quad (1.16)$$

The term promolecule refers to reference electron density model prior to molecule formation. It is equivalent to the IAM model [Spackman, 1986]. In the several deformation densities, neutral spherical atoms are subtracted from the observed density [Wang, 1976].

The *experimental deformation electron density* maps are calculated from the observed structure factors using the following equation:

$$\Delta\rho_{exp}(\mathbf{r}) = \frac{1}{V_{cell}} \sum_{\mathbf{H}} [|F_{obs}(\mathbf{H})| e^{i\varphi_{mult}} - |F_{IAM}(\mathbf{H})| e^{i\varphi_{IAM}}] e^{-2\pi i \mathbf{H} \mathbf{r}_j} \quad (1.17)$$

where φ_{mult} are the phase obtained from the best multipolar model and $\Delta\rho_{exp}$ include the thermal smearing effects.

The *dynamic deformation electron density* of the model:

$$\Delta\rho_{dyn}(\mathbf{r}) = \frac{1}{V_{cell}} \sum_{\mathbf{H}} [|F_{mult}(\mathbf{H})| e^{i\phi_{mult}} - |F_{IAM}(\mathbf{H})| e^{i\phi_{IAM}}] e^{-2\pi i \mathbf{H} \cdot \mathbf{r}_j} \quad (1.18)$$

while the *static deformation electron density* maps:

$$\rho_{static}(\mathbf{r}) = P_{val} \kappa^3 \rho_{val,IAM}(\kappa, \mathbf{r}) - N_{val} \rho_{val,IAM}(\mathbf{r}) + \sum_{l=0}^{l_{max}} \kappa'^3 R_l(\kappa', \mathbf{r}) \sum_{m=0}^{+l} P_{lm} d_{lm\pm}(\theta, \varphi) \quad (1.19)$$

are free from thermal effects and can be directly compared with the theoretical maps.

The deformation density has been used extensively in charge-density studies for recognition of bonding features and for diagnostic purposes, especially for showing the charge accumulation in the bonding and lone pairs regions. However, the deformation maps cannot produce quantitative information on the chemical bonding because it is a thermally averaged function and is subject to the definition of the reference density. In addition they lose qualitative information when the chemical bond under investigation is less conventional than that in simple organic molecules [Gatti, 2013].

The deformation and residual density maps should be calculated after each step of the refinement process to assess the quality of model under construction and to diagnose directly a wrong refinement path and unrealistic outputs.

1.2.7 Electrostatic potential

The related physical properties from experimental electron density are net atomic charge, dipole moment, electric field or electric gradient, electrostatic potential and so on. Electrostatic potential is an important property in the study of molecular region recognition, intermolecular interactions, chemical reactivity, and especially so when both the transfer of electrons between and the reactants' ED polarization are negligible [Pathak, 1990; Gadre, 1999].

The **Electrostatic potential** for an assembly of positive point nuclei and continuous distribution of negative electronic charge is calculated from the charge density using the following equation:

$$\Phi(\mathbf{r}) = \sum_{k=1}^M \frac{Z_k}{|R_k - \mathbf{r}|} - \int \frac{\rho(\mathbf{r}')}{|\mathbf{r}' - \mathbf{r}|} d\mathbf{r}' \quad (1.20)$$

where R_k is the position and Z_k is the charge of the k -th nucleus. Sign of the potential

the negative regions of the molecule will determine the approach of electrophilic reagents. An advantage of the experimental electrostatic potential over the potential from single-molecule calculation is that many-body effects in the crystal are taken into account. Electrostatic potential of an atom, functional group or a molecule in a crystal can be calculated in order to find the electrophilic or nucleophilic sites that play a crucial role in molecular recognition. It is noteworthy that the electrostatic forces have a long-distance character and they determine the path along which the reactant molecules approach each other.

1.2.8 AIM theory and topological analysis

A quantitative investigation of the bonding was performed by means of a topological analysis according to AIM theory [Bader, 1990]. The topology of the electron density is based on the gradient of electron density given in equation 1.25.

$$\nabla\rho(\mathbf{r}) = \mathbf{i} \frac{\partial\rho(\mathbf{r})}{\partial x} + \mathbf{j} \frac{\partial\rho(\mathbf{r})}{\partial y} + \mathbf{k} \frac{\partial\rho(\mathbf{r})}{\partial z} \quad (1.25)$$

The analysis is based in the identification of critical points (CPs) where the gradient is zero ($\nabla\rho(\mathbf{r})=0$).

The characteristics of the total electron density topology may be analyzed by a search of the critical points (CP) such as minima, maxima, or saddle points (Figure 1.7).

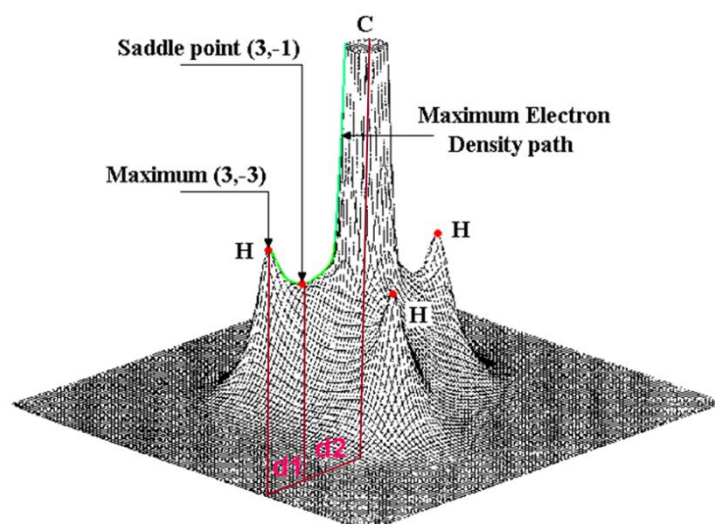


Figure 1.7. 3-D representation of the electronic charge density. The CP are indicated.

The characteristic of CP is extracted from the Hessian matrix, which is 3×3

matrix of the partial second derivatives of the electron density:

$$H_{ij} = \frac{\partial^2 \rho}{\partial x_i \partial x_j}, \quad i \leq j = 1, 2, 3 \quad (1.26)$$

The rank of this matrix (*i.e.* the number of the non-zero eigenvalues), which equals three for all stable molecules, and its signature, which is then algebraic sum of the eigenvalues signs are assigned to each CP. The three eigenvalues are labeled $\lambda_{1,2,3}$ with the condition: $\lambda_1 \leq \lambda_2 \leq \lambda_3$. There are four possible critical points of rank three:

1. **(3, -3)** atomic critical point: all curvatures are negative and charge density (ρ) is a local maximum – it leads to the definition of the topological atom, which is the union of this attractor and associated basin;

2. **(3, -1)** bond critical point (BCP) which is an effect of interaction between two topological atoms, with a bond path (BP) being the interaction line of the maximum density linking these two atoms, passing by BCP; at the BCP two curvatures are negative and ρ is a maximum in the plane defined by their corresponding axes; ρ is a minimum along the third axis that is perpendicular to this plane;

3. **(3, +1)** ring critical point (RCP): two curvatures are positive and ρ is a minimum in the plane defined by their corresponding axes; ρ is a maximum along the third axis that is perpendicular to this plane;

4. **(3, +3)** cage critical point (CCP) is found inside the molecule surrounded by ring surfaces: all curvatures are positive and ρ is a local minimum.

The pairs of trajectories originating at this point and terminating at the two (3,-3) CPs define the line of maximum density linking two atoms. The existence of this atomic interaction line indicates charge accumulation between the nuclei, a necessary condition for a bond formation. The interaction line corresponding to equilibrium nuclear separation is referred to as the bond path (BP), and its presence is considered a sufficient condition for two nuclei to be bonded. The definition and the classification of the chemical bond in the topological analysis of ρ are based on the existence of a (3,-1) CP between neighboring atoms and the properties of charge density at this point. This point is characterized by one positive curvature λ_3 , along the internuclear line and negative curvatures, λ_1 and λ_2 in two perpendicular directions.

Based on the AIM theory, the two negative curvatures of ρ at the BCP define the bond ellipticity ε as:

$$\varepsilon = \frac{\lambda_1}{\lambda_2} - 1 \quad (1.27)$$

which is a measure of the extent to which charge is preferentially accumulated in a plane perpendicular to the BP. Since $\varepsilon = 0$ for a cylindrically symmetric bond and is greater than 0 for a double bond, it is a measure of the π character and the extent of conjugation.

An important function of the electron density is the Laplacian and can be obtained from the second derivatives of the total electron density. The Laplacian of electron density is the sum of the three eigenvalues of curvature of diagonal elements in the Hessian matrix:

$$\nabla^2 \rho(\mathbf{r}) = \frac{\partial^2 \rho(\mathbf{r})}{\partial x^2} + \frac{\partial^2 \rho(\mathbf{r})}{\partial y^2} + \frac{\partial^2 \rho(\mathbf{r})}{\partial z^2} = \lambda_1 + \lambda_2 + \lambda_3 \quad (1.28)$$

Relatively high charge density $\rho(\mathbf{r})$ and $\nabla^2(\mathbf{r}) < 0$, (the electron density is locally concentrated at \mathbf{r}) are considered to characterize a shared-shell bond, while a low ρ and $\nabla^2(\mathbf{r}) > 0$, (the electron density is locally depleted at \mathbf{r}) indicate a closed-shell interaction (i.e. ionic, hydrogen bond or van der Waals interaction). The local properties of ρ at the BCP are thus characteristic of the particular type of interaction occurring between bonded atoms.

According to the AIM theory, the molecular space is partitioned into "basins" Ω , each corresponding to the space spanned by the set of paths ending at an attractor [Bader 1985, Bader, 1990; Bader 1998, Lecomte, 2003]. The surface separating basins are mathematically defined by trajectories of $\nabla\rho$ that terminate at a (3, -1) bond critical point. Since trajectories never cross, an interatomic surface is endowed with the property of zero-flux, that is a surface that is not crossed by any trajectory of $\nabla\rho$:

$$\nabla\rho(\mathbf{r}) \cdot \mathbf{n}(\mathbf{r}) = 0, \quad \forall \mathbf{r} \in S(\Omega, \mathbf{r}), \mathbf{n}(\mathbf{r}) \perp S(\Omega, \mathbf{r}) \quad (1.29)$$

where S is the interaction surface and is a unit vector perpendicular to the surface at point \mathbf{r} .

For a system in a stationary state an AIM property is obtained by integration of the corresponding property density (such as charge, volume, multipolar moments or energy) over the atomic basin:

$$A(\mathbf{\Omega}) = \int_{\Omega} A\rho(\mathbf{r})d\mathbf{r} \quad (1.30)$$

where A is a scalar, vector or tensor, *ex.* dipole moment:

$$\vec{\mu}(\mathbf{\Omega}) = \int_{\Omega} \vec{r}\rho(\mathbf{r})d\mathbf{r} \quad (1.31)$$

It implies the important consequence, that the physical property of the total system is a sum of its atomic properties:

$$A = \int_{\Omega} A(\mathbf{\Omega}) \quad (1.32)$$

It should be noticed that in order to calculate the formal charge of any atom, the integrated atom charge (AIM charge) has to be subtracted from the neutral value:

$$q = N_{neut} - N_{int} \quad (1.33)$$

According to Bader [Bader, 1990] (1990) and Cremer & Kraka [Cremer and Kraka, 1984 a, b] the atomic interaction may be characterized according to the values of $\rho(\mathbf{r}_c)$ and $\nabla^2\rho(\mathbf{r}_c)$ and also the kinetic energy density $G(\mathbf{r}_c)$ and the local energy density $H(\mathbf{r}_c)$ at the (3,-1) bond critical points in electron density.

$$H(\mathbf{r}_c) = G(\mathbf{r}_c) + V(\mathbf{r}_c) \quad (1.34)$$

The total energy density $H(\mathbf{r}_c)$ is defined as the sum of a kinetic energy density $G(\mathbf{r}_c)$, and a potential energy density $V(\mathbf{r}_c)$ where $G(\mathbf{r}_c)$ is always positive and $V(\mathbf{r}_c)$ is negative.

The energy density can not be calculated directly from experimental results but Abramov [Abramov, 1997] has proposed the empirical formula:

$$G(\mathbf{r}_c) = \frac{3}{10} (3\pi^2)^{\frac{2}{3}} \rho^{\frac{5}{3}}(\mathbf{r}_c) + \frac{1}{6} \nabla^2 \rho(\mathbf{r}_c) \quad (1.35)$$

The Laplacian and the energy density are related by:

$$2G(\mathbf{r}_c) + V(\mathbf{r}_c) = \left(\frac{1}{4}\right) \nabla^2 \rho(\mathbf{r}_c) \quad (1.36)$$

The sign of $H(\mathbf{r}_c)$ determines whether the accumulation of charge at \mathbf{r} is stabilized ($H(\mathbf{r}_c) < 0$) or destabilized ($H(\mathbf{r}_c) > 0$). The covalent bond is characterized by a predominance of a local potential energy density at BCP, i.e. $H(\mathbf{r}_c) < 0$. On the other

hand, the closed shell interaction is characterized by the positive $H(\mathbf{r}_c) > 0$. The electron density at BCP, $\rho(\mathbf{r}_c)$, is a direct indicator of the strength of such interaction.

Classifications of the different interactions have been summarized by Gatti [Gatti, 2005] in Figure 1.8.

The dichotomous classification^a based on the sign of $\nabla^2 \varrho_b$

Property	Shared shell, $\nabla^2 \varrho_b < 0$ Covalent and polar bonds	Closed-shell, $\nabla^2 \varrho_b > 0$ Ionic, H-bonds and vdW molecules
λ_1 VSCC ^b	$\lambda_{1,2}$ dominant; $ \lambda_{1,2} / \lambda_3 > 1$ The VSCCs of the two atoms form one continuous region of charge concentration	λ_3 dominant; $ \lambda_{1,2} / \lambda_3 \ll 1$ $\nabla^2 \varrho > 0$ over the entire interaction region. The spatial display of $\nabla^2 \varrho$ is mostly atomic-like
ϱ_b Energy lowering	Large By accumulating ϱ in the interatomic region	Small Regions of dominant $V(\mathbf{r})$ are separately localized within the boundaries of interacting atoms
Energy components	$2G_b < V_b $; $G_b/\varrho_b < 1$; $G_{b\parallel} \ll G_{b\perp}$; $H_b < 0$	$2G_b > V_b $; $G_b/\varrho_b > 1$, $G_b \gg G_{b\perp}$; H_b any value

Bond polarity is increasing \dashrightarrow \dashleftarrow Bond covalency is increasing

The classification^c based on the adimensional $|V_b|/G_b < 1$ ratio

Shared shell (SS)	Transit region, incipient covalent bond formation	Closed-shell (CS)
$ V_b /G_b > 2$	$1 < V_b /G_b < 2$	$ V_b /G_b < 1$
$H_b < 0$; $\nabla^2 \varrho_b < 0$ Bond degree (BD) = $H_b/\varrho_b \equiv$ Covalence degree (CD)	$H_b < 0$; $\nabla^2 \varrho_b > 0$ BD \equiv CD	$H_b > 0$; $\nabla^2 \varrho_b > 0$ BD \equiv Softness degree (SD)
BD large and negative	BD negative and smaller in magnitude than for SS interactions	SD positive and large
The larger is BD the more covalent is the bond	BD Approaching zero at the boundary with CS region	The larger is SD the weaker and closed-shell in nature is the bond

The classification^d based on the atomic valence shell and on both the local (*bcp*) and integral properties

	ϱ_b	$\nabla^2 \varrho_b$	G_b/ϱ_b	H_b/ϱ_b	$\delta(A,B)$	$\oint_{AB} \varrho(\mathbf{r}_s) d\mathbf{r}_s$
<i>Bonds between light atoms</i>						
Open-shell (covalent bonds); e.g. C–C, C–H, B–B	Large	$\ll 0$	< 1	$\ll 0$	\sim Formal bond order	Large
Intermediate interactions (polar bonds, donor-acceptor bonds; e.g. C–O, H ₃ B–CO)	Large	any value	≥ 1	$\ll 0$	$<$ Formal bond order	Large
Closed-shell (ionic bonds, HBs, van der Waals interactions; e.g. LiF, H...O, Ne...Ne)	Small	> 0	≥ 1	> 0	~ 0	Small
<i>Bonds between heavy atoms</i>						
Open-shell (e.g. Co–Co)	Small	~ 0	< 1	< 0	Formal bond order (unless bond delocalisation occurs)	Medium/large
Donor acceptor (e.g. Co–As)	Small	> 0	~ 1	< 0	$<$ Formal bond order	Medium/large

Figure 1.8. Three different classifications according to the AIM parameters. Reproduced from [Gatti, 2005].

1.2.9 *d*-orbital calculation

Though deformation density maps have implied important information for a qualitative assessment of the nature of chemical bonding, there is an obvious need for a quantitative evaluation of the results [Holladay, 1983]. In the case of transition-metal atoms *d*-orbital occupancies have been derived from least-squares multipole

population coefficients, using point-group specific relations, which are valid under the assumption that the d orbitals can be represented by single Slater-type orbitals and that the overlap between metal atom and ligand orbitals is small [Stevens & Coppens, 1979].

Based on Hansen-Coppens model [Hansen & Coppens, 1978], the d -orbital occupancies P_i can be derived from the experimental multipole populations by use of

$$P_i = \mathbf{M}^{-1} P_{lm\pm} \quad (1.37)$$

where $P_{lm\pm}$ is a vector containing the coefficients of the 15 spherical-harmonic functions generated by the products of the d -orbitals, for which $l = 0, 2$ or 4 [Holladay, 1983], and the P_i is a 15-element vector of the coefficients of the following fomula:

$$\rho_d = \sum_{i=1}^5 P_i d_i^2 + \sum_{i=1}^5 \sum_{j>1}^5 P_{ij} d_i d_j \quad (1.38)$$

where ρ_d is the d -electron density. The inverse matrix, \mathbf{M}^{-1} given in Figure 1.9 represented the generalized expression from which point group specific expression can be derived by omission of symmetry forbidden terms.

One has to take into account the local symmetry defined for the metal atom (Figure 1.9 and 1.10). Furthermore it has been demonstrated [Sabino, 2003] that the choice of the local coordinates system in case of low-symmetry complex is very important.

<i>d</i> -orbital populations	Mutipole populations											
	P_{00}	P_{20}	P_{22}	P_{40}	P_{42}	P_{44}						
P_{z^2}	0.200	1.04	0.00	1.40	0.00	0.00						
P_{xz}	0.200	0.520	0.943	-0.931	1.11	0.00						
P_{yz}	0.200	0.520	-0.943	-0.931	-1.11	0.00						
$P_{x^2-y^2}$	0.200	-1.04	0.00	0.233	0.00	1.57						
P_{xy}	0.200	-1.04	0.00	0.233	0.00	-1.57						
Mixing terms	P_{21}	P_{21-}	P_{22}	P_{22-}	P_{41}	P_{41-}	P_{42}	P_{42-}	P_{43}	P_{43-}	P_{44-}	
P_{z^2}/xz	1.09	0.00	0.00	0.00	3.68	0.00	0.00	0.00	0.00	0.00	0.00	
P_{z^2}/yz	0.00	1.09	0.00	0.00	0.00	3.68	0.00	0.00	0.00	0.00	0.00	
P_{z^2}/x^2-y^2	0.00	0.00	-2.18	0.00	0.00	0.00	1.92	0.00	0.00	0.00	0.00	
P_{z^2}/xy	0.00	0.00	0.00	-1.85	0.00	0.00	0.00	2.30	0.00	0.00	0.00	
P_{xz}/yz	0.00	0.00	0.00	1.60	0.00	0.00	0.00	1.88	0.00	0.00	0.00	
P_{xz}/x^2-y^2	1.88	0.00	0.00	0.00	-1.06	0.00	0.00	0.00	2.10	0.00	0.00	
P_{xz}/xy	0.00	1.88	0.00	0.00	0.00	-1.06	0.00	0.00	0.00	2.10	0.00	
P_{yz}/x^2-y^2	0.00	-1.88	0.00	0.00	0.00	1.06	0.00	0.00	0.00	2.10	0.00	
P_{yz}/xy	1.88	0.00	0.00	0.00	-1.06	0.00	0.00	0.00	-2.10	0.00	0.00	
$P_{x^2-y^2}/xy$	0.00	0.00	0.00	0.00	0.00	0.00	0.00	0.00	0.00	0.00	3.14	

Figure 1.9. Matrix \mathbf{M}^{-1} reproduced from [Holladay, 1983]

	Point group	Allowed values of l, m_{\pm} *	Dimension of M
I	$1, \bar{1}$	$l = 0, 2, 4, \text{all } m$	15×15
II	$2, m, 2/m$	$00, 20, 22+, 22-, 40, 42+, 42-, 44+, 44-$	9×9
III	$222, m2m, mmm$	$00, 20, 22+ 40, 42+, 44+$	6×6
IV	$4, 4/m, \bar{4}$	$00, 20, 40, 44+, 44-$	$5 \times 5 (4 \times 4)^\dagger$
V	$422, \bar{4}2m, 4mm, 4/mmm$	$00, 20, 40, 44+$	4×4
VI	$3, \bar{3}$	$00, 20, 40, 43+, 43-$	$5 \times 5 (4 \times 4)^\dagger$
VII	$32, 3m, \bar{3}m$	$00, 20, 40, 43+$	4×4
VIII	$6, \bar{6}, 6/m, 622, 6mm, \bar{6}m2, 6/mmm$	$00, 20, 40$	3×3
IX	$23, m\bar{3}, 432, \bar{4}3m, m\bar{3}m$	$00, 40 + (0.7403)44+\ddagger$	2×2

* Principal symmetry axis is z axis.
† Dimension can be reduced by rotation of coordinate system, see text.
‡ This function is usually described as the cubic harmonic K_4 .

Figure 1.10. Local symmetry reproduced from [Holladay, 1983].

1.2.10 Source function

Early in 1998, Bader and Gatti demonstrate that it is possible to view the electron density ρ at any point \mathbf{r} within a molecule as consisting of contributions from a source operating at all other points [Bader, 1998]. For a closed system with boundaries at infinity, the following equation gives the density at a point \mathbf{r} within an atomic basin:

$$\rho(\mathbf{r}) = \int \text{LS}(\mathbf{r}, \mathbf{r}') d\mathbf{r}' \quad (1.39)$$

the local source is expressed as:

$$\text{LS}(\mathbf{r}, \mathbf{r}') = -(1/4\pi) \nabla^2 \rho(\mathbf{r}') / |\mathbf{r} - \mathbf{r}'| \quad (1.40)$$

where $\nabla^2 \rho(\mathbf{r}')$ is the Laplacian of the electron density at a point \mathbf{r}' and $(4\pi |\mathbf{r} - \mathbf{r}'|^{-1})$ is a Green function or an influence function [Arfken, 1985].

The effectiveness of the Laplacian of the density in producing the electron distribution depends on the distance between the element of Laplacian of the density $\nabla^2 \rho(\mathbf{r}') d\mathbf{r}'$ and the point of interest given by \mathbf{r}' . The integral over a basin Ω of the local source for the density at \mathbf{r} is the source function from Ω , $S(\mathbf{r}, \Omega)$. Hence, the density at a point could be seen as caused by an internal source contribution from the atom where the point is located and by a sum of source contributions from the remaining atoms or groups of atoms within a molecule:

$$\rho(\mathbf{r}) = S(\mathbf{r}, \Omega) + \sum_{\Omega' \neq \Omega} S(\mathbf{r}, \Omega') \quad (1.41)$$

The integrated source function (SF) provides a measure of the relative importance of each atomic basin contribution to the density at the reference point.

Generally, Source Function (SF) is a relatively novel tool, which brings

additional perspective on chemical bonding properties. The source function enables one to view chemical bonding and other chemical paradigms from a totally new perspective and using only information from the electron density observable and its derivatives [Gatti, 2003; Gatti, 2013]. As a new topological descriptor, SF have been used for understanding chemical transferability, characterizing the hydrogen-bonded systems, the inorganic and metallorganic systems, illustrating the hypervalency, and the electron conjugation [Gatti, 2007; Gatti, 2012, Farrugia, 2009a, b].

1.2.11 Programs for charge density refinement and analysis

There are two important programs for charge density refinement and analysis using the Hansen – Coppens model:

MoPro package [Guillot, 2001; Jelsch, 2005], containing MoproGUI, Import2Mopro, VMopro, MoproView, can perform charge density refinement using least squares method. MoPro uses the Hansen-Coppens multipolar model to refine the charge density. All the charge density parameters can be refined by manual selection, in a step by step procedure or can be refined using automatic refinement option. After charge density refinement, one can use VMopro to output charge density properties, and display in the graphical interface, MoProViewer [Guillot, 2011], which makes it simpler with good user experience.

XD2006 [Volkov, 2006], is a computer program package for multipole refinement, topological analysis of charge densities and evaluation of intermolecular energies from experimental or theoretical structure factors.

These two softwares will be used in this work.

1.2.12 Charge density from theory

In theory, the many-electron wave function $\Psi_n(r_1, \dots, r_N, t)$, with r_i denoting a vector containing the coordinates of electron i and n being the index of the electronic state is the central object for the calculation of molecular properties in quantum chemistry. [Born, 1926]. Hence, also the electron density of any molecule can be calculated from this wave function according to Born-Oppenheimer approximation [Born, 1927].

In practice, the electron density is usually calculated by density functional theory (DFT). This method is based on the electron density rather than wave function as

central quantity for the calculation of molecular properties and chemical descriptors [Fux, 2012].

1.3 Polyoxometalates

1.3.1 POM chemistry

POM chemistry involves the scientific studies of the structures, reactions, properties, and applications of polyoxometalates compounds and polyoxometalates materials, i.e., matter in its various forms that contain polyoxometalate clusters. Polyoxometalates (POMs), formed by the early transition metal ions such as vanadium (V), molybdenum (Mo) and tungsten (W) in their high oxidization states with bridged oxide anions, are a unique class of well-defined inorganic nanocluster compounds with much diversity in size, composition, structure and function. In fact, they can be considered as the “oligomeric” or molecular states and model compounds of the corresponding “polymeric” metal oxides with extended solid state structure [Pope, 1983]. The first salt of POM, ammonium 12-molybdophosphate, $(\text{NH}_4)_3[\text{PMo}_{12}\text{O}_{40}]$ was reported by Berzelius in 1826, as a yellow precipitate from the aqueous solution of phosphoric acid and ammonium molybdate. In the following century, various POMs were synthesized, but the exact structures were unknown. Thanks to the modern technique of single-crystal X ray diffraction pioneered by Max von Laue in 1912, J. F. Keggin, reported the most important structure of the heteropoly acid $[\text{H}_3\text{PW}_{12}\text{O}_{40}] \cdot 6\text{H}_2\text{O}$ by analyzing thirty-two powder X-ray lines [Keggin, 1933], which was confirmed shortly afterwards by Bradley and Illingworth’s investigation of $[\text{H}_3\text{PW}_{12}\text{O}_{40}] \cdot 29\text{H}_2\text{O}$ [Bradley, 1936].

As Michael T. Pope said in 1991, *polyoxometalate chemistry is an old field with new dimensions in several disciplines* [Pope, 1991]. A lot of key features are exploring rapidly today after a rise in popularity of POMs, which started in the early 1990s as a result of a review by Müller [Müller, 2004]. These researches were also well-documented in 1998, in a Chemical Reviews special thematic issue directed by Hill where the history, developments, and application of the many areas covered by POM chemistry are developed [Hill, 1998]. In recent twenty years, the chemistry of POMs has gained dramatic development and is remarkable for their significance in quite diverse disciplines. L. Cronin and D. L. Long said that POM chemistry is a key

emerging area that promises to allow the development of sophisticated designer molecule-based materials and devices that exploit developments in instrumentation, nano-scale science, and material fabrication methods [Long, 2010].

1.3.2 POM structure

There are several thousands of compounds, which fall into the polyoxometalate field, displaying a large range of shapes and sizes with a seemingly endless number of structure types. The reason for this high number of structurally characterized POM compounds is due to the developments in instrumentation and novel synthetic approaches. In terms of technique development, fast and routine single crystal data collection has allowed the area to accelerate to the point that the bottle neck has moved to structure refinement or to crystallization of new compounds rather than the time taken for data collection and initial structure solution.

In general, the class of compounds known as polyoxometalates are based upon metal oxide building blocks with a general formula $\{MO_x\}_n$, where M= Mo, W, V, Nb and $x= 4-7$ [Pope, 1991]. POM clusters are generally anionic and thus can be complex with additional cations as linkers, which can include heteroatom templates. They can also form lacunary structures, whereby some of the cage atoms are removed to create vacancies that can be filled by linker atoms. As shown in Figure 1.12, it presents a classification of the polyoxometalate formulae that are currently known, and also shows how the structures relate to each other in a “polyoxometalate periodic table”. This table encompasses the nuclearity, type, and the broad range of structures presently known.

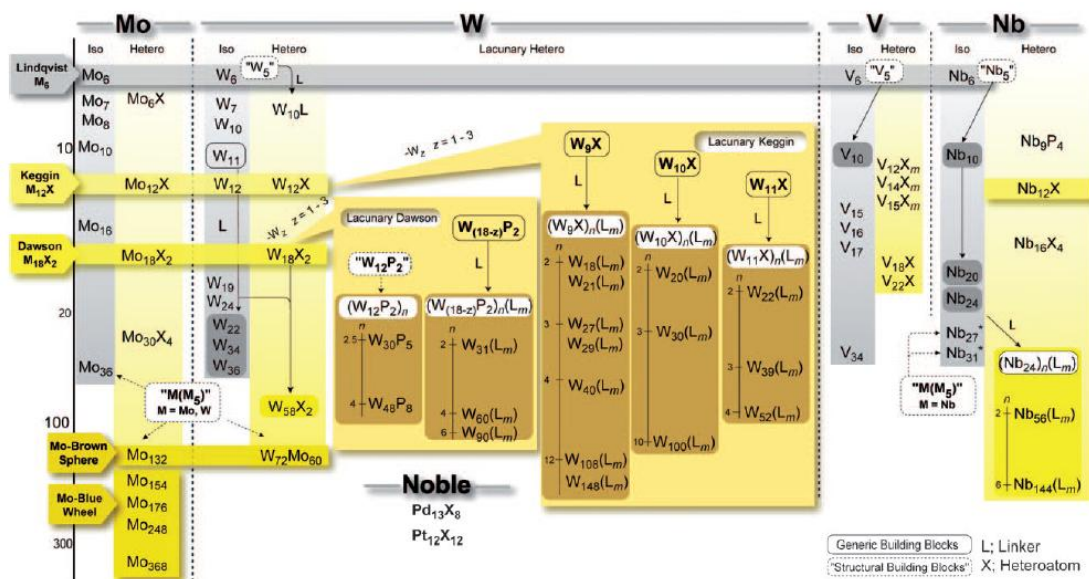


Figure 1.12. Polyoxometalate periodic table from [Long, 2010].

As for pure isolate inorganic polyoxometalates, the structures of POMs can be classified into three subsets:

1) **Isopolyanions** are composed of a metal oxide framework, without internal heteroatom/heteroanion. Therefore, they are often much more unstable than their heteropolyanion counterparts [Long, 2003]. However they also have interesting physical properties, such as high charges and strongly basis oxygen surfaces, which means they are attractive units for use as building blocks [Long, 2006]. The typical structure is Lindqvist type $[M_6O_{19}]^{n-}$ (Figure 1.13a).

2) **Heteropolyanions** are metal oxide clusters that include heteroatom/heteroanion. This group is the most explored POM clusters subset studied. Much of this research has examined catalytic properties of POMs, with great emphasis on the archetypal Keggin $[XM_{12}O_{40}]^{n-}$ (Figure 1.13 b) [Jeannin, 1998]. The other typical heteropolyanions are Anderson (Figure 1.13 c), Dawson (Figure 1.13 d), etc.

3) **Large POM clusters** are related to molybdenum blue species, which was first reported by Scheele in 1783. Their composition was largely unknown until Müller *et al.* reported the synthesis and structural characterization in 1995 of a very high-nuclearity cluster $\{Mo_{154}\}$ (Figure 1.13 e). It corresponds to a ring topology, that crystallizes from a solution of molybdenum blue [Müller, 1995]. Changing the pH and increasing the amount of reducing agent along with incorporation of acetate ligands, facilitates the formation of a $\{Mo_{132}\}$ spherical ball-like cluster (Figure 1.13 f) [Müller, 1995]. This class of highly reduced POM clusters is one of the most exciting

developments in POM chemistry, with many potential spin-off applications in nanoscience.

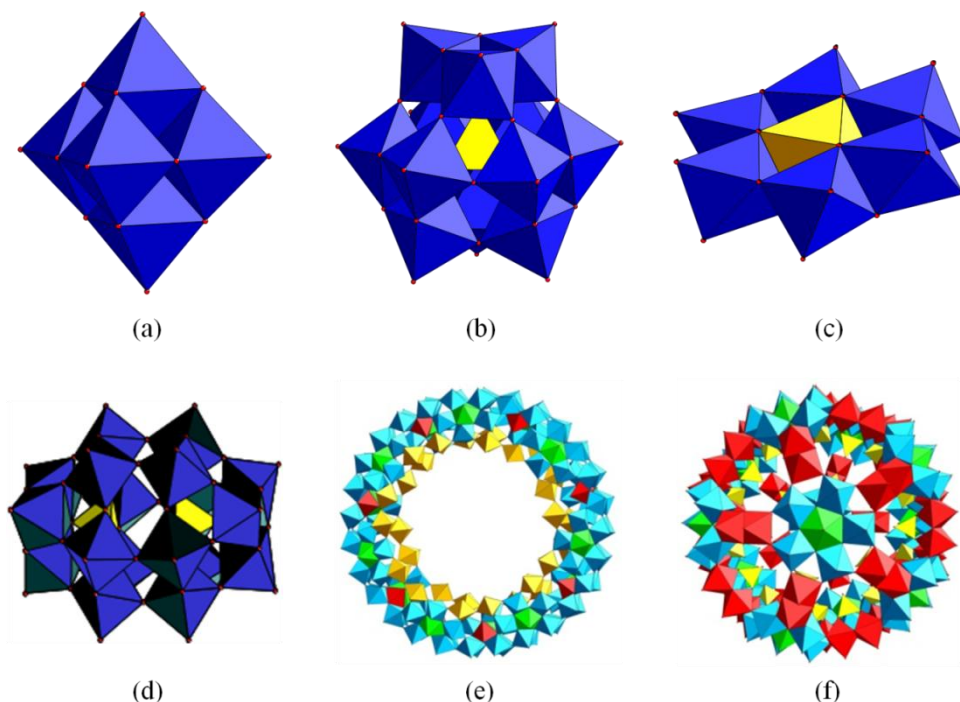


Figure 1.13. Representative structural families of POMs: (a) Lindqvist type structure, (CSD Refcode: MATPDE10, [Allcock, 1973]); (b) Keggin type structure, (CSD Refcode: BARXIB, [Knoth, 1981]); (c) Anderson type structure, (CSD Refcode: PUBDEV, [Luis, 1998]); (d) Dawson type structure, (CSD Refcode: WIPSOD, [Neier, 1995]); (e) Large POM cluster, Mo_{154} (CSD-59058, [Müller, 1995]); (f) Large POM cluster, Mo_{132} (CSD Refcode: GIWHEZ, [Müller, 1998]).

1.3.3 Functionalized POMs

Although POMs have been investigated for about two hundred years, a few POM-based materials have exhibited, practical applications according to their molecular characteristics. The development of POM-based functional materials is a difficult and challenging subject. To introduce organic segments into/onto POM cluster for obtaining organic-inorganic hybrid materials is a feasible methodology. Functionalization of POMs using organic ligands or organometallic units provides a novel strategy to fabricate POM-based organic-inorganic hybrid materials.

According to the nature of the interaction between the organic and inorganic components, there are two classes of POM-based organic-inorganic hybrids [Sanchez, 1999]. As shown in Figure 1.14, the first class (class I) gathers all the systems where no covalent bonds are shared between the organic and the inorganic parts. Only

electrostatic interactions, hydrogen bonds, or Van der Waals interactions are involved. In the second class (class II), the organic and inorganic moieties are linked *via* strong covalent or ionic-covalent bonds. The anionic character of POMs naturally allows their association with organic counter cations into class I hybrids. Considering class II hybrids, the organic ligands can substitute an oxo group of the POM and be directly linked to the metallic center [Dolbecq, 2010].

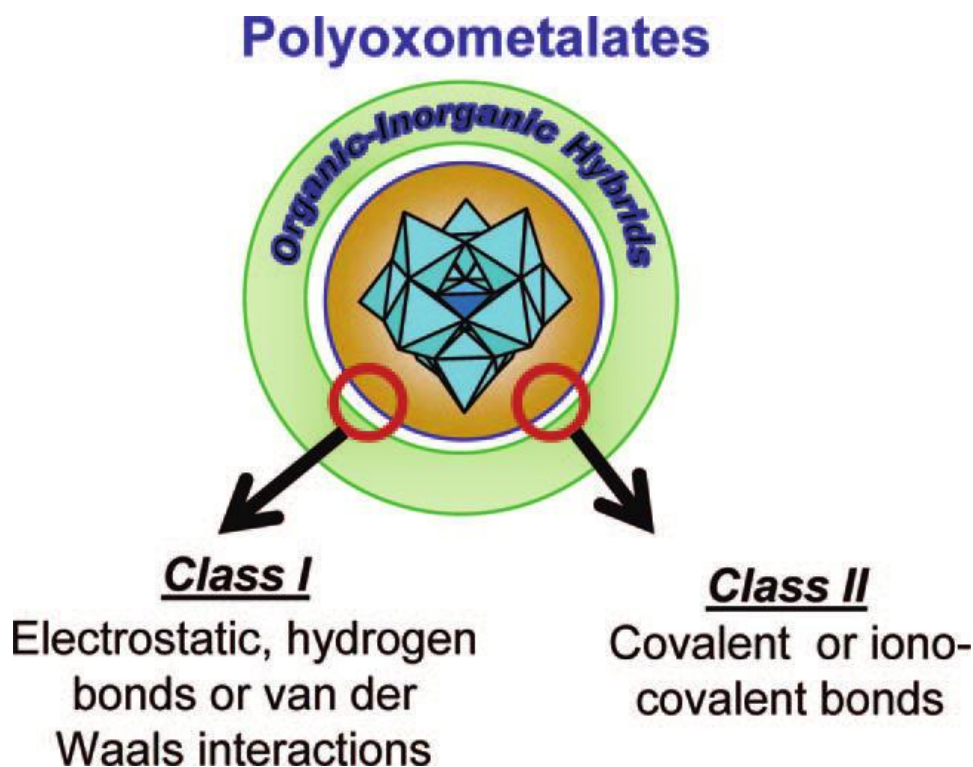


Figure 1.14. Definition of the two classes (I and II) of organic/inorganic hybrid POMs [Dolbecq, 2010].

The details about functionalized POMs are illustrated in *Chemical Review* of 2010 by Anne Dolbecq [Dolbecq, 2010]. As a result, the organo-functionalized POMs not only combine the advantages of organic materials, such as good processability, controllable structures and various electronic properties, with those of inorganic POM clusters, such as good chemical stability and strong electron acceptability, but also may bring exciting synergistic effects [Nalwa, 1997]. Therefore, such classes of hybrid materials have received intense attention with their unique structures and potential novel properties (so called “adding values”), which are described in the following text.

1.3.4 Applications of POMs

POMs have shown different applications in many fields including nano science, chirality, various materials, catalysis, medicine chemistry, analytical chemistry, charge transfer complex/hybrid, self-assembly.

1) **Nano science.** The applications of POM cluster in nano science can be divided into three aspects: POM-based nano architecture [Long, 2010], POM-based nanoparticles [Wang, 2012], POM-based carbon nanotube (CNT) [Song, 2012].

2) **Analytical chemistry.** Polyoxometalates have been used for detection and separation, based particularly on properties such as their high molecular weight, their electrochemical activity and reductibility to form colored species. A variety of elements can be incorporated. Recently, it is worthy to point out that POMs had played a key role in protein crystallography. Ada E. Yonath, who has been awarded in 2009 for Nobel Prize in Chemistry, utilized heteropolytungstates in ribosomal crystallography [Janell, 2001]. In this research, the heteropolytungstates, $(\text{NH}_4)_6(\text{P}_2\text{W}_{18}\text{O}_{62}) \cdot 14 \text{H}_2\text{O}$, was found to be extremely useful in inducing post crystallization rearrangements. These led to a significant increase in the internal order of crystals of the small ribosomal subunits from *Thermus thermophilus*, manifested in a dramatic extension of the resolution of their diffraction patterns, from the initial 7–9 Å to 3 Å. The current 3.3 Å electron density map of this particle, constructed using phases obtained from this W cluster together with other metal compounds, shows the recognizable overall morphology of the small ribosomal subunit. As a matter of fact the $[\text{V}_{10}\text{O}_{28}]^{6-}$ anion has been considered as a crystallization agent [Bosnjakovic-Pavlovic, 2011].

3) **Material.** According to the benefits accomplished by exploring new clusters, the development of novel POM-based multifunctional materials can be expected. In the past few years, the latest progress on POM-based molecular and composite materials, particularly highlighting the emergence of applications that are closely related to surface, electronic, energy, environment, life science, and so on [Song, 2012].

4) **Catalysis.** The stability, combined with the extensively alterable molecular properties of POMs, including heteropoly acids (HPAs), makes them attractive as catalysts. The easy acidity control, the reduction potential, the solubility and most properties important in catalytic turnover have already led to the commercialization of

several homogeneous or heterogeneous catalytic processes based on POMs [Hill, 2007].

5) **Chirality.** Owing to the potential applications in catalysis, analytical chemistry, ion exchange, magnetism, biological chemistry and medicine, tremendous efforts have been dedicated to exploring polyoxometalate (POM) chemistry. Chiral POM-based materials are particularly attractive due to the combination of the advantage of POMs with the importance of chirality. Nearly 100 chiral POM-based compounds were reported, which were mainly used as asymmetric catalysts, molecular recognition and nonlinear optical materials. In addition, the chirality within POM systems has attracted the attention of theoretical chemists and research was carried out to explore the origin of chirality by density functional theoretical methods [Du, 2013].

6) **Self-assembly.** Large, hydrophilic polyoxoanions with high solubility in water and/or other polar solvents demonstrate unique solution behavior by self-assembling into single layer, hollow, spherical “blackberry” structures, which is obviously different from small, simple ions. The blackberry structures show certain similarities to spherical viral capsids, from the overall structure to the formation kinetics. More amazingly, these inorganic macro-ions demonstrate some features usually believed to belong only to complex biological molecules, such as the self-recognition in dilute solutions. Meanwhile, polyoxometalates-based organic–inorganic hybrid materials demonstrate amphiphilic properties by self-assembling into vesicles and reverse vesicles in polar and non-polar solvents, respectively, and form monolayer at the water/air interface. Different from conventional amphiphiles, these hybrids show pH-dependent and counterion-dependent self-assembly behaviors with controllable functionality, e.g. fluorescence and catalytic activity, due to the high and tunable charges and the functionalities of POM polar head groups [Yin, 2012].

1.4 Polyoxovanadates

1.4.1 POVs' structures

Polyoxovanadates are the most important series in the large family of POMs, due to the various and changeful structures. In 1983, M. T. Pope illustrates that vanadium, in its higher oxidation state, gives many isopolyvanadates that exhibit a large variety of structures, ranging from chain metavanadates $[\text{VO}_3^-]_n$, to layered oxides $[\text{V}_2\text{O}_5]$ and compact polyanions $[\text{V}_{10}\text{O}_{28}]^{6-}$ [Pope, 1983]. Even polyanionic hollow cages

such as $[V_{15}O_{36}]^{5-}$, in which anions are encapsulated, have been reported [Pope, 1991]. Such a rich structural chemistry is due to the ability of vanadium to adopt a variety of coordination geometries, $[VO_6]$, $[VO_5]$, $[VO_4]$ units and different oxidation states (V^V , V^{IV}). During the past 30 years, a large number of new polyoxovanadates and their related properties has mainly reported by the groups of Müller (*University of Bielefeld, Germany*), Zubieta (*Syracuse university, USA*), Hill (*Emory University, USA*), Hayashi (*Kanazawa University, Japan*), T. B. Liu (*University of Akron, USA*), Wei (*Tsinghua University, China*), and Daniel (*Freie Universit ät Berlin, Germany*)

Hayashi, in his review [Hayashi, 2011], has described the different species of POV structures such like tetravanadate (V4 unit), hexavanadates (V6 unit), decavanadate (V10 unit), dodecavanadates (V12 unit), and other heteropolyoxovanadates, lacunary polyoxovanadates, given a good understanding on the classification of complicated structures of polyoxovanadates.

1.4.2 Generality of functionalized hexavanadates

In POM chemistry, Lindqvist anion ($[M_6O_{19}]^{n-}$), generated by condensation of six MO_6 octahedra and with approximately O_h symmetry, is important in the chemistry of Mo^{VI} , W^{VI} , Nb^V , and Ta^V . The Lindqvist type like $[M_6O_{19}]^{2-}$, $[W_6O_{19}]^{2-}$, and $[Nb_6O_{19}]^{2-}$, can exist as isolate states, but the isolated hexavanadate exists as $[V_6O_{19}]^{n-}$ unit rarely. Duo to the high negative charge concentrated around the V6 cluster and small radius of V atom, in the text-book, "M. T. Pope, Heteropoly and Isopoly Oxometalates, Springer-Verlag, Berlin, 1983", it says there is no $[V_6O_{19}]$ unit found.

However, the chemists have never stopped studying the synthesis of $[V_6O_{19}]$ unit. To stabilize the highly negative core, a protection of the nucleophilic surface oxygen atoms is required. By using positively charged protecting groups, it is possible to compensate this high negative charge of the hexavanadate ion. The protection by adding groups on the surface oxygen atoms is the effective method. Therefore, there are two main methods to protect the V6 core.

The first method is introducing the capping groups to construct the V6 organometallic complexes for stabilizing the high negative O atoms. Enlighten by the synthesis methods used in other Lindqvist POM structures, Chae [Chae, 1989] and Hayashi [Hayashi, 1989] have in parallel published the same V6 compounds synthesized by using different routes, which construct the first V6 structure (Figure 1.15).

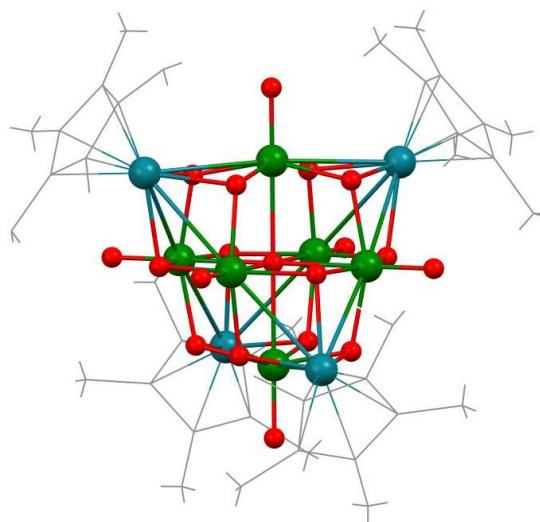


Figure 1.15. Structure of $[(C_5Me_5)Rh]_4(V_6O_{19})$, CSD refcode: VALPUT [Chae, 1989], VALPUT01 [Hayashi, 1989], VALPUT11 [Hayashi, 1991].

Piepenbrink *et al* [Piepenbrink, 2002] have found another way to stabilize and synthesize V6 species by functionalizing V6 with alkoxo groups. The substitution of bridging oxygen atoms with alkoxide ligands produces an alkoxohexavanadate core [Chen, 1992a]. The substitution of all bridging oxygen atoms with CH_3O^- or $C_2H_5O^-$ ligands produces neutral hexavanadates, $[V^{IV}_4V^V_2O_7(OR)_{12}]$. Although the capping groups or alkoxides are labile and almost certainly dissociate at some stage in solution, the free form of $[V_6O_{19}]^{8-}$ has never been isolated. A V^V hexavanadate without a bulky capping group, $[V_6O_{12}(OCH_3)_7]^-$, was prepared by Hill's group [Hou, 1993]. This serves to diminish the charge, and to reduce the oxidation state of V^{IV} which is preferred by the introduction of alkoxide ligands [Chen, 1992b].

Among the alkoxo-hexavanadates species, there is an important type of functionalized hexavanadates, which is named arm-like functionalized V6; they possess tripodal ligands. There are five tripodal ligands (Figure 1.16), which have previously been used in the synthesis of oxo-vanadium and oxo-molybdenum clusters [Brechin, 2005].

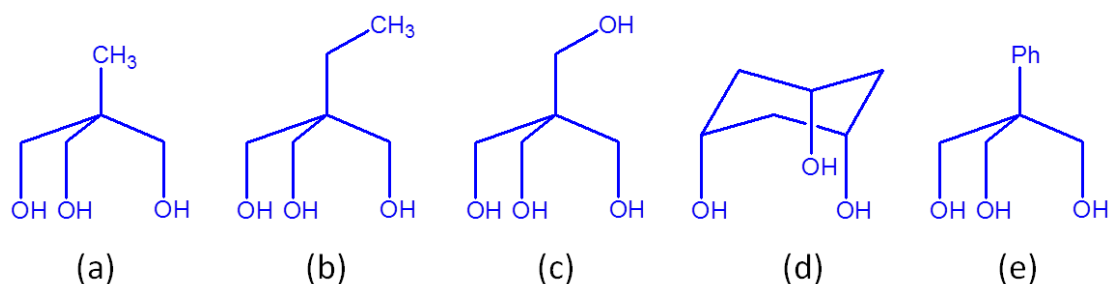


Figure 1.16. Frequently-used tripodal ligands. (a) (b) (c) 1,1,1-tris(hydroxymethyl)ethane (H_3thme); (d) 1,1,1-tris(hydroxymethyl)propane (H_3tmp); (e) pentaerythritol (H_4peol) [Brechin, 2005].

Zubieta group has done the pioneering work in functionalized V6, trisalkoxy-hexavanadates, with tripodal-type ligands, as shown in Figure 1.17, leading to a new method of functionalized V6 preparation [Chen, 1992a; Chen, 1992b; Chen, 1993; Khan, 1992; Khan, 1993].

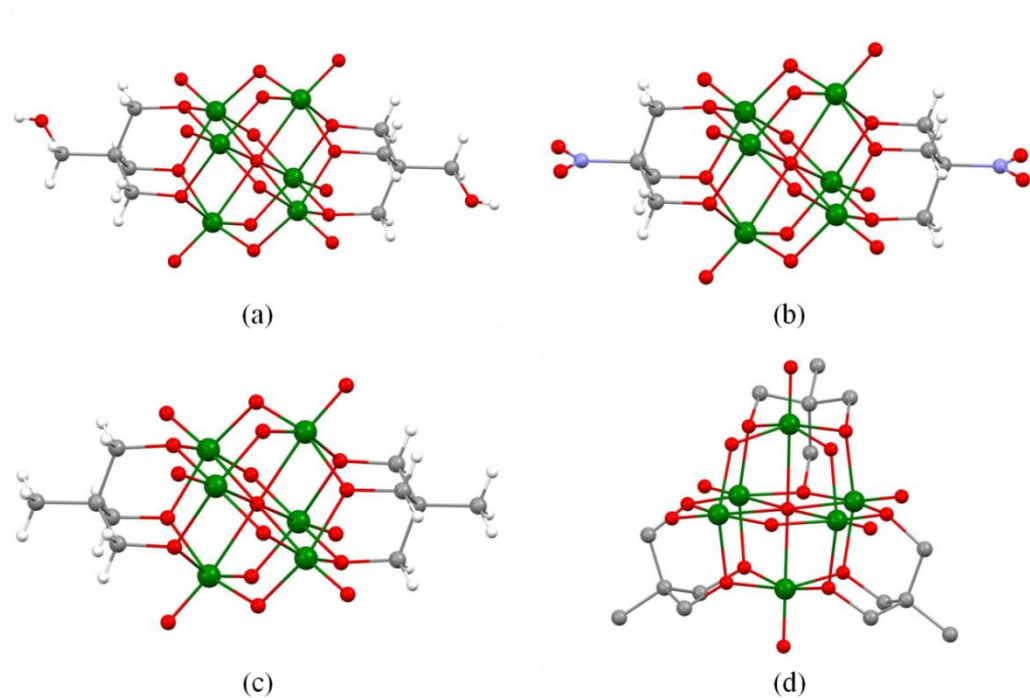


Figure 1.17. Functionalized hexavanadates with two or three symmetrical tris(alkoxy) substituents: (a) V_6-OH (CSD refcode: VERDIF10, [Chen, 1992b]); (b) V_6-NH_2 (CSD refcode: VERDAX10, [Chen, 1992b]); (c) V_6-CH_3 (CSD refcode: VERDEB10, [Chen, 1992b]); (d) $[V_6O_{19}](C_3H_9)_3$ (CSD refcode: JOXCII, [Khan, 1992]).

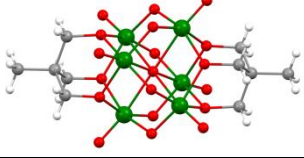
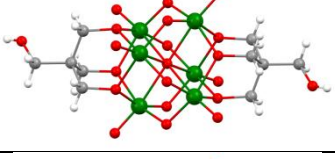
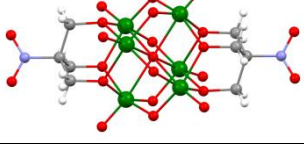
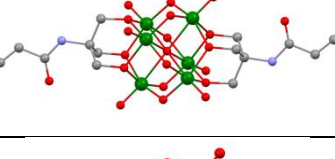
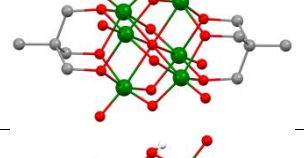
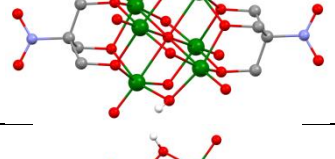
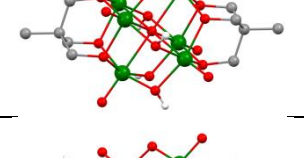
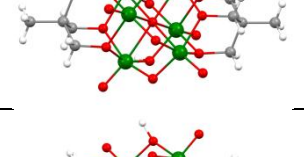
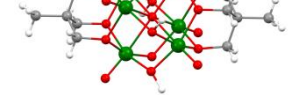
1.4.3 Previous X-ray structure of functionalized hexavanadates

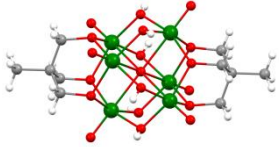
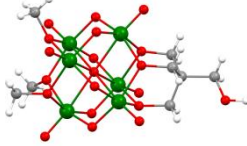
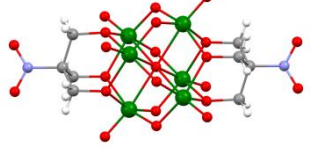
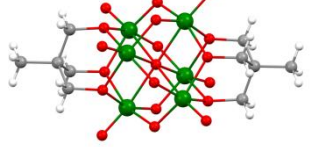
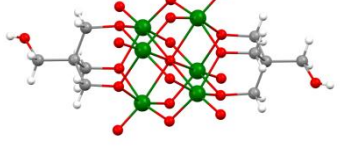
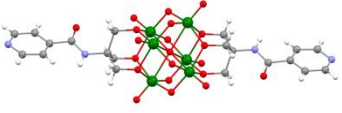
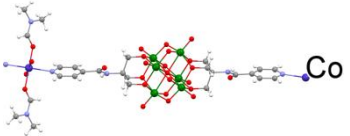

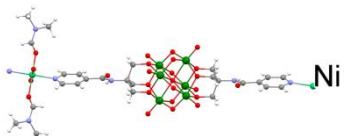
After the initial characterization of $[(C_5Me_5)Rh]_4(V_6O_{19})$ by Chae [Chae, 1989] and Hayashi [Hayashi, 1989], a great number of functionalized V6 have been

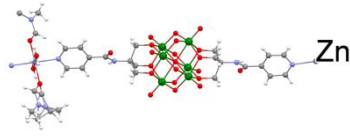
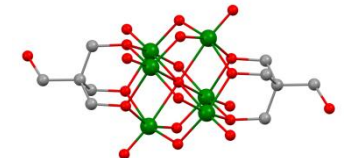
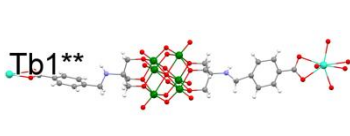
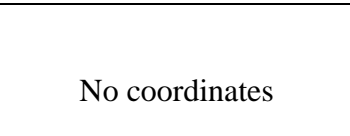
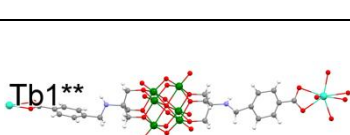
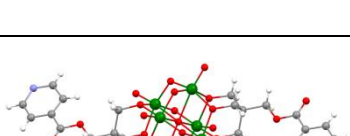
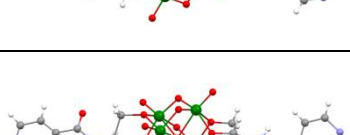
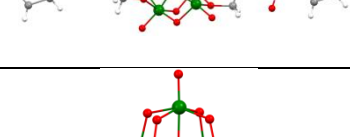
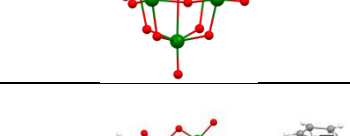
investigated. Owing to the great efforts by Zubieta, Müller, Hill and other groups, a series of functionalized hexavanadates has been synthesized by introducing different organic ligands.

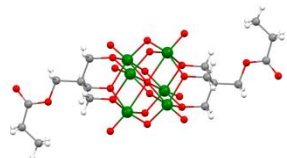
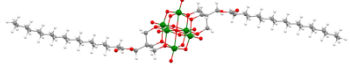
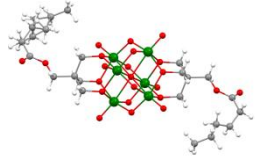
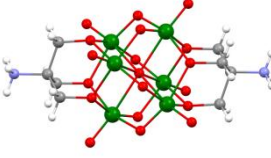
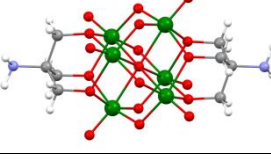
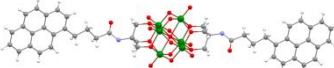
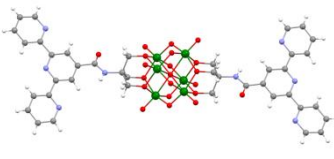
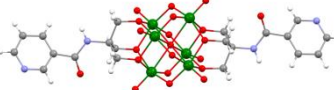
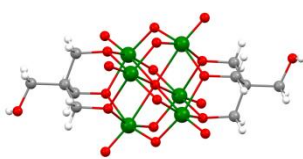
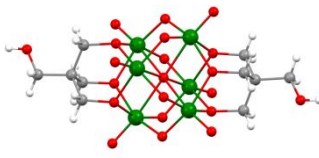
For our investigations, we just focus on the arm-like functionalized V6 with two symmetrical tripodal ligands, which are listed in Table 1.2.

Table 1.2. List of functionalized V6 with two opposite organic ligands ranked by the year of publishing.

CSD Refcode	Structure of functionalized hexavanadate	R factor	Cation or other molecule	Reference
VERDEB		5.61	Bu ₄ N ⁺	Chen, 1990
VERDIF		5.44	Bu ₄ N ⁺ , N(CH ₃) ₂ CHO	Chen, 1990
VERDAX		5.15	Bu ₄ N ⁺	Chen, 1990
KURBEE		6.0	Bu ₄ N ⁺	Chen, 1992a
KURBII		3.4	C ₅ H ₆ N ⁺ , N(CH ₃) ₂ CHO	Chen, 1992a
KURBOO		5.8	Bu ₄ N ⁺ , CH ₂ Cl ₂	Chen, 1992a
KURBUU		5.8	Bu ₄ N ⁺ , C ₁₂ H ₁₂ N ₂	Chen, 1992a
PAGSOF		4.3	(C ₂ H ₅) ₂ O, N(CH ₃) ₂ CHO	Chen, 1992b
PAGSUL		4.3	Bu ₄ N ⁺	Chen, 1992b

PAGTAS		4.2	Bu_4N^+ , CH_2Cl_2 , $\text{C}_{12}\text{H}_{12}\text{N}_2$	Chen, 1992b
PELYIO		6.62	Bu_4N^+	Chen, 1992b
VERDAX10		4.9	Bu_4N^+	Chen, 1992b
VERDEB10		5.5	Bu_4N^+	Chen, 1992b
VERDIF10		4.9	Bu_4N^+ , $\text{N}(\text{CH}_3)_2\text{CHO}$	Chen, 1992b
XIHGAX	No coordinate	10.76	Co^{2+} , $\text{N}(\text{CH}_3)_2\text{CHO}$	Hill, 2006
NEMDEP		6.74	Bu_4N^+ , $\text{N}(\text{CH}_3)_2\text{CHO}$	Han, 2006
NEMDIT		7.78	Co^{2+} , $\text{N}(\text{CH}_3)_2\text{CHO}$	Han, 2006
NEMDOZ		9.76	Mn^{2+} , $\text{N}(\text{CH}_3)_2\text{CHO}$	Han, 2006
NEMDUF		9.73	Ni^{2+} , $\text{N}(\text{CH}_3)_2\text{CHO}$	Han, 2006

NEMFAN		8.98	Zn^{2+} , $\text{N}(\text{CH}_3)_2\text{CHO}$	Han, 2006
ZEVMEs		4.6	CH_6N_3^+ , H_2O	Müller, 1995
LOFVUY		8.79	Tb^{2+} , $(\text{CH}_3)_2\text{NCHO}$	Han, 2007
LOFWAF	No coordinates	5.45	$\text{CH}_3\text{CON}(\text{CH}_3)_2$	Han, 2007
LOFVUY01		13.18	Tb^{2+} , $(\text{CH}_3)_2\text{NCHO}$	Han, 2007
EGEMUZ		7.7	Bu_4N^+	Allain, 2008
EGENEK		8.75	Bu_4N^+ , CH_3CN , H_2O	Allain, 2008
IMIPUQ		9.98	$\text{C}_6\text{H}_{15}\text{CuN}_2\text{O}_2^+$, $\text{C}_6\text{H}_{13}\text{CuN}_2^{2+}$	Wang, 2010
WAFVUW		4.25	Bu_4N^+ , $\text{N}(\text{CH}_3)_2\text{CHO}$	Schulz, 2010
EMIFEM		7.09	Bu_4N^+	Yin, 2011

OQETOU		5.76	Bu_4N^+	Wu, 2011a
EMIFEM01		7.09	Bu_4N^+	Wu, 2011a
OQETUA		4.13	Bu_4N^+	Wu, 2011a
SAJWEH		7.81	CH_3SOCH_3	Li, 2011
SAJWIL		4.18	Bu_4N^+	Li, 2011
SAJWOR		8.67	Bu_4N^+ , $\text{N}(\text{CH}_3)_2\text{CHO}$, H_3O^+	Li, 2011
UCOTEN		5.29	Bu_4N^+ , $\text{N}(\text{CH}_3)_2\text{CHO}$	Santoni, 2011
SAMMOK		4.13	Bu_4N^+ , $\text{N}(\text{CH}_3)_2\text{CHO}$	Santoni, 2012
GIFROE		5.74	Bu_4N^+ , CH_3CN	Wu, 2013
GIFRUK		3.99	Bu_4N^+ , H_2O	Wu, 2013

1.4.4 Structure description of functionalized hexavanadates

In the previous charge density study on decavanadate (V10) [Bosnjakovic-Pavlovic, 2009], due to the complexity of the structure, it was necessary to characterize precisely the different environment of oxygen and vanadium atoms. There are four types of O atoms in the V10 anion (Figure 1.18 a). The first type corresponds to oxygen atoms bonded to only one vanadium atom (O1x). The second type corresponds to oxygen atoms shared between two vanadium atoms (O2x). The third type of oxygen atoms concerns those shared between three vanadium atoms (O3x). The fourth type of oxygen atoms, have a sixfold coordination of vanadium atom building an almost regular $\{VO_6\}$ octahedron (O6x).

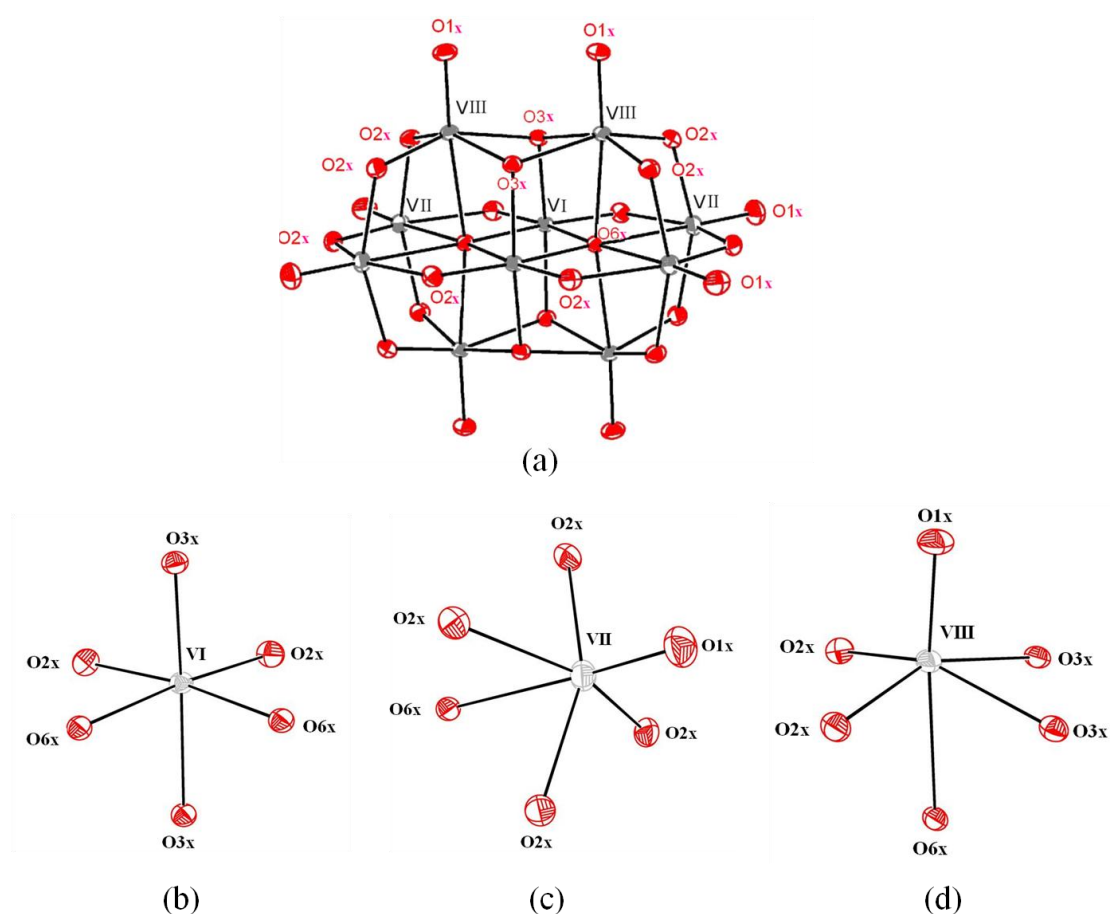


Figure 1.18. Labeling scheme and type of atoms in the decavanadate ion. Reproduced from [Bošnjaković-Pavlović, 2010].

Considering the different chemical environment of vanadium atoms, there are three types of vanadium atoms (Figure 1.8 b, c and d): the first type (type I), presents two V-O_{2x}, two V-O_{3x} and two V-O_{6x} bonds. The second kind of vanadium atoms

(type II) presents four V-O2x, one V-O1x and one V-O6x bonds. The third type of vanadium atoms (type III) presents two V-O2x, two V-O3x, one V-O1x and one V-O6x bonds.

The same labelling is used for functionalized V6, to describe the different O atoms. There are also four types of O atoms (Figure 1.19 a). The types of O1x, O2x, and O6x atoms are the same with the corresponding ones in V10 anion, while the type of O3x atoms are connected with two V atoms and one C atom of organic ligand. In the functionalized V6 core, there are six chemically equivalent V atoms, whose type is VII according to the V10 anion labelling. Each of V atom is bonded to one O1x atom, one O6x atom, two O2x atoms, and two O3x atoms (Figure 1.19 b).

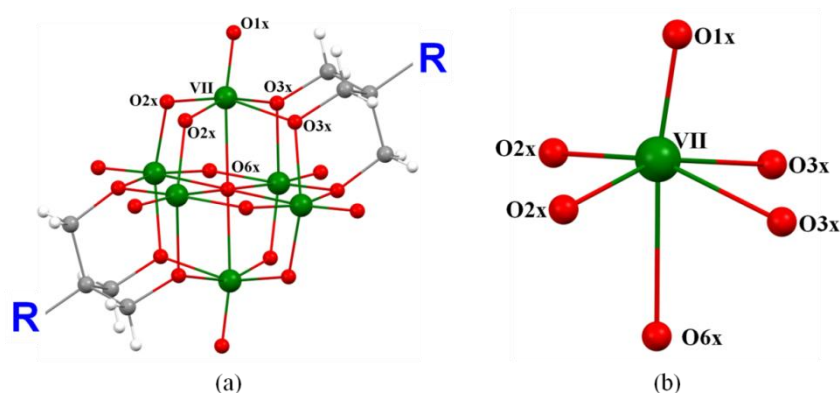


Figure 1.19. Labeling scheme and type of atoms in the functionalized V6 ion. (a) Structure of functionalized V6 anion; (b) Chemical surroundings of V atom.

In order to compare all V-O distances of this functionalized V6 series with literature, we have examined the organic / organometallic crystallographic data base (CSD) [Allen, 2002].

Table 1.3. V-O distances (\AA) of functionalized V6 and V10 in previous reported structures from CSD (39 functionalized V6 compounds, 368 V10 compounds).

Bond	Functionalized V6 from CSD		V10 anion from CSD	
	Average	<Min, Max>	Average	<Min, Max>
VII-O1x	1.601	1.570, 1.621	1.605	1.592-1.619
VII-O2x	1.848	1.736, 2.023	1.881	1.821-1.913
VII-O3x	2.017	1.954, 2.108	-	-
VII-O6x	2.250	2.195, 2.344	2.316	2.289-2.365

1.5 Experimental and theoretical charge density analysis of POMs and POVs

Chemical bonding features in transition metal complexes are a major topic in coordination chemistry. The complexity of the orbital splitting used in the ligand field is well known. That makes the bonding characterization interesting and challenging. Recently, experimental X-ray determination of the accurate electron density in compounds containing transition metals has grown as a major area. Most of the progress is due to the recent availability of fast instrumentation like area detectors which provide full and very accurate data sets in short times even for large unit-cell crystals. Electronic configurations of the *3d* metal ion play important role in coordination chemistry; taking the advantage of the X-ray absorption spectroscopy available in synchrotron radiation facility, the exact electronic configuration can be monitored. The recent improvements on both experiment and theory have made the charge density analysis more accessible to even more complicated system, for example, the excited state or the meta-stable states. There are significant charge density studies on *3d* transition metal such as V, Cr, Mn, Co, Ni, Cu and Zn, however, it exists a few number of the studies on compounds containing *4d* electrons [Wang, 2013].

As for the experimental charge density analysis in POMs/POVs field, except the only one research on decavanadates (V10) in our group, there is no experimental study done by an other group. The theoretical calculations performed for an isolated $[V_{10}O_{28}]^{6-}$ anion [Rohmer, 1991; Kempf, 1992; Rohmer, 1998; Henry, 2002] are shown in Table 1.4 and will be compared with our results.

Table 1.4. Previous theoretical calculation for $[V_{10}O_{28}]^{6-}$ anion.

References	Methods	Results
Rohmer, 1991	<i>Ab initio</i> SCF	Topology of the electrostatic potential
Kempf, 1992	<i>Ab initio</i> SCF	Topology of the electrostatic potential, Topology of the charge density, atomic net charge
Rohmer, 1998	<i>Ab initio</i> (Hartree-Fock and DFT)	Topology of the electrostatic potential
Henry, 2002	PACHA	Atomic net charge

In this research, a cytosine-decavanadate compound have been synthesized and crystallized, $\text{Na}_3[\text{V}_{10}\text{O}_{28}] (\text{C}_4\text{N}_3\text{OH}_5)_3(\text{C}_4\text{N}_3\text{OH}_6)_3 \cdot 10\text{H}_2\text{O}$, and its crystal structure has been determined from a single-crystal X-ray diffraction. A high resolution X-ray diffraction experiment at 210 K (in P1 space group) was carried out. The data were refined using a pseudo-atom multipole model to get the electron density and the electrostatic properties of the decavanadate-cytosine complex. Static deformation density maps and topological analysis were used for this purpose. To get insight into the reactivity of the decavanadate anion, the atomic net charges and the molecular electrostatic potential have been determined [Bosnjakovic-Pavlovic, 2009]. In order to plot some graphs in the same orientation and to compare with decavanadate anion theoretical calculations we have performed (*vide supra*, chapter 4), we have noticed that the EP values mapped on the decavanadate molecular surface in the published papers [Bosnjakovic-Pavlovic, 2008; Bosnjakovic-Pavlovic, 2009; Bosnjakovic-Pavlovic, 2010; Bosnjakovic-Pavlovic, 2011] were wrong. Instead of $[-8.7 \sim -4.9]$, one has to read $[-0.7 \sim -1.3] \text{ e}\cdot\text{\AA}^{-1}$. Figure 1.20 represents the decavanadate molecular surface colored by EP values as calculated by Bosnjakovic-Pavlovic *et al* [Bosnjakovic-Pavlovic, 2009] with the correct EP scale.

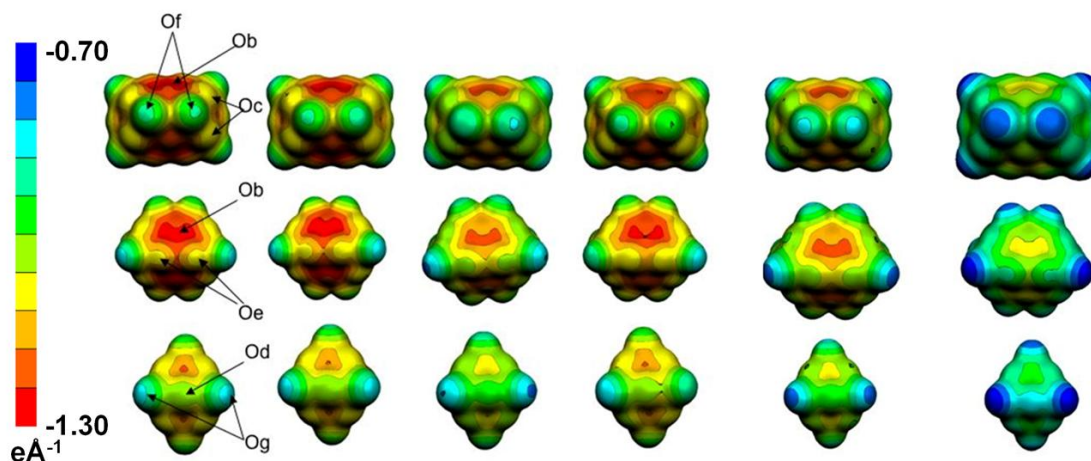


Figure 1.20. Experimental EP on the molecular surface ($0.007 \text{ e}\cdot\text{\AA}^{-3}$) (column 1-4). Column 1-3: $\text{Na}_3[\text{V}_{10}\text{O}_{28}] (\text{C}_4\text{N}_3\text{OH}_5)_3(\text{C}_4\text{N}_3\text{OH}_6)_3 \cdot 10\text{H}_2\text{O}$, column 4: $(\text{NH}_4)_6 [\text{V}_{10}\text{O}_{28}] \cdot 6\text{H}_2\text{O}$. EP of the DV isolated from the crystal computed from the multipole refinement (column 1), from the charge determined by the AIM method (column 2), and by a κ refinement (columns 3 and 4).

Theoretical EP (columns 5-6) computed from the charge determined by the Mulliken partitioning (column 5) [Kempf, 1992] and by a PACHA partitioning (column 6) [Henry, 2002]. Reproduced from [Bosnjakovic-Pavlovic, 2009].

Schulz *et al.* have studied the theoretical electrostatic potential of $(\text{Bu}_4\text{N})_2[\{\text{FcC}(\text{O})\text{NHC}(\text{CH}_2\text{O})_3\}_2\text{V}_6\text{O}_{13}]$ [Schulz, 2010]. As shown in Figure 1.21, the oxygen non bonding lone pairs remain also virtually nonbonding. Due to the presence of the highly electronegative oxygen atoms, the overall electrostatic potential is also markedly negative.

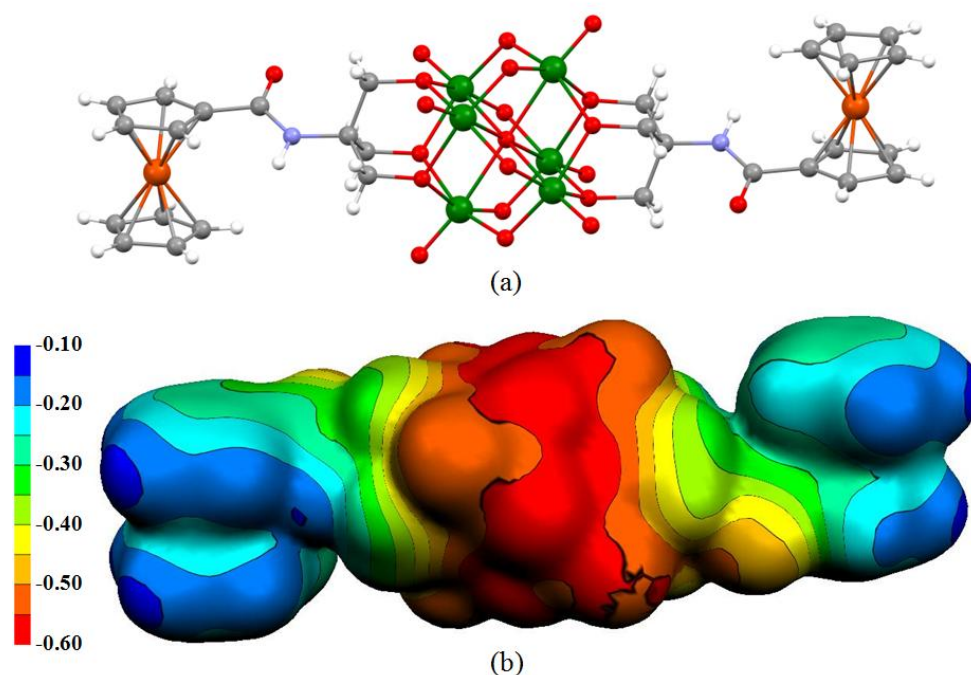


Figure 1.21. Theoretical EP of $(\text{Bu}_4\text{N})_2[\{\text{FcC}(\text{O})\text{NHC}(\text{CH}_2\text{O})_3\}_2\text{V}_6\text{O}_{13}]$. (Refcode: WAFVUW)
 (a) Structure of its V6 anion; (b) Theoretical EP (from -0.50 to -0.10 $e\cdot\text{\AA}^{-1}$). Plotted from electrostatic potential cube files provided by Schulz *et al.*

In parallel, there are many theoretical calculation performed in POMs field about DFT/TD-DFT calculation, HOMO/LUMO analysis, NBO analysis, Mulliken charge analysis, and electrostatic potential. Lopez *et al.* [Lopez, 2002] have studied the molecular electrostatic potential maps and the relative energy of the various protonated forms of $[\text{SiW}_9\text{V}_3\text{O}_{40}]^{7-}$ and $[\text{SiW}_9\text{Mo}_3\text{O}_{40}]^{4-}$. As shown in Figure 1.22, red color identifies regions in which the electrostatic potential is negative (nucleophilic regions) and blue color denotes positive or less negative electrostatic potential regions (electrophilic sites). When tungsten atoms are substituted by molybdenum atoms in SiW12, the electronic reorganization is quite small and the basicity of the substituted anion is not very different from that of the single-addenda anion. Clearly, bridging oxygens are generally more basic than terminal oxygens in the MEP of SiW_9Mo_3 since the regions close to terminal OMo and OW oxygen sites (dark blue) are the least

basic, and the accessible nucleophilic regions (red) are close to the bridging oxygens [Lopez, 2002]. For an accurate comparison, it is important to notice that the EP value is at isodensity surface (0.017 au), whereas we generally use an isodensity surface (0.001 au). Moreover the EP scale is not indicated.

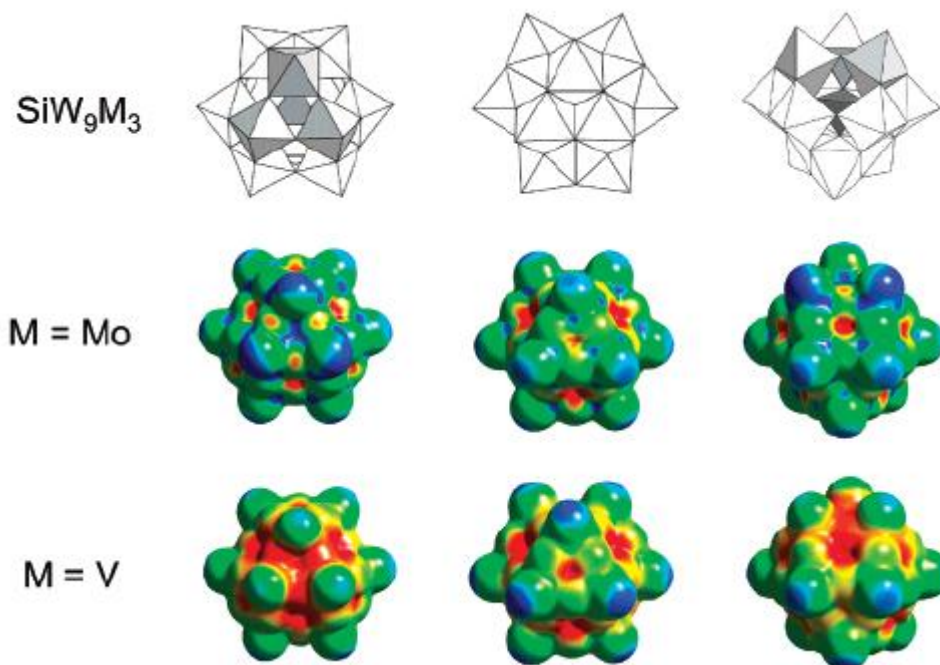


Figure 1.22. Molecular electrostatic potentials (MEPs) from three different viewpoints for the SiW_9M_3 derivatives with M) Mo and V [Lopez, 2002].

Miro *et al.* [Miro, 2012] have reported that a new wheel-shaped polyoxometalate $\{[W_5O_{21}]_3[(UVIO_2)_2(\mu-O_2)]_3\}^{30-}$ (U_6W_{15}) and protonated $H_{18}\{[W_5O_{21}]_3[(UVIO_2)_2(\mu-O_2)]_3\}^{12-}$ ($H_{18}U_6W_{15}$) have been synthesized and structurally characterized. As shown in Figure 1.23, the calculated electrostatic potential reveals the protonation of several μ -oxo bridges reducing the polyoxometalate total charge. The U_6W_{15} electrostatic potential is presented in the top of Figure 1.23 revealing that the negative charge is more localized on internally directed O atoms including both uranyl terminal oxygens and μ -oxo ligands between tungsten and tungsten–uranium centers. Furthermore, the electrostatic potential of $H_{18}U_6W_{15}$ shows that now the charge is more distributed among the nanowheel structure but still the uranyl oxygens are the more negative centers.

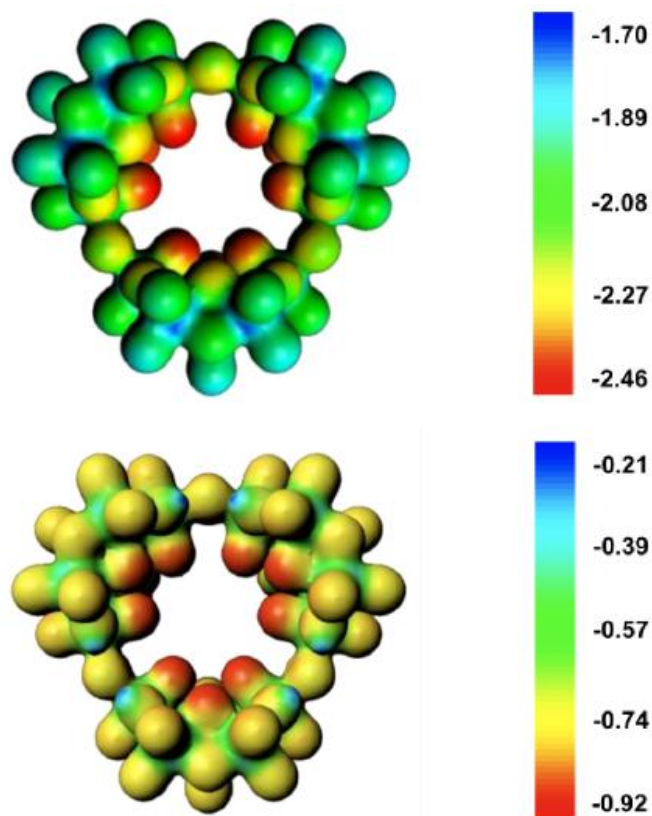


Figure 1.23. *Electrostatic potential plot for the U6W15 (top) and H18U6W15 (bottom) species. [Miro, 2012].*

1.6 Conclusion

In conclusion, except the experimental charge density analysis of decavanadate by Dr. Bošnjaković-Pavlović in our group seven years ago, there is no any report about electronic/electrostatic/topological properties based on charge density determination. Though there are some theoretical charge density studies on POM/POV compounds, most of them focused on molecular electrostatic potentials only. However, a pertinent charge density research for obtaining important chemical informations, especially chemical bonding features and chemical reactivity, is without concerning. In POM/POV field, there are lots of research on synthesis, structure characterization, various properties determined by equipments. The charge density can provide important and meaningful chemical information for better understanding the inherent properties of the target compound itself. The chemical information obtained from charge density analysis enables us to know how the structure can exist, how the compound exhibits chemical and biological reactivity, and where the interaction sites/regions localize. Hence, the charge density analysis of

functionalized hexavanadates, experimentally and theoretically, is an important contribution for POM/POV field.

**2. EXPERIMENTAL CHARGE DENSITY
ANALYSIS OF FUNCTIONALIZED
HEXAVANADATE V6-C3**

2.1 Introduction

This chapter presents the experimental charge density analysis of a functionalized V6 compound, $[(C_4H_9)_4N]_2[V_6O_{13}\{(OCH_2)_3CCH_2OCCH_2CH_3\}_2]$ (V6-C3). In section 2.2, the experiment and the methodology of charge density refinement are described for the title compound. Section 2.3 contains all the results of crystal structure, electronic and topological properties based on charge density analysis. Section 2.4 make some discussions about chemical bonding and reactivity.

2.2 Experiment and refinement

2.2.1 Synthesis of functionalized hexavanadates

Due to the great efforts from Zubieta's group [Chen, 1990; Chen, 1992a, Chen, 1992b; Chen, 1993; Khan, 1992; Khan, 1993] and Müller's group [Müller, 1995], different series of functionalized hexavanadates have been synthesized. As shown in Figure 2.1, the main synthetic strategy for such complexes was to prepare the tris(alkoxo) ligands which react with a POV precursor, such as decavanadate or metavanadate salts. This functionalized process is a one-step reaction, the resulting product, a functionalized V6, is called first-functionalized V6.

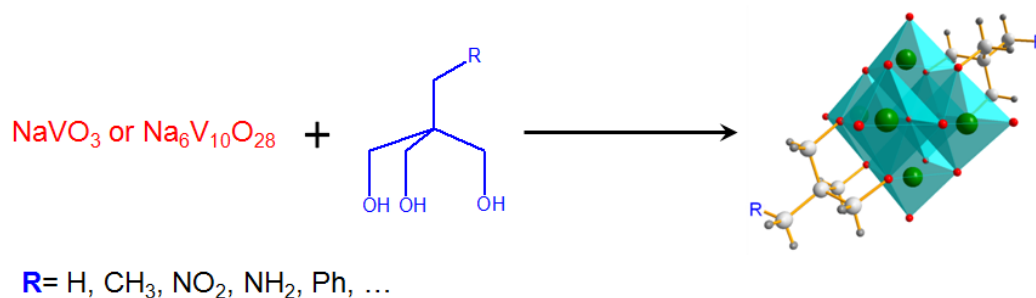


Figure 2.1. Synthetic strategy of first-functionalized hexavanadates

However, there are a few tris(alkoxo) ligand types, which could form the family of first-functionalized hexavanadates. It is possible to functionalize the V6 cluster if tris(alkoxo) ligands carry functional groups such as $-OH$, $-NH_2$. Due to the high oxidizability when the V6 unit is constructed from POV precursor, it is difficult to obtain the first-functionalized hexavandates carrying a $-NH_2$ group. In order to avoid this problem, Hill's group [Hill, 2006; Han, 2006; Han, 2007; Li, 2011] and others groups [Allain, 2008; Schulz, 2010; Santoni, 2011; Santoni, 2012] have attempted to modify the tris(alkoxo) ligands before the functionalization on V6 core, and have

obtained several functionalized hexavanadates carrying long-distance organic ligands. In Wei's group, the pentaerythritol-derivatized hexavanadate $(\text{Bu}_4\text{N})_2[\text{V}_6\text{O}_{13}\{(\text{OCH}_2)_3\text{CCH}_2\text{OH}\}_2]$ was selected for further organic modification as it has two reactive hydroxyl groups [Yin, 2011; Wu, 2011]. Esterification is a common organic reaction that has been recently applied to the post-functionalization of POM hybrids with hydroxyl groups. For the synthesis process of functionalized hexavanadate, V6-C3 used in this thesis, there are two main steps, which are shown in Figure 2.2.

Step 1: *Synthesis of V6OH-TBA.* The compound V6OH-TBA was prepared according to Zubietta and Müller's previous work [Müller, 1995], except that tetrabutyl ammonium was used as the counter ions. An amount of 25.9 g $\text{NaVO}_3 \cdot 2\text{H}_2\text{O}$ was dissolved into 250 mL deionized water. 1 M hydrochloric acid HCl was added dropwise until reaching $\text{pH} = 3$ and then 8 g pentaerythritol was added to the solution. The mixture was stirred at 80 °C for 48h and then filtrated. The dark red filtrate was carefully added to a solution of tetrabutylammonium bromide (50g Bu_4NBr dissolved in 100 mL water) and orange solid was collected by filtration. The product was washed by 100 mL deionized water for three times and then dried for use.

Step 2: *Synthesis of V6-C3.* A mixture of 1.26g (1mmol) compound V6OH-TBA, 0.236g (2 mmol) propionic anhydride, 0.01g DMAP (4-(N,N-dimethylamino) pyridine), 0.202 g (2 mmol) triethylamine and 20mL CH_3CN was stirred at room temperature for 48h. Then the solution was poured into 50ml deionized water and the red precipitate was collected by filtration.

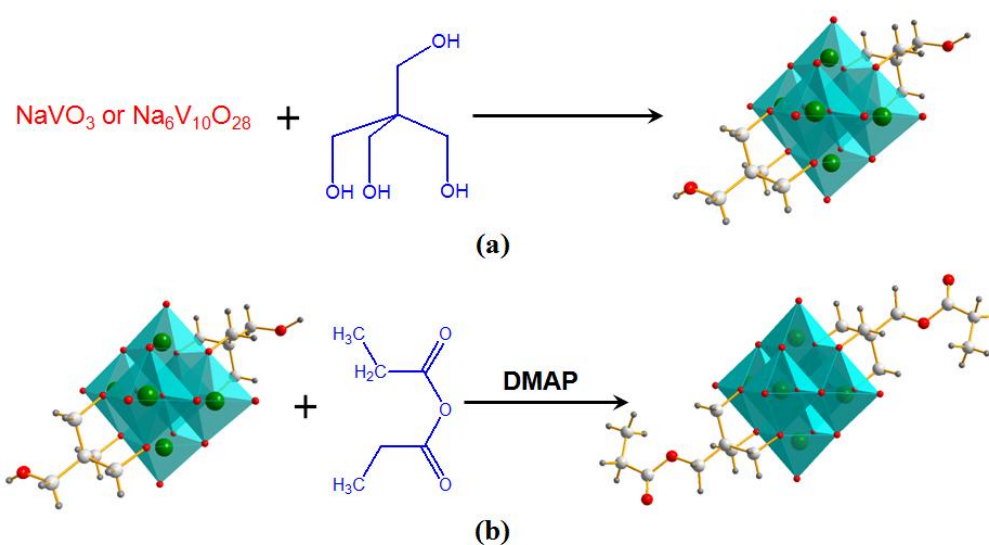


Figure 2.2. The synthesis process of the functionalized hexavanadate, V6-C3. (a) Step1, synthesis of V6OH; (b) Step 2, synthesis of V6-C3.

2.2.2 Crystallization of V6-C3

The crystallization process is as follows: the red block crystals are obtained by diffusion of Et₂O into their solution of acetic anhydride in room temperature (Figure 2.3). The size of V6-C3 crystal for diffraction experiment is 0.3 mm × 0.28 mm × 0.20 mm. Table 2.1 gives the detail information of the crystal data.

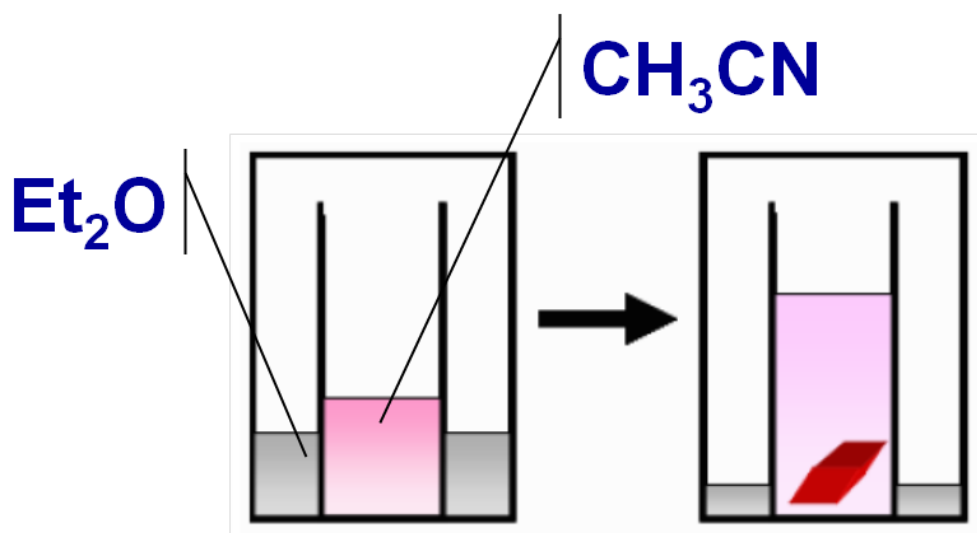


Figure 2.3. The crystallization of functionalized V6-C3.

2.2.3 Data collection and data reduction

The X-ray diffraction data of functionalized hexavanadate V6-C3 were collected at 100.0 K on a Kappa CCD APEX II diffractometer using graphite monochromated MoK α X-radiation (wavelength $\lambda = 0.71073 \text{ \AA}$). The data spots were recorded as ω -scans ($\Delta\omega = 1.0^\circ$) in order to reconstruct accurate three dimensional diffracted intensity peak profiles. The exposure times for the recorded frames vary from 10 s (low order data) to 30 s (high order data). 27 889 unique reflections were collected up to a resolution of $\sin\theta_{\max} = H/2 = 1.06 \text{ \AA}^{-1}$, where H is the Bragg vector modulus. An empirical absorption correction was applied using SADABS [Sheldrick, 2003] computer program. SORTAV program [Blessing, 1997] was used for sorting and averaging data revealing the excellent quality of the measurements.

2.2.4 IAM refinement

The crystal structure of V6-C3 was solved using SIR94 program [Altomare, 1993] and refined using SHELX 97 [Sheldrick, 1997; Sheldrick, 2008] implemented in WinGX package [Farrugia, 1999]. All atoms, except the hydrogen ones were refined

by using anisotropic thermal parameters. Thermal ellipsoid plots were obtained using the program ORTEP3 [Burnett, 1996].

2.2.5 Charge density refinement

The electron density of V6-C3 is described using the program package MoPro [Guillot, 2000; Jelsch, 2005], which is based on the multipole formalism developed by Hansen and Coppens [Hansen & Coppens, 1978]. $y_{lm\pm}$ is modulated by a Slater-type radial function $R_{nl}(r) = Nr^{n_l} \exp(-\zeta_l r)$, where N is the normalization factor. The exponents ζ_l (in bohr⁻¹) of the radial functions are chosen equal to 3.1, 3.8 and 4.5 and $n_l = 2, 2, 3$ up to octupoles ($l = 3$) for C, N and O atoms respectively; for V atoms, $\zeta_l = 5.98$ and $n_l = 4, 4, 4, 4$ up to hexadecapoles ($l = 4$); $\zeta_l = 2.0$ bohr⁻¹ and $n_l = 1$ (dipole level, $l = 1$) for the H atoms. Table 2.1 gives the details of structure refinement and charge density refinement.

Vanadium element is a $3d$ transition metal, which could imply some difficulties when refining the electron density because of the significantly different radial extension of the $3d$ and $4s$ valence orbitals. It is well established [Coppens, 1985; Macchi, 1999; Ozerov, 2001; Farrugia, 2003] that $3d$ transition metals imply some difficulties when refining the deformation density because of the significantly different radial extension of the $3d$ and $4s$ valence orbitals. In view of these problems, it is a common practice to treat the $4s$ density as "core" density [Rees, 1976; Martin, 1982]. According to a previous charge density analysis performed on a decavanadate (V10), model for V atoms is based on $4s^0 3d^3$ configuration, where V^{2+} contains 18 core electrons [Bošnjaković-Pavlović, 2009]. In order to conserve electronic neutrality, we have attributed the formal charges as follows: $[(Bu_4N)_2]^{2+}$ $[V_6O_{13}\{(OCH_2)_3CCH_2OCOCH_2CH_3\}]^{2-}$. Two refinement strategies have been used: i) refinement strategy 1, where anion and cation are refined separately, implying no charge transfer between anion and cation; ii) refinement strategy 2, where anion and cation are refined together authorizing charge transfer between anion and cation.

Table 2.1. Crystallographic details of V6-C3.

Sample and crystal data	
Chemical formula	C ₄₈ H ₉₈ N ₂ O ₂₃ V ₆
Formula weight	688.46
Temperature	100(2) K
Wavelength	0.71073 Å
Crystal size	0.20 x 0.18 x 0.25 mm
Crystal habit	clear red block
Crystal system	monoclinic
Space group	<i>P</i> 2 1/ <i>c</i>
<i>a</i>	10.866(5) (Å)
<i>b</i>	14.776(5) (Å)
<i>c</i>	19.636(5) (Å)
α	90 (Å)
β	122.924(2) (Å)
γ	90 (Å)
Volume	3123.76 (Å ³)
<i>Z</i>	4
Density (calculated)	1.464 g/cm ³
Absorption coefficient	0.935 mm ⁻¹
<i>F</i> (000)	1444
Data collection and structure refinement	
Diffractometer	Kappa CCD APEX II
Radiation source	Mo K α
Theta range	2.46 to 48.86 °
Index ranges	-22 ≤ <i>h</i> ≤ 22, 0 ≤ <i>k</i> ≤ 31, 0 ≤ <i>l</i> ≤ 41
Reflections collected	326479
Independent reflections	27889 [<i>R</i> _{int} = 0.0319]
Absorption correction	multi-scan
Structure solution technique	direct methods
Structure solution program	SHELXS-1997
Refinement method	Full-matrix least-squares on <i>F</i> ²
Refinement program	SHELXL-1997
Goodness-of-fit on <i>F</i> ²	1.056
Δ/σ_{\max}	0.03
Final <i>R</i> indices	20073 data, <i>I</i> > 2 σ (<i>I</i>), <i>R</i> ₁ = 2.75%, <i>wR</i> ₂ = 7.30% all data, <i>R</i> ₁ = 3.51%, <i>wR</i> ₂ = 7.71%
Largest diff. peak and hole	0.93 and -0.58 eÅ ⁻³
Charge density refinement	
Reflections used in Mopro	17817, <i>I</i> > 3 σ (<i>I</i>)
Resolution range used	0.06 - 1.06 Å ⁻¹
κ -refinement	<i>R</i> ₁ = 2.73%, <i>wR</i> ₂ = 3.27%, GOF = 1.28
Multipole refinement	<i>R</i> ₁ = 1.97%, <i>wR</i> ₂ = 1.92%, GOF = 0.91

Strategy 1: we have not authorized a charge transfer between the anion and cation. All steps of the refinements were separated. In each step, the anion was firstly refined, then the cation. The general scheme of refinement was the following: first, scale factor, and non-hydrogen atoms anisotropic displacement parameters were refined over all data. A high-order refinement ($\sin \theta/\lambda \geq 0.8 \text{ \AA}^{-1}$) of the coordinates and the anisotropic displacement parameters of the non-hydrogen atoms was then performed. Subsequently, the multipole parameters and κ parameters were introduced sequentially and refined for the non-hydrogen atoms for all data. Finally, the coordinates and anisotropic thermal displacement parameters of the non-hydrogen atoms are allowed to be refined. In the final step, the isotropic thermal displacement parameters of the hydrogen atoms were refined. Refinement of this model was stable and converged to the lowest least-squares indices. In the end of the cycles, the thermal anharmonicity parameters for V atoms were refined.

Strategy 2: Based on Strategy 1, we permit the charge transfer between cation and anion. We refine the multipole populations and the corresponding κ parameters of cation and anion in the same step.

2.3 Results

2.3.1 Crystal structure description

The X-ray structural analysis reveals that the asymmetric unit of the compound $[(C_4H_9)_4N]_2[V_6O_{13}\{(OCH_2)_3CCH_2OCCH_2CH_3\}_2]$ (V6-C3) is composed of one half of a centrosymmetric functionalized V6 anion, one tetrabutylammonium (TBA) cations (Figure 2.4). The functionalized V6-C3 crystallized in a monoclinic system with space group symmetry $P2_1/c$.

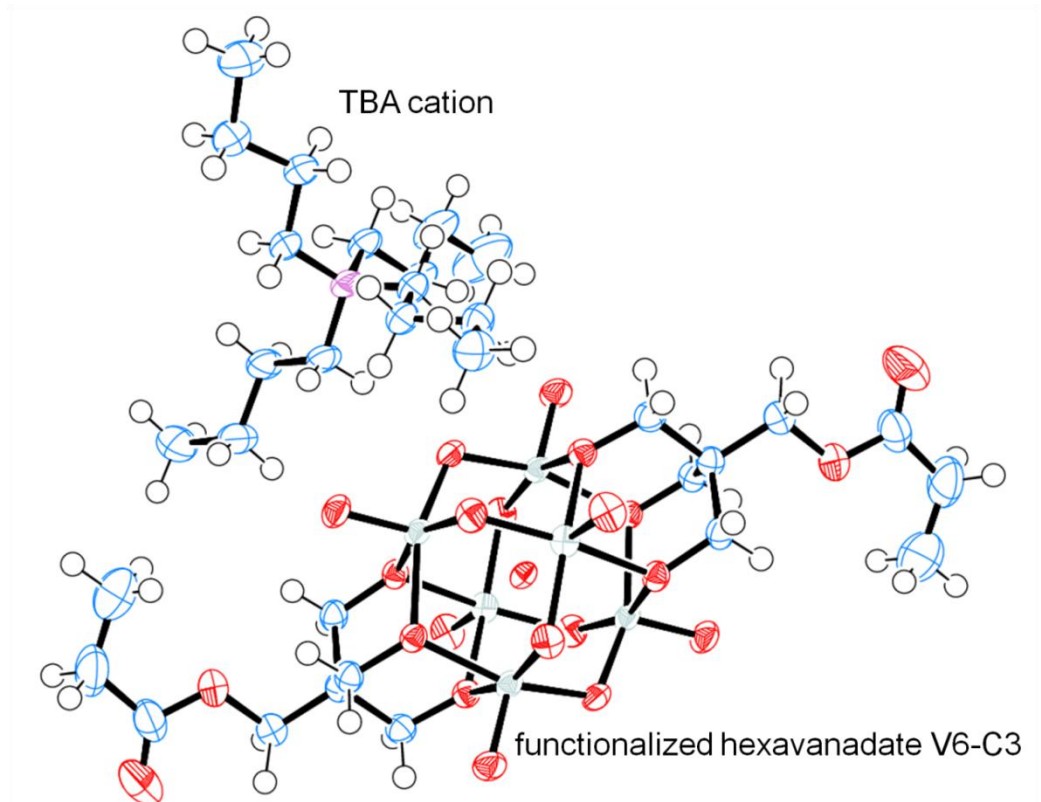


Figure 2.4. ORTEP view of the functionalized hexavanadate V6-C3.

2.3.1.1 V6 core of functionalized [V6-C3]²⁻

Due to the functionalization, the V6 cluster was stabilized by the organic ligands. The functionalized V6-C3 anion is composed of V6 core and two tris(alkoxo) ligands (Figure 2.5). The V6 core presents the Lindqvist structure, in which there are six VO6 units, each of them form an octahedron. The six small {VO6} octahedrons constitute a big octahedron, which is V6 core (Figure 2.5). The different oxygen types have been described in §1.4.4. The O61 atom is in the geometric center of the octahedron. In the opposite sides of the V6 core, there are two symmetrical organic ligands (Figure 2.5a, Figure 2.6). Tables of atomic coordinates, thermal displacement parameters, and bond angles are in Appendix (table A2.1, A2.2 and A2.3). The V-O interatomic distances are listed in Table 2.2, and the other bond distances are listed in Appendix table A2.4.

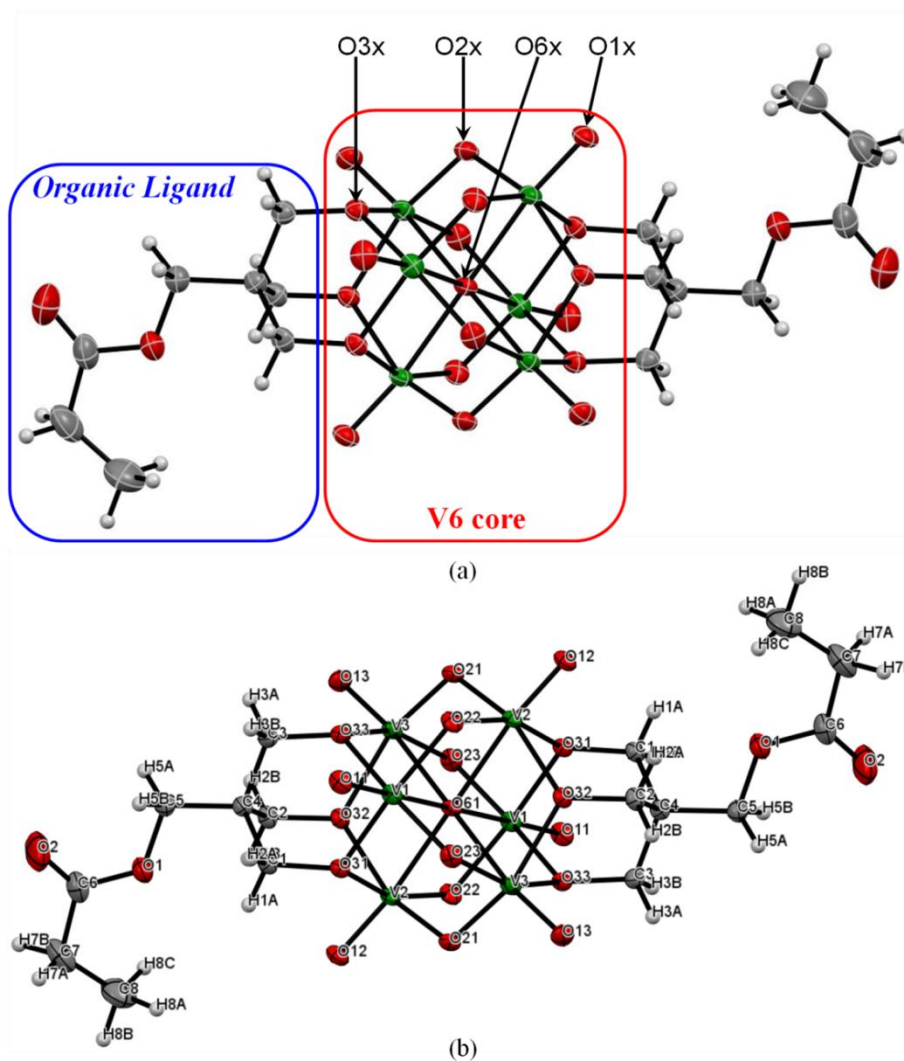


Figure 2.5. Structure of $[V_6-C_3]^{2-}$. (a) V_6 core, organic ligand, and the the types of O atoms; (b) Labeling of atoms for $[V_6-C_3]^{2-}$.

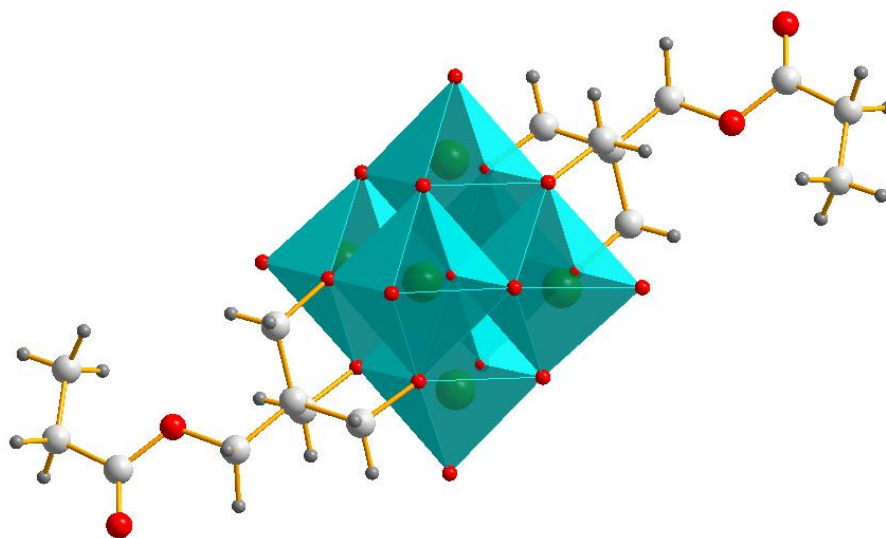


Figure 2.6. The octahedral structure of $[V_6-C_3]^{2-}$.

Table 2.2. Bond lengths (Å) in $[V_6-C_3]^{2-}$ with estimated standard deviations in parentheses.

Vandium atoms	Vanadium type	Bond	Distance
V1	VII	V1-O11	1.6094(4)
		V1-O22	1.8552(6)
		V1-O23	1.7831(8)
		V1-O31	1.9984(6)
		V1-O33	2.0465(7)
		V1-O61	2.2396(5)
V2	VII	V2-O12	1.6064(5)
		V2-O21	1.8700(7)
		V2-O22	1.7827(4)
		V2-O31	2.0460(5)
		V2-O32	1.9921(7)
		V2-O61	2.2380(7)
V3	VII	V3-O13	1.6090(7)
		V3-O21	1.7785(5)
		V3-O23	1.8729(4)
		V3-O32	2.0452(7)
		V3-O33	1.9915(5)
		V3-O61	2.2445(8)

2.3.1.2 Organic ligands of functionalized $[V_6-C_3]^{2-}$

The O3x atoms are the linkage of V6 core and the organic ligands (Cx-C4 bonds, Figure 2.7). Table 2.3 lists the distances of these bonds and presents the statistical results obtained by CSD searching.

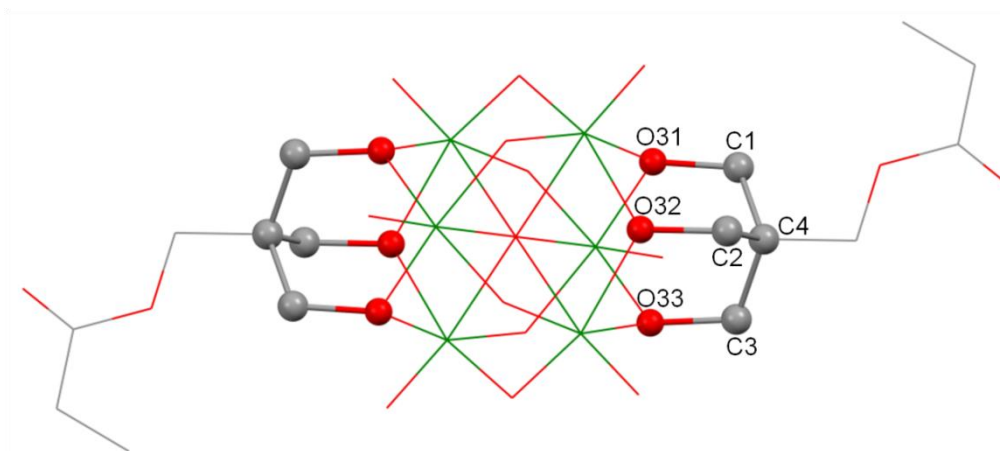


Figure 2.7. O3x-Cx bond and Cx-C4 bond. H atoms have been omitted.

Table 2.3. O3x-Cx and Cx-C4 bond distances (Å) in organic ligand with estimated standard deviations in parentheses and corresponding bonds retrieved in CSD.

Bond type	Interatomic distance					
	Experimental data of V6-C3				V6 in CSD ^[a]	
	Bond	Distance	Average	<Min, Max>	Average	<Min, Max>
O3x-Cx	O31-C1	1.4239(5)	1.425	1.424, 1.427	1.429	1.322, 1.491
	O32-C2	1.4267(5)				
	O33-C3	1.4270(5)				
Cx-C4	C1-C4	1.5338(5)	1.535	1.534, 1.537	1.533	1.416, 1.632
	C2-C4	1.5366(4)				
	C3-C4	1.5340(5)				

[a] The statistical data is from 39 functionalized V6 compounds searched in CSD.

2.3.1.3 The TBA cation

The asymmetric unit of the title compound V6-C3 contains one tetrabutylammonium (TBA) cation, which takes +1 charge (Figure 2.8). The [V6-C3]²⁻ anion was counter-balanced by TBA cation. In TBA cation, there are four chemical equivalent chains connected through the bonds N-Cx1, Cx1-Cx2, Cx2-Cx3 and Cx3-Cx4. The POM clusters are usually big size of anions, and need to be stabilized *via* the similar size of cations, which can be explained by “HSAB (hard-soft acid-base) theory” [Pearson, 1963]. The main bond distances of TBA are listed in Table 2.4. A comparison is made with the reported crystallographic results of TBA cations in POM compounds containing at least one element among Mo, V, W, or Nb.

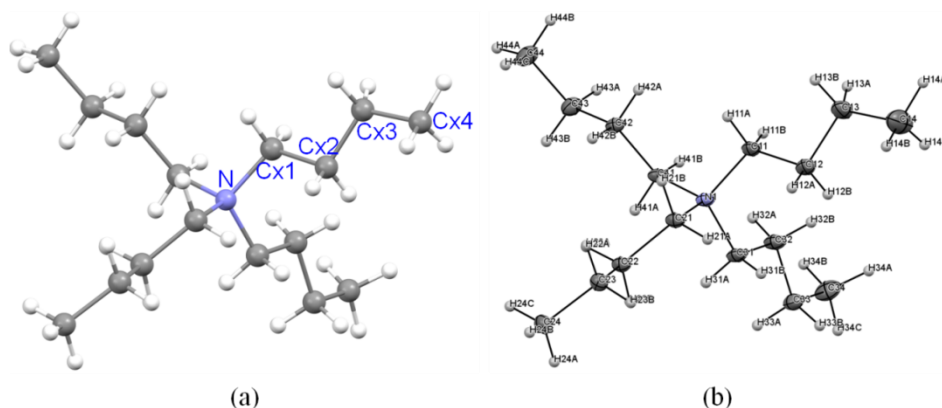


Figure 2.8. The structure of TBA cation in functionalized V6-C3.(a) The types of atoms in TBA cation;(b) ORTEP view of TBA cation and the labeling of the atoms.

Table 2.4. Selected bond lengths (Å) in TBA cation with estimated standard deviations in parentheses and corresponding bonds retrieved in CSD.

		Interatomic distance				
		Experimental data of V6-C3			TBA in CSD [a]	
Bond	Bond	Distance	Average	<Min, Max>	Average	<Min, Max>
N1-Cx1	N1-C11	1.5229(1)	1.521	1.518, 1.524	1.523	1.072, 1.922
	N1-C21	1.5199(1)				
	N1-C31	1.5238(1)				
	N1-C41	1.5177(1)				
Cx1-Cx2	C11-C12	1.5205(1)	1.519	1.514, 1.521	1.511	0.778, 1.982
	C21-C22	1.5213(1)				
	C31-C32	1.5136(1)				
	C41-C42	1.5190(1)				
Cx2-Cx3	C12-C13	1.5209(1)	1.525	1.521, 1.527	1.529	0.880, 2.082
	C22-C23	1.5272(1)				
	C32-C33	1.5264(1)				
	C42-C43	1.5261(1)				
Cx3-Cx4	C13-C14	1.4975(2)	1.514	1.498, 1.521	1.477	0.718, 2.571
	C23-C24	1.5160(1)				
	C33-C34	1.5212(1)				
	C43-C44	1.5210(1)				

[a] The statistical data is from 589 POM compounds searched in CSD.

2.3.2 Crystal packing

The crystal structure of the functionalized V6-C3 is constructed by an extensive network of hydrogen bondings, which involves [V6-C3]²⁻ and the [TBA]⁺. Table 2.6 reports the most significant non covalent interactions according to the usual criterium ($d(D \cdots A) < 3.5 \text{ \AA}$). These non covalent interactions are of a unique type: C-H \cdots O.

Table 2.5. Distances (Å) and angles (°) of the hydrogen bonds in [V6-C3]²⁻ anion and TBA cation (D donor, A acceptor). (i) = $x-1, -y-1/2, z-1/2$, (ii) = $x, -y-1/2, z-1/2$, (iii) = $-x+1, y-1/2, -z+1/2$, (iv) = $-x+1, -y, -z+1$, (v) = $-x+2, -y, -z+1$. All O atoms are from symmetry, x, y, z

D-H ···A	d(H-A)	d(D···A)	∠DHA
C31-H31B ···O22	2.251	3.075	130.59
C5-H5B ···O2	2.364	2.684	94.65
C32-H32A ⁽ⁱⁱⁱ⁾ ···O11	2.381	3.299	140.67
C23-H23B ^(iv) ···O33	2.399	3.478	169.40
C21-H21B ⁽ⁱ⁾ ···O2	2.401	3.317	140.53
C41-H41B ⁽ⁱⁱⁱ⁾ ···O23	2.433	3.215	127.27
C1-H1A ···O1	2.448	2.829	98.81
C2-H2A ···O1	2.454	2.828	98.39
C42-H42A ⁽ⁱⁱⁱ⁾ ···O13	2.459	3.464	152.39
C13-H13A ⁽ⁱⁱ⁾ ···O12	2.465	3.470	152.60
C5-H5A ^(v) ···O13	2.476	3.466	150.29
C21-H21A ···O22	2.492	3.242	124.77
C24-H24A ^(iv) ···O21	2.585	3.400	133.28
C2-H2A ···O12	2.587	3.057	105.02
C11-H11A ⁽ⁱ⁾ ···O2	2.590	3.378	128.28
C11-H11B ⁽ⁱⁱⁱ⁾ ···O23	2.590	3.395	129.92
C13-H13A ⁽ⁱⁱⁱ⁾ ···O21	2.590	3.430	133.17
C2-H2B ···O13	2.591	3.073	105.76
C3-H3A ···O13	2.593	3.061	104.82
C3-H3B ^(iv) ···O11	2.617	3.081	104.72
C1-H1A ···O12	2.622	3.073	103.88
C31-H31A ···O12	2.622	3.415	128.94
C1-H1B ^(iv) ···O11	2.626	3.087	104.57
C43-H43A ⁽ⁱⁱⁱ⁾ ···O23	2.653	3.407	125.56
C11-H11B ^(iv) ···O31	2.657	3.690	157.80
C12-H12A ···O11	2.692	3.646	145.77

As presented in Table 2.5, all of the H bond acceptors are O atoms, which belongs to $[V6-C3]^{2-}$, and most of them are especially from V6 core. Focusing on the hydrogen bond network built by $[V6-C3]^{2-}$ is the way to understand the molecular packing (Figure 2.9). As shown in Figure 2.9 a, all expanding contacts of C-H \cdots O bonds derive from $[V6-C3]^{2-}$. Around $[V6-C3]^{2-}$, there are two other $[V6-C3]^{2-}$ and six TBA cations (Figure 2.9 a). This represents the coordination packing sphere of $[V6-C3]^{2-}$. TBA cation is surrounded by three $[V6-C3]^{2-}$ (Figure 2.9 b). The behavior of these non covalent interactions indicates that the V6 core is an electron reservoir, which usually acts as an electron acceptor in charge transfer molecules [Yamase, 1998; Coronado, 2005].

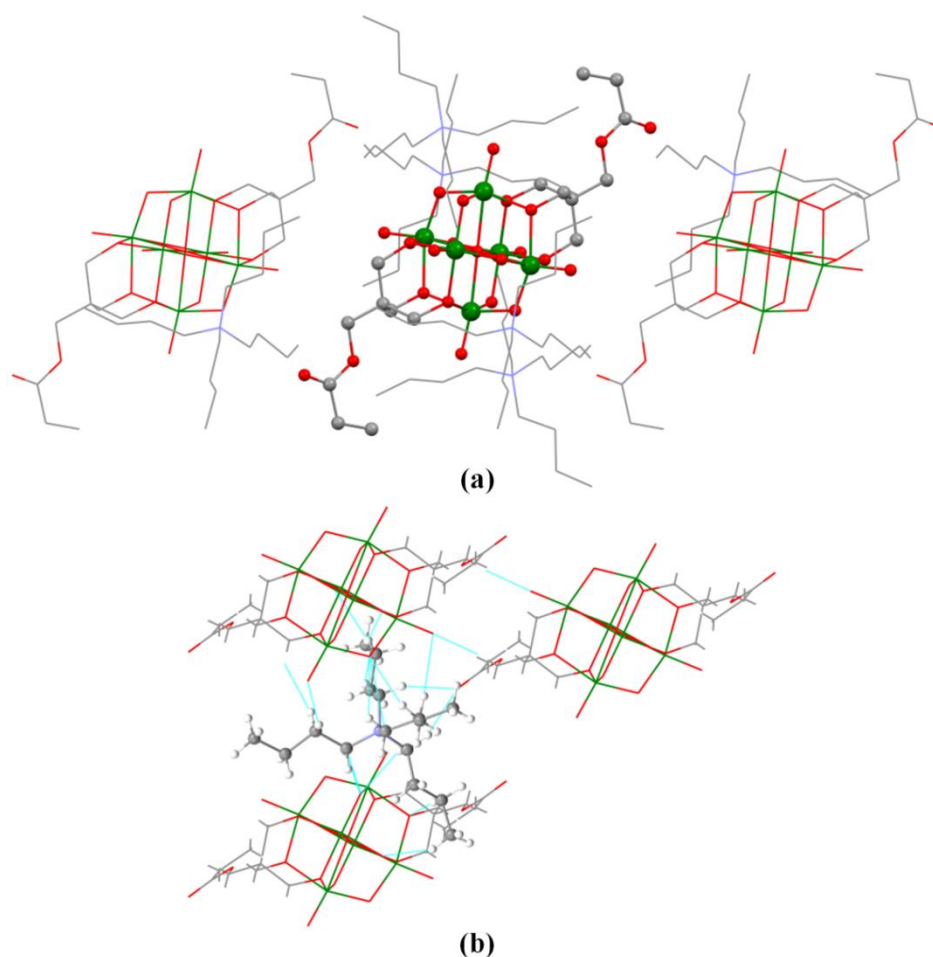


Figure 2.9. Hydrogen bond network built by : (a) $[V6-C3]^{2-}$, the center $[V6-C3]^{2-}$ is shown by ball-and-stick style, the surrounding anions and cations are shown by wireframe style. H atoms have been omitted; (b) TBA cation, the center TBA cation is displayed by ball-and-stick style, the surrounding $[V6-C3]^{2-}$ are displayed by wireframe style.

The chains and layers in the structure, as shown in Figure 2.10 and Figure 2.11,

two adjacent $[V6-C3]^{2-}$, are linked by a couple of C-H \cdots O hydrogen bonds (C5-H5A \cdots O13, 2.476 Å) and form a 1D chain parallel to the crystallographic *a* axis.

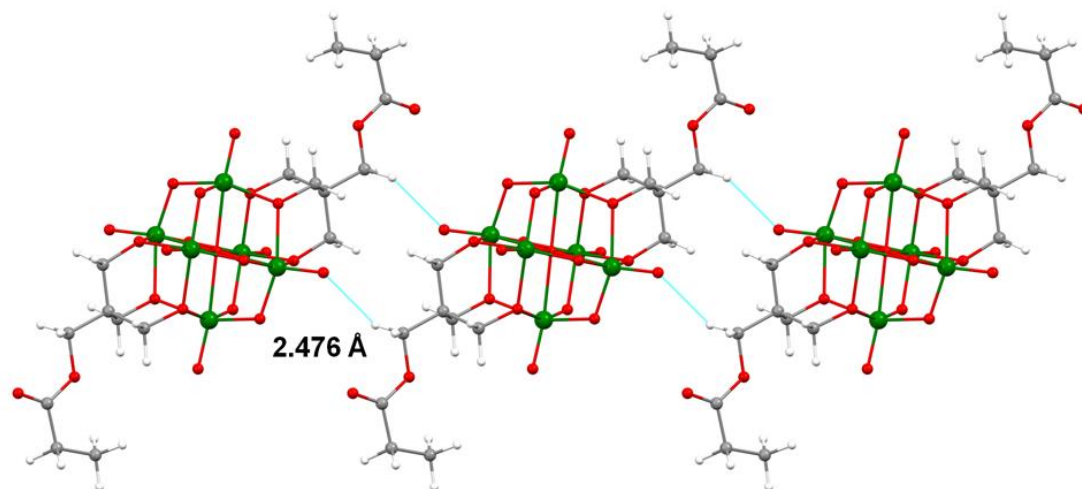


Figure 2.10. The 1D chain formed through C-H \cdots O hydrogen bonds in crystalline V6-C3, along *c* axis.

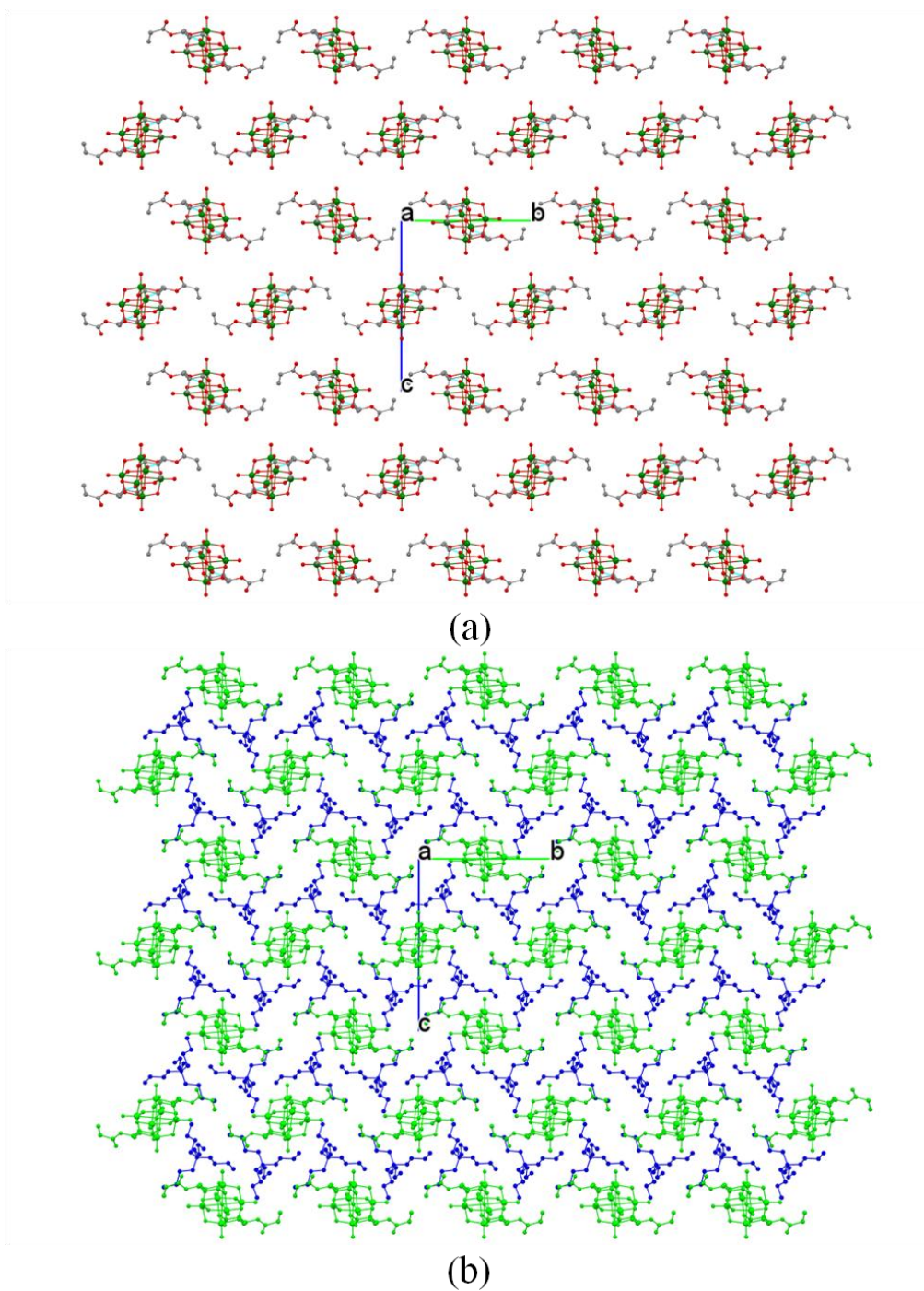


Figure 2.11. Molecular crystal packing of V6-C3 along **a** axis. H atoms have been omitted. (a) $[V6-C3]^{2-}$ chains and layer formed by C-H...O hydrogen bonds. TBA cations have been omitted; (b) TBA cations are filling in the areas between two neighboring functionalized V6-C3 anions. $[V6-C3]^{2-}$ and TBA cations are displayed by green and blue respectively.

2.3.3 Electron density

2.3.3.1 Plane definitions of the 2D electron density

According to the geometry of V6-C3, the main results of 2D electron density will be presented in five different planes as described below:

Plane 1: **V-O61-V**, in V6 core (Figure 2.12a). The three vanadium atoms are chemically equivalent. This plane exhibits the electron density distribution of four types of V-O chemical bonds. For an accurate description of the electron density distribution in different directions, there are in fact three planes: V1-O61-V2 (Figure 2.12 b), V1-O61-V3 (Figure 2.12 c), and V2-O61-V3 (Figure 2.12 d).

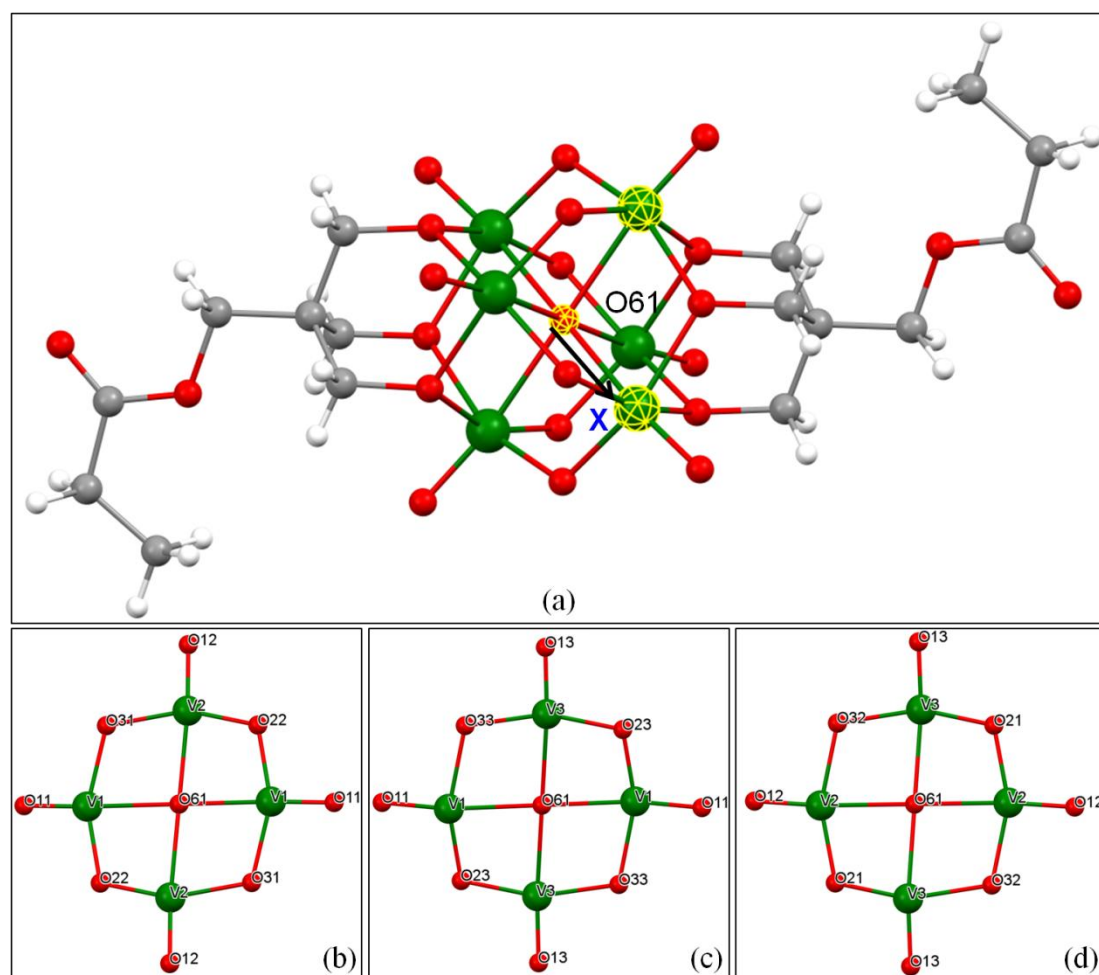


Figure 2.12. Plane 1, V-O61-V plane. (a) Definition for V-O61-V plane, the center atom is O61, the X and Y directions are the two different V atoms; (b) Plane V1-O61-V2; (c) Plane V1-O61-V3; (d) Plane V2-O61-V3.

Plane 2: **V-O3x-Cx**, the linkage between V6 core and organic ligand (Figure 2.13 a). This plane allows the understanding the electron density distribution of the linkage

site between V6 core and organic ligand, in other word, the linkage of electron donor and electron acceptor in POV-based charge transfer molecule. Precisely, there are also six planes: V1-O31-C1 (Figure 2.14b), V1-O33-C3 (Figure 2.13 c), and V2-O31-C1 (Figure 2.13 d), V2-O32-C2 (Figure 2.13 e), V3-O32-C2 (Figure 2.13 f), and V3-O33-C3 (Figure 2.13 g).

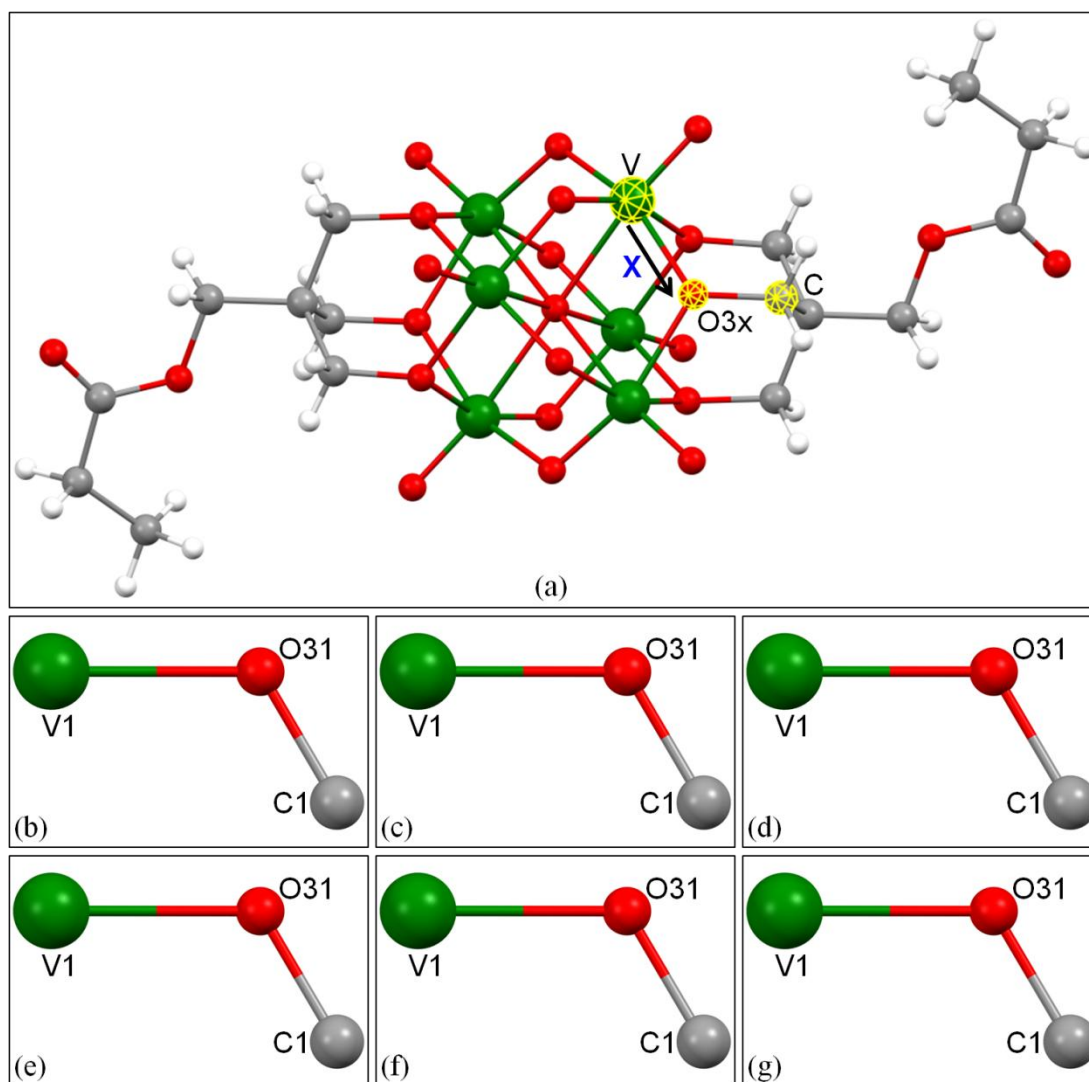


Figure 2.13. Plane 2, V-O3x-Cx plane. (a) Definition for V-O3x-Cx plane, the center of the plane is V, the organo-bridge O atom, the X and Y directions are O3x and Cx atom; (b) Plane of V1-O31-C1; (c) Plane of V1-O33-C3; (d) Plane of V2-O31-C1; (e) Plane of V2-O33-C2; (f) Plane of V3-O32-C2; (g) Plane of V3-O33-C3.

Plane 3: O3x-Cx-C4, in the organic ligand (Figure 2.14a). This plane is defined to present the electron density distribution of the tris(alkoxo) ligands in $[V6-C3]^{2-}$.

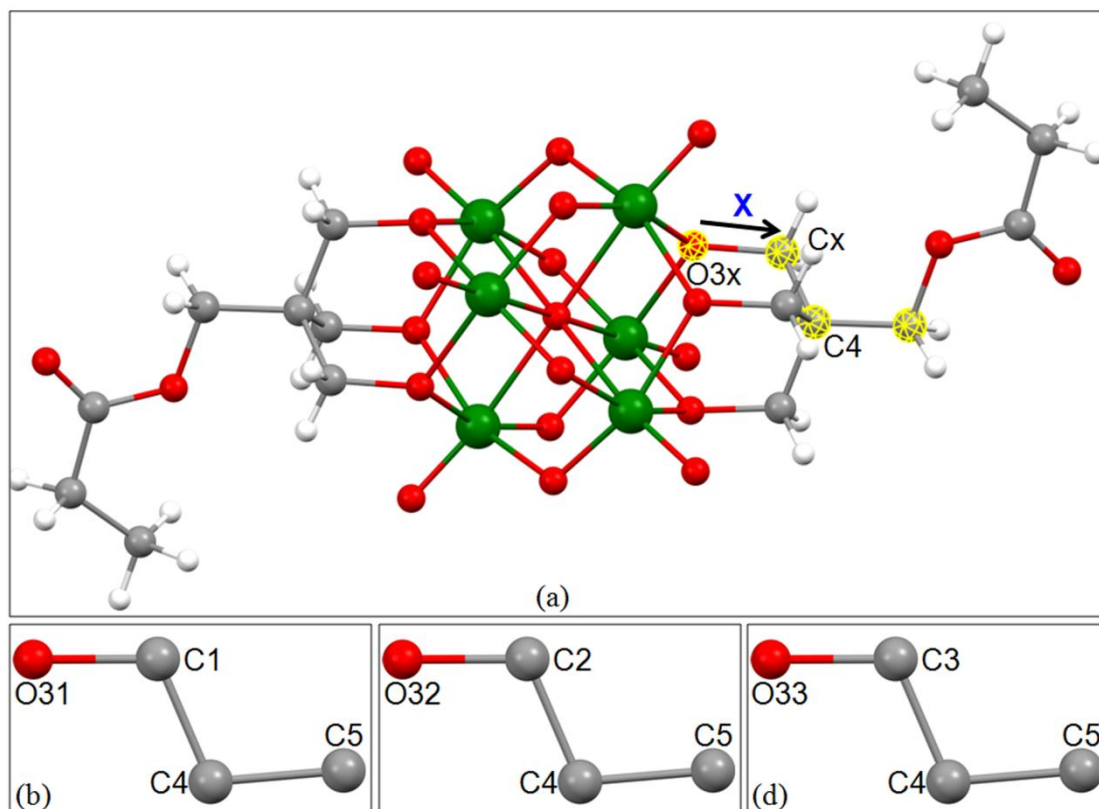


Figure 2.14. Plane 3, $O3x-Cx-C4$. (a) Definition for $O3x-Cx-C4$ plane, the center atom is $O3x$, the X and Y directions are Cx and $C4$, this plane contains the $C5$ (The torsion of $O3x-Cx-C4-C5$ is just 1.1°); (b) Plane of $O31-C1-C4$; (c) Plane of $O32-C2-C4$; (d) Plane of $O33-C3-C4$.

Plane 4: $O1-C6-O2$, in the organic ligand (Figure 2.15a). This plane presents the electron density distribution around the ester group in $[V6-C3]^{2-}$.

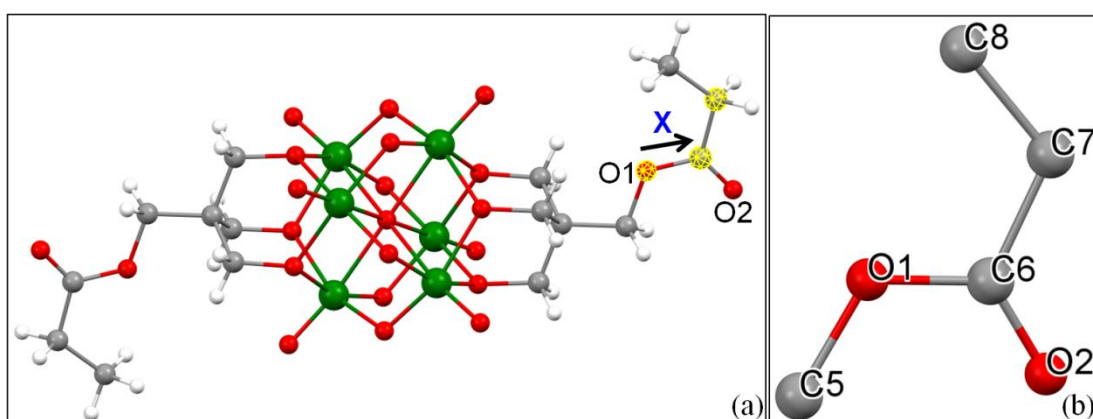


Figure 2.15. Plane 4, $O1-C6-O2$. (a) Definition for $O1-C6-O2$ plane, the center atom is $C6$, the X and Y directions are the neighbouring $O1$ and $O2$; (b) Plane of $O1-C6-O2$.

Plane 5: $N1-Cx1-Cx2$ (Figure 2.16a). This plane depicts the electron density

distribution of four nitrogen-carbon chains in TBA cation.

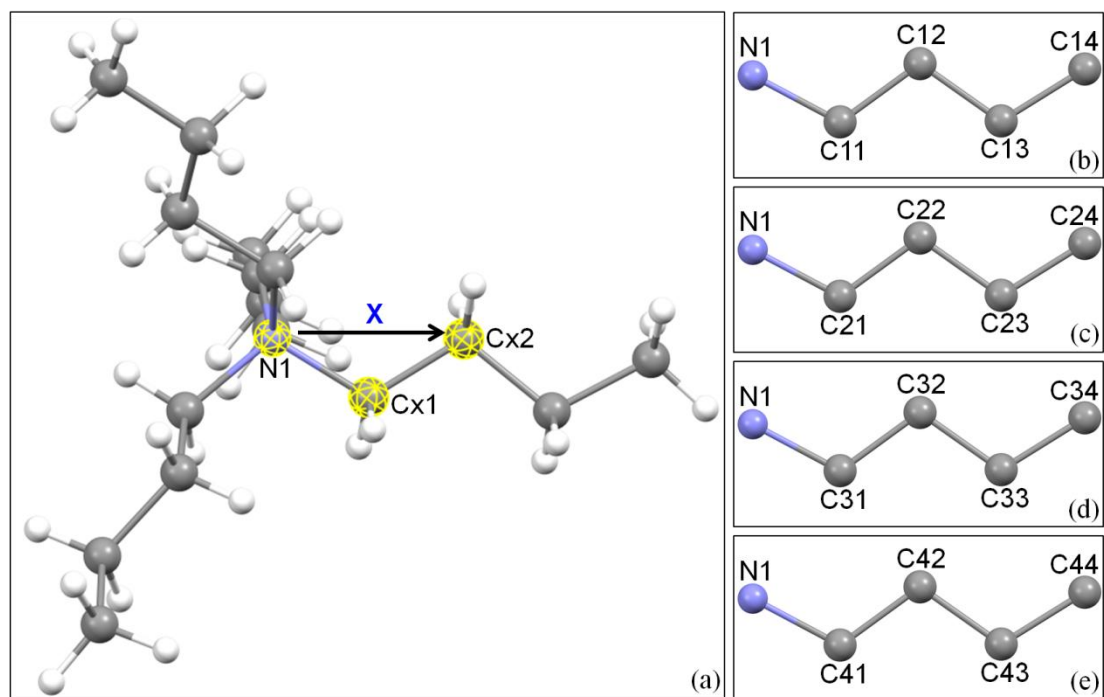


Figure 2.16. The plane 5, N1-Cx1-Cx2. (a) The definition for N1-Cx1-Cx2 plane, the center atom is N1, the X and Y directions are the neighbouring Cx2 and Cx1; (b) Plane of N1-C11-C12; (c) Plane of N1-C21-C22; (d) Plane of N1-C31-C32; (e) Plane of N1-C41-C42.

2.3.3.2 Residual density maps

The residual deformation electron density maps of the functionalized V6-C3 are presented in Figure 2.17.

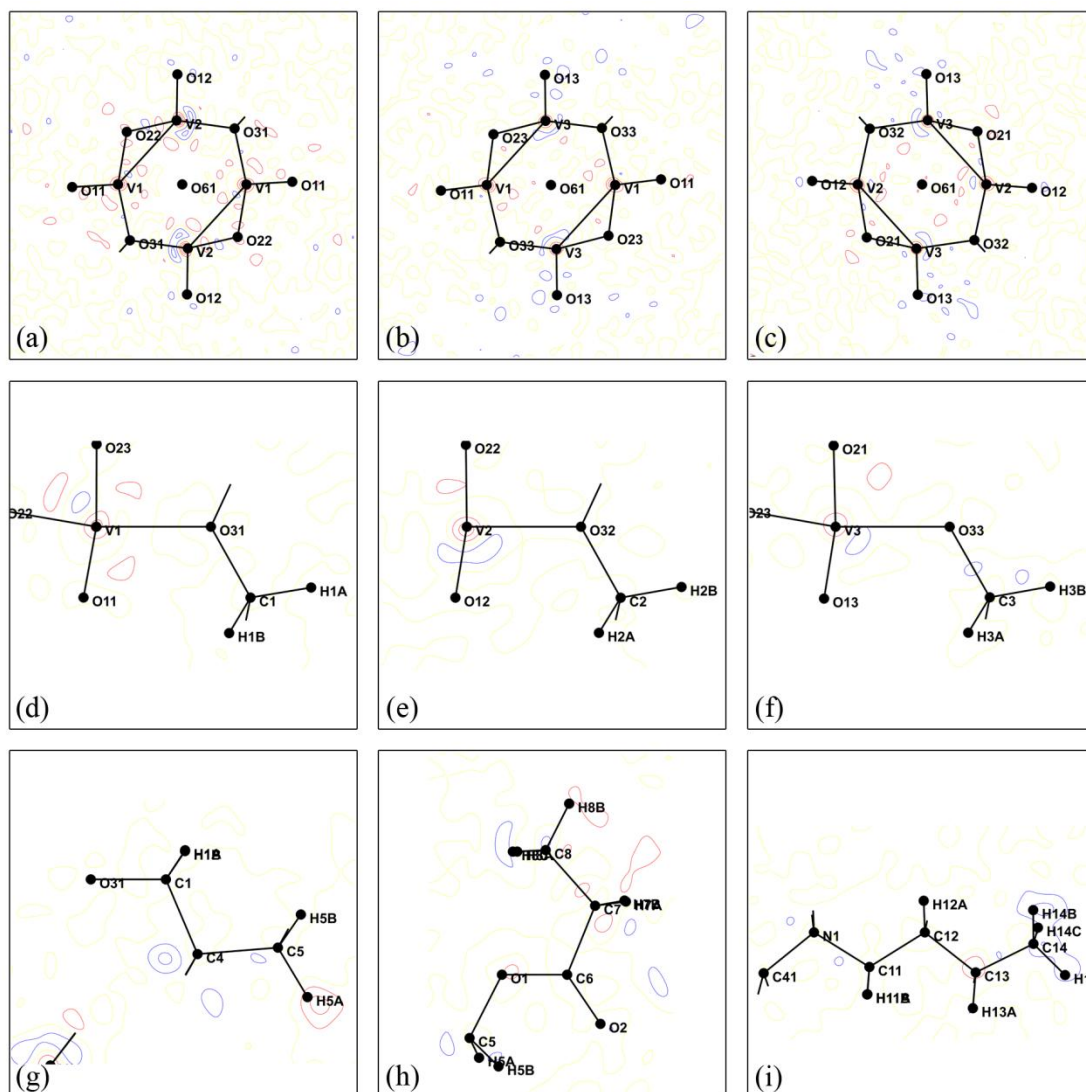


Figure 2.17. 2D residual deformation electron density maps for five planes. Contour intervals are $0.1 \text{ e} \text{ \AA}^{-3}$. Positive and negative contours are in blue and red. (a) (b) (c) Residual density maps of plane 1, V-O61-V. (d) (e) (f) Residual density maps of plane 2, V-O3x-C1. (g) Residual density maps of plane 3, O3x-Cx-C4, and (h) plane 4, O1-C6-O2. (i) Residual density maps of plane 5, N1-Cx1-C2x.

2.3.3.3 Experimental deformation density

The experimental multipole deformation electron density maps of the functionalized V6-C3 are presented in Figure 2.18.

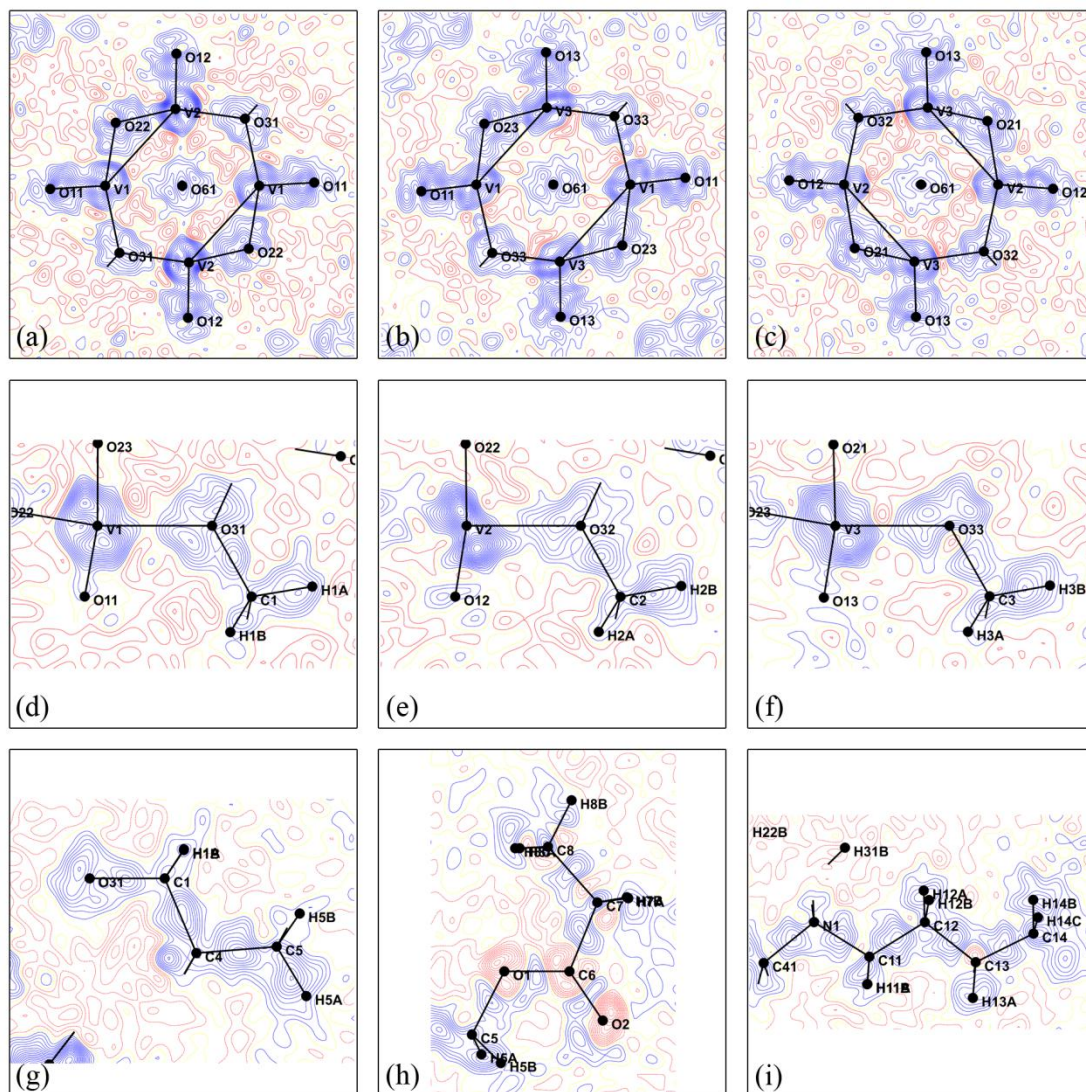


Figure 2.18. 2D experimental deformation electron density maps for five planes. Contour intervals are $0.05 e \text{ \AA}^{-3}$. Positive and negative contours are in blue and red. (a) (b) (c) Plane 1, V-O61-V, V1-O61-V2; (d) (e) (f) Plane 2, V-O3x-C1; (g) Plane 3, O3x-Cx-C4; (h) Plane 4, O1-C6-O2; (i) Plane 5, N1-Cx1-C2x.

2.3.3.4 Dynamic deformation density

The dynamic multipole deformation electron density maps of the functionalized V6-C3 are presented in Figure 2.19.

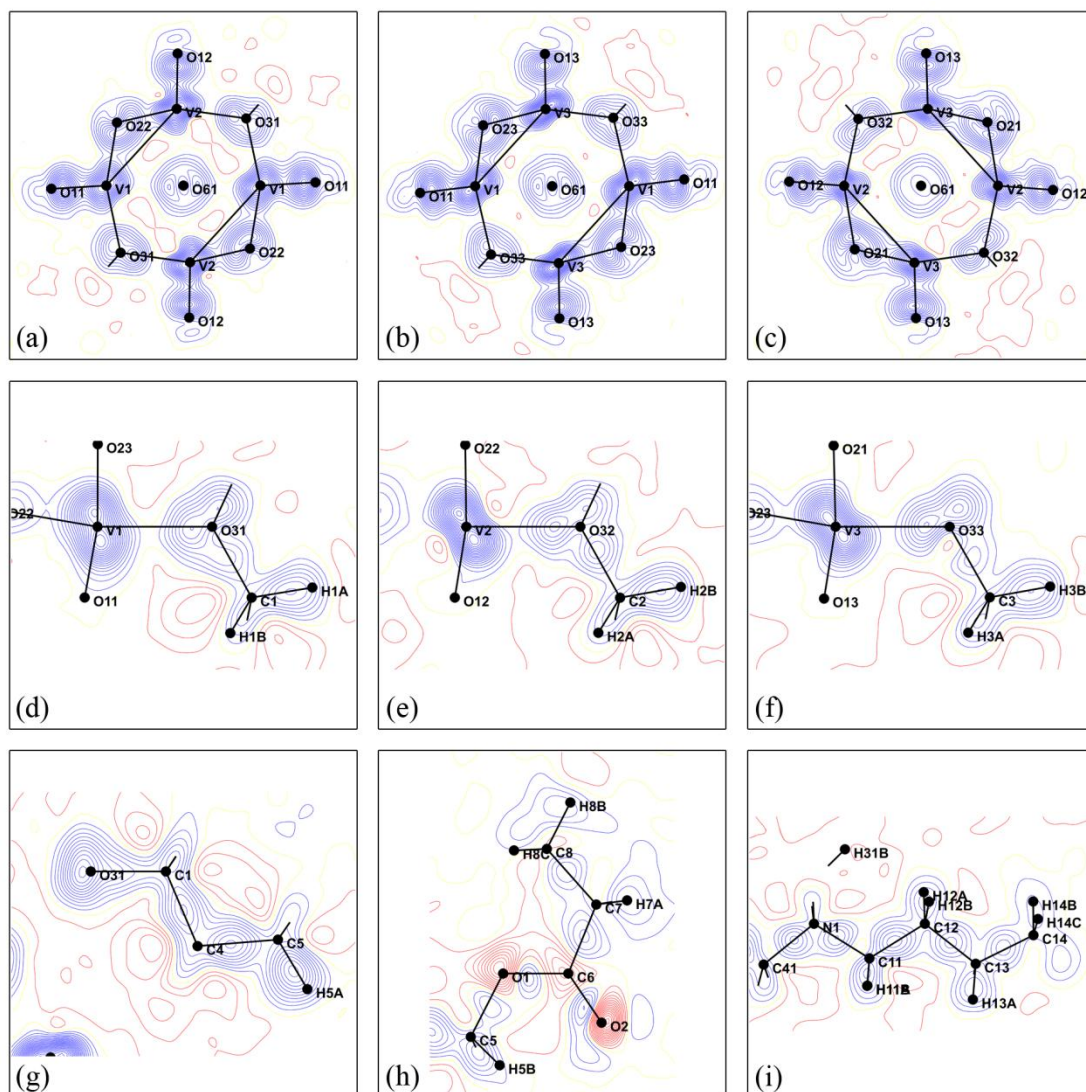


Figure 2.19. 2D dynamic deformation electron density maps for five planes. Contour intervals are $0.05 e\text{\AA}^{-3}$. Positive and negative contours are in blue and red. (a) (b) (c) Plane 1, V-O61-V, V1-O61-V2; (d) (e) (f) Plane 2, V-O3x-C1; (g) Plane 3, O3x-Cx-C4; (h) Plane 4, O1-C6-O2; (i) Plane 5, N1-Cx1-C2x.

2.3.3.5 Static deformation density

The experimental static deformation electron density maps of the functionalized V6-C3 are presented in Figure 2.20.

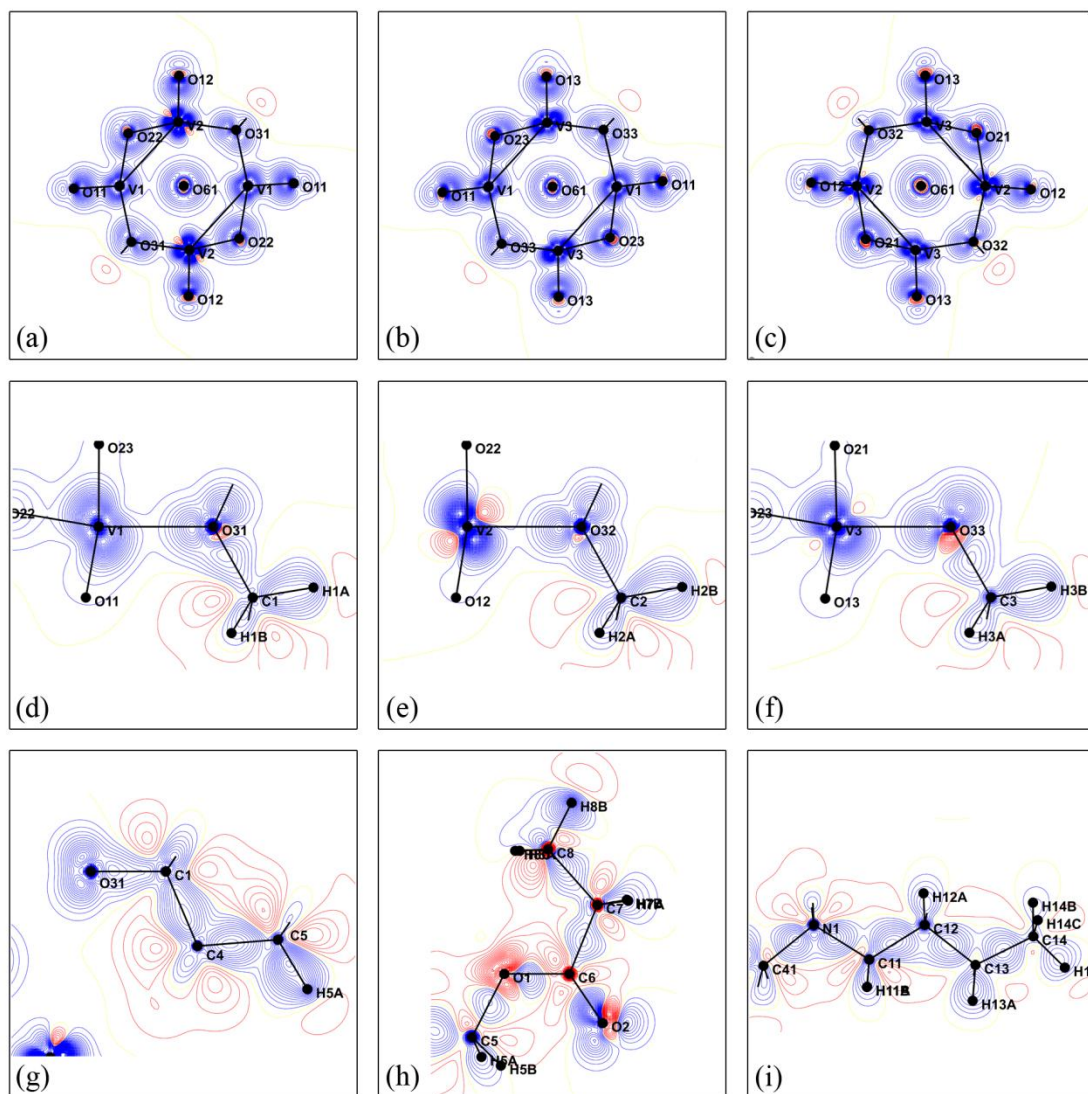


Figure 2.20. 2D static deformation electron density maps for five planes. Contour intervals are $0.05 \text{ e}\text{\AA}^{-3}$. Positive and negative contours are in blue and red. (a) (b) (c) Plane 1, V-O61-V, V1-O61-V2; (d) (e) (f) Plane 2, V-O3x-C1; (g) Plane 3, O3x-Cx-C4; (h) Plane 4, O1-C6-O2; (i) Plane 5, N1-Cx1-C2x.

2.3.3.6 Laplacian of total electron density

The Laplacian of total electron density maps of the functionalized V6-C3 are presented in Figure 2.21.

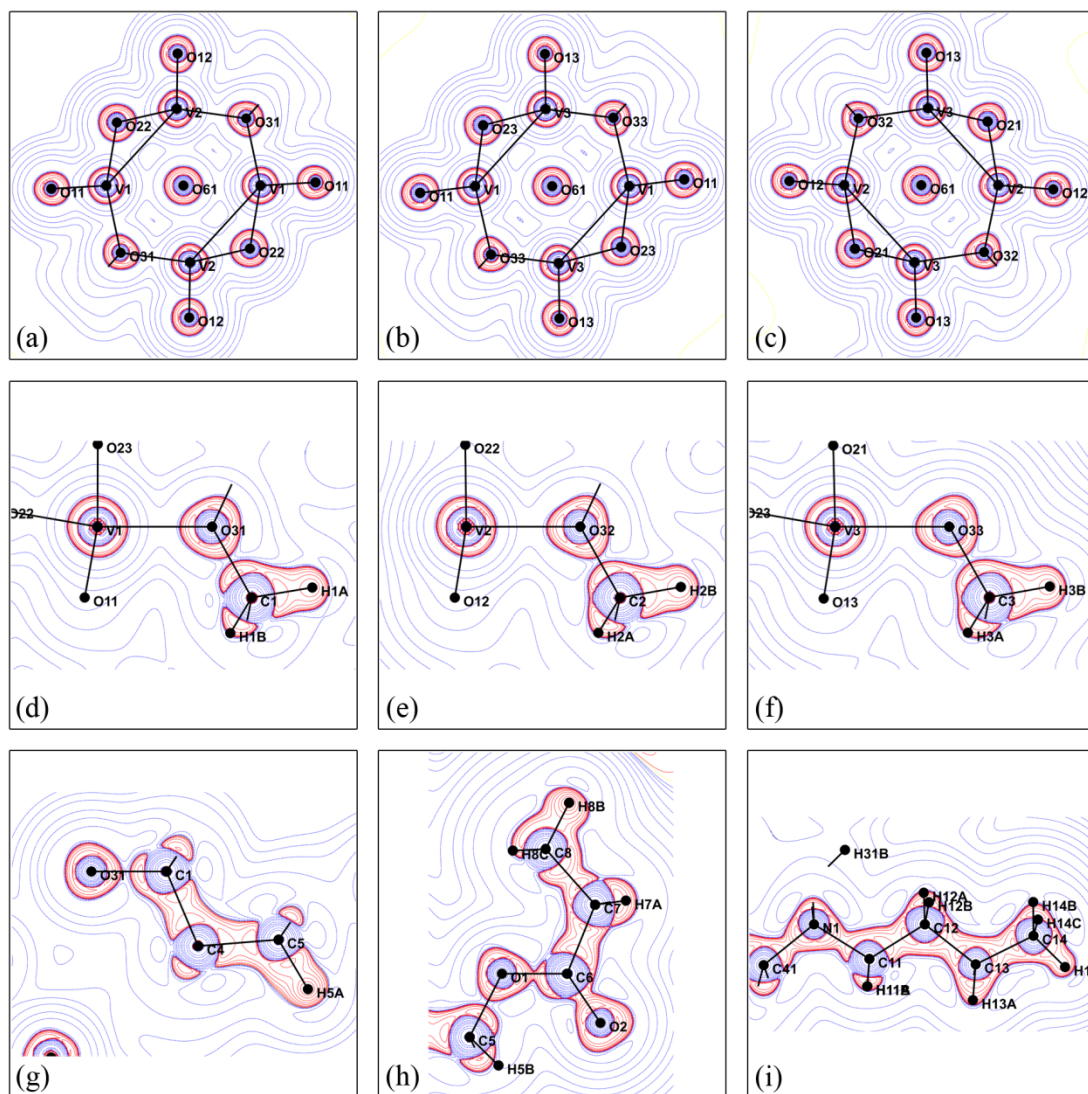


Figure 2.21. 2D Laplacian of total electron density maps for five planes. Contour intervals are $\pm 2, 4, 8 \cdot 10^n \text{ e}\text{\AA}^{-5}$ ($n=-1, 0, 1, 2$). Positive and negative contours are in blue and red. (a) (b) (c) Plane 1, V-O61-V, V1-O61-V2; (d) (e) (f) Plane 2, V-O3x-C1; (g) Plane 3, O3x-Cx-C4; (h) Plane 4, O1-C6-O2; (i) Plane 5, N1-Cx1-C2x.

2.3.3.7 Static deformation density of non covalent bonds

The experimental static deformation electron density maps of selected hydrogen bonds are presented in Figure 2.22.

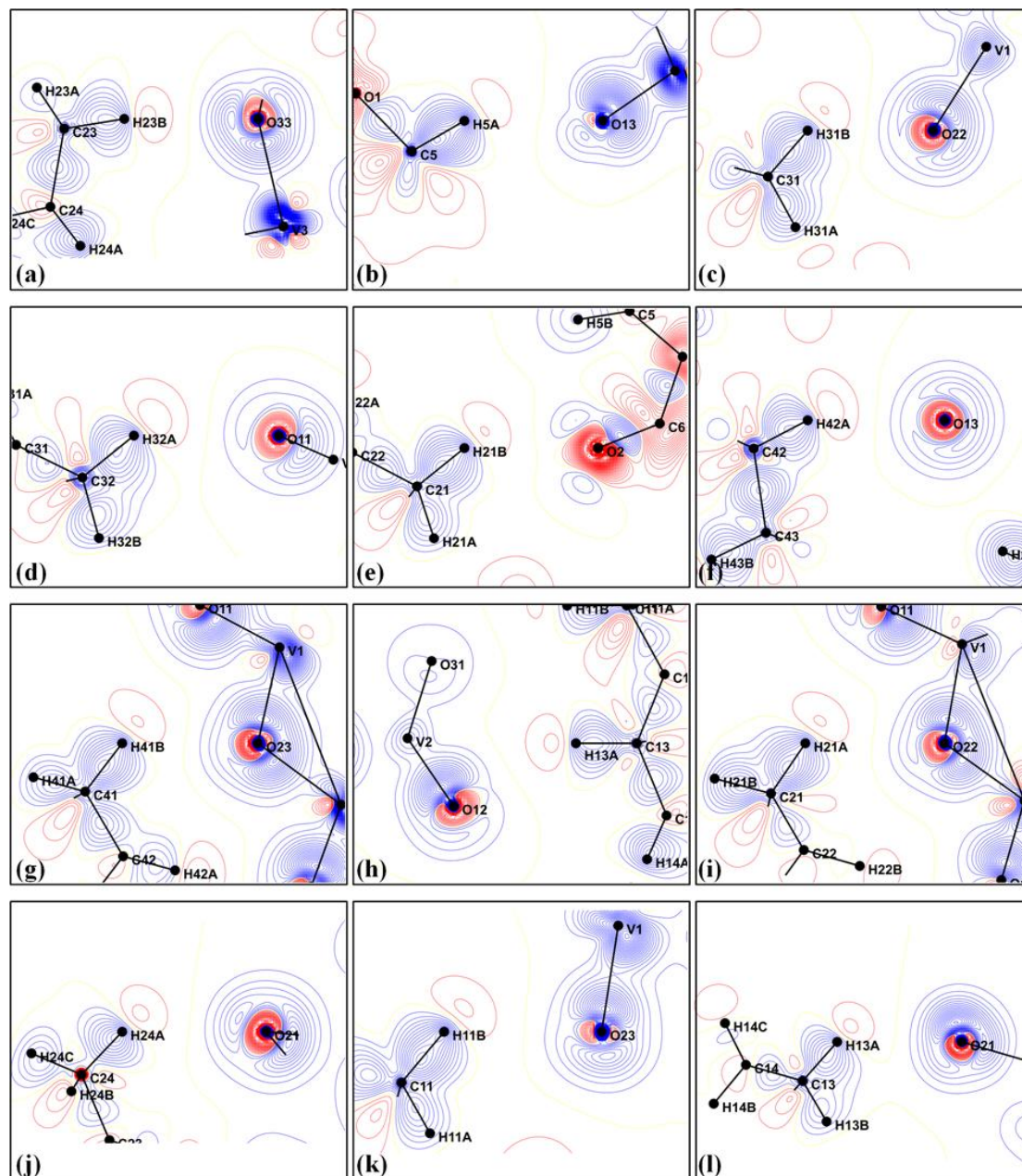


Figure 2.22. 2D static deformation electron density maps for 12 C-H...O bonds ranked by $\rho(r_c)$. The Contour intervals are $0.05 \text{ e}^{\text{\AA}^{-3}}$. Positive and negative contours are in blue and red.

2.3.4 Topological analysis of total electron density

2.3.4.1 Topological analysis of total electron density of V6 core

Experimental electron distributions are analyzed in terms of their topological features according to Bader's AIM theory [Bader, 1990]. Topological parameters of the electron density for the (3, -1) bond critical points (BCPs) in V6 core are given in Table 2.6. The BCPs in functionalized V6-C3 anion are shown in Figure 2.23.

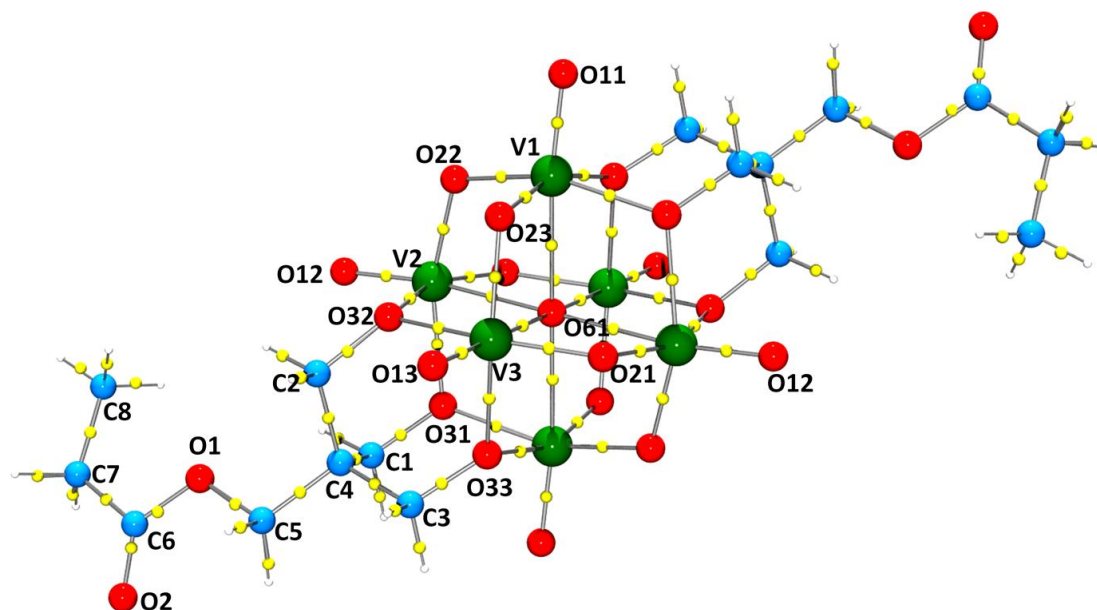


Figure 2.23. Bond critical points in $[V6-C3]^{2-}$, the yellow balls represent the BCPs.

2.3.4.2 Topological analysis of total electron density of organic ligand

Topological parameters of the electron density for the (3, -1) bond critical points (BCPs) in the organic ligand are given in Table 2.7 and Figure 2.23, while topological parameters of C-H bonds are compiled in Appendix (table A2.5).

2.3.4.3 Topological analysis of total electron density of TBA cation

Topological parameters of the electron density for the (3, -1) bond critical points (BCPs) in TBA cation are given in Table 2.8 while topological parameters of C-H bonds are presented in Appendix (table A2.5). The BCPs of TBA cation are shown in Figure 2.24.

2.3.4.4 Topological analysis of total electron density of non covalent bonds

Topological parameters of the electron density for the (3, -1) bond critical points

(BCPs) of non covalent bonds in Table 2.9. The 12 strongest C-H \cdots O bonds are selected to plot the experimental deformation density maps in Figure 2.22.

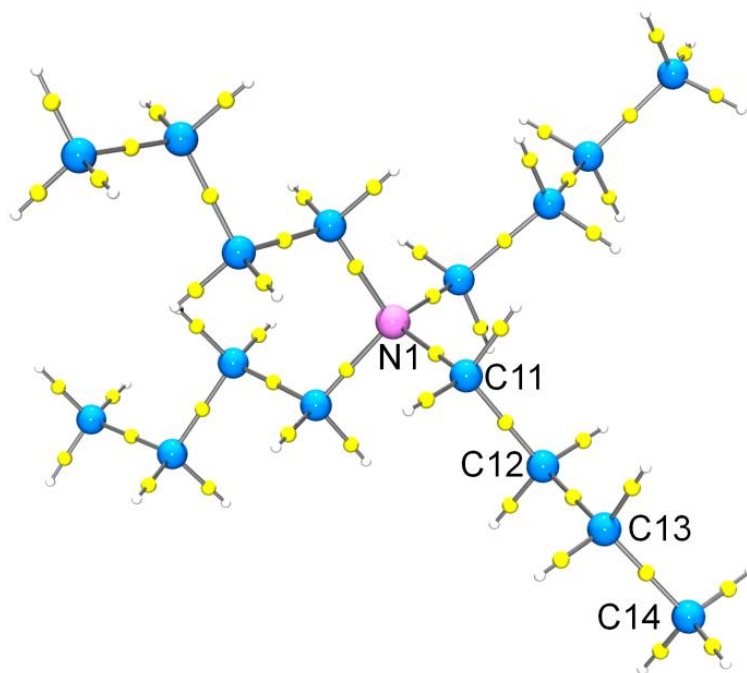


Figure 2.24. Bond critical points for TBA cation, the yellow balls represent the BCPs.

Table 2.6. Results of the topological analysis of charge density at (3,-1) bond critical point (BCP) of V6 core. $\rho(\mathbf{r}_c)$ is the electron density at the BCP ($e\text{\AA}^{-3}$), $\nabla^2\rho(\mathbf{r}_c)$ is Laplacian of the total density at the BCP ($e\text{\AA}^{-5}$), the ε is ellipticity, λ_1 , λ_2 , λ_3 are the eigenvalues at the BCP, $G(\mathbf{r}_c)$, $V(\mathbf{r}_c)$, and $H(\mathbf{r}_c)$ are kinetic energy density, local energy density, and the total energy density respectively (the units are au, equal to $e\text{Bohr}^{-5}$).

Type	Bond	d_{12}	d_{1-bcp}	$\rho(\mathbf{r}_c)$	$\nabla^2\rho(\mathbf{r}_c)$	λ_1	λ_2	λ_3	ε	$G(\mathbf{r}_c)$	$V(\mathbf{r}_c)$	$H(\mathbf{r}_c)$
V-O1x	V1-O11	1.615	0.8436	1.835	33.10	-14.03	-13.62	60.75	0.032	0.556	-0.770	-0.213
	V2-O12	1.612	0.8405	1.827	32.94	-14.58	-14.25	61.77	0.023	0.553	-0.764	-0.211
	V3-O13	1.616	0.841	1.746	33.36	-12.90	-12.72	58.98	0.014	0.532	-0.719	-0.186
V-O2x	V1-O23	1.784	0.9207	1.087	21.55	-7.62	-7.32	36.49	0.041	0.286	-0.348	-0.062
	V1-O22	1.858	0.9519	0.848	17.95	-5.45	-5.28	28.67	0.032	0.215	-0.243	-0.028
	V2-O22	1.786	0.9214	1.045	21.53	-7.25	-7.14	35.93	0.015	0.277	-0.331	-0.054
	V2-O21	1.875	0.9219	0.831	17.91	-5.24	-5.23	28.39	0.002	0.211	-0.237	-0.026
	V3-O21	1.778	0.9193	1.084	22.02	-7.61	-7.42	37.05	0.026	0.289	-0.349	-0.060
	V3-O23	1.877	0.9547	0.824	17.62	-5.29	-5.19	28.09	0.019	0.208	-0.233	-0.025
V-O3x	V1-O31	2.000	1.0058	0.570	12.14	-3.42	-3.27	18.83	0.046	0.131	-0.135	-0.005
	V1-O33	2.050	1.0312	0.504	11.11	-2.93	-2.86	16.90	0.024	0.115	-0.114	0.000
	V2-O32	1.993	0.9805	0.570	12.09	-3.35	-3.31	18.75	0.012	0.130	-0.135	-0.005
	V2-O31	2.045	1.0151	0.488	10.53	-2.74	-2.66	15.93	0.030	0.109	-0.109	0.000
	V3-O33	1.992	1.0112	0.584	12.82	-3.55	-3.46	19.83	0.026	0.137	-0.142	-0.004
	V3-O32	2.047	1.0295	0.503	10.93	-2.92	-2.87	16.72	0.017	0.113	-0.114	0.000
V-O6x	V1-O61	2.239	1.1151	0.299	6.36	-1.38	-1.34	9.08	0.030	0.060	-0.054	0.006
	V2-O61	2.237	1.1152	0.289	6.28	-1.33	-1.30	8.91	0.023	0.059	-0.052	0.007
	V3-O61	2.244	1.1218	0.282	6.04	-1.25	-1.25	8.54	0.000	0.056	-0.050	0.006

Table 2.7. Results of the topological analysis of charge density at (3,-1) bond critical point (BCP) of organic ligand. $\rho(\mathbf{r}_c)$ is the electron density at the BCP ($e\text{\AA}^{-3}$), $\nabla^2\rho(\mathbf{r}_c)$ is Laplacian of the total density at the BCP ($e\text{\AA}^{-5}$), the ε is ellipticity, $\lambda_1, \lambda_2, \lambda_3$ are the eigenvalues at the BCP, $G(\mathbf{r}_c)$, $V(\mathbf{r}_c)$, and $H(\mathbf{r}_c)$ are kinetic energy density, local energy density, and the total energy density respectively (the units are au, equal to $e\text{Bohr}^{-5}$).

Type	Bond	d_{12}	d_{1-bcp}	$\rho(\mathbf{r}_c)$	$\nabla^2\rho(\mathbf{r}_c)$	λ_1	λ_2	λ_3	ε	$G(\mathbf{r}_c)$	$V(\mathbf{r}_c)$	$H(\mathbf{r}_c)$
C _x -O _{3x}	C1-O31	1.420	0.579	1.852	-10.96	-13.58	-13.25	15.87	0.025	0.257	-0.628	-0.371
	C2-O32	1.423	0.562	1.816	-10.49	-12.63	-12.40	14.54	0.019	0.249	-0.608	-0.358
	C3-O33	1.420	0.584	1.850	-9.79	-12.34	-12.09	14.64	0.021	0.264	-0.630	-0.366
C-O	C5-O1	1.448	0.599	1.706	-9.41	-11.84	-11.28	13.71	0.050	0.225	-0.548	-0.323
	C6-O1	1.331	0.448	1.823	-4.67	-13.84	-12.83	22.00	0.079	0.292	-0.632	-0.340
	C6-O2	1.210	0.395	2.237	31.71	-20.79	-19.19	71.70	0.083	0.675	-1.021	-0.346
C-C	C1-C4	1.534	0.774	1.689	-11.71	-11.26	-10.53	10.08	0.069	0.204	-0.530	-0.326
	C2-C4	1.538	0.773	1.692	-11.11	-11.12	-10.08	10.08	0.103	0.209	-0.534	-0.325
	C3-C4	1.535	0.773	1.708	-11.41	-10.88	-10.36	9.83	0.050	0.212	-0.542	-0.330
	C4-C5	1.524	0.739	1.696	-12.64	-10.98	-10.71	9.04	0.025	0.200	-0.531	-0.331
	C6-C7	1.513	0.748	1.535	-9.26	-9.93	-8.60	9.28	0.155	0.179	-0.455	-0.275
	C7-C8	1.517	0.804	1.489	-5.97	-9.47	-8.25	11.75	0.148	0.190	-0.442	-0.252

Table 2.8. Results of the topological analysis of charge density at (3,-1) bond critical point (BCP) of TBA cation. $\rho(\mathbf{r}_c)$ is the electron density at the BCP ($e\text{\AA}^{-3}$), $\nabla^2\rho(\mathbf{r}_c)$ is Laplacian of the total density at the BCP ($e\text{\AA}^{-5}$), the ε is ellipticity, $\lambda_1, \lambda_2, \lambda_3$ are the eigenvalues at the BCP, $G(\mathbf{r}_c)$, $V(\mathbf{r}_c)$, and $H(\mathbf{r}_c)$ are kinetic energy density, local energy density, and the total energy density respectively (the units are au, equal to $e\text{Bohr}^{-5}$).

Type	Bond	d_{12}	d_{1-bcp}	$\rho(\mathbf{r}_c)$	$\nabla^2\rho(\mathbf{r}_c)$	λ_1	λ_2	λ_3	ε	$G(\mathbf{r}_c)$	$V(\mathbf{r}_c)$	$H(\mathbf{r}_c)$
N-Cx1	N1-C11	1.521	0.891	1.591	-8.42	-9.85	-9.83	11.25	0.002	0.200	-0.487	-0.287
	N1-C21	1.518	0.890	1.598	-8.58	-9.90	-9.87	11.19	0.003	0.201	-0.491	-0.290
	N1-C31	1.520	0.891	1.593	-8.46	-9.89	-9.82	11.24	0.007	0.200	-0.489	-0.288
	N1-C41	1.516	0.890	1.602	-8.66	-9.92	-9.88	11.15	0.004	0.201	-0.493	-0.291
Cx1-Cx2	C11-C12	1.521	0.780	1.713	-11.06	-10.60	-10.57	10.11	0.003	0.216	-0.546	-0.330
	C21-C22	1.521	0.780	1.716	-11.10	-10.60	-10.60	10.10	0.000	0.216	-0.548	-0.331
	C31-C32	1.516	0.778	1.727	-11.28	-10.73	-10.63	10.07	0.009	0.218	-0.553	-0.335
	C41-C42	1.522	0.780	1.713	-11.04	-10.58	-10.57	10.11	0.001	0.216	-0.546	-0.330
Cx2-Cx3	C12-C13	1.520	0.752	1.681	-10.57	-10.08	-9.83	9.35	0.025	0.210	-0.530	-0.320
	C22-C23	1.527	0.766	1.668	-10.32	-9.95	-9.75	9.38	0.021	0.208	-0.523	-0.315
	C32-C33	1.526	0.762	1.670	-10.37	-9.96	-9.78	9.37	0.018	0.208	-0.524	-0.316
	C42-C43	1.528	0.763	1.665	-10.28	-9.94	-9.73	9.39	0.022	0.208	-0.522	-0.314
Cx3-Cx4	C13-C14	1.501	0.765	1.722	-11.47	-10.53	-9.99	9.04	0.054	0.215	-0.550	-0.334
	C33-C34	1.527	0.768	1.661	-10.46	-10.07	-9.60	9.20	0.049	0.205	-0.519	-0.314
	C23-C24	1.519	0.768	1.677	-10.78	-10.16	-9.78	9.16	0.039	0.207	-0.527	-0.319
	C43-C44	1.522	0.769	1.673	-10.66	-10.16	-9.68	9.17	0.050	0.207	-0.525	-0.318

Table 2.9. Results of the topological analysis of charge density at (3,-1) bond critical point (BCP) of H bonds, ranked by decreasing $\rho(\mathbf{r}_c)$. $\rho(\mathbf{r}_c)$ is the electron density at the BCP ($e\text{\AA}^{-3}$), $\nabla^2\rho(\mathbf{r}_c)$ is Laplacian at the BCP ($e\text{\AA}^{-5}$), the ε is ellipticity, λ_1 , λ_2 , λ_3 are the eigenvalues at the BCP, $H(\mathbf{r}_c)$ is the total energy density (the units are au, equal to $e\text{Bohr}^{-5}$).

Bond	d_{12}	d_{1-bcp}	$\rho(\mathbf{r}_c)$	$\nabla^2\rho(\mathbf{r}_c)$	λ_1	λ_2	λ_3	ε	$H(\mathbf{r}_c)$
C23-H23B ..O33	2.399	1.341	0.094	1.475	-0.36	-0.34	2.18	0.059	0.003
C5-H5A ..O13	2.476	1.374	0.084	1.003	-0.31	-0.30	1.61	0.023	0.002
C31-H31B ..O22	2.251	1.430	0.064	1.030	-0.23	-0.22	1.48	0.045	0.002
C32-H32A ..O11	2.381	1.452	0.056	0.918	-0.20	-0.17	1.28	0.176	0.002
C21-H21B ..O2	2.401	1.419	0.054	0.996	-0.22	-0.19	1.40	0.158	0.003
C42-H42A ..O13	2.459	1.420	0.053	0.974	-0.19	-0.18	1.35	0.056	0.002
C41-H41B ..O23	2.433	1.511	0.047	0.736	-0.16	-0.14	1.03	0.143	0.002
C13-H13A ..O12	2.465	1.468	0.045	1.091	-0.17	-0.16	1.43	0.063	0.003
C21-H21A ..O22	2.492	1.514	0.043	0.724	-0.14	-0.12	0.98	0.167	0.002
C24-H24A ..O21	2.585	1.468	0.042	0.843	-0.15	-0.14	1.13	0.071	0.002
C11-H11B ..O23	2.590	1.517	0.042	0.743	-0.15	-0.13	1.03	0.154	0.002
C13-H13A ..O21	2.590	1.530	0.041	0.663	-0.13	-0.12	0.91	0.083	0.002
C11-H11A ..O2	2.590	1.512	0.039	0.642	-0.13	-0.11	0.88	0.182	0.002
C43-H43A ..O23	2.653	1.496	0.036	0.840	-0.14	-0.11	1.10	0.273	0.002
C12-H12A ..O11	2.691	1.650	0.026	0.384	-0.05	-0.05	0.49	0.000	0.001
C44-H44B ..O13	2.771	1.575	0.025	0.400	-0.07	-0.07	0.54	0.000	0.001
C23-H23B ..O22	2.754	1.605	0.023	0.605	-0.08	-0.07	0.75	0.143	0.002

2.3.5 Atomic net charges

The charge density refinement has been done with two strategies: i) Strategy 1, no charge transfer between functionalized V6-C3 anion and TBA cation; ii) Strategy 2, the charge transfer is allowed between anion and cation.

In this thesis, experimental atomic net charges are derived: i) from the experimental monopole population (P_{val}) after κ refinement (the κ charges) and ii) from an integration over the topological atomic basins Ω [Bader, 1990] (the AIM charges).

The electron configuration of V atom is $4s^03d^3$, so the initial charge of V is +2 e. In order to conserve the electron-neutrality, we attributed the -7 e charge to the O atoms in functionalized V6-C3 anion and +1 e to N atom in TBA cation.

2.3.5.1 Atomic net charges of V6 core

The atomic net charges of the functionalized V6 core in the title compound are listed in Table 2.10.

Table 2.10. Experimental atomic net charge (e) and κ values of the functionalized V6 core.

Atom	Type	Initial charge	Experimental refinement				AIM charge	
			Strategy1		Strategy2		Strategy 1	Strategy 2
			κ	charge	κ	charge		
V1	VII	+2.000	1.035	+1.658	1.041	+1.616	+1.206	+1.156
V2		+2.000	1.038	+1.692	1.046	+1.662	+1.332	+1.288
V3		+2.000	1.044	+1.724	1.050	+1.690	+1.281	+1.231
O11	O1x	-0.609	0.984	-0.579	0.984	-0.601	-0.762	-0.746
O12		-0.609	0.977	-0.605	0.977	-0.612	-0.628	-0.625
O13		-0.609	0.963	-0.818	0.962	-0.845	-0.826	-0.843
O21	O2x	-0.609	0.960	-0.953	0.960	-0.973	-1.044	-1.063
O22		-0.609	0.971	-0.818	0.970	-0.847	-0.825	-0.821
O23		-0.609	0.959	-0.915	0.959	-0.938	-0.946	-0.957
O31	O3x	-0.609	0.980	-0.682	0.980	-0.704	-1.052	-1.073
O32		-0.609	0.981	-0.617	0.981	-0.637	-0.984	-0.998
O33		-0.609	0.971	-0.807	0.970	-0.836	-1.084	-1.108
O61	O6x	-0.609	0.936	-1.378	0.935	-1.419	-1.090	-1.111

2.3.5.2 Atomic net charges of the organic ligand

The atomic net charges of the organic ligand in the title compound are listed in Table 2.11.

Table 2.11. Experimental atomic net charge (*e*) and κ values of organic ligand.

Atom	Type	Initial charge	Experimental multipole charge				AIM charge	
			Strategy1		Strategy2		Strategy 1	Strategy 2
			κ	charge	κ	charge		
O1	O	-0.609	<i>0.994</i>	+0.335	<i>0.993</i>	+0.315	-0.470	-0.468
O2		-0.609	<i>0.958</i>	+0.227	<i>0.959</i>	+0.213	-0.384	-0.371
C1	C	0.000	<i>1.080</i>	+0.264	<i>1.079</i>	+0.236	+0.363	+0.343
C2		0.000	<i>1.059</i>	+0.077	<i>1.059</i>	+0.054	+0.206	+0.185
C3		0.000	<i>1.053</i>	+0.021	<i>1.053</i>	+0.012	+0.128	+0.108
C4		0.000	<i>1.045</i>	-0.178	<i>1.045</i>	-0.199	+0.037	+0.005
C5		0.000	<i>1.039</i>	-0.025	<i>1.039</i>	-0.038	+0.158	+0.160
C6		0.000	<i>1.026</i>	+0.876	<i>1.024</i>	+0.850	+2.081	+2.053
C7		0.000	<i>0.958</i>	-0.550	<i>0.959</i>	-0.548	+0.029	-0.019
C8		0.000	<i>1.011</i>	+0.376	<i>1.008</i>	+0.343	+0.590	+0.560
H1A	H	0.000	<i>1.160</i>	-0.037	<i>1.160</i>	-0.041	+0.167	+0.164
H1B		0.000	<i>1.160</i>	-0.037	<i>1.160</i>	-0.041	+0.169	+0.166
H2A		0.000	<i>1.160</i>	-0.045	<i>1.160</i>	-0.051	+0.143	+0.126
H2B		0.000	<i>1.160</i>	-0.045	<i>1.160</i>	-0.051	+0.141	+0.131
H3A		0.000	<i>1.160</i>	-0.037	<i>1.160</i>	-0.041	+0.135	+0.132
H3B		0.000	<i>1.160</i>	-0.037	<i>1.160</i>	-0.041	+0.142	+0.139
H5A		0.000	<i>1.160</i>	-0.205	<i>1.160</i>	-0.207	-0.114	-0.113
H5B		0.000	<i>1.160</i>	-0.205	<i>1.160</i>	-0.207	-0.097	-0.099
H7A		0.000	<i>1.160</i>	+0.237	<i>1.160</i>	+0.232	+0.222	+0.226
H7B		0.000	<i>1.160</i>	+0.237	<i>1.160</i>	+0.232	+0.224	+0.228
H8A		0.000	<i>1.160</i>	+0.053	<i>1.160</i>	+0.050	-0.038	-0.037
H8B		0.000	<i>1.160</i>	+0.053	<i>1.160</i>	+0.050	-0.042	-0.044
H8C		0.000	<i>1.160</i>	+0.053	<i>1.160</i>	+0.050	-0.039	-0.038

2.3.5.3 Atomic net charge of TBA cation

The atomic net charges of TBA cation in the title compound are listed in Table 2.12.

Table 2.12. Experimental atomic net charge (e) and κ values of the TBA cation.

Atom	Type	Initial charge	Experimental multipole charge				AIM charge	
			Strategy1		Strategy2		Strategy 1	Strategy 2
			κ	charge	κ	charge		
N(1)	N	1.000	1.027	+0.072	1.030	+0.083	-1.060	-1.043
C(11)	C	0.000	1.056	0.000	1.060	+0.026	-0.200	-0.182
C(12)		0.000	1.034	-0.200	1.038	-0.179	-0.413	-0.380
C(13)		0.000	1.022	-0.269	1.025	-0.255	-0.473	-0.447
C(14)		0.000	1.008	-0.243	1.013	-0.221	-0.099	-0.112
C(21)		0.000	1.056	0.000	1.060	+0.026	-0.211	-0.195
C(22)		0.000	1.034	-0.200	1.038	-0.179	-0.416	-0.384
C(23)		0.000	1.022	-0.269	1.025	-0.255	-0.476	-0.451
C(24)		0.000	1.008	-0.243	1.013	-0.221	-0.082	-0.096
C(31)		0.000	1.056	0.000	1.060	+0.026	-0.204	-0.186
C(32)		0.000	1.034	-0.200	1.038	-0.179	-0.417	-0.384
C(33)		0.000	1.022	-0.269	1.025	-0.255	-0.474	-0.444
C(34)		0.000	1.008	-0.243	1.013	-0.221	-0.090	-0.103
C(41)		0.000	1.056	0.000	1.060	+0.026	-0.203	-0.186
C(42)		0.000	1.034	-0.200	1.038	-0.179	-0.416	-0.383
C(43)		0.000	1.022	-0.269	1.025	-0.255	-0.479	-0.454
C(44)		0.000	1.008	-0.243	1.013	-0.221	-0.088	-0.103
H(11A)	H	0.000	1.160	+0.044	1.160	+0.050	+0.246	+0.252
H(11B)		0.000	1.160	+0.044	1.160	+0.050	+0.245	+0.251
H(12A)		0.000	1.160	+0.148	1.160	+0.156	+0.251	+0.245
H(12B)		0.000	1.160	+0.148	1.160	+0.156	+0.254	+0.256
H(13A)		0.000	1.160	+0.104	1.160	+0.110	+0.207	+0.209
H(13B)		0.000	1.160	+0.104	1.160	+0.110	+0.213	+0.216
H(14A)		0.000	1.160	+0.117	1.160	+0.122	+0.084	+0.097
H(14B)		0.000	1.160	+0.117	1.160	+0.122	+0.083	+0.096
H(14C)		0.000	1.160	+0.117	1.160	+0.122	+0.083	+0.096
H(21A)		0.000	1.160	+0.044	1.160	+0.050	+0.249	+0.244
H(21B)		0.000	1.160	+0.044	1.160	+0.050	+0.246	+0.252
H(22A)		0.000	1.160	+0.148	1.160	+0.156	+0.253	+0.255
H(22B)		0.000	1.160	+0.148	1.160	+0.156	+0.252	+0.245
H(23A)		0.000	1.160	+0.104	1.160	+0.110	+0.210	+0.212
H(23B)		0.000	1.160	+0.104	1.160	+0.110	+0.210	+0.208
H(24A)		0.000	1.160	+0.117	1.160	+0.122	+0.078	+0.091
H(24B)		0.000	1.160	+0.117	1.160	+0.122	+0.079	+0.093
H(24C)		0.000	1.160	+0.117	1.160	+0.122	+0.078	+0.092
H(31A)		0.000	1.160	+0.044	1.160	+0.050	+0.247	+0.247
H(31B)		0.000	1.160	+0.044	1.160	+0.050	+0.245	+0.241
H(32A)		0.000	1.160	+0.148	1.160	+0.156	+0.254	+0.255
H(32B)		0.000	1.160	+0.148	1.160	+0.156	+0.255	+0.256
H(33A)		0.000	1.160	+0.104	1.160	+0.110	+0.211	+0.221
H(33B)		0.000	1.160	+0.104	1.160	+0.110	+0.210	+0.211
H(34A)		0.000	1.160	+0.117	1.160	+0.122	+0.079	+0.093
H(34B)		0.000	1.160	+0.117	1.160	+0.122	+0.078	+0.092
H(34C)		0.000	1.160	+0.117	1.160	+0.122	+0.080	+0.103

H(41A)		0.000	1.160	+0.044	1.160	+0.050	+0.246	+0.252
H(41B)		0.000	1.160	+0.044	1.160	+0.050	+0.249	+0.254
H(42A)		0.000	1.160	+0.148	1.160	+0.156	+0.253	+0.255
H(42B)		0.000	1.160	+0.148	1.160	+0.156	+0.253	+0.254
H(43A)		0.000	1.160	+0.104	1.160	+0.110	+0.211	+0.213
H(43B)		0.000	1.160	+0.104	1.160	+0.110	+0.213	+0.215
H(44A)		0.000	1.160	+0.117	1.160	+0.122	+0.081	+0.094
H(44B)		0.000	1.160	+0.117	1.160	+0.122	+0.079	+0.093
H(44C)		0.000	1.160	+0.117	1.160	+0.122	+0.079	+0.092

2.3.6 *d* orbital populations of the vanadium atoms

The coordination environments of the vanadium atoms are depicted in Figure 2.25. The coordination polyhedrons are slightly distorted octahedra, therefore we have chosen to refine the vanadium Plm parameters with $l = 0, 2, 4$ in agreement with Holladay *et al.* [Holladay, 1983]. For all V atoms, *z* axis is chosen in the direction of the closest atom, and the *x* axis toward the second closest atom. Using a 15 x 15 matrix, we have determined for each vanadium atom the *d* orbital populations given in Table 2.13, with the same type V atoms from V10 anion [Bošnjaković-Pavlović, 2010].

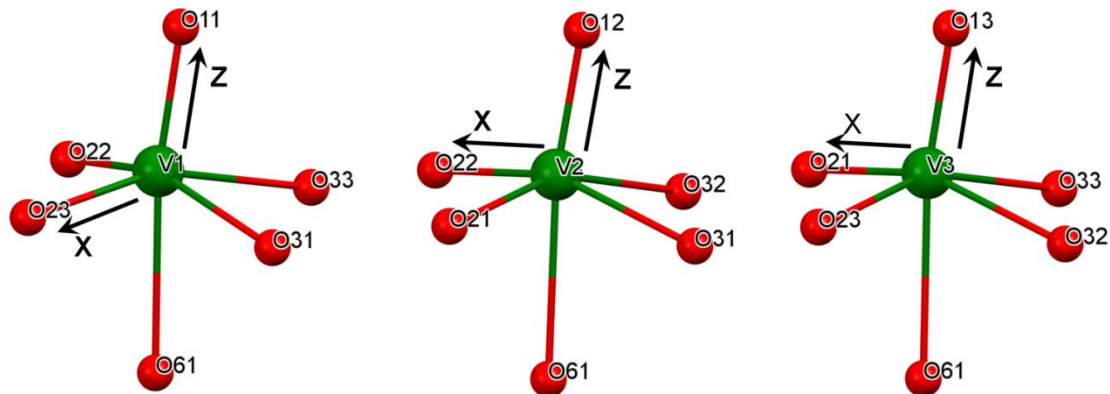


Figure 2.25. Distorted coordination octahedra of vanadium atoms. The *z* axis in the local coordinate system is oriented always vertical in the direction of the closest oxygen atom.

Table 2.13. Experimental determination of the *d* orbital (*e*) population of the vanadium in the V6-C3 and V10 [Bošnjaković-Pavlović, 2009]. In bold the *d* orbital having the highest population for a given vanadium. The oxydation state is calculated as the difference between the neutral configuration d^5 and the *d* orbital population after refinement. The density at the BCP of shortest V-O bond is indicated.

	V6-C3 by MM-1			V6-C3 by MM-2			V10	
	V1	V2	V3	V1	V2	V3	V3	V5
$d(z^2)$	0.816	0.672	0.614	0.828	0.684	0.622	0.765	0.645
	22.83%	19.54%	17.85%	22.86%	19.64%	17.84%	23.70%	20.10%
$d(x^2-y^2)$	0.649	0.785	0.823	0.656	0.796	0.831	0.545	0.675
	18.15%	22.83%	23.93%	18.11%	22.85%	23.84%	16.80%	21.00%
$d(xy)$	0.543	0.753	0.720	0.553	0.775	0.727	0.599	0.619
	15.19%	21.90%	20.94%	15.27%	22.25%	20.85%	18.40%	19.10%
$d(xz)$	0.761	0.683	0.692	0.770	0.685	0.704	0.705	0.615
	21.29%	19.86%	20.12%	21.26%	19.67%	20.20%	21.80%	19.10%
$d(yz)$	0.806	0.546	0.590	0.815	0.543	0.602	0.625	0.664
	22.55%	15.88%	17.16%	22.50%	15.59%	17.27%	19.30%	20.70%
<i>d</i> orbital population	3.575	3.439	3.439	3.622	3.483	3.486	3.215	3.196
Oxidation state	1.425	1.561	1.561	1.378	1.517	1.514	1.785	1.804
Shortest V-O	V1-O11	V2-O12	V3-O13	V1-O11	V2-O12	V3-O13	V3-O11	V5-O10
Distance (Å)	1.615	1.612	1.616	1.617	1.613	1.618	1.611	1.612
$\rho(\mathbf{r}_c)$ ($e\text{Å}^{-3}$)	1.835	1.827	1.746	1.84	1.828	1.748	1.71	1.75

2.3.7 Electrostatic potential

In order to obtain information on the chemical reactivity of the compound, it is useful to color the reactive surface of the molecule with the electrostatic potential values. The nucleophilic molecular regions correspond to the most negative electrostatic potential. The experimental electrostatic potential can be calculated at the final step of the two refinements (κ refinement and multipole refinement) using the refinement strategy 1 and strategy 2.

2.3.7.1 Electrostatic potential of functionalized V6-C3 anion

There are two ways to describe the electrostatic potential of functionalized V6-C3 anion: i) experimental electrostatic potential mapped on the 3D isodensity surface ($0.007 \text{ e}\text{\AA}^{-3} / 0.001 \text{ a.u.}$) as shown in Figure 2.26; ii) experimental EP isovalue surface at a particular cut-off (here $\pm 0.75 \text{ e}\text{\AA}^{-1}$) as shown in Figure 2.27.

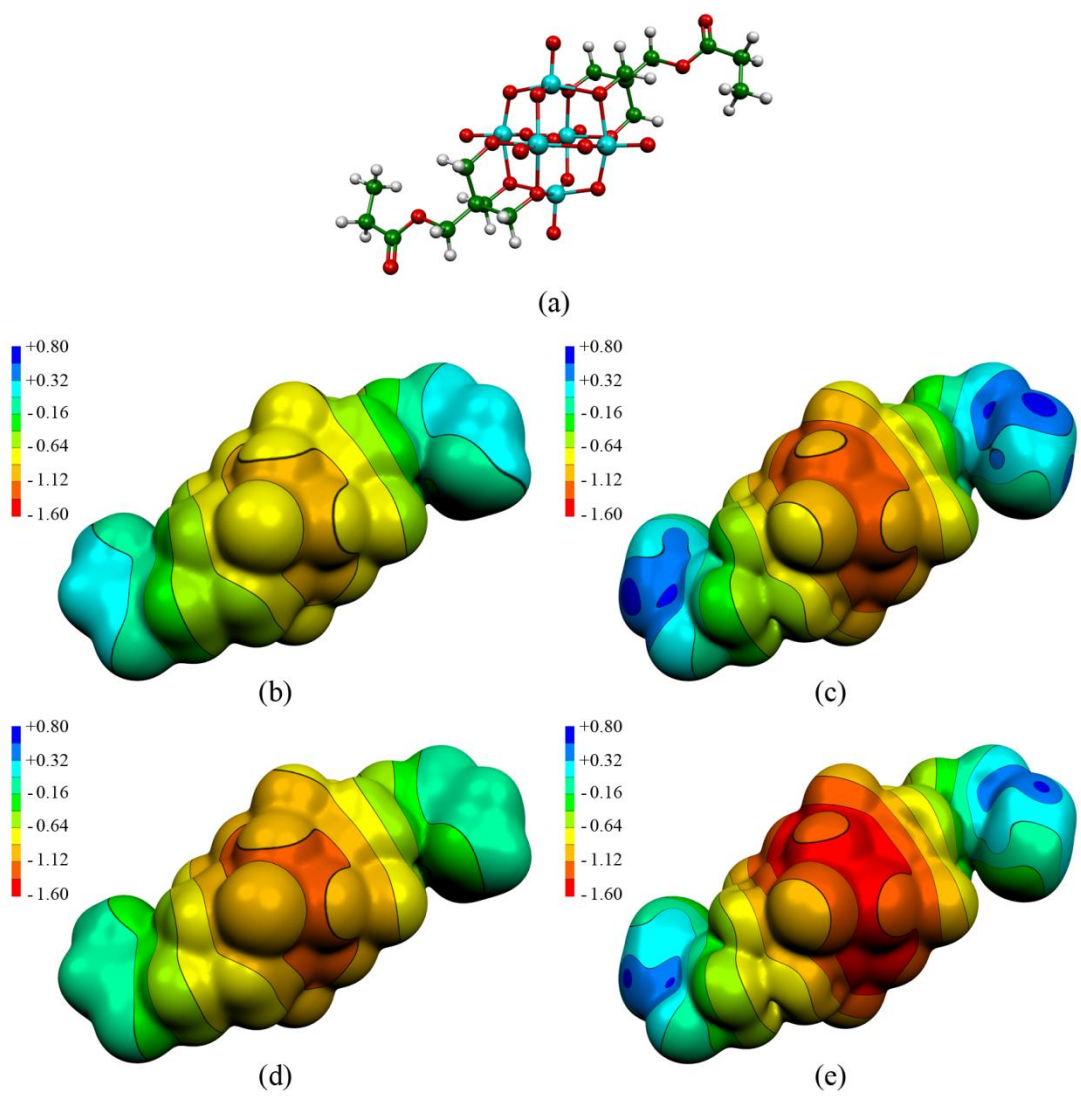


Figure 2.26. EP ($e \cdot \text{\AA}^{-1}$) mapped on isodensity surface ($0.007 e \text{\AA}^{-3}$) for $[\text{V6-C3}]^{2-}$ using the same color scale from $-1.60 e \text{\AA}^{-1}$ to $+0.80 e \text{\AA}^{-1}$. (a) Structure of $[\text{V6-C3}]^{2-}$. (b) κ -refinement, strategy 1; (c) multipole refinement, strategy 1; (d) κ -refinement, strategy 2; (e) multipole refinement, strategy 2.

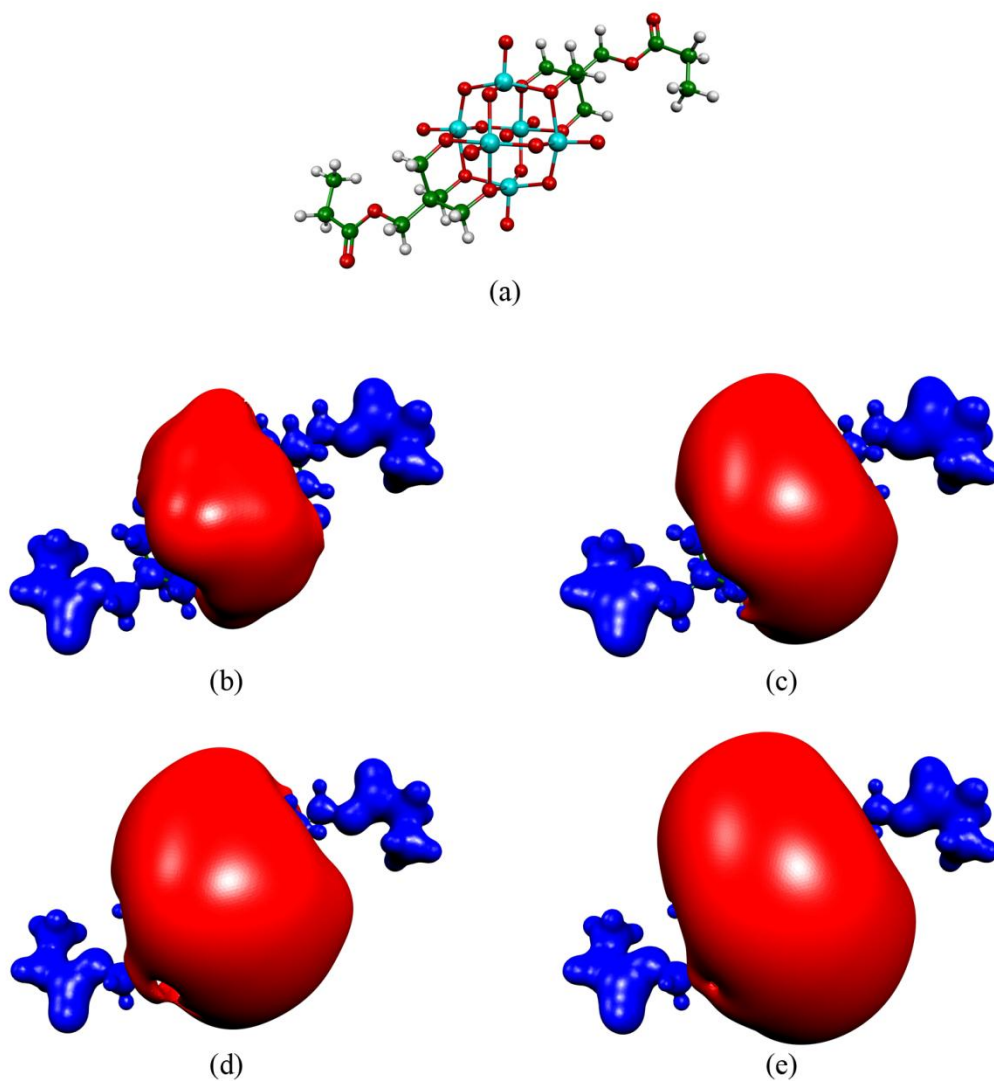


Figure 2.27. EP isovalue surface (cutoff $\pm 0.75 \text{ e}\text{\AA}^{-1}$) of $[\text{V6-C3}]^{2-}$. (a) Structure of functionalized V6-C3 anion. (b) refinement, strategy 1; (c) multipole refinement, strategy 1; (d) refinement, strategy 2; (e) multipole refinement, strategy 2.

2.3.7.2 Electrostatic potential of TBA cation

Figure 2.28 shows the electrostatic potential projected on the 3D isodensity surface ($0.007 \text{ e}\text{\AA}^{-3}$) of TBA cation.

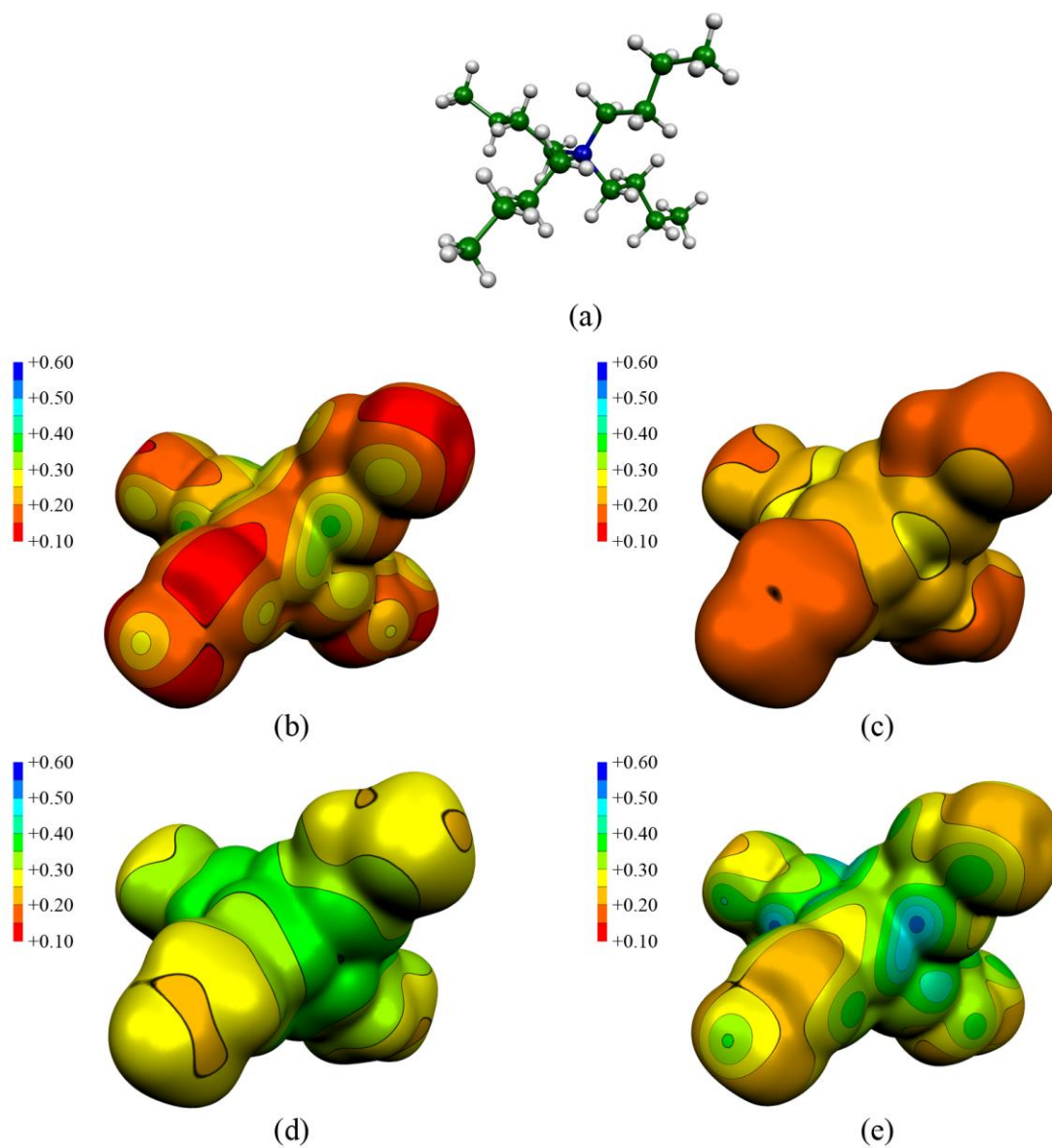


Figure 2.28. EP ($\text{e}\text{\AA}^{-1}$) mapped on isodensity surface ($0.007 \text{ e}\text{\AA}^{-3}$) for TBA cation using the same color scale from $+0.10 \text{ e}\text{\AA}^{-1}$ to $+0.60 \text{ e}\text{\AA}^{-1}$. (a) Structure of $[\text{V}_6\text{-C}_3]^{2+}$. (b) refinement, strategy 1; (c) multipole refinement, strategy 1; (d) refinement, strategy 2; (e) multipole refinement, strategy 2.

2.3.8 Source function analysis

The different charge density indicators, like topological parameters, QTAIM, electrostatic potential can provide useful chemical information about chemical bonding and chemical reactivity. Source function (SF), a particular topological indicator, has been used for understanding chemical model of inorganic and metallorganic systems [Gatti, 2013] and metal–metal bonding in *d*-block organometallic compounds [Gatti, 2007].

The topological analysis of four different V-O bonds provide a general chemical bonding information about V-O atomic interaction, and AIM charge distribution and electrostatic potential feature illustrate the chemical reactivity of functionalized V6-C3. Because the title compound is an inorganic-organic hybrid molecule exhibiting charge transfer property, SF approach can give new and deeper insight into the origin and mechanisms of chemical transferability, which is an good complementary description in a unified picture. Figure 2.29 shows the local source along the V-O bonds and integrated source function (ISF) of four different type of V-O bonds. In advance, for knowing how the three parts of molecule contribute the $\rho(\mathbf{r}_c)$ of four V-O bonds, we calculate the integrated SF for all the reference points (BCPs) in V6 core. Summation of the integrated SF contribution percentage of the three moieties (see Figure 2.5), which are summarized in Table 2.14.

Summations on organic ligand, V6 core and TBA of the atom percentage contributions are given in Table 2.15.

Table 2.14. SF contributions percentage from three moieties at BCPs of four type V-O bonds.

BCPs	SF contribution percentage		
	V6 core	Organic ligand	TBA cation
VII-O1x	95.20%	2.89%	1.84%
VII-O2x	90.09%	6.24%	3.59%
VII-O3x	76.58%	17.54%	5.84%
VII-O6x	61.77%	26.33%	10.99%

Table 2.15. SF contributions percentage from three moieties at BCPs of three moieties.

	SF contribution percentage		
	V6 core	Organic ligand	TBA cation
BCPs in V6 core	87.03%	8.94%	4.03%
BCPs in organic	8.64%	89.90%	1.46%
BCPs in cation	-0.53%	0.76%	99.77%

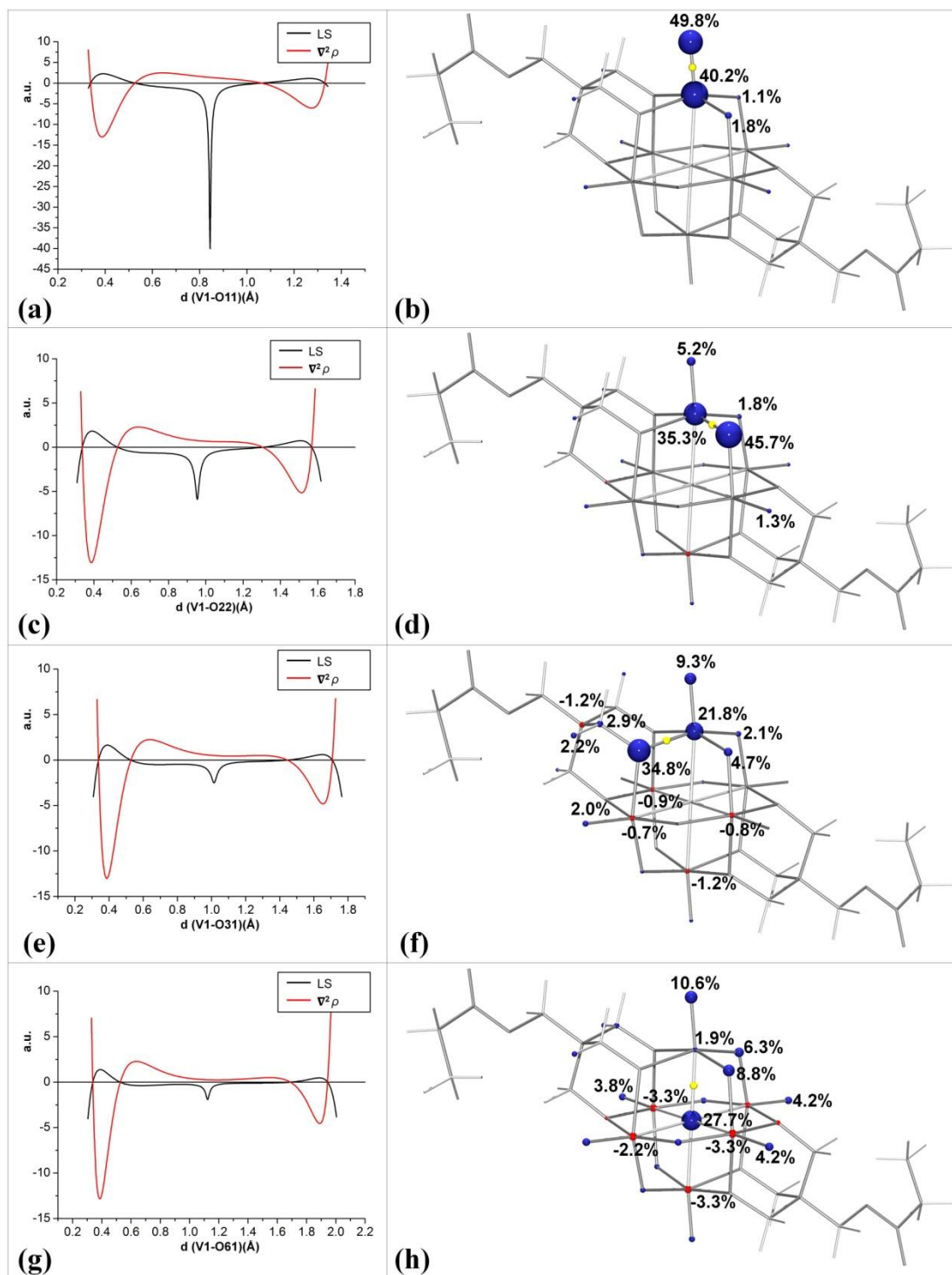


Figure 2.29. Local source function and integrated source function of four V-O bonds. (a) (c) (e) (g) The laplacian and local source profiles along the V- O bond; (b) (d) (f) (h) Integrated source function (SF contribution) for BCPs of V-O bonds. The volume of the spheres on the atomic centers are proportional to the percentage contributions from the atomic basins; positive contributions are shown as the blue spheres, and negative contributions (sinks) are shown as the red spheres. The BCPs are shown as the yellow spheres.

2.4 Discussion

2.4.1 From geometrical analysis to charge density analysis

For a better understanding of the chemical information obtained from the high resolution X-Ray diffraction experiment, the structural characterization of functionalized V6-C3 is described from a geometrical analysis to a charge density analysis. The charge density analysis provides the important chemical information, containing chemical bonding and chemical reactivity, which are useful descriptors for comprehending the electronic and topological properties.

In 1997, the text book “X-ray charge densities and chemical bonding” illustrated the relationship between experimental charge density and chemical bonding, especially focusing on deformation density, which is a traditional way to study experimentally chemical bonding in crystals and molecules [Tsirelson, 1996]. Deformation electron density, which is electron density differences in given suitable molecular or crystalline planes relative to a non bonded state (typically the IAM model), have been largely investigated in the past [Coppens, 1997]. This approach has been adopted in the chemical bond studies since it offers a natural and efficient way to overcome the problem of the finite set of experimental data in the Fourier density sums. However, the deformation electron density cannot produce quantitative information on the chemical bonding. In addition, there is a loss of some qualitative information when the chemical bond under investigation is less conventional than that in simple organic molecules. In the past twenty years, the primary focus of experimental CD studies has progressively shifted from the deformation to the total density [Coppens, 2004; Koritsanszky, 2001, Chopra, 2012]. The Quantum Theory of Atoms in Molecules, QTAIM, [Bader, 1990, Matta, 2007] is certainly the most complete density-based topological tool for chemical bonding studies from an experimental or a theoretical approach. The topological analysis based on QTAIM method initiated a vigorous debate on chemical bonding [Matta, 2003; Bader, 2009] and provides a better acceptance of charge density studies, which are the necessary and sufficient condition for the existence of chemical bonding [Bader, 1990; Bader, 1998].

In this thesis, firstly, we used the combination of deformation electron density observation, *d*-orbital population analysis, and topological parameters containing the

new topological indicators, *eg*, source function, to better reveal the chemical bonding features inside the functionalized V6-C3. Secondly, the electrostatic potential, AIM charge distribution, and integrated source function are examined to understand the chemical reactivity and charge transfer behavior. The following section contains discussions on these two aspects.

2.4.2 Chemical bonding in functionalized V6-C3 anion

2.4.2.1 V-O bonding

Generally, in the functionalized V6 core, the study of the chemical bonding features of V6 core is applied to four V-O bonds, which are the basic chemical units of V6 core, as shown in Figure 2.30.

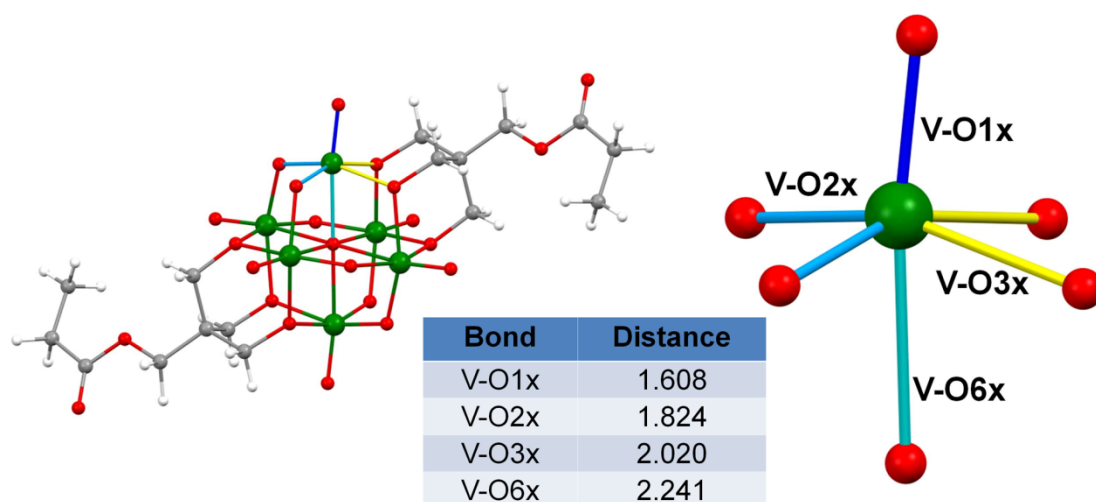


Figure 2.30. Four V-O bonds and average distances (Å) in $[V6-C3]^{2-}$.

As shown in Table 2.2, the V-O interatomic distances issued from the four O atom types are in the range: $1.6064(5) \text{ \AA} < V-O < 2.2445(8) \text{ \AA}$. The relatively large distortion observed for the constituted $\{VO_6\}$ octahedra already well exhibited by the wide range of the V-O distance is confirmed by the examination of the O-V-O angles deviating in many cases of being close to 15° (the smallest angle: $\angle O32-V3-O61 = 76.70^\circ$, the biggest angle: $\angle O23-V1-O11 = 104.68^\circ$) from their ideal values (90°) (Appendix, table A2.3).

Due to the chemical equivalent environment (Figure 2.30), there is only one type of V atoms (VII), the distance of the same types V-O bonds are similar. The V-O bond distances are in a relatively narrow range as presented in Table 2.17. In order to compare the title compound with the literature we have retrieved the structures from

the organic crystallographic database (CSD) [Allen, 2002] (Table 2.16).

Table 2.16 Comparison of V-O distance (Å) (our experimental data of V6-C3, previous reported structures of functionalized hexavanadates, as presented in Table 1.1, 39 functionalized V6 compounds; and V10 anions from CSD base, 368 compounds).

Bond	Interatomic distance			
	Experimental data of V6-C3		CSD data	
			Func. V6	V10
Average	<Min, Max>	Average	Average	
VII-O1x	1.608	1.606, 1.609	1.601	1.605
VII-O2x	1.824	1.779, 1.873	1.848	1.881
VII-O3x	2.020	1.992, 2.047	2.017	2.002
VII-O6x	2.241	2.238, 2.245	2.250	2.316

According to the type of oxygen atoms, we observe the average V-O bond distances are as the following range: V-O1x (1.608 Å) < V-O2x (1.824 Å) < V-O3x (2.020 Å) < V-O6x (2.241 Å). For the first type of oxygen atoms, the average distance of V-O1x is 1.608 Å, which is similar with the statistical data of functionalized V6 and V10 searched from CSD; the second, third, and fourth type O atoms presenting the V-O2x, V-O3x, and V-O6x as the average distances 1.824 Å, 2.020 Å, and 2.241 Å respectively, which are in high agreement with the CSD searching results (Table 2.17). Interatomic distances of V-O and angles of O-V-O observed for the V6 core of the title compound exhibit the geometries which are quite similar to those found in previously reported structures of functionalized hexavanadates (V6) series and decavanadate (V10) series.

For an understanding of chemical bonding features of the four types of V-O bonds, the following results will be used i) electron density maps; ii) topological analysis of the electron density for V-O bonds; iii) source function analysis. These three properties will be examined in details.

1. Electron density maps

The static deformation density maps for three planes of V6 core are shown in Figure 2.21 a, b, c (§2.3.3.5), in which the charge density distribution around V, O atoms and the different V-O bonds are presented. In order to have a better visualization of the deformation density features around V and O atom, we have

plotted the density maps just containing V and O densities respectively (Figure 2.31 b, c). The static deformation density maps of decavanadate (V10) in different plans are also represented for comparison (Figure 2.31 d, e, f). Furthermore, the final refinement results of V10 [Bosnjakovic-Pavlovic, 2009] have been used to plot new figures presented in this manuscript.

For the three vanadium atoms, the electron density distribution is very similar and shows a significant charge accumulation around the metal atom, in agreement with the fact that these atoms are in an equivalent chemical environment. These accumulations are oriented toward the O6x atoms. Since V-O6x distance (2.241 Å) are the longest V-O bond in the V6 core, the density accumulations can be interpreted as the counterpart of the charge depletion occurring along the opposite and shorter V-O bonds. The electron density distribution of V atoms in V10 has a similar behavior with V6-C3.

The differences in static deformation electron density maps in the vicinity of oxygen atoms (Figure 2.31 b) are well expressed. The highest electron density peak is found between the shortest V-O1x in V6-C3 (1.608 Å) and V10 (1.612 Å). The lone pair density distribution for the O1x atom is observed in the two structures (V6-C3, O11 and O12; V10, O10 and O11), but exhibits the different density shape. The main reason is due to the fact that the number of H bonds is greater in V10 than it in V6-C3. The O1x deformation density are distributed symmetrically along the V-O1x bonds in V6-C3. For the central O atoms (O6x), we have found a practically spherical electron distribution in V6-C3 (Figure 2.31 b), which is in good agreement with the result in V10 (Figure 2.31 f).

In V10, for the bridge-O atoms O22, we can see the symmetrically distributed density (Figure 2.31 e, f) in the same chemical environment; the two neighboring V-O bond distances are 1.887 Å and 1.879 Å. In V6 core, for O22, though the two neighboring V atoms are the same type (type II), the distances of V1-O22 and V2-O22 are 1.855 Å, 1.783 Å. Consequently, the deformation density of O22 is asymmetrically distributed. The reason of the asymmetrical deformation density of O2x and O3x atoms is due to the symmetrical pre-structure of V6 cage, which is changed by the functionalization.

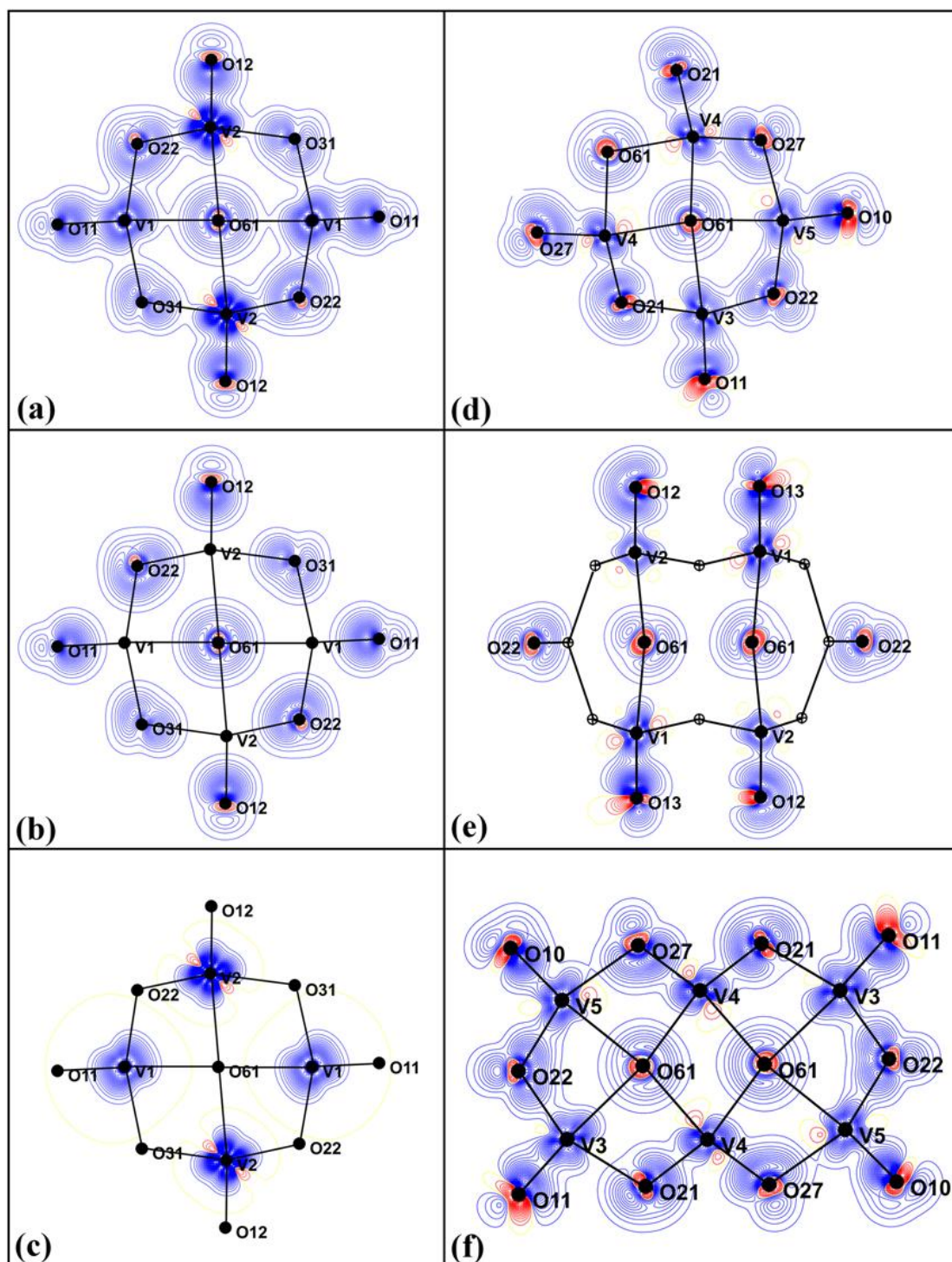


Figure 2.31. Static deformation density maps for V-O bonding in $[V6-C3]^{2-}$ (left column) and V10 anion (right column) (contours $0.05 e\text{\AA}^{-3}$). (a) V and O deformation density, V1-O61-V2 plane in V6-C3; (b) O deformation density, V1-O61-O2 plane; (c) V deformation density, V1-O61-O2 plane; (d) V5 and V3 are defined as type II V atom, V5-O61-V3 plane; (e) XZ plane in V10; (f) horizontal plan in V10.

A focus on each of the four V-O bonds is done through the 2D deformation

density and the corresponding Laplacian distribution maps (Figure 2.32). From the observation of the left column (deformation density distribution for V-O bonds), one can observe along the bond line that the longer bond is, the lower the deformation density is. The highest deformation density distribution appears between bond V1-O11 and the lone pair region of O11, but there is no obvious deformation density concentrated around the bond critical point (BCP). The right column is dedicated to the corresponding Laplacian of electron density of V-O bonds. We can observe that the different polarization patterns of four types of O atoms. For example, there are two polarizations of the electron density appearing for O11 and O22, because the former has one connection with atom and lone electron pair, the latter O22 has two adjacent V atoms. O3x (O31) atom displays three polarization directions toward two V atoms and one C atom belonging to the organic ligand. However, there is no polarization for O61, which is agreement with the deformation density distribution due to the fact that O61 atom is located at the symmetry inversion centre, connected with six V atoms. Despite the various polarization patterns of the O atoms, the Laplacian distributions of V atoms in different orientations are similar, this is due to the fact that V atoms possess a concentrated density, which is not easily polarized through connections with O atoms.

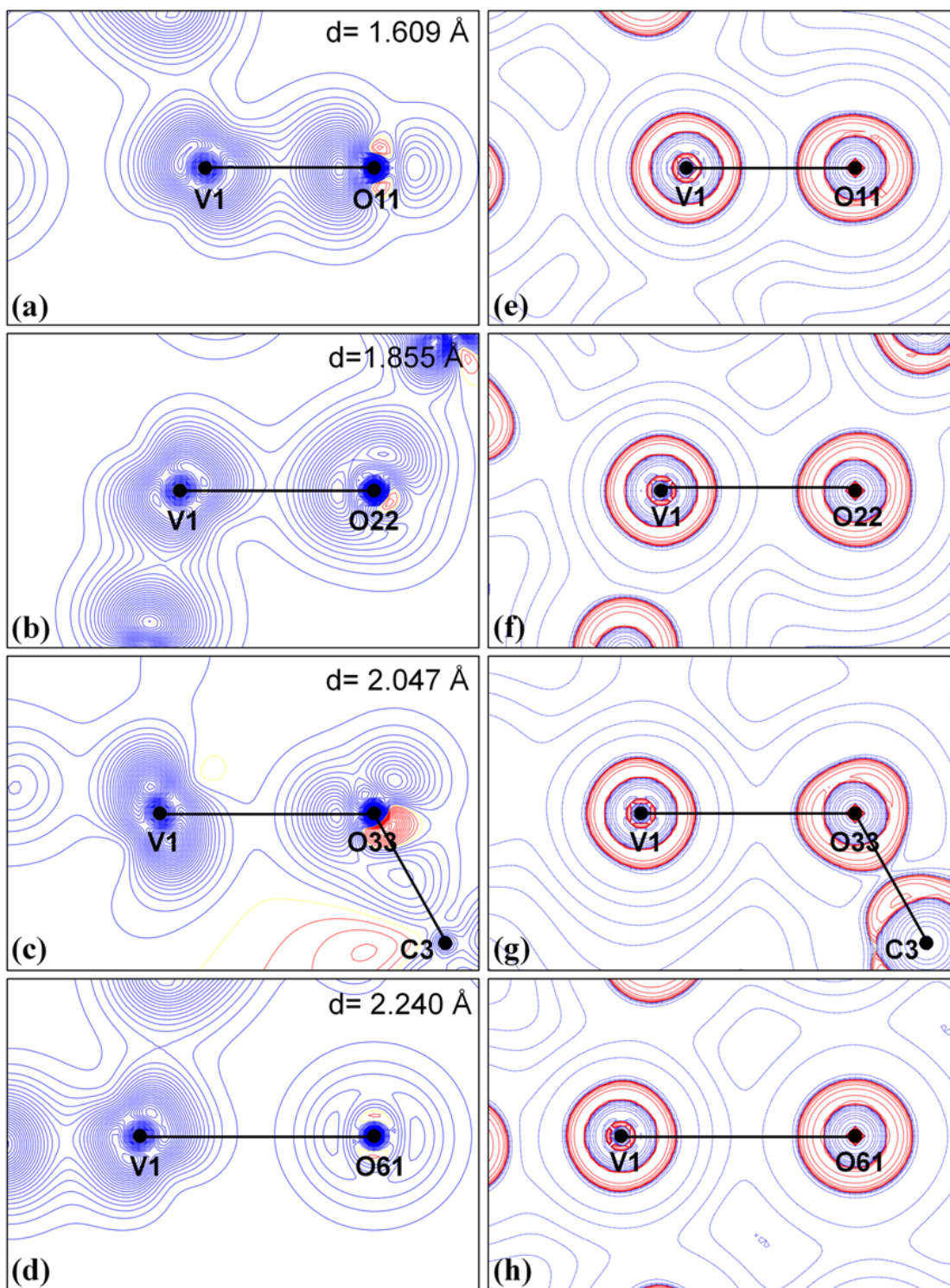


Figure 2.32. Static deformation density maps (contours: $0.05 e\text{\AA}^{-3}$) and Laplacian of density maps (contours: $\pm 2, 4, 8 \cdot 10^n e\text{\AA}^{-5}$, $n = -1, 0, 1, 2$) for V-O bonds in V6 core. The corresponding atoms are labeled, and the bond distances are marked. (a) (b) (c) (d) Static deformation density maps for V1-O11, V1-O22, V1-O31, and V1-O61; (e) (f) (g) (h) Laplacian of total electron density maps for V1-O11, V1-O22, V1-O31, and V1-O61.

2. Topological analysis of the electron density for V-O bonds

To understand the nature of the chemical bonding in V6 core, the experimental total electron density has been investigated through topological analysis using the QTAIM method [Bader, 1990]. Topological parameters of the electron density for the (3, -1) bond critical point in V6 core are given in Table 2.7 (§ 2.3.4.1).

All V-O bonds are characterized by a very large positive curvature at the bond critical point along the direction of the bond path (λ_3). The values of Laplacian, which equals the sum of the three curvatures at the bond critical point, is largely dominated by λ_3 and therefore is positive for the whole range of V-O distances. It has been established that the positive values of Laplacian are characteristic of "closed-shell" interactions governed by the contraction of the charge density toward each of interacting nuclei [Bader, 1969]. As presented in the Table 2.7, $\rho(\mathbf{r}_c)$ values range from $0.282 \text{ e}\text{\AA}^{-3}$ for the longest V-O bond (V3-O61 = 2.244 \AA) to the relatively high value of $1.835 \text{ e}\text{\AA}^{-3}$ for V1-O11. The $\nabla^2\rho(\mathbf{r}_c)$ value ranges from 6.04 to $33.36 \text{ e}\text{\AA}^{-5}$.

For understanding the relationship between V-O distances (from V6-C3 and V10 anion) and different topological properties at BCPs, the following three graph present the topological properties at the position of BCPs on the V-O bonds from V6-C3 and V10.

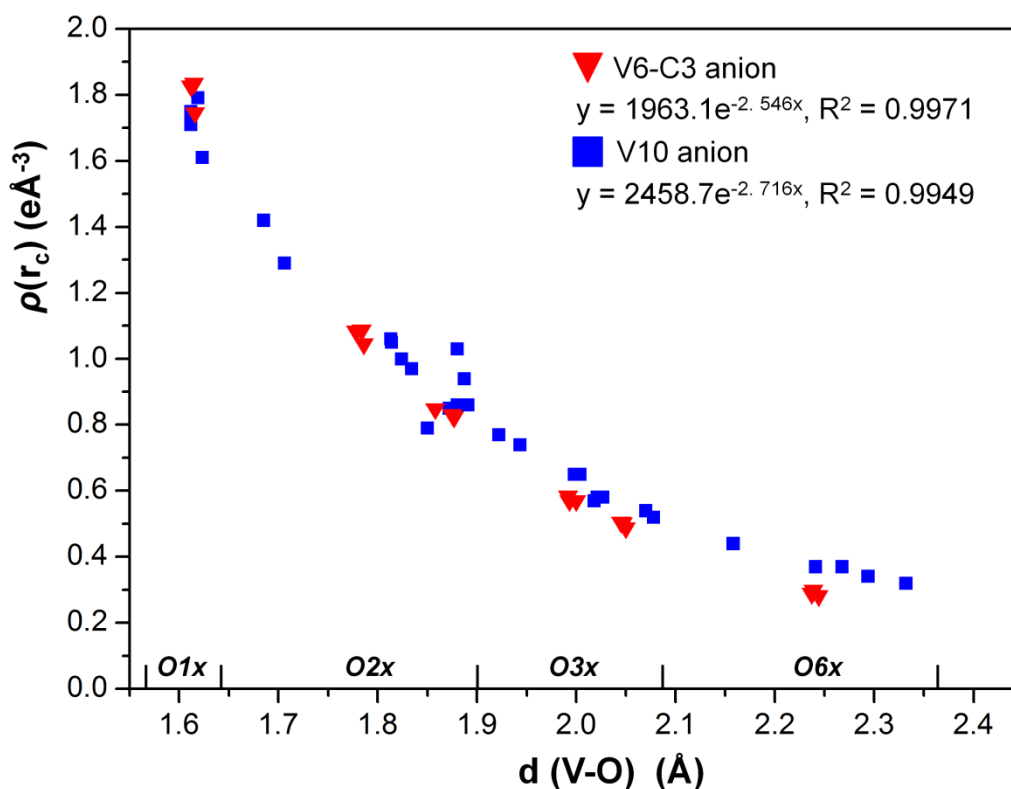


Figure 2.33. Behavior of $\rho(\mathbf{r}_c)$ versus V-O interatomic distance

The relationship between $\rho(\mathbf{r}_c)$ and $d(\text{V-O})$ (in the range 1.612 Å – 2.332 Å) is presented in Figure 2.33. According to this graph, we observe that $\rho(\mathbf{r}_c)$ at the BCP is a decreasing function of the V-O interatomic distances. In the previous research on V10, as shown with blue square in Figure 2.33, the experimental $\rho(\mathbf{r}_c)$ [Bosnjakovic-Pavlovic, 2009] was compared with theoretical $\rho(\mathbf{r}_c)$ [Kempf, 1992], which lead the author to the conclusion that the topological parameters fit well with classification of the vanadium atoms and V-O bonding. However, the graph indicates us more exact behavior that $\rho(\mathbf{r}_c)$ of V-O bond is associated to V-O interatomic distance, not only the type of V-O chemical bonding, which can be also demonstrated by the graph of the behaviour of $\nabla^2\rho(\mathbf{r}_c)$ vs V-O distance (Figure 2.34). The trends of $\rho(\mathbf{r}_c)$ and $\nabla^2\rho(\mathbf{r}_c)$ are in high agreement. This can provide us a predicted information about the relationship between $\rho(\mathbf{r}_c)$ and bond length, which is important for POVs' structural design and construction.

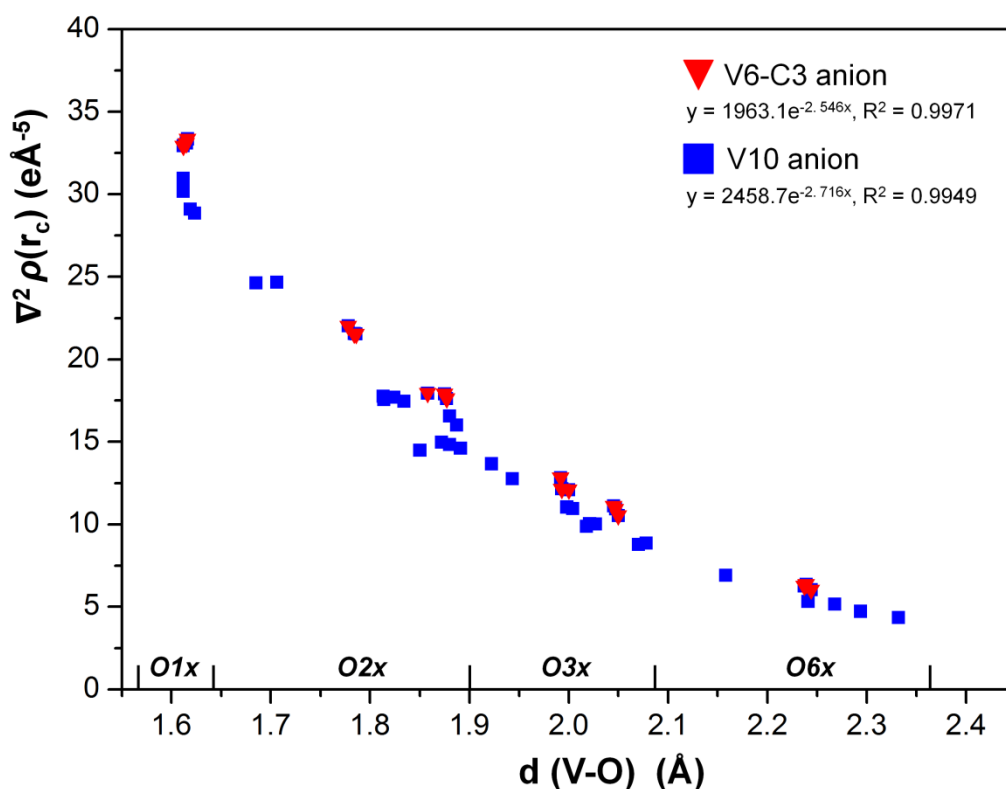


Figure 2.34. Behavior of $\nabla^2\rho(\mathbf{r}_c)$ versus V-O interatomic distance.

It is clear from the Table 2.6 (§ 2.3.4.1) that the observation of the position of the BCP on the V-O bond raises the following remarks: i) d_1+d_2 is always very close to the interatomic distance; ii) the position of the BCP is generally at the middle of the bond, except for the shortest V-O bond (V-O1x) where large discrepancies are

observed.

The total energy density according to the Abramov formula [Abramov, 1997] has also been calculated and presents a quite good behavior leading to significant energy for shortest V-O bonds (V-O1x) in V6-C3 and V10 (Figure 2.35). From Table 2.7 and Figure 2.35, the $H(\mathbf{r}_c)$ is in the following rank: V-O1x (-0.203 au) > V-O2x (-0.043 au) > V-O3x (-0.014 au) > V-O6x (0.019 au). That means that the most stable V-O bond (the most strongest one) is the terminal V-O bond (V-O1x). The weakest V-O bonds are V-O6x with the longest distance.

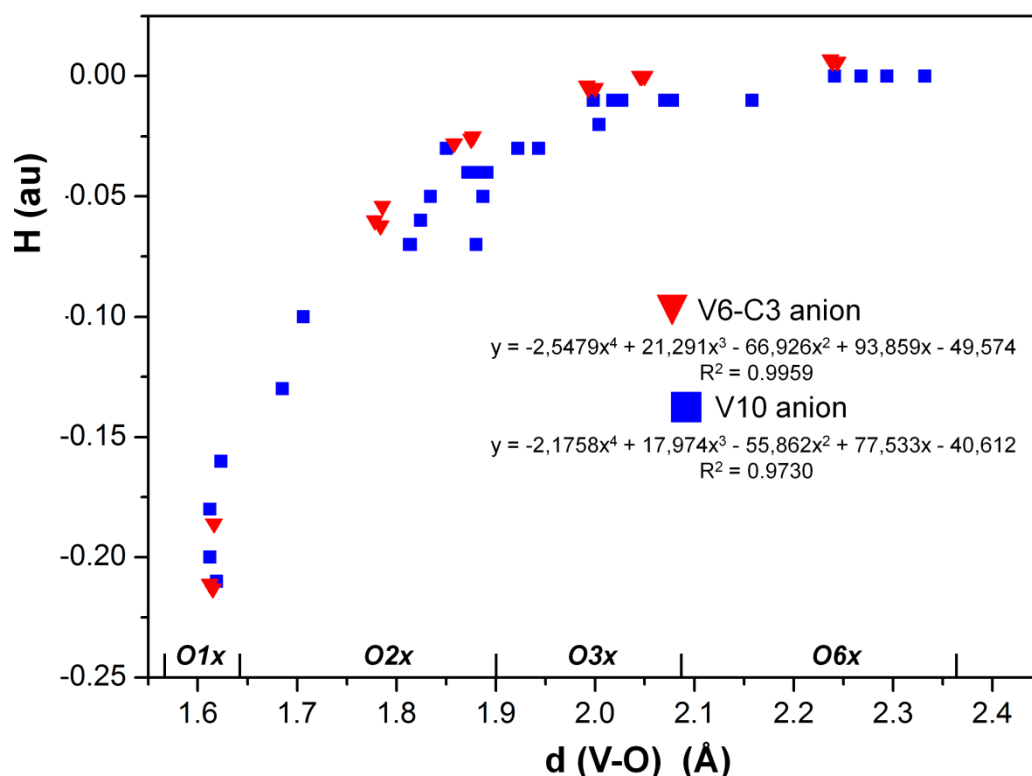


Figure 2.35. Behavior of total energy density at BCP versus V-O interatomic distance.

Due to the fact that the BCP is located in the valence-shell depletion region of both the V and O atoms, the absolute value of the Laplacian profile in the V-O bond is not a good topological descriptor for the degree of covalency in the bonds. Hence the 4s electrons, the outermost valence shell, are not visible in the Laplacian [Sagar, 1988; Shi, 1988]. Therefore, it is better to compare the Laplacian profile in V6 core to that of a non bonded reference, e.g., an IAM model (Independent Atom Model). The density and Laplacian profiles along the four V-O bonds for the multipole model (MM) and the IAM model are shown in Figure 2.36.

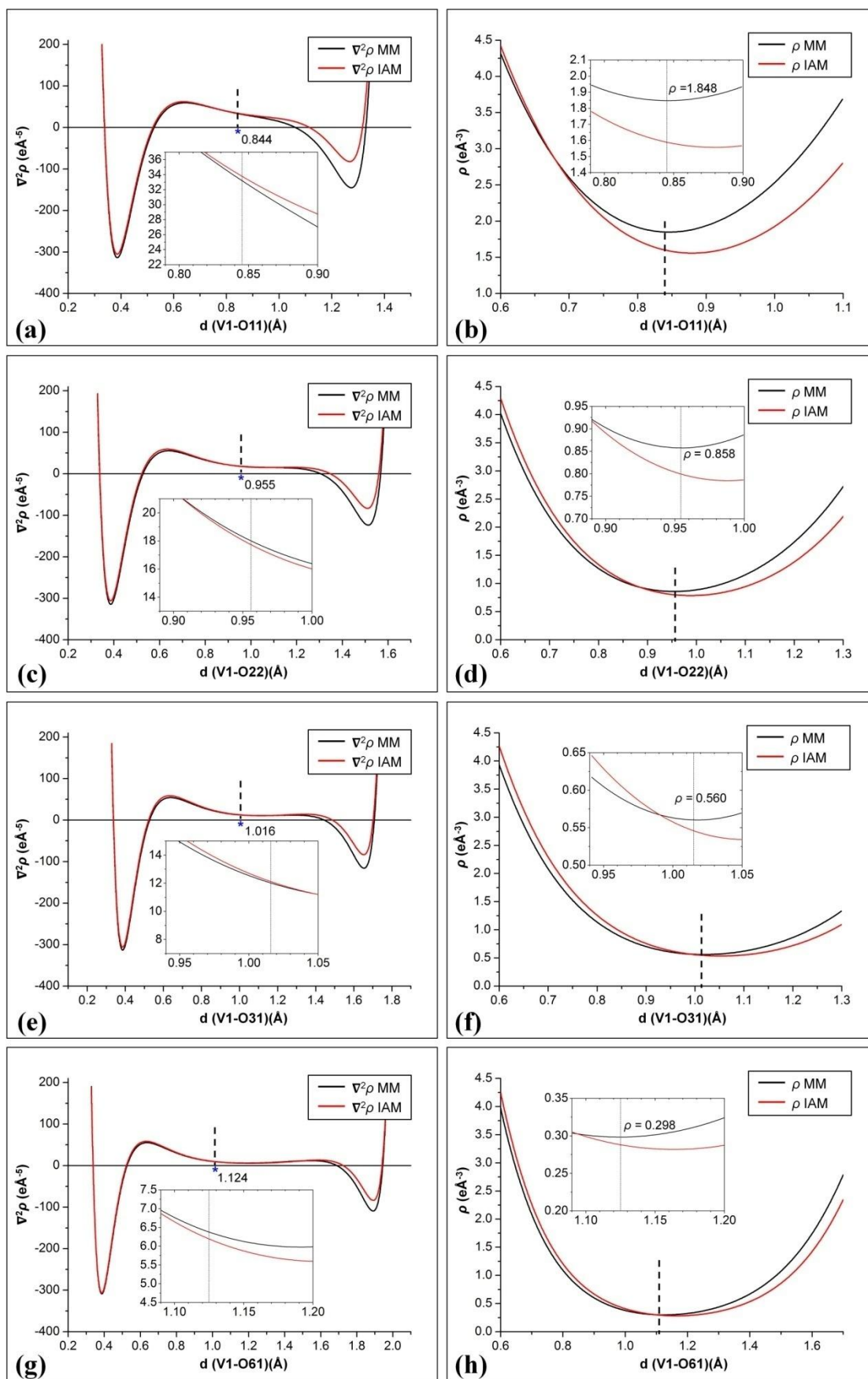


Figure 2.36. Plots of the Laplacian (left) and the density (right) profiles along the V-O bonds.

From the Laplacian profiles of four V-O bonds at the left column, the values of Laplacian at BCPs present no significant differences. For the four type of V-O bonds, we can observe that there is an almost same Laplacian distribution from V nuclei to 0.6 Å along the bond path. Comparing with the lowest Laplacian of IAM model, there is no obvious difference, because there is no significant valence-shell depletion in vanadium atom. We can also observe that the positions with the most negative Laplacian value are at 0.385 Å from V nuclei, which indicates that this is the VSCC (Valence Shell Charge Concentration) of V atom.

In contrast, the VSCC for O is more pronounced in MM model than in IAM model. This is expected due to the charge transfer from V atom to O atom. Such charge transfer is also visible in the $\rho(\mathbf{r}_c)$ profiles at the right column, where there is a shift of the profile toward the V to O atoms in the MM density compared to the IAM density. In the part of V-BCP (d_1), for each V-O bond, the IAM density is higher than the MM density, while in the part BCP-O (d_2) and the position of BCP, the IAM density is lower than the MM density.

For VSCC region of V atom, the Laplacian of the (3, -3) critical points are negative, and the values are listed in Table 2.17. Figure 2.36 presents the six (3, -3) critical points in the VSCC region since the V atom is connected with six O atoms.

Table 2.17. Results of the topological analysis of charge density at (3,-1) bond critical points (BCPs) of V-O bonds and VSCC around V atom.

Bond	Distance (Å)	D_{V1-CP} (Å)	$\rho(\mathbf{r}_c)$ ($e.\text{Å}^{-3}$)	$\nabla^2\rho(\mathbf{r}_c)$ ($e.\text{Å}^{-5}$)	Radius (Å)	ρ_{vscs} ($e.\text{Å}^{-3}$)	$\nabla^2\rho_{vscs}$ ($e.\text{Å}^{-5}$)
V1-O11	1.609	0.844	1.848	33.10	0.385	12.418	-324.99
V1-O22	1.855	0.955	0.858	18.14		12.011	-321.33
V1-O23	1.783	0.921	1.087	21.55		12.356	-338.31
V1-O31	1.998	1.016	0.560	12.02		11.998	-321.55
V1-O33	2.047	1.035	0.488	10.53		12.341	-338.49
V1-O61	2.240	1.124	0.298	6.39		12.341	-326.20

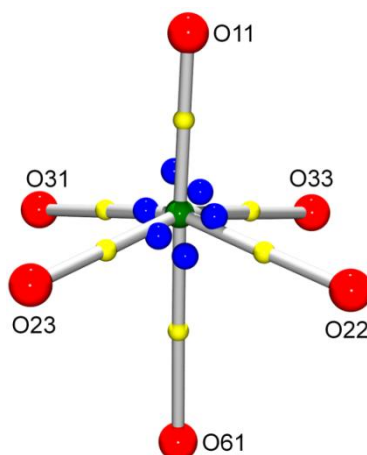


Figure 2.36. Bond critical points (yellow ball) of six V-O bonds and (3, -3) points (blue ball) around V atom.

3. Source function analysis

Source Function (SF), as a relatively new topological descriptor ([Gatti, 2003], [Gatti, 2012], [Gatti, 2013]), has so far been applied to several classes of bonding type, including HBs [Gatti, 2004], multi-centre bonds, metal-metal (M-M) and metal-ligand (M-L) bonds in organometallic systems [Farrugia, 2006; Gatti, 2007; Overgaard, 2008; Farrugia, 2009a; Overgaard, 2009; Wu, 2011; Jorgensen, 2013; Cole, 2013; Wu, 2014]. However, the local source function (LS) analysis dedicated to the behavior of the SF along the bond path (and not the integrated source function, or the Source function contribution) is extremely rare [Overgaard, 2008].

In this section, we focus on the simultaneous observation of the Laplacian and LS profiles (Figure 2.29 in § 2.3.8), as suggested by Gatti ([Gatti, 2004], [Gatti, 2012], [Gatti, 2013]). This would help to reveal the nature of four different V-O bonds and their chemical reactivity. When the Laplacian values increase, the LS values decrease, with an inversion of their sign. The reason is that the LS is defined in terms of the Laplacian as mention in the Eq. 1.40 in Chapter 1. Basically, the difference is that the LS profile explicitly relates the Laplacian of the density at a point along the bond path to the value of the electron density at what is reckoned as the most representative point of a chemical interaction. Three different information could be extracted from the combined observation of the LS and Laplacian profiles.

Firstly, the analysis of the LS profiles along the four V-O bond lines provide the interesting and different fingerprints of chemical bonding features. In details, LS profiles indicate whether a point along the bond line is acting as a source or a sink for the density at BCP. From the four V-O bond graphs, combining the Laplacian and the

LS profiles, we can observe that there are two greatest sources from the VSCC of V where the strongest charge-assisted regions corresponding to the lowest Laplacian distributions.

Secondly, the LS profiles show that the regions around BCPs act as a modest sink for the density at BCP. The V-O interaction represents a borderline region, the source being negative and the Laplacian being positive. This is in agreement with the electron density depletion observed in topological analysis (Figure 2.37). This “odd” behavior is generally an indication of a large departure of the atomic density distribution from that it has when isolated, with the chemical bonding inducing a noticeable asymmetry.

Thirdly, the minima at the BCP positions of four V-O bonds, present different LS negative values. According to [Gatti, 2012], the dominant kinetic energy act as a negative source, like a sink. As the bond distances increase, the absolute $LS(r_c)$ values decrease.

As the basic unit of the V6 core is constituted of V-O bonds, the analysis of SF contribution for V-O bonds would be a good way to describe the electron density delocalization in the functionalized V6-C3. This aspect will be discussed in §2.4.6.

2.4.2.2 Atomic net charges for V and O atoms in V6 core

The atomic net charges from two charge density refinement are listed in Table 2.11, §2.3.5. V atoms carry an average charge +1.69 e (strategy 1) and +1.66 e from the κ refinement. The AIM charge of V atoms, correspond to the average value is +1.27 e (strategy 1) and +1.23 e (strategy 2), which are less positive than the κ charges from monopole populations. The κ parameter values of two strategies are similar, 1.04, which show that the electron density is slightly contracted. In comparison, the κ charges of V atoms in V10 anion are +1.80 e. The κ parameter values of the O atoms in the core are in a narrow range from +0.94 to +0.98, which show the electron density is slightly expanded. The κ charge are in a large range from -0.58 e to -1.38 e for strategy 1, and also a large range from -0.60 e to -1.42 e. Comparing the different atomic charge, we observe that AIM V charge is more positive than the corresponding κ charge, while the AIM O charge is more negative than the κ charge. These results well represent the fact that the AIM charge takes into account the polarized charge density, while the κ charge is obtained from a spherical

model.

In order to investigate the relationship between AIM charge and the chemical environment, the experimental AIM charges for V and O atoms from V6 core of V6-C3 and V10 anion [Bosnjakovic-Pavlovic, 2010] are discussed (Table 2.18). The classification of V and O is described detail in chapter 1, §1.4.4. Though there are three types of V atoms in V10 anion, the V atoms AIM charges are in a relative narrow range. All the V atoms are connected with six O atoms, leading to only one type of V atom (VII), that implies an equivalent chemical environment, and therefore a similar positive charge. However, the O atoms are of different types and present various AIM charge values.

As shown in Table 2.18, in functionalized V6-C3, the average AIM charges of different types of O atoms in V6-C3 are in the order: O6x (-1.09 e) < O3x (-1.04 e) < O2x (-0.94 e) < O1x (-0.74 e). As illustrated in the previous section (§ 2.4.2.1), the different V-O bonds show a smooth behavior in term of topological properties. This order is also expressed on the average charges remain the same for the V10 compound except for O61.

Table 2.18. Experimental AIM charge (*e*) of V and O atoms in functionalized V6-C3 core and decavanadate V10 anion.

Type	Functionalized V6-C3			Decavanadate V10		
	Atom	Charge	Average	Atom	Charge	Average
VI	-	-	-	V4	+1.688	+1.688
VII	V1 V2 V3	+1.206 +1.332 +1.281	+1.273	V3 V5	+1.540 +1.509	+1.525
VIII	-	-	-	V1 V2	+1.533 +1.535	+1.534
O1x	O11 O12 O13	-0.762 -0.628 -0.826	-0.739	O10 O11 O12 O13	-0.620 -0.717 -0.668 -0.572	-0.644
O2x	O21 O22 O23	-1.044 -0.825 -0.946	-0.938	O20 O21 O22 O23 O24 O25 O27	-0.808 -0.783 -0.797 -0.900 -0.857 -0.799 -0.733	-0.811
O3x	O31 O32 O33	-1.052 -0.984 -1.084	-1.040	O31 O32	-0.873 -0.918	-0.896
O6x	O61	-1.090	-1.090	O61	-0.724	-0.724

2.4.2.3 *d* orbital population of vanadium atoms

Due to the open-shell and for the first row transition metals, the lack of a distinct fourth shell of charge concentration and the quite contracted radial extension of the $3d$ orbitals, means that the BCP for almost any bonds to these metals will invariably fall in a zone of charge depletion, i.e. resulting in a positive Laplacian.

From the topological analysis, each O atom exhibits the bonding feature with V atom. Focusing on the density distribution of V atom, and considering the coordination environment of it, the determination of d orbital populations could show a coincident result. Table 2.13 lists the d orbital populations and the occupied percentages for the title compound in two refinement strategies and the decavanadate anion [Bosnjakovic-Pavlovic, 2009].

There is a slight difference between the results from two charge density refinements. The d -orbital population analysis is coherent with an oxidation state for the V atoms of +2 in the $4s^0 3d^3$ configuration. The occupied percentages for d orbitals are between 15% - 24%, which is in good agreement with the features observed in the crystal structure, deformation density maps and topological analysis. The d orbitals in V6-C3 and V10 present the similar occupied percentage, because the V atoms bear to a same chemical environment.

2.4.3 Chemical bonding in functionalized linkage and organic ligand

O3x are the atoms which act as the link between the V6 core and the organic moiety, assuring the functionalized linkage. Therefore, the investigation on the chemical bonding around O3x is important to better understand the functionalization. O3x are involved in two V-O3x bonds and one Cx-O3x bond. The V-O3x bonding features have been presented in § 2.4.2.1. For this section, the discussion is focused on Cx-O3x bonding.

As shown in Table 2.4, the three Cx-O3x bond distances are from 1.424 Å to 1.427 Å, in a very narrow range, which illustrates that these three bonds are in the same geometric situation due to the fact the Cx atoms (C1, C2, C3) are connected to the central C4 atom. The average Cx-O3x bond distance, 1.425 Å, is in high agreement with the statistical results of Cx-O3x (1.429 Å) in CSD. The Cx-C4 bond distances have the same behavior with the bond O3x-Cx: narrow range, 1.534 Å to 1.537 Å, and an almost same average bond distances compare to CSD searching

results (1.535 Å vs 1.533 Å).

2.4.3.1 Electron density maps

The static deformation density (Figure 2.20 d-g) and Laplacian density maps (Figure 2.21 d-g) are presented for the Cx-O3x bonds in different planes.

As for the plane type 2 (3 planes), defined from the V6 core part, V-O3x-Cx, the density distributions of these planes are quite similar. There are three charge accumulations oriented toward two connected V atoms and one C atom. The density distributions toward two V atoms exhibit symmetrical accumulation. In the Laplacian of density maps, the O3x show three polarizations. In comparison with the density distribution of the O2x atom, we have found that the density in the O3x-V bond is less pronounced than the corresponding O2x-V one. This is due to the fact that the Cx atom polarizes the density, which belongs to the O2x-V if there is no functionalization.

The electron density for Cx-O3x and C-C bonds is exhibited in Figure 2.38 (plane type 3, O3x-Cx-C4). The figure shows a comparative representation of the static deformation density and Laplacian of electron density for the Cx-O3x bonds. Generally, the maps are in good agreement with each other, and show the expected chemical bonding features. We plot the 3D static deformation density and Laplacian of density maps for a better representation of the Cx-O3x bond features (Figure 2.39).

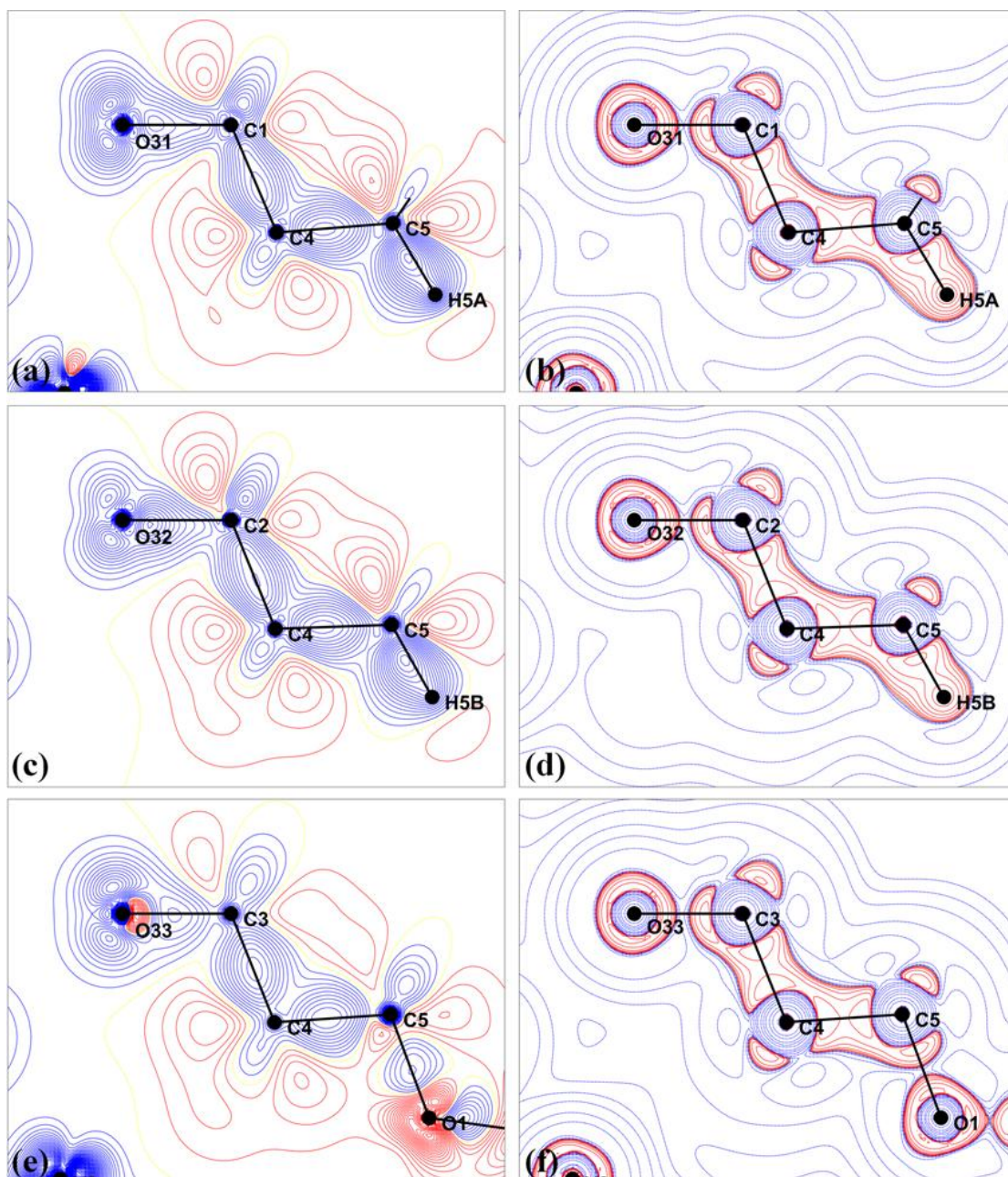


Figure 2.38. Static deformation density maps (contours: $0.05 \text{ e} \text{ \AA}^{-3}$) and Laplacian of density maps (contours: $\pm 2, 8 \cdot 10^n \text{ e} \text{ \AA}^{-5}$, $n = -1, 0, 1, 2$) for $Cx-O3x$ and $Cx-C4$ bonds. The right column is the corresponding Laplacian density maps for the same planes in the left column.

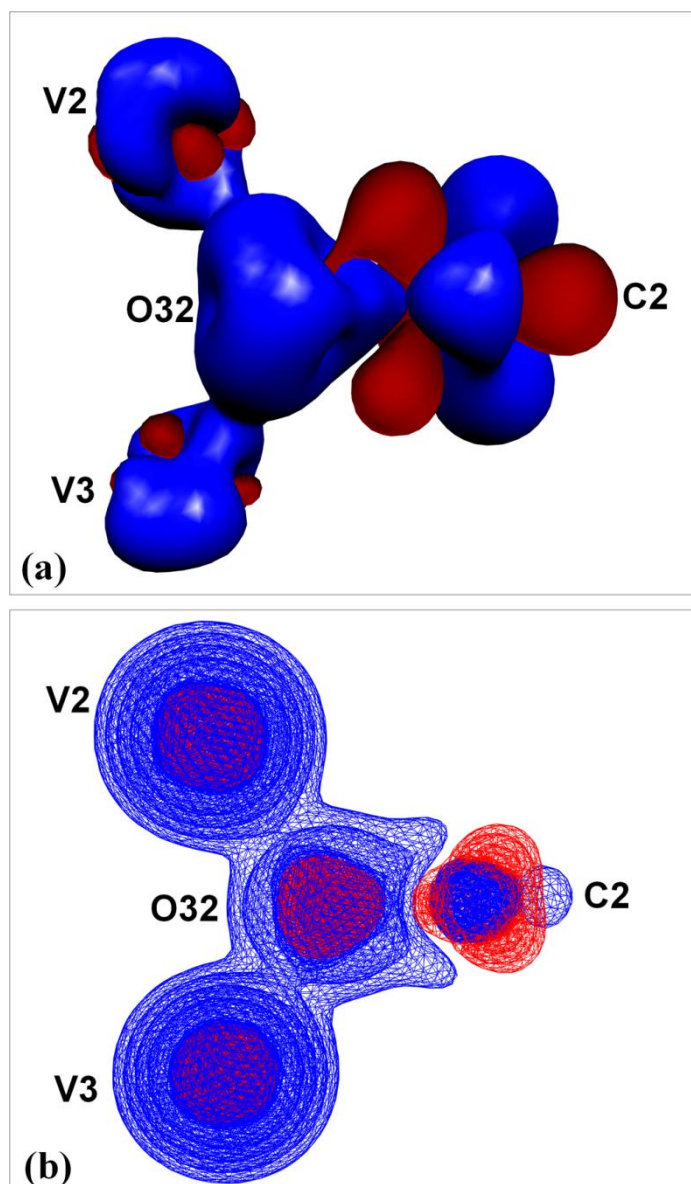


Figure 2.39. 3D static deformation density maps (isosurface cutoff: $\pm 0.05 e\text{\AA}^{-3}$) and Laplacian of density maps (isosurface cutoff: $\pm 1.00 \cdot 2^n e\text{\AA}^{-5}$, $n=0, 1, \dots, 6$) for Cx-O3x bond (C2-O32).

In the organic ligand, there is an ester group; the deformation electron density distribution is shown as the plane 4, O1-C6-O2 (Figure 2.21 h). There is a low density distributed around C6 and O1. Though there is also low residual density for this part, the density distribution of C6 and O1 are unusual (Figure 2.40). The topological analysis could reveal why there is an unusual density distribution in the next section.

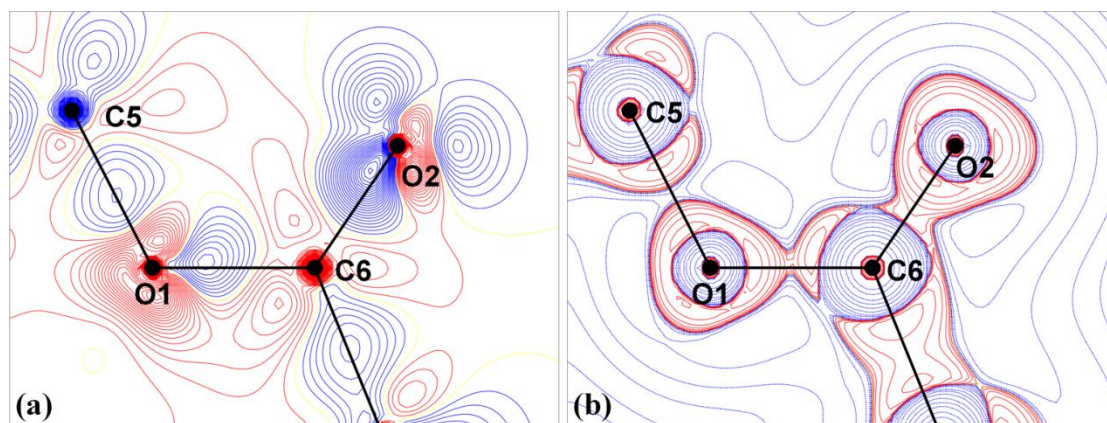


Figure 2.40. Static deformation density maps (contours: $0.05 \text{ e}\text{\AA}^{-3}$) and Laplacian of density maps (contours: $\pm 2, 4, 8 \times 10^n \text{ e}\text{\AA}^{-5}$, $n = -1, 0, 1, 2$) for ester group in organic ligand.

2.4.3.2 Topological analysis

Topological parameters of the electron density for the (3, -1) bond critical points in the organic ligands are given in Table 2.7 (§ 2.3.4.2).

The BCPs of C-C bonds are always located around the middle of the bonds. We observed that the three C_x-C₄ bonds (C₁-C₄, C₂-C₄, C₃-C₄) show the almost same topological behaviours, which are in agreement with the density maps (Figure 2.41).

As usual, the BCP of C-O bonds is always located closer to the less electronegative carbon atom ($d_1 < d_2$). There are three chemically equivalent C_x-O_{3x} bonds, exhibiting similar topological properties. The values of $\rho(\mathbf{r}_c)$ (from 1.816 to $1.852 \text{ e}\text{\AA}^{-3}$), $\nabla^2\rho(\mathbf{r}_c)$ (from -10.96 to $-9.79 \text{ e}\text{\AA}^{-5}$), and $H(\mathbf{r}_c)$ (from -0.371 to -0.358 au.) are in narrow ranges. The other C-O bonds (C₅-O₁, C₆-O₁, C₆-O₂), belonging to the ester group in the organic ligand, have different topological parameters, especially the $\nabla^2\rho(\mathbf{r}_c)$ value of C₆-O₂ is positive. In order to better understand the topological properties, we plot the Laplacian/density profile of four type C-O bonds (Figure 2.41). In the graphs, we can observe that the $\nabla^2\rho(\mathbf{r}_c)$ of C_x-O_{3x}, C₅-O₁, and C₆-O₁ are negative, corresponding to a shared shell interaction, which illustrates that the bonds are covalent. However, for the C₆-O₂ double bond, the $\nabla^2\rho(\mathbf{r}_c)$ is positive at BCP, though the $\rho(\mathbf{r}_c)$ and $H(\mathbf{r}_c)$ have similar values with the other C-O bonds. This is due to the fact that λ_3 has a high positive value ($71.70 \text{ e}\text{\AA}^{-5}$). The possible reasons arise from the refinement, where O₂ presents high U_{eq} value (0.051 \AA^2 , Appendix Table A2.2).

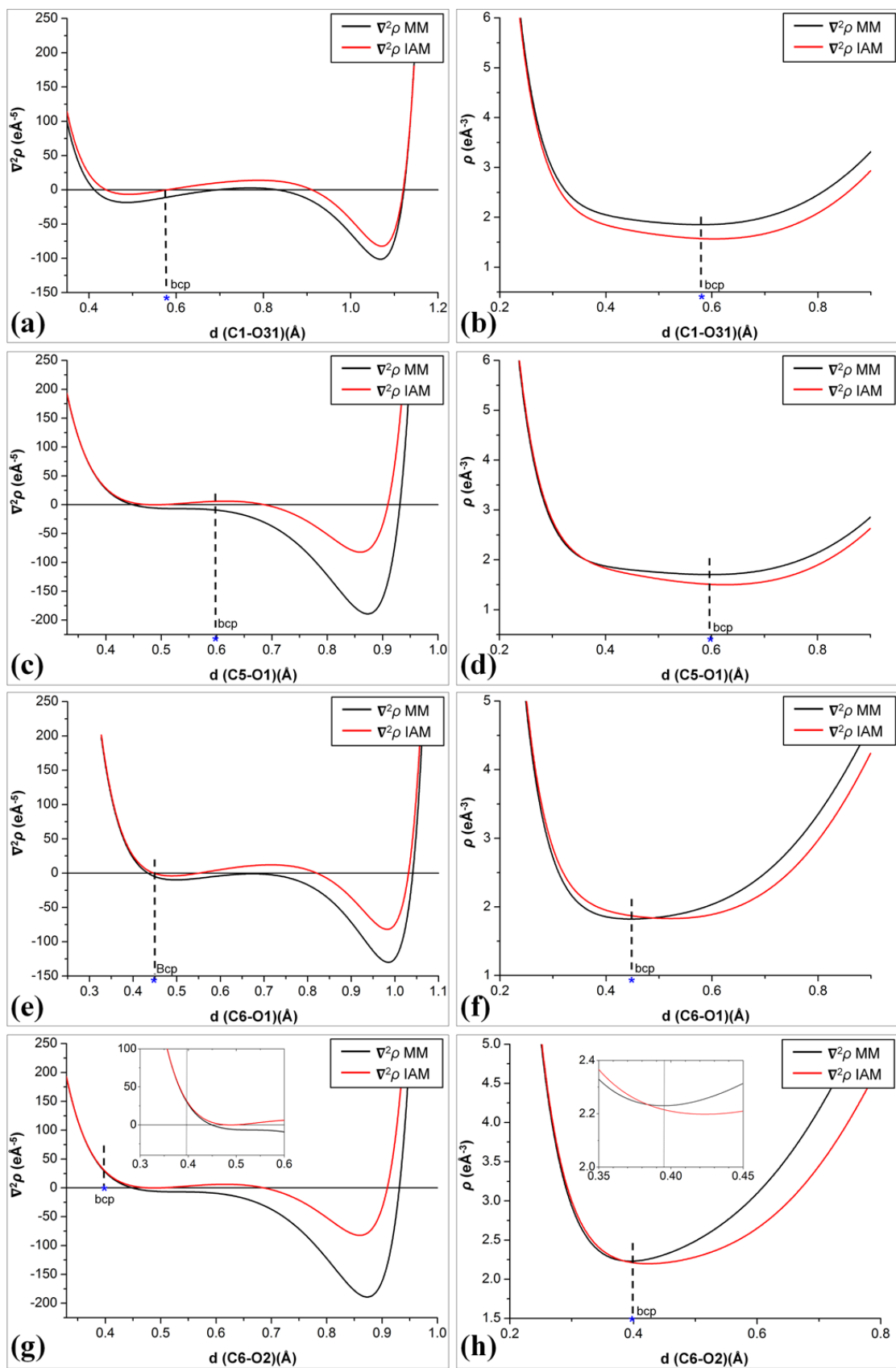


Figure 2.41. Laplacian (left) and the density (right) profiles along the C-O bonds.

2.4.4 Chemical bonding in TBA cation

The TBA cation is used for the stabilization of large size of POM/POV anions. In addition to the HSAB (hard and soft acids and bases) theory explanation [Pearson, 1963], we can find, from a crystallographic view, the reason why TBA cation is good counter ion to the crystalline POM/POV compounds.

There are four chains in the TBA cation, due to the same chemical environment, the bonds are classified as N1-Cx1, Cx1-Cx2, Cx2-Cx3 and Cx3-Cx4. The average distance of these bonds are in this order: Cx3-Cx4 (1.514 Å) < Cx1-Cx2 (1.519 Å) < N1-Cx1 (1.521 Å) < Cx2-Cx3 (1.525 Å), which is agreement with average distances of reported results by the CSD statistical research. However, the bond distances in CSD are in a wide range, which illustrate that different POM structures possess different packing mode in crystalline state *via* C-H \cdots O. TBA cation has many C-H bonds where the chains are flexible due to the C-C and N-C bonds are σ type. This structural feature makes TBA cation to fit various POM/POV cations by non covalent bonds.

During the multipole refinement, the same C and H atom types in the four chains were constrained to have the same charge density parameters. As shown in Figure 2.21 i, the most of electron density is concentrated on the covalent bonds. There is a relative high residual density around C14 (Figure 2.20 i), due to its high thermal motion ($U_{eq} = 0.0592$). From the topological parameters, we can observe that $\rho(\mathbf{r}_c)$ and $\nabla^2\rho(\mathbf{r}_c)$ are consistent with the bond distances.

2.4.5 Non covalent bonding

In the classical crystallography, the non covalent bonds are defined by bond distances and bond angles. From the view of charge density study, the topological analysis can be used for the characterization of H-bonds [Espinosa, 1998]. This analysis enables one to correlate the properties of the electron density at the BCPs of H bonds with the interatomic distance.

The crystal packing analysis has been presented in § 2.3.2, and the C-H \cdots O interactions ordered by distance in Table 2.5. In this table the only criteria used for selecting the H bond was the simplest one ($d(D\dots A) < 3.0\text{\AA}$). Table 2.9 contains the topological properties at the BCPs of the H-bonds, which are relatively strong ($\rho(\mathbf{r}_c) > 0.020 \text{ e\AA}^{-3}$) in crystalline functionalized V6-C3. It is very interesting to compare

accurately the results of the topology and packing.

In the following Table 2.19, the most closest 20 H-bonds from packing study are listed, but there are only 13 BCPs of H bonds can be searched in topological analysis. For the C-H \cdots O interaction, one can suppose that a small \angle DHA angle will imply only a short contact and therefore an absence of BCP. Additionally, Dr. Bosnjakovic-Pavlovic also got the similar information from the combined studies of criteria analysis and topological analysis [Bosnjakovic-Pavlovic, 2008]. From these observations, we can conclude that: i) the closest H bond is not the strongest one; ii) the “significant” H bonds are with the angle \angle DHA > 120 °; iii) this observation can guide us to identify the C-H \cdots O bond with the acceptor O belonging to the V-O bonds in POV compounds.

Table 2.19. Comparison of H-bonds defined from crystal packing and topological analysis. $\rho(r_c)$ is the electron density at the BCP ($e\text{\AA}^{-3}$). The symmetry codes have been defined in Table 2.10. The highest $\rho(r_c)$ is in bold.

D-H \cdots A	packing		topology
	d(H-A) (Å)	\angle DHA (°)	$\rho(r_c)$ ($e\text{\AA}^{-3}$)
C31-H31B \cdots O22	2.251	130.59	0.064
C5-H5B \cdots O2	2.364	94.65	No BCP
C32-H32A ⁽ⁱⁱⁱ⁾ \cdots O11	2.381	140.67	0.056
C23-H23B ^(iv) \cdots O33	2.399	169.40	0.094
C21-H21B ⁽ⁱ⁾ \cdots O2	2.401	140.53	0.054
C41-H41B ⁽ⁱⁱⁱ⁾ \cdots O23	2.433	127.27	0.047
C1-H1A \cdots O1	2.448	98.81	No BCP
C2-H2A \cdots O1	2.454	98.39	No BCP
C42-H42A ⁽ⁱⁱⁱ⁾ \cdots O13	2.459	152.39	0.053
C13-H13A ⁽ⁱⁱ⁾ \cdots O12	2.465	152.60	0.045
C5-H5A ^(v) \cdots O13	2.476	150.29	0.084
C21-H21A \cdots O22	2.492	124.77	0.043
C24-H24A ^(iv) \cdots O21	2.585	133.28	0.042
C2-H2A \cdots O12	2.587	105.02	No BCP
C11-H11A ⁽ⁱ⁾ \cdots O2	2.590	128.28	0.039
C11-H11B ⁽ⁱⁱⁱ⁾ \cdots O23	2.590	129.92	0.042
C13-H13A ⁽ⁱⁱⁱ⁾ \cdots O21	2.590	133.17	0.041
C2-H2B \cdots O13	2.591	105.76	No BCP
C3-H3A \cdots O13	2.593	104.82	No BCP
C3-H3B ^(iv) \cdots O11	2.617	104.72	No BCP

Figure 2.42 shows the relationship between C-H...O distance and topological properties. Generally, the longer C-H...O is, the lower $\rho(\mathbf{r}_c)$ and $\nabla^2\rho(\mathbf{r}_c)$ values are. The C-H...O bond belongs to the category of weak or very weak H-bonds. It has been already noticed that it is difficult to observe electron density deformation for such a bond. This trend reminds verified for the C-H...O bonds in our compound. That observation does not indicate that there is no interaction, but that this interaction is not detectable using the tool of the static electron density deformation density. The experimental static deformation density maps for the most strongest 12 C-H...O bonds are shown in Figure 2.22 as the $\rho(\mathbf{r}_c)$ order. A slight polarisation of the oxygen lone pair could be observed for one of the strongest C-H...O bond (C23-H23B...O33), (Figure 2.22 a). It is worthy to point out that C5-H5A...O13 is the key non-covalent bond to form the 1D [V6-C3]²⁻ chain (Figure 2.22 b).

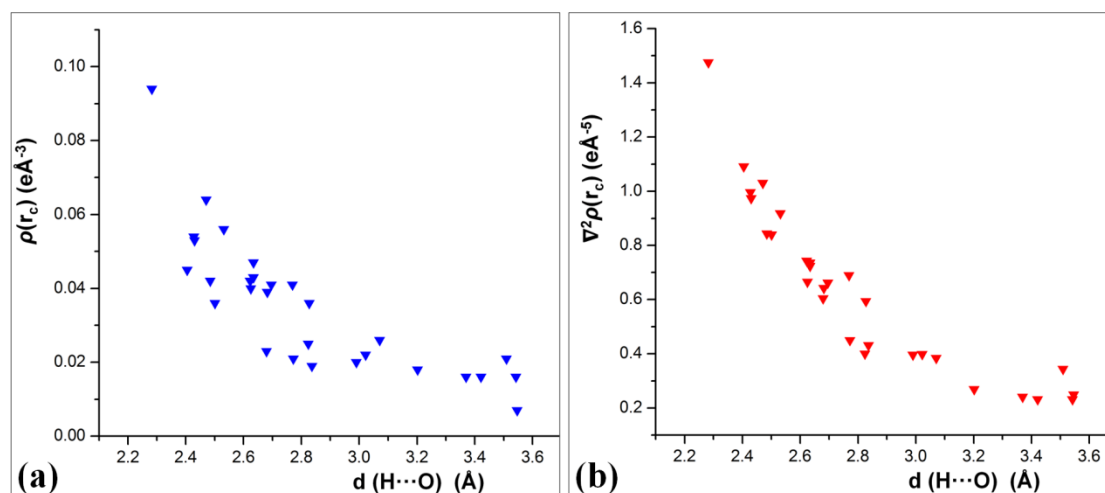


Figure 2.42. Relationship between topological properties and H bond distances after charge density refinement; (a) Behavior of $\rho(\mathbf{r}_c)$ versus $d(H\cdots O)$; (b) behavior of $\nabla^2\rho(\mathbf{r}_c)$ versus $d(H\cdots O)$.

2.4.6 Chemical reactivity and charge transfer

2.4.6.1 Electrostatic potential

The electrostatic potential of [V6-C3]²⁻ mapped on the molecular surface (isodensity, 0.007 eÅ⁻³) from four different refinements are presented in Figure 2.27. Comparing EP from the different refinement, for the same type O atoms, the absolute values obtained from the multipole refinement are generally higher than those obtained from the κ -charges (MM-1 > κ -1, MM-2 > κ -2). Because the charge density refinement strategy 2 permits the charge transfer between [V6-C3]²⁻, some additional

charge is obtained from TBA cation, so that the absolute values of strategy 2 are generally higher than those of strategy 1 (κ -2 > κ -1, MM-2 > MM-1). Depending on the different refinement, the EP features in the organic ligand and TBA cation show the inverse trends. The more negative EP values in V6 core are, the more positive EP values in the organic ligand and TBA cation are. This observation is in agreement with κ charge and AIM charge distribution.

Generally, the EP values in the vicinity of V6 core are negative, while the EP values around organic ligand are positive. Though $[V6-C3]^{2-}$ is an anion, with -2 e, due to the strongest ability electron reservoir of POV structure, the V6 core concentrates the most of negative charge. Some differences are found between the EP values from the κ -refinement and the multipole refinement using different strategy. The EP values in the vicinity of O atoms in V6 core are listed in Table 2.19.

Table 2.19 Electrostatic potential ($e\text{\AA}^{-1}$) at the molecular surface (isodensity, $0.007 e\text{\AA}^{-3}$) from different refinements.

Atom	Electrostatic potential from different refinement			
	κ -1 ^[a]	MM-1 ^[b]	κ -2 ^[c]	MM-2 ^[d]
O1x	-0.62 ~ -0.86	-0.79 ~ -1.09	-0.84 ~ -1.03	-0.91 ~ -1.23
O2x	-0.86 ~ -0.98	-1.09 ~ -1.30	-1.10 ~ -1.23	-1.34 ~ -1.60
O3x	-0.68 ~ -0.92	-0.79 ~ -1.20	-0.90 ~ -1.16	-1.02 ~ -1.45
OL ^[e]	-0.64 ~ +0.08	-0.64 ~ +0.80	-0.64 ~ +0.32	-0.64 ~ +0.80
TBA	+0.10 ~ +0.40	+0.20 ~ +0.30	+0.20 ~ +0.40	+0.20 ~ +0.60

[a] κ -1: κ refinement, strategy 1;

[b] MM-1: multipole refinement, strategy 1;

[c] κ -2: refinement, strategy 2;

[d] MM-2: multipole refinement, strategy 2;

[e] OL: organic ligand.

Despite the fact that refinements are performed in different strategy the EP distribution always exhibits this order: O2x < O3x < O1x. This order is different with the EP features in V10, whose EP value is ordered as O3x < O2x < O1x [Bosnjakovic-Pavlovic, 2009]. In order to recognize the EP distributed on the molecular surface, as an example, the EP mapped on the molecular surface from MM-1 is presented in Figure 2.43. We should mention that the O3x in V6 is connected with organic ligand, the adjacent atom C atoms and H atom, which slightly decrease the EP value around O3x. In V10, O3x surrounded by a pure inorganic environment, is

connected with three V atoms. The highest EP (Figure 2.43) is distributed in a triangular area formed by three O atoms, which are two O2x atoms and one O3x atoms.

EP can be used as a tool for predicting the chemical reactivity, especially for the non covalent interactions in combination with the results of topological analysis of non covalent interaction in crystalline V6-C3. There are six significant C-H...O2x bonds, four C-H...O1x bonds and one C-H...O 3x. Such result is in agreement with the EP distribution, hence the EP values are the most negative in the vicinity of the three oxygen atoms defining the yellow triangle (Figure 2.43). That provides a predictable pattern for non covalent interactions and figures out the probable chemical reaction sites. In this type of functionalized V6 compounds, under a proper condition, O1x and O2x could act as potential reaction sites [Khan, 1992, Müller, 1995, Spandl, 2003]. This aspect will be discussed in more details in chapter 5.

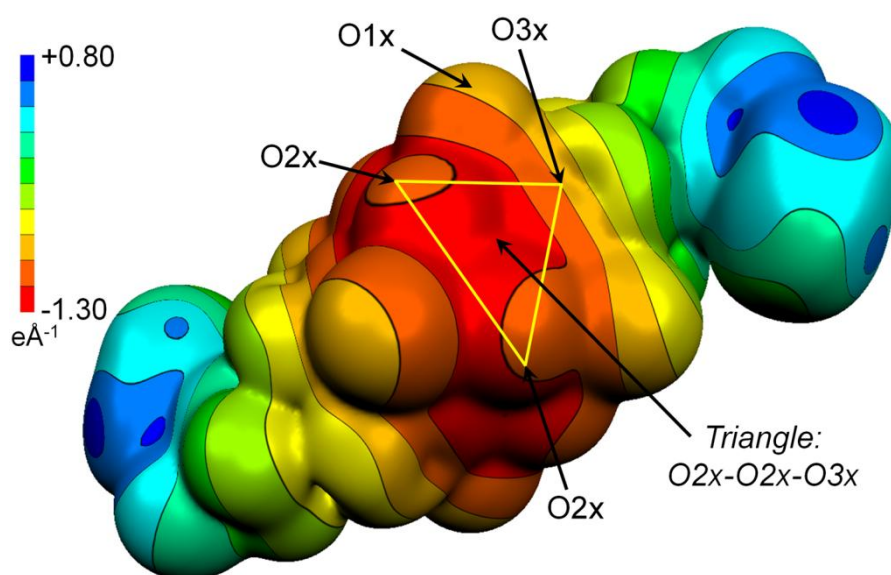


Figure 2.43. Electrostatic potential mapped on molecular surface from MM-1.

In order to graphically exhibit the intermolecular charge transfer in a better way, between V6 core and the organic ligand, the electrostatic potentials are mapped as the isovalue surface at $\pm 0.75 \text{ e}\text{\AA}^{-1}$ (Figure 2.27). The red part (negative) is localized around the V6 core, which corresponds to the most nucleophilic regions, while the blue part (positive) is concentrated over the organic ligand, which represents the most electrophilic regions. This property reveals the most important features of this hybrid compound. The different volumes of the negative surface, corresponding to the nucleophilic region, are in agreement with those of the AIM distributions in different

refinements. According to the fact that the multipole model is closer to the reality than the κ model, the EP obtained from the multipole refinement will be only discussed in the following paragraph.

2.4.6.2 AIM charge distribution

Summations of AIM charges for different moieties in V6-C3 are listed in Table 2.20. At the initial refinement step, the -2 e anionic formal charge was equally distributed on the oxygen atoms, leading to a value of +0.44 e on V6 core and -2.44 e for the organic ligand. The final values at the end of the refinement (strategy 1) indicate a strong polarization of the functionalized V6 anion (-9.76 e for the V6 core and +7.51 e for the two organic ligands). In comparison to the strategy 1, there is an enhancement of the intermolecular charge transfer (ICT) in crystalline state, which indicates that the V6 core is slightly more negative and the organic ligand is slightly more positive (+7.07 e) leading to a more negatively charged functionalized V6 (-10.23 e). Consequently, some charges are also transferred from the cation to V6 core through several C-H \cdots O weak hydrogen bonds.

Table 2.20. Summations of atomic charges(e) for different moieties

Moiety	Initial Charge	κ charge		AIM charge	
		κ -1	κ -2	MM-1	MM-2
V6 core	+0.44	-4.82	-5.47	-9.76	-10.23
OL	-2.44	+2.82	+2.33	+7.51	+7.07
[V6-C3] ²⁻	-2.00	-2.00	-3.14	-2.25	-3.16
TBA cation	+2.00	+2.00	+3.12	+1.67	+2.64
Total	0.00	0.00	-0.02	-0.58 ^[a]	-0.52

[a] Due to the huge size of V6-C3 structure, the AIM charges calculation failed to maintain electrical neutrality with an error -0.58/ -0.52e for the two strategies. We can note that 0.58/ 0.52 e just corresponds respectively to 0.12%/ 0.11% of the total number of electrons (468 e) unit cell of V6-C3.

The above analysis of AIM charge and EP proves that there is a charge transfer between V6 core and the organic ligands in crystalline V6-C3 (Figure 2.44).

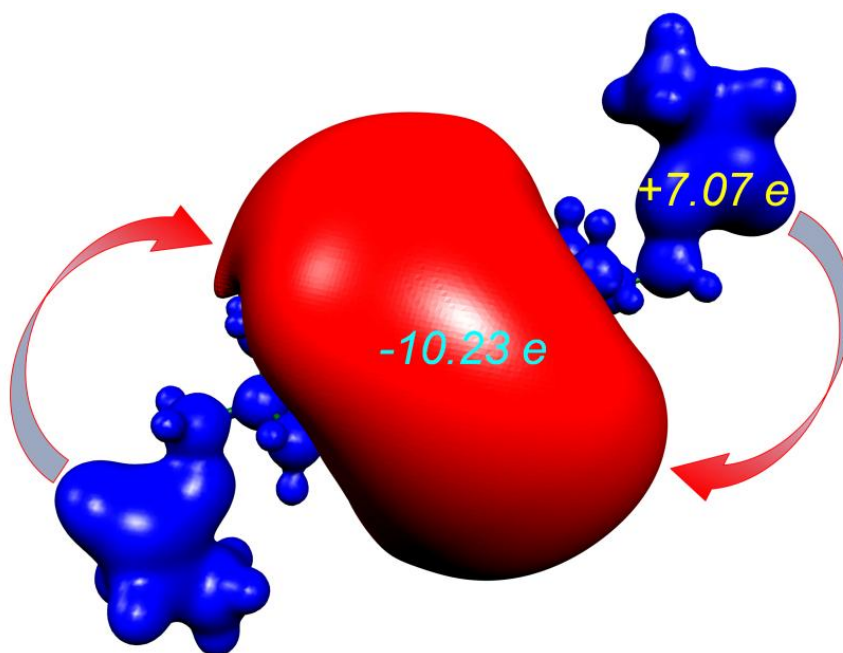


Figure 2.44. Charge transfer between V6 core and organic ligand.

2.4.6.3 Integrated source function analysis

The AIM charge distribution and EP analysis provide us the result of charge transfer. Another way to estimate the charge transfer, is to use the integrated source function. Topologically speaking, a BCP, as the sole indicator, is associated with only two atoms, it connects and it is thus inherently unable to directly visualize an interaction involving more than two centres, even the whole molecule or other “non-local” parts in the system. In other word, by using the integrated SF, the electron density at the BCP, taken as the most representative density point for the two bonded atoms, is determined not only from the contributions of these two atoms, but also, in principle, from those of all the remaining atoms in the system, so bringing indirectly to the ‘non-local’ roles into the bonding [Gatti, 2013].

The results of integrated source function are presented, as SF contribution, in Table 2.14, 2.15 and Figure 2.23, right column, § 2.3.8. We have calculated the SF contributions for BCPs in four types of V-O bonds (Figure 2.45, Table 2.14). For the shortest V-O1x, the shortest one, the most contribution to $\rho(\mathbf{r}_c)$ is from the V6 core (95.20%), 89.97% SF contribution from two connected atoms, the local part as C. Gatti said. As the V-O distance increases, the contributions from V6 core and local part at BCP of corresponding V-O bonds decrease. For example, the contribution to BCPs of V-O6x is only 61.77% from V6 core, and 29.5% from local part. In contrary,

the contribution from the “non-local” parts at the BCPs of V-O bonds increases as the V-O bond distance increases. There is only 2.89% contribution from the organic ligand at V-O1x, but for O-6x, the contribution is 26.33%. We can observe that the indirect contribution is so high, which proves that V6 core can harvest much more density from “non-local” parts, organic ligand and TBA cations. In other word, the electron density in the organic ligand and TBA cation is delocalized to the V6 core. This observation is another evidence of the charge transfer existing inside the hybrid compound.

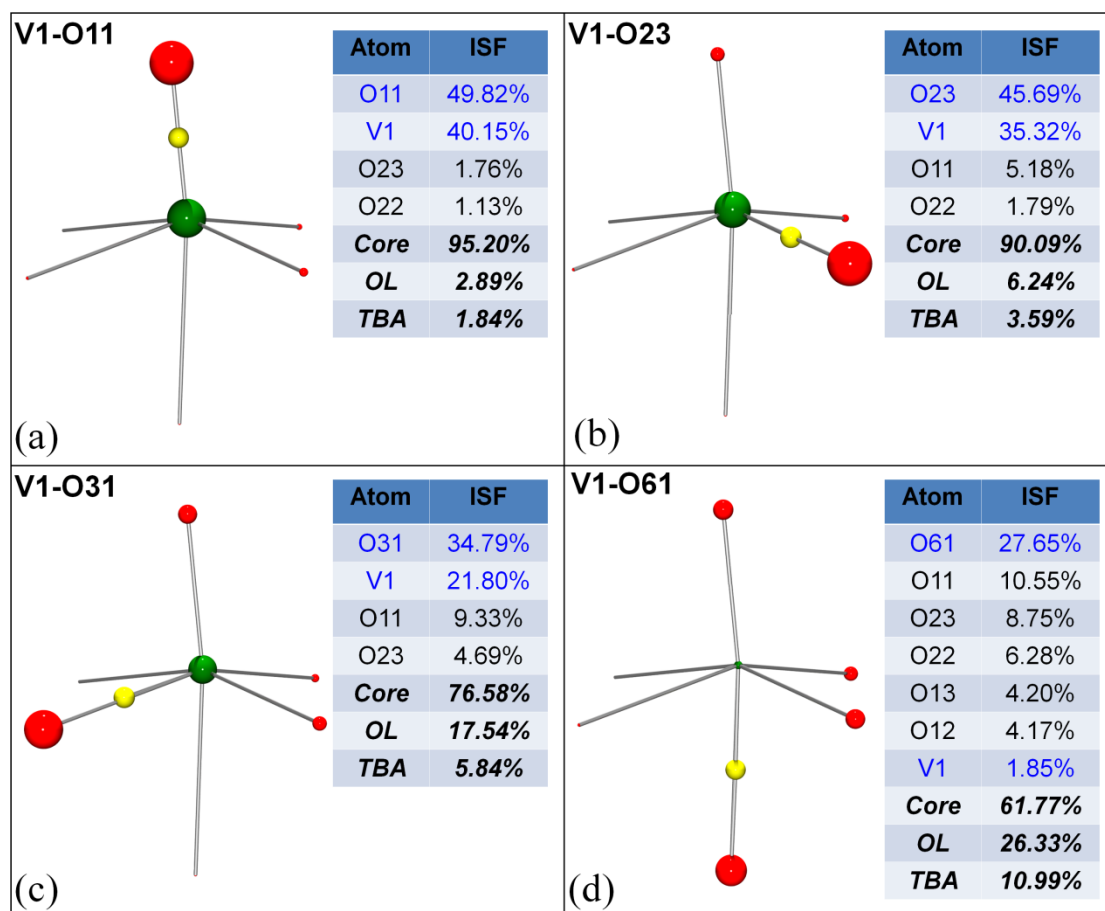


Figure 2.45. SF contribution for four V-O bonds from local part and non-local parts.

Summations on the organic ligand, V6 core and cations of the atom percentage contributions are given in Table 2.17, § 2.3.8. There is 87.03 % of the electron density at BCPs in V6 core originating from the V6 core itself, while 8.94 % comes from the organic ligand and 4.03 % from the cations. The percentages on the diagonal of Table 2.15 originate from the corresponding parts and display the main contributions. While the other contribution ($8.94 + 4.03 = 12.07$ %) seems small, it nevertheless indicates a delocalization of the electron density. All these results are in agreement with the fact

that V6 core has a strong electron-containing capacity, which had never been characterized by direct experimental evidences before.

2.5 Conclusion

In this chapter we have presented an high resolution X-ray diffraction study on a V6-C3. We have given a complete description of the chemical bonding features especially concerning the V-O bond using various properties which can be extracted from the charge density study (deformation density, topology analysis, local source function profile). This characterization has been compared to the behavior of the V-O bonds in V10. In order to access to reactivity of this compound we have determined the charge and the EP distributions. We have shown that it exists, inside this hybrid compound a charge transfer. The V6 core bearing a strong negative charge (-10.23 e) while the organic ligand is positively charged (+7.07 e). We have also used the integrated source function for a better understanding of the atomic contributions at each BCP.

**3. PRELIMINARY EXPERIMENTAL
CHARGE DENSITY ANALYSIS OF
FUNCTIONALIZED HEXAVANADATE
V6OH**

3.1 Introduction

This chapter presents a preliminary experimental charge density analysis of a functionalized V6 compound, $\text{Na}_2[\text{V}_6\text{O}_{13}\{(\text{OCH}_2)_3\text{CCH}_2\text{OH}\}_2] \cdot 3.5\text{H}_2\text{O}$. In § 3.2, the experimental and refinement information are detailed while § 3.3 contains all the results. The discussions of the chemical bonding features and reactivity are done with the other compounds in chapter 5.

3.2 Experiment and refinement

3.2.1 Synthesis and crystallization

The synthesis of the title compound, $\text{Na}_2[\text{V}_6\text{O}_{13}\{(\text{OCH}_2)_3\text{CCH}_2\text{OH}\}_2] \cdot 3.5\text{H}_2\text{O}$ (simplified as V6OH), consists in the step 1 for synthesis of V6-C3 without the TBA cation exchange, as showed in Figure 3.1.

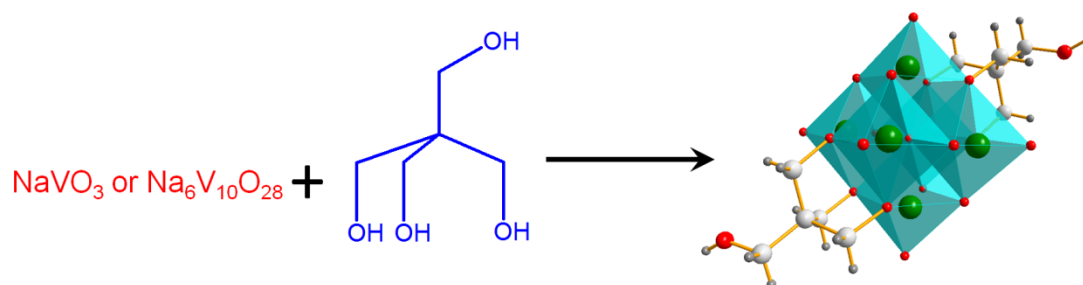


Figure 3.1. Synthesis process of the title functionalized hexavanadate, V6OH. V6 core are shown in octahedral style.

The compound V6OH-TBA was prepared according to Zubieta and Müller's previous work [Müller, 1995], except that tetrabutyl ammonium was used as the counter ions. An amount of 25.9 g $\text{NaVO}_3 \cdot 2\text{H}_2\text{O}$ was dissolved into 250 mL deionized water. 1 M hydrochloric acid HCl was added dropwise until reaching pH = 3 and then 8 g pentaerythritol was added to the solution. The mixture was stirred at 80 °C for 48h and then filtrated. The dark red filtrate was dissolved in distilled water, the red crystal were formed within one week from the solution, kept at room temperature. The crystal samples for high resolution X-ray experiment were obtained by twice recrystallization from deionized water.

3.2.2 Crystallographic refinement

The data collection, data reduction, and IAM refinement are similar to that of V6-C3. For multipole refinement, we use the same strategy as for V6-C3. The model for V atoms is based on $4s^0 3d^3$ configuration, where V^{2+} contains 18 core electrons. In order to conserve electronic neutrality, we have attributed the formal charges as follows: $[Na_2]^{2+}[V_6O_{13}\{(OCH_2)_3CCH_2OH\}_2]^{2-} \cdot 3.5H_2O$. In this model, we have not authorized a charge transfer between the different ions and water. The multipole refinement process are the same with **Strategy 1** for V6-C3 in chapter 2. The Table 3.1 gives the details of the X-ray diffraction experiment and multipole refinement.

Table 3.1. X-ray diffraction experiment and refinement details.

Sample and crystal data	
Chemical formula	C ₁₀ H ₃₂ Na ₂ O ₂₈ V ₆
Formula weight	951.97
Temperature	100(2) K
Wavelength	0.71073 Å
Crystal size	0.062 x 0.077 x 0.225 mm
Crystal habit	clear light red plate
Crystal system	monoclinic
Space group	<i>C</i> 2/ <i>c</i>
<i>a</i>	22.3943(1) (Å)
<i>b</i>	11.7501(5) (Å)
<i>c</i>	12.8043(6) (Å)
α	90 (Å)
β	122.924(2) (Å)
γ	90 (Å)
Volume	2828.1(2) (Å ³)
<i>Z</i>	4
Density (calculated)	2.236 g/cm ³
Absorption coefficient	2.048 mm ⁻¹
F(000)	1904
Data collection and structure refinement	
Diffractionmeter	Bruker D8 VENTURE
Radiation source	Mo K/ α
Theta range	2.35 to 52.15 °
Index ranges	-49<= <i>h</i> <=49, -26<= <i>k</i> <=26, -28<= <i>l</i> <=28
Reflections collected	343850
Independent reflections	16777 [<i>R</i> _{int} = 0.0377]
Absorption correction	multi-scan
Structure solution technique	direct methods
Structure solution program	SHELXS-1997
Refinement method	Full-matrix least-squares on F ²
Refinement program	SHELXL-2013
Goodness-of-fit on F ²	1.056
Δ/σ_{\max}	0.03
Final R indices	14083 data, <i>I</i> >2 σ (<i>I</i>), <i>R</i> 1 = 2.75%, <i>wR</i> 2 = 7.30% all data, <i>R</i> 1 = 3.51%, <i>wR</i> 2 = 7.71%
Largest diff. peak and hole	1.908 and -2.142 eÅ ⁻³
R.M.S. deviation from mean	0.142 eÅ ⁻³
Multipole refinement	
Reflections used in Mopro	13652, <i>I</i> >3 σ (<i>I</i>)
Resolution range used	0.058 - 1.112 Å ⁻¹
<i>R</i> 1	2.14%
<i>wR</i> 2	2.30%
GOF	1.216

3.3 Results

3.3.1 Crystal structure description

The X-ray structural analysis reveals that the asymmetric unit of the compound contains half of a centrosymmetrical functionalized $[V_6OH]^{2-}$ anion, one sodium cation, and three and half of water molecules (Figure 3.2). The different moieties are defined in the same way for V6-C3 in chapter 2. We should mention here $Na_2[V_6O_{13}\{(OCH_2)_3CCH_2OH\}_2] \cdot 3.5H_2O$ is a new crystal structure. The other functionalized V6OH with different cations and co-crystal solvent molecules have been reported: i) TBA cation, DMF (CSD refcode: VERDIF10) [VERDIF 10]; ii) TBA cation, CH_3CN (CSD refcode: GIFROE) [Wu, 2013]; iii) TBA cation, H_2O (CSD refcode: GIRRUK) [Wu, 2013].

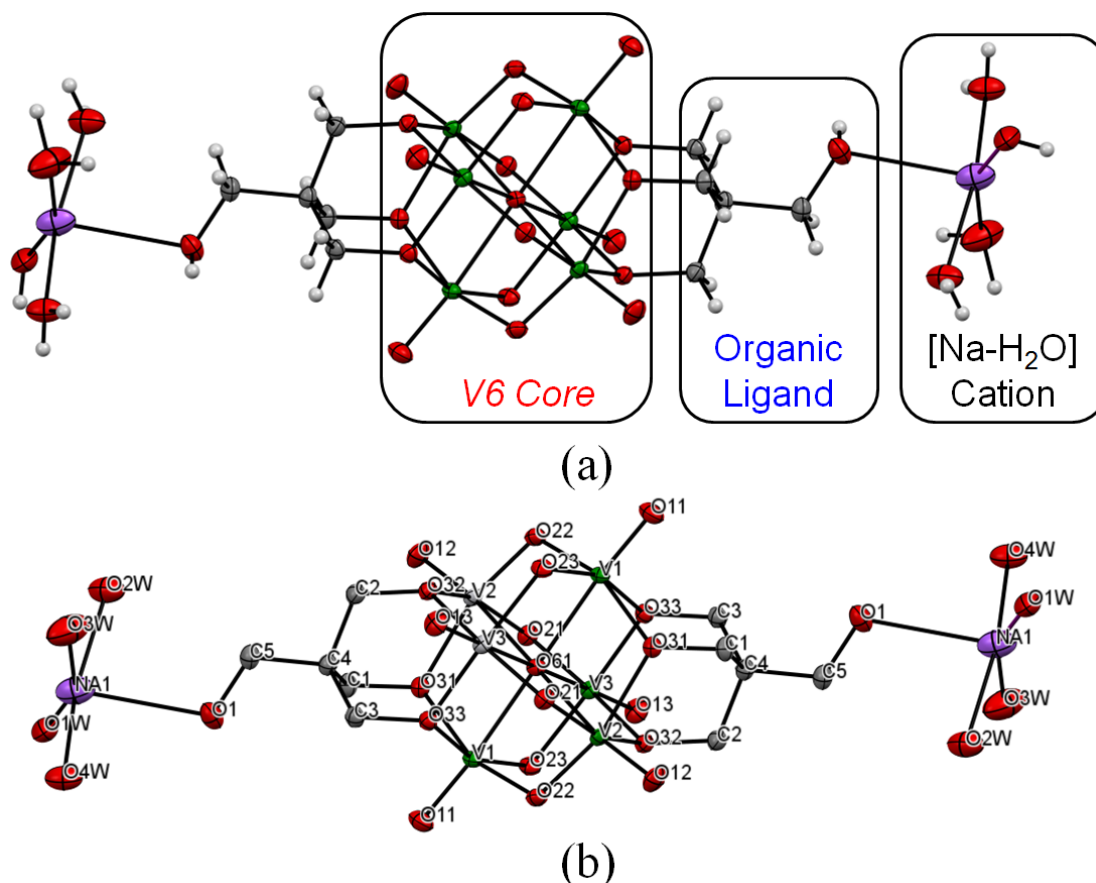


Figure 3.2. ORTEP view of the functionalized V6OH. Two asymmetric units are represented. (a) The different moieties are defined as V6 core, organic ligand, and Na- H_2O cation; (b) The atom labels are given by the same labeling way with functionalized V6-C3. All V atoms is type II, the O atoms are classified as O1x, O2x, O3x, and O6x. The H atoms have been omitted.

3.3.1.1 Functionalized [V6OH]²⁻ anion

The functionalized [V6OH]²⁻ anion is formed by V6 core, the same moiety with functionalized [V6-C3]²⁻, and two tris(alkoxo) ligands with –OH groups. Tables of atomic coordinates, thermal displacement parameters, and bond angles are in Appendix (table A3.1, table A3.2 and table A3.3). The V-O interatomic distances, Cx-O3x and Cx-C4 bond distances are listed in Table 3.2.

Table 3.2. Bond distances (Å) in [V6OH]²⁻.

Type	Bond	Distance	Average
V-O1x	V1-O11	1.5973	1.604
	V2-O12	1.6076	
	V3-O13	1.6065	
V-O2x	V1-O22	1.9292	1.840
	V1-O23	1.7727	
	V2-O21	1.9025	
	V2-O22	1.7663	
	V3-O21	1.7608	
	V3-O23	1.9077	
V-O3x	V1-O33	2.0619	2.008
	V1-O31	1.9465	
	V2-O32	1.9691	
	V2-O31	2.0546	
	V3-O32	2.0514	
	V3-O33	1.9663	
V-O6x	V1-O61	2.2509	2.237
	V2-O61	2.2163	
	V3-O61	2.2451	
Cx-O3x	C1-O31	1.4402	1.440
	C2-O32	1.4329	
	C3-O33	1.4455	
Cx-C4	C1-C4	1.5333	1.533
	C2-C4	1.5314	
	C3-C4	1.5351	

3.3.1.2 Sodium cation

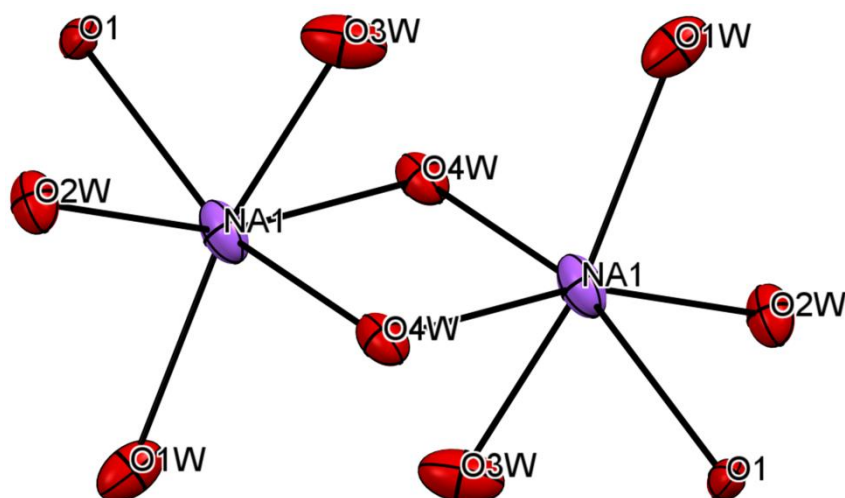


Figure 3.3. ORTEP view of the environment of sodium atom. Two asymmetric units are represented. The H atoms have been omitted.

The asymmetric unit contains one sodium atom. Each sodium atom is in octahedral coordination: Na^+ is surrounded by five water molecules and one oxygen atom belonging to $[\text{V6OH}]^{2-}$ (O1 in the organic ligand), as shown in Figure 3.3. The corresponding bond distances are listed in Table 3.3. The Na-Ow distances are in a narrow range (2.3138 to 2.3911 Å), which is in agreement with the Na-Ow distances in $[\text{V}_{10}\text{O}_{28}] (\text{C}_4\text{N}_3\text{OH}_5)_3 (\text{C}_4\text{N}_3\text{OH}_6)_3 \cdot 10\text{H}_2\text{O}$ [Bošnjaković-Pavlovic, 2010].

Table 3.3. Bond distances (Å) in around sodium cation.

Bond	Distance	Average
Na1-O1	2.7577	
Na1-O1W	2.3693	2.348
Na1-O2W	2.3138	
Na1-O3W	2.3159	
Na1-O4W	2.3911	
Na1-Na1	4.0225	

3.3.2 Crystal packing

The crystal structure of the title compound is stabilized by an extensive network of hydrogen bonds, which involved the $[\text{V6OH}]^{2-}$ and the water molecules. Table 4.4 presents the most significant hydrogen bond features according to the usual criteria

($d(D\cdots A) < 3.5\text{\AA}$, $\angle DHA > 120^\circ$). We can observe that most of the acceptors belonging to the V6 core. The crystal packing along **c** axis and **b** axis is presented in Figure 3.4 and Figure 3.5 respectively.

Table 3.4. Distances (\AA) and angles ($^\circ$) of the hydrogen bonds in V6OH (*D* donor, *A* acceptor). Symmetry operators: (i) = $x, 1-y, -1/2+z$; (ii) = $x, 1-y, 1/2+z$; (iii) = $x, 1+y, z$; (iv) = $1-x, y, 1/2-z$; (v) = $1-x, 1-y, -z$; (vi) = $1/2-x, 1/2-y, -z$; (vii) = $1/2-x, 1/2+y, -1/2-z$; (viii) = $1/2+x, 1/2-y, -1/2+z$; (ix) = $-1/2+x, 1/2+y, z$.

O-H...O	D-H ...A	d (H-A)	d(D ...A)	$\angle DHA$
	O3W-H3BW ⁽ⁱⁱ⁾ ...O12	1.845	2.829	153.20
	O1-H1O ⁽ⁱⁱ⁾ ...O21	1.991	2.819	175.13
	O4W-H4AW ⁽ⁱⁱ⁾ ...O22	2.054	2.864	156.70
	O4W-H4AW ⁽ⁱⁱ⁾ ...O21	2.063	2.876	167.43
	O1W-H1AW ⁽ⁱⁱⁱ⁾ ...O22	2.120	2.868	157.08
	O2W-H2AW ^(iv) ...O1	2.217	3.001	158.76
	O3W-H3AW ^(v) ...O32	2.391	3.190	131.33
	O2W-H2BW ^(v) ...O13	2.532	3.480	160.13
	O4W-H4BW ^(vi) ...O23	2.597	3.275	125.69
	O4W-H4AW ^(vii) ...O33	2.652	3.282	134.37
	O2W-H2AW ^(viii) ...O11	2.740	3.319	126.00
	O3W-H3AW ^(ix) ...O23	2.823	3.415	130.26
C-H...O	D-H ...A	d (H-A)	d(D ...A)	$\angle DHA$
	C1-H1B ⁽ⁱ⁾ ...O13	1.782	2.815	176.14
	C5-H5B ⁽ⁱⁱ⁾ ...O12	2.081	2.936	169.41
	C2-H2B ^(iv) ...O12	2.361	3.228	145.87

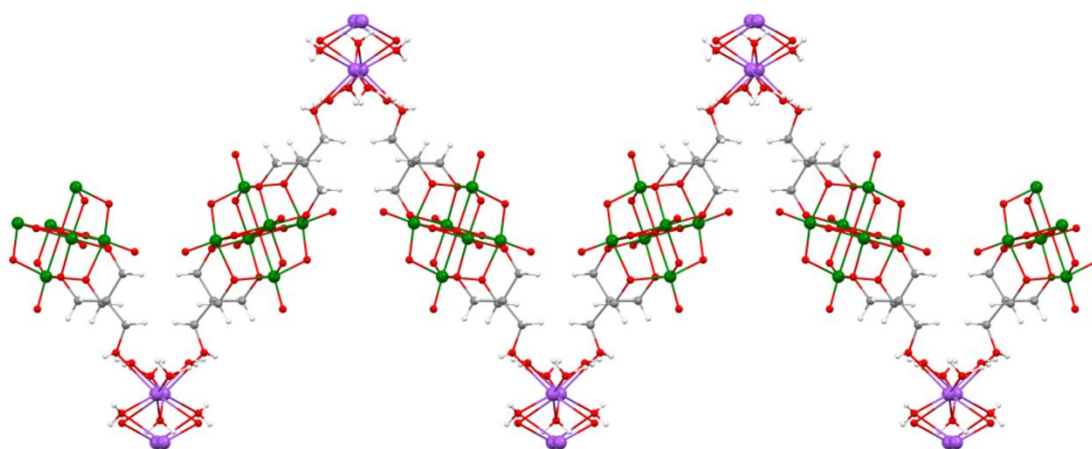


Figure 3.4. V6OH chain along *c* axis.

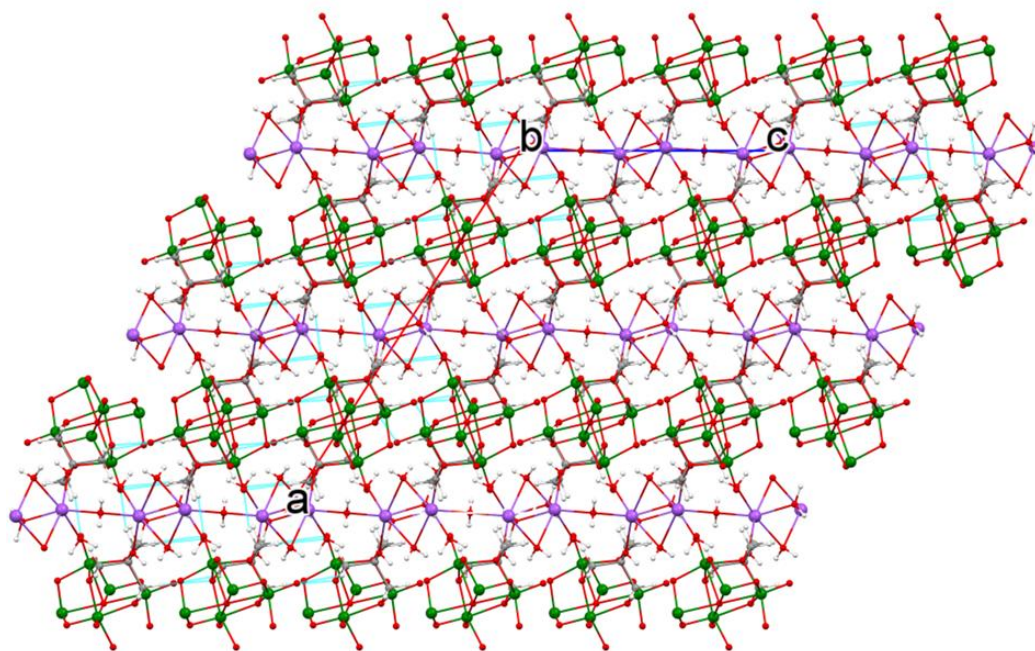


Figure 3.5. Crystal packing along **b** axis in V6OH.

3.3.3 Electron density maps

The planes of 2D density maps have been already defined as the same as for V6-C3 (§ 2.3.3.1). 2D experimental static deformation density and residual density maps of plane 1 for V6 core in V6OH are presented in Figure 3.6. Figure 3.7 presents the deformation density of plane 2 and 3 for functionalization linkage and organic ligand. The residual density in the corresponding plane is also given. One has to notice that there are significant residual density centered on the vanadium atoms. Up to now, attempts to reduce this density failed. That is why we use the adjective *preliminary* for the title of this chapter.

3.3.4 Topological analysis of the total electron density

Topological parameters of the total electron density for the (3,-1) bond critical points (BCPs) of V-O bonds in V6 core and of are given in Table 3.5. Topological parameters of the electron density for the (3,-1) bond critical points (BCPs) in the functionalized linkage and organic ligand are given in Table 3.6.

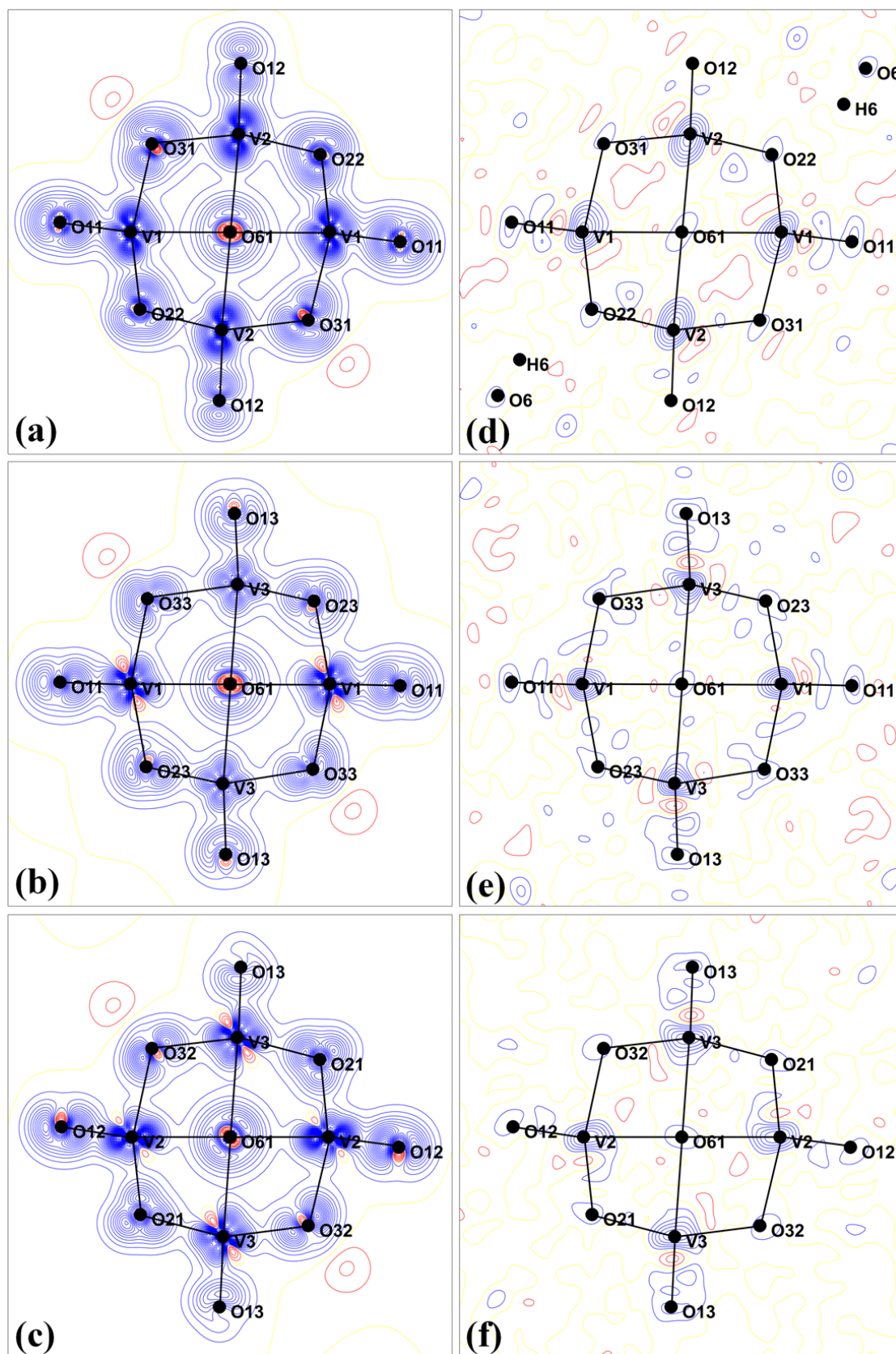


Figure 3.6. 2D static deformation electron density ($0.05 \text{ e}\text{\AA}^{-3}$) and residual density ($0.1 \text{ e}\text{\AA}^{-3}$, resolution range, cutoff $0 - 0.80 \text{ \AA}^{-1}$) maps of plane 1 for V6 core in V6OH. Positive and negative contours are in blue and red.

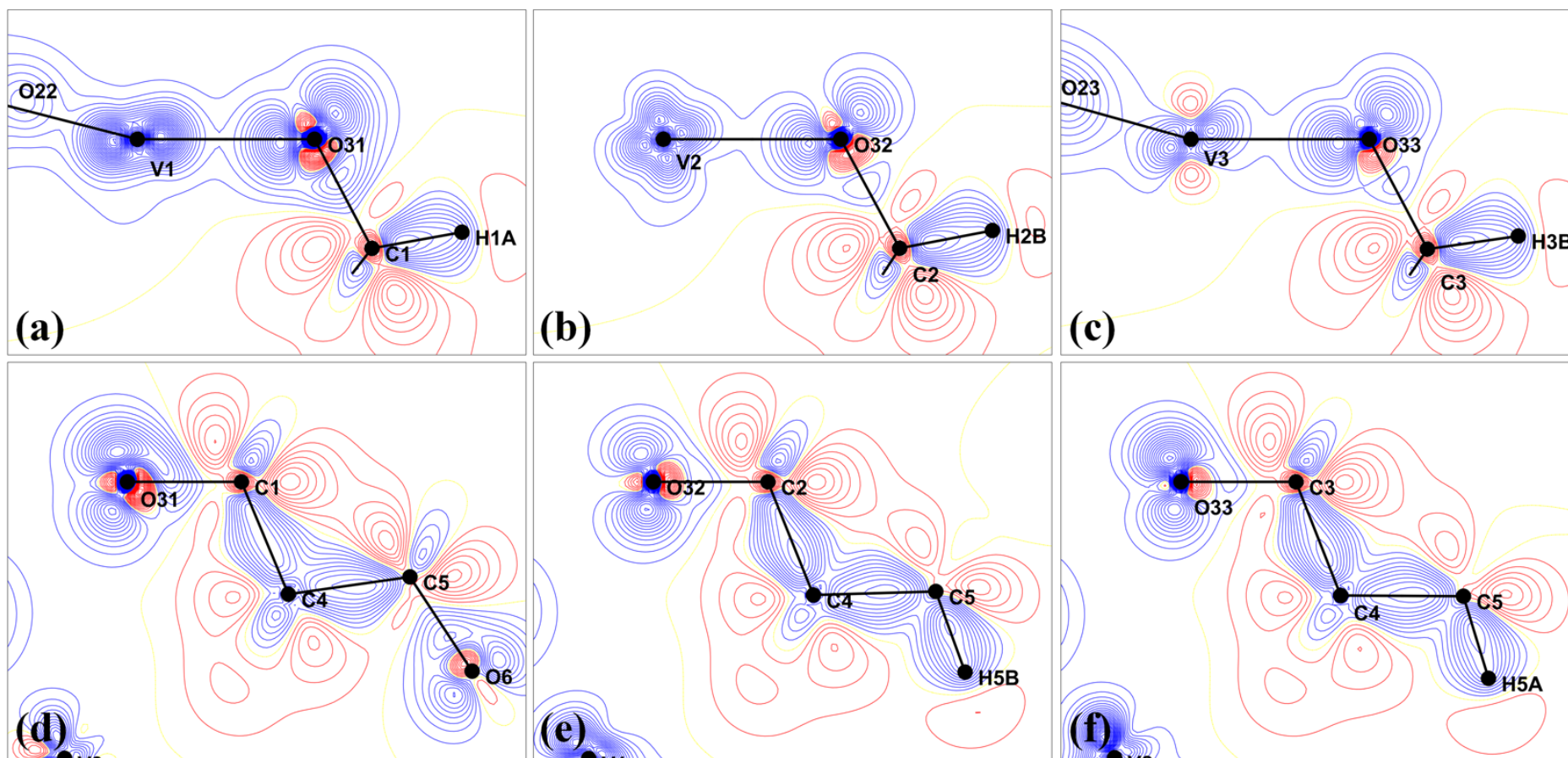


Figure 3.7. 2D static deformation electron density maps for plane 2 (above) and plane 3 (below) in V6OH. Contour intervals are $0.05 \text{ e}\text{\AA}^{-3}$. Positive and negative contours are in blue and red.

Table 3.5. Results of the topological analysis of charge density at (3,-1) bond critical point (BCP) of V6 core in functionalized V6OH. $\rho(\mathbf{r}_c)$ is the electron density at the BCP ($e\text{\AA}^{-3}$), $\nabla^2\rho(\mathbf{r}_c)$ is Laplacian of the total density at the BCP ($e\text{\AA}^{-5}$), the ε is ellipticity, λ_1 , λ_2 , λ_3 are the eigenvalues at the BCP, $G(\mathbf{r}_c)$, $V(\mathbf{r}_c)$, and $H(\mathbf{r}_c)$ are kinetic energy density, local energy density, and the total energy density respectively (the unit is au, equal to $e\text{Bohr}^{-5}$)

Type	Bond	d_{12}	d_{1-bcp}	$\rho(\mathbf{r}_c)$	$\nabla^2\rho(\mathbf{r}_c)$	λ_1	λ_2	λ_3	ε	$G(\mathbf{r}_c)$	$V(\mathbf{r}_c)$	$H(\mathbf{r}_c)$
V-O1x	V1-O11	1.607	0.846	1.747	32.97	-13.33	-13.14	59.44	0.014	0.530	-0.718	-0.188
	V2-O12	1.609	0.851	1.737	33.12	-13.66	-13.42	60.20	0.018	0.528	-0.713	-0.185
	V3-O13	1.597	0.852	1.646	32.75	-12.28	-12.17	57.20	0.009	0.500	-0.660	-0.160
V-O2x	V1-O22	1.761	0.915	1.150	23.09	-8.07	-8.04	39.20	0.004	0.310	-0.381	-0.071
	V1-O23	1.907	0.978	0.685	14.48	-3.96	-3.92	22.36	0.010	0.164	-0.177	-0.013
	V2-O21	1.761	0.915	1.054	21.8	-7.31	-6.87	35.98	0.064	0.281	-0.336	-0.055
	V2-O22	1.901	0.972	0.737	15.52	-4.53	-4.42	24.47	0.025	0.179	-0.197	-0.018
	V3-O21	1.931	0.989	0.684	14.52	-4.25	-4.21	22.98	0.010	0.164	-0.177	-0.013
	V3-O23	1.772	0.920	1.048	21.68	-7.07	-6.86	35.61	0.031	0.279	-0.333	-0.054
V-O3x	V1-O31	2.052	1.035	0.522	11.16	-2.96	-2.86	16.98	0.035	0.117	-0.119	-0.002
	V1-O33	1.965	1.003	0.602	12.78	-3.57	-3.48	19.82	0.026	0.140	-0.146	-0.007
	V2-O31	1.969	0.995	0.648	13.67	-3.86	-3.79	21.32	0.018	0.152	-0.163	-0.011
	V2-O32	2.055	1.040	0.474	10.24	-2.63	-2.51	15.38	0.048	0.105	-0.104	0.001
	V3-O32	1.945	0.994	0.668	14.32	-4.19	-3.96	22.47	0.058	0.160	-0.171	-0.011
	V3-O33	2.063	1.044	0.466	10.04	-2.56	-2.49	15.09	0.028	0.103	-0.102	0.001
V-O6x	V1-O61	2.245	1.129	0.289	6.05	-1.28	-1.27	8.60	0.008	0.057	-0.051	0.006
	V2-O61	2.215	1.117	0.319	6.83	-1.50	-1.49	9.82	0.007	0.065	-0.059	0.006
	V3-O61	2.248	1.128	0.290	6.04	-1.30	-1.29	8.63	0.008	0.057	-0.051	0.006

Table 3.6. Results of the topological analysis of charge density at (3,-1) bond critical point (BCP) of organic ligand in functionalized V6OH. $\rho(\mathbf{r}_c)$ is the electron density at the BCP ($e\text{\AA}^{-3}$), $\nabla^2\rho(\mathbf{r}_c)$ is Laplacian of the total density at the BCP ($e\text{\AA}^{-5}$), the ε is ellipticity, $\lambda_1, \lambda_2, \lambda_3$ are the eigenvalues at the BCP, $G(\mathbf{r}_c)$, $V(\mathbf{r}_c)$, and $H(\mathbf{r}_c)$ are kinetic energy density, local energy density, and the total energy density respectively (au).

Type	Bond	d_{12}	d_{1-bcp}	$\rho(\mathbf{r}_c)$	$\nabla^2\rho(\mathbf{r}_c)$	λ_1	λ_2	λ_3	ε	$G(\mathbf{r}_c)$	$V(\mathbf{r}_c)$	$H(\mathbf{r}_c)$
Cx-O3x	C1-O31	1.431	0.565	1.662	-8.15	-11.98	-11.80	15.63	0.015	0.222	-0.528	-0.306
	C2-O32	1.438	0.590	1.573	-6.06	-11.26	-11.20	16.41	0.005	0.211	-0.486	-0.274
	C3-O33	1.442	0.596	1.549	-5.53	-11.12	-11.01	16.61	0.010	0.209	-0.475	-0.266
C-O	C5-O1	1.423	0.560	1.717	-8.94	-12.34	-10.50	13.90	0.175	0.231	-0.556	-0.324
Cx-C4	C1-C4	1.530	0.763	1.633	-10.54	-11.29	-11.06	11.81	0.021	0.197	-0.503	-0.306
	C2-C4	1.532	0.753	1.686	-11.52	-12.03	-11.39	11.90	0.056	0.205	-0.529	-0.324
	C3-C4	1.534	0.754	1.680	-11.45	-12.03	-11.32	11.90	0.063	0.204	-0.526	-0.323
C-C	C4-C5	1.542	0.764	1.642	-10.36	-11.10	-10.90	11.65	0.018	0.200	-0.508	-0.308
O-H	O6-H6	0.954	0.758	2.278	-34.09	-36.95	-36.16	39.02	0.022	0.234	-0.822	-0.588
C-H	C1-H1A	1.072	0.739	1.751	-16.96	-17.49	-16.72	17.25	0.046	0.186	-0.548	-0.362
	C1-H1B	1.105	0.760	1.659	-14.71	-16.04	-15.50	16.82	0.035	0.175	-0.503	-0.328
	C2-H2A	1.082	0.745	1.724	-16.31	-17.11	-16.32	17.12	0.048	0.182	-0.534	-0.352
	C2-H2B	1.102	0.758	1.667	-14.93	-16.23	-15.55	16.84	0.044	0.176	-0.507	-0.331
	C3-H3B	1.076	0.742	1.739	-16.67	-17.39	-16.48	17.19	0.055	0.184	-0.542	-0.357
	C3-H3A	1.106	0.761	1.656	-14.67	-16.07	-15.39	16.79	0.044	0.175	-0.502	-0.327
	C5-H5A	1.081	0.738	1.758	-15.77	-16.90	-16.30	17.43	0.037	0.196	-0.556	-0.360
C5-H5B	1.078	0.736	1.761	-15.88	-17.07	-16.22	17.41	0.052	0.196	-0.557	-0.361	

3.3.5 Atomic net charge

The atomic net charges of all atoms in V6OH are listed in Table 3.7.

Table 2.11. Experimental atomic net charge (*e*) and κ values of the functionalized V6 core.

Atom	Type	Initial charge	κ refinement		AIM charge	
			κ	charge	charge	average
V1	VII	+2.000	1.080	+1.984	+1.751	+1.754
V2		+2.000	1.069	+1.900	+1.747	
V3		+2.000	1.065	+2.001	+1.763	
O11	O1x	-0.737	0.959	-0.879	-0.747	-0.615
O12		-0.737	0.971	-0.697	-0.547	
O13		-0.737	0.970	-0.703	-0.552	
O21	O2x	-0.737	0.968	-0.807	-0.752	-0.772
O22		-0.737	0.968	-0.890	-0.779	
O23		-0.737	0.963	-0.883	-0.786	
O31	O3x	-0.737	0.953	-0.956	-1.137	-1.012
O32		-0.737	0.966	-0.760	-0.941	
O33		-0.737	0.968	-0.761	-0.957	
O61	O6x	-0.737	0.944	-1.176	-1.089	-1.089
O1	O (O-H)	0.000	0.976	-0.501	-1.289	-
C(1)	C	0.000	1.032	0.188	0.305	-
C(2)		0.000	1.032	0.188	0.276	-
C(3)		0.000	1.032	0.188	0.289	-
C(4)		0.000	1.024	0.041	-0.008	-
C(5)		0.000	1.007	0.016	0.110	-
H(1A)	H	0.000	1.125	0.122	0.158	-
H(1B)		0.000	1.125	0.122	0.159	-
H(2A)		0.000	1.125	0.122	0.157	-
H(2B)		0.000	1.125	0.122	0.157	-
H(3B)		0.000	1.125	0.122	0.158	-
H(3A)		0.000	1.125	0.122	0.164	-
H(5A)		0.000	1.115	0.021	0.104	-
H(5B)		0.000	1.115	0.021	0.103	-
H(6)		0.000	1.127	0.145	0.609	-
Sum charge of V6 core		-2.000	-4.078		-4.960	
Sum charge of Organic ligand		0.000	2.078		2.904	
Sum charge of V6OH anion		-2.000	-2.000		-2.056	

3.3.6 Electrostatic potential

Electrostatic potential of $[V_6OH]^{2-}$ is presented in Figure 3.8.

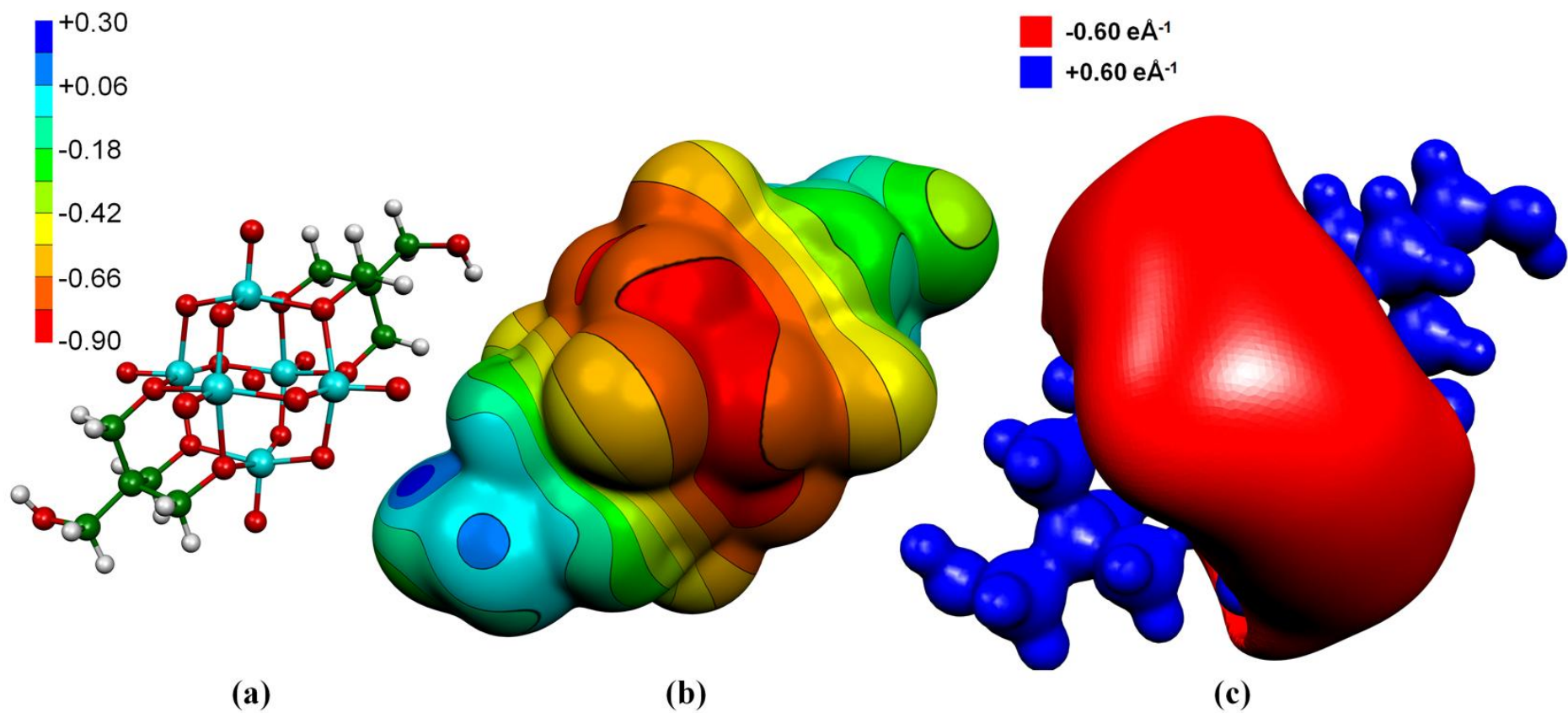


Figure 3.8. Experimental electrostatic potential of $[V_6OH]^{2-}$. (a) Structure of $[V_6OH]^{2-}$; (b) EP ($e.\text{\AA}^{-1}$) mapped on isodensity surface ($0.007 e.A^{-3}$); (c) EP isovalue surface with cutoff $\pm 0.60 e.A^{-1}$.

3.4 Discussion and conclusion

The high residual density around V atoms in V6OH indicates that there are some problems with the multipole refinement or the absorption correction. Though there are some problems with refinement, the results from charge density determination can also provide us the important electronic and topological information about chemical bonding and chemical reactivity. This will be discussed in chapter 5.

**4. THEORETICAL CHARGE DENSITY
ANALYSIS OF FUNCTIONALIZED
HEXAVANADATES AND
DECAVANADATE**

4.1 Introduction

In this chapter, three different types of POV compounds (isolated POVs, short functionalized V6, and long functionalized V6) are chosen for DFT calculations in order to understand the electronic, electrostatic and topological properties. The computational methods are described in section 4.2. Based on the computed density, the related properties are presented in section 4.3. In section 4.4, the discussion is focused on the theoretical calculation results, and conclude which computational method is suitable for the chosen POVs.

4.2 Computational methods

4.2.1 Model structures

4.2.1.1 Functionalized V6-C3

The crystal packing analysis indicates that there are six TBA cations and two adjacent $[\text{V6-C3}]^{2-}$ around the central $[\text{V6-C3}]^{2-}$. Therefore three model structures (Figure 4.1) have been chosen for DFT calculations in order to understand the differences of electronic, electrostatic and topological properties between the isolated $[\text{V6-V3}]^{2-}$ (model 1) and the $[\text{V6-C3}]^{2-}$ anion in crystalline environment (model 2 and 3).

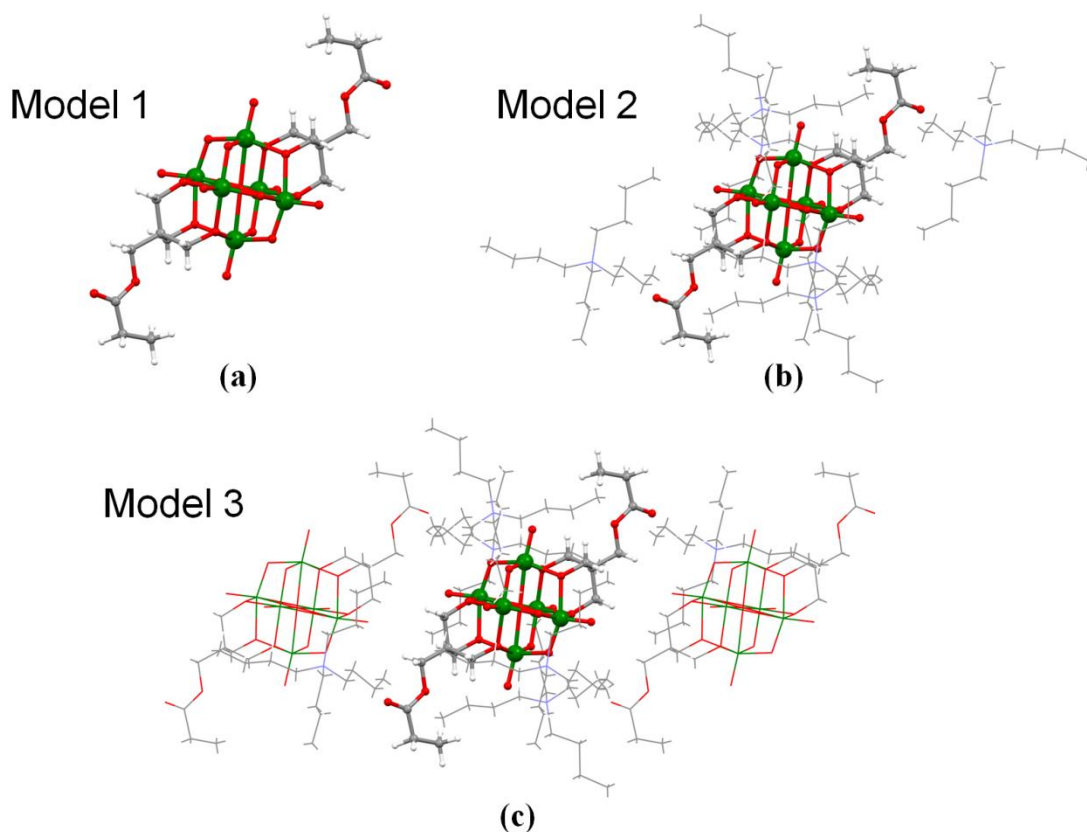


Figure 4.1. Three models of V6-C3 in DFT calculation. (a) Model 1, isolated functionalized V6-C3 anion, $[V6-C3]^{2-}$; (b) Model 2, six TBA around the center $[V6-C3]^{2-}$; (c) Model 3, the central $[V6-C3]^{2-}$ in the real crystalline environment.

However, because of the following reasons, only model 1 has been chosen for DFT calculations presented in this manuscript:

- (1) The non covalent interactions between the central $[V6-C3]^{2-}$ and the surrounding molecules are weak C-H \cdots O bonds (see § 2.3.4.4, Table 2.10);
- (2) In the literatures, the isolated model without counter cation were chosen for DFT calculations [Kempf, 1992; Schulz, 2010];
- (3) Due to the huge size of model 2 and 3, the calculations in Gaussian cost too much time and memory.
- (4) A technical reason prevented us from plotting the electrostatic potential only around the central $[V6-C3]^{2-}$ in model 2 and 3.

4.2.1.2 List of the model structures for computational study

It is impossible to analyze all functionalized V6 compounds by experimental charge density study for the following reasons: i) the rarity of single crystal with high quality for charge density determination experiment; ii) the long time-consuming for

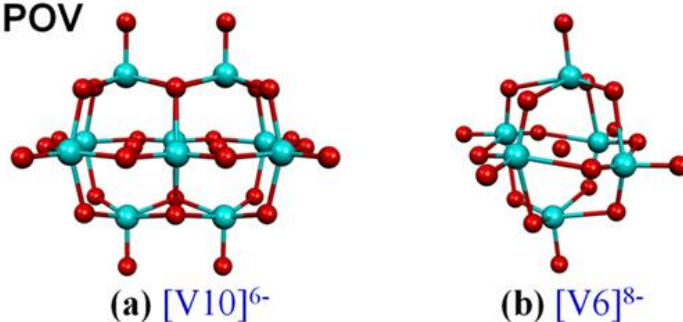
solving the problems in charge density refinement and data processing. Based on the sufficient chemical information obtained from experimental charge density analysis of three POV compounds (V10, V6-C3, V6OH), we have selected three different types of functionalized V6 series for studying the theoretical electron density and their topological properties (Figure 4.2). The three types of functionalized V6 compounds, depending of the structural features, can represent the reported functionalized V6 in Table 1.2, chapter 1.

Type I, isolated pure inorganic POVs. There are two species, $[\text{V10}]^{6-}$ ($[\text{V}_{10}\text{O}_{28}]^{6-}$), and $[\text{V6}]^{8-}$ ($[\text{V}_6\text{O}_{19}]^{8-}$), without the covalent-bonded organic ligands;

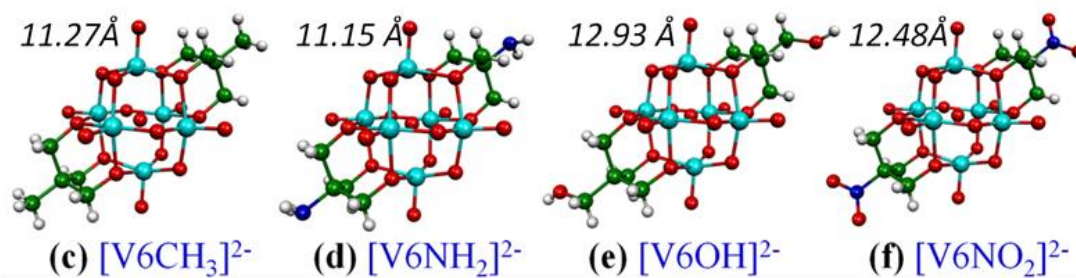
Type II, short functionalized V6 series. The type is defined as the short rigid length of the functionalized V6 anions ($< 13 \text{ \AA}$);

Type III, long functionalized V6 series. The rigid length of the functionalized V6 anions is $> 13 \text{ \AA}$. The lengths for each functionalized V6 anion are marked in Figure 4.2.

I. Isolated POV



II. Short functionalized V6 series



III. Long functionalized V6 series

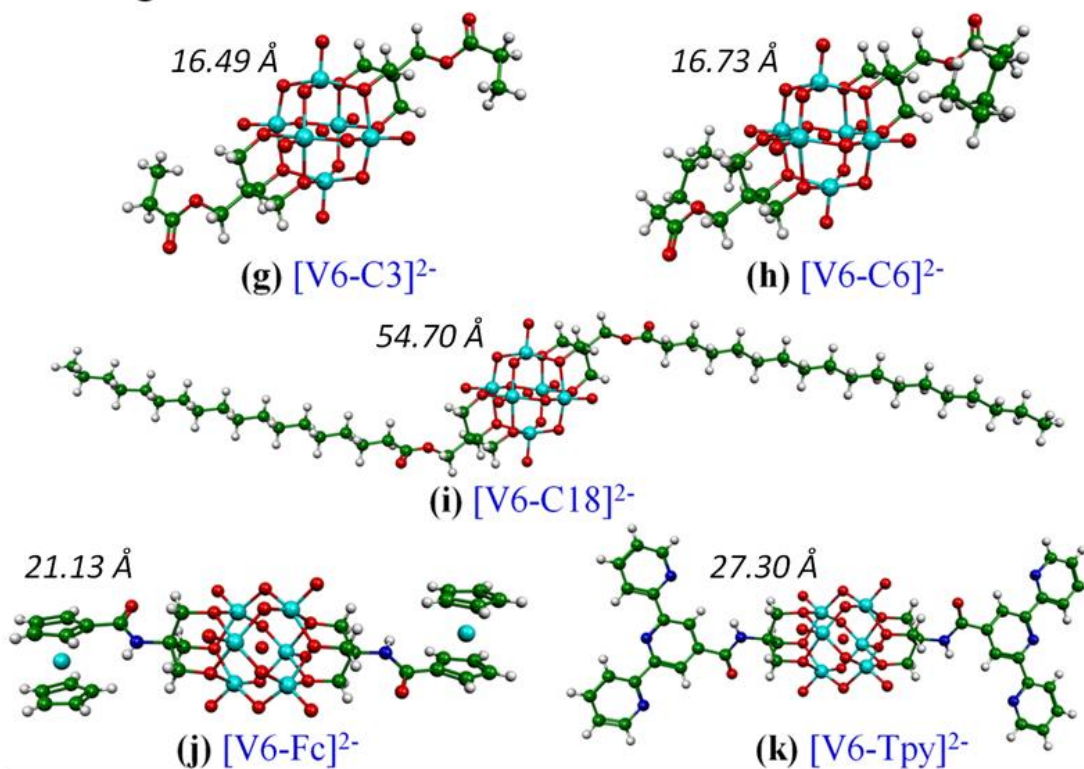


Figure 4.2. Three types of functionalized V6 compounds. CSD refcode: (c) VERDEB10, [Chen, 1992b]; (d) SAJWIL, [Li, 2011]; (f) VERDAX10, [Chen, 1992b]; (h) OQETUA, [Wu, 2011a]; (i) EMIFEM, [Wu, 2011a]; (j) WAFVUW, [Schulz, 2010]; (k) UCOTEN, [Santoni, 2011].

4.2.2 Computational details

DFT calculations were performed with Gaussian 09 (EM64L-G09RevC.01) [Frisch, 2010]. To understand how computational methods affect the density and related properties from theoretical electron density, different functionals and basis sets are employed in DFT calculation (Table 4.1). All the functionals are the hybrid functionals, which include a mixture of Hartree-Fock exchange with DFT exchange-correlation (B3LYP: [Becke, 1993]; M06/M06-2X, [Zhao, 2008]; B3PW91: [Perdew, 1986]). The basis sets take into account polarization and the diffuse functions (6-31+G(d, p): [Rassolov, 2001]; 6-311+G(d, p)/ 6-311++G(d, p): [Binning, 1990]; cc-pVTZ: [Dunning, 1989]).

The atomic coordinates of $[\text{V}_{10}\text{O}_{28}]^{6-}$ [Bošnjaković-Pavlović, 2008], $[\text{V}_6\text{OH}]^{2-}$ (chapter 3), and $[\text{V}_6\text{-C}_3]^{2-}$ (chapter 2) are obtained from the corresponding high resolution X-ray diffraction experimental nuclei positions, without geometrical optimization. Due to the fact that the isolated $[\text{V}_6\text{O}_{19}]^{8-}$ does not exist in crystalline state, its atomic coordinates are built from V6-C3 after removing the organic ligands. The geometry has been optimized by M06/6-31+G(d, p). The atomic coordinates of other V6 series are obtained from CSD, (refcodes and references are given in Table 1.2, chapter 1, with the geometrical optimization at 6-31+G(d, p) level. The computed densities are converged at cc-pVTZ level, except $[\text{V}_6\text{-C}_{18}]^{2-}$, which is converged at 6-311+G(d, p) level because the density cannot be converged at cc-pVTZ level in a reasonable time.

From Gaussian fchk file, a subsequent topological analysis and AIM charges are performed with AIMAll (Version 14.11.23) [Keith, 2014].

Based on Gaussian calculations, theoretical deformation density maps have been generated as a difference between the total theoretical electron density for a system and that derived from the Clementi's promolecule [Clementi, 1974]. Theoretical Laplacian of the total electron density maps and the density ρ and Laplacian $\nabla^2\rho$ along the bond path are computed by Cubegen and Multiwfn [Lu, 2012] utility codes together with Mathematica additional routines.

Table 4.1. Functionals and basis sets employed in DFT calculations by Gaussian 09.

Type	Structure	Functional	Basis set	Total energy (au)	
I	$[\text{V}_6\text{O}_{19}]^{8-}$	M06	6-31+G(d, p) ^[a]	-7090.45	
		B3LYP	6-31+G(d, p)	-7091.43	
		M06	cc-pVTZ ^[b]	-7091.48	
II	$[\text{V}_6\text{CH}_3]^{2-}$	M06-2X	6-31+G(d, p) ^[a]	-7484.85	
		M06-2X	cc-pVTZ ^[b]	-7485.73	
	$[\text{V}_6\text{NH}_2]^{2-}$	M06	6-31+G(d, p) ^[a]	-7516.77	
		M06	cc-pVTZ ^[b]	-7517.79	
	$[\text{V}_6\text{OH}]^{2-}$	M06-2X	6-31G(d, p)	-7635.08	
		M06-2X	6-31+G(d, p)	-7634.85	
		M06-2X	cc-pVTZ ^[b]	-7636.15	
	$[\text{V}_6\text{NO}_2]^{2-}$	M06-2X	6-31+G(d, p) ^[a]	-7814.99	
		M06-2X	cc-pVTZ ^[b]	-7816.24	
	III	$[\text{V}_6\text{-C3}]^{2-}$	M06-2X	6-31G(d, p)	-8018.56
M06-2X			6-31+G(d, p)	-8018.66	
M06			6-31+G(d, p)	-8018.73	
M06-2X			6-311++G(d, p)	-8019.66	
M06-2X			cc-pVTZ ^[b]	-8020.09	
B3PW91			6-31+G(d, p)	-8018.97	
M06			cc-pVTZ ^[b]	-8019.87	
B3PW91			cc-pVTZ	-8020.26	
$[\text{V}_6\text{-C6}]^{2-}$		M06-2X	6-31+G(d, p) ^[a]	-8254.67	
		M06	6-31+G(d, p)	-8254.66	
		M06-2X	cc-pVTZ ^[b]	-8256.25	
$[\text{V}_6\text{-C18}]^{2-}$		M06	6-31+G(d, p)	-9195.79	
		M06-2X	6-31+G(d, p) ^[a]	-9196.06	
		M06-2X	6-311+G(d, p) ^[b]	-9197.37	
$[\text{V}_6\text{-TPY}]^{2-}$		M06-2X	6-31+G(d, p) ^[a]	-9224.15	
		M06-2X	6-311++G(d, p)	-9226.28	
		M06-2X	cc-pVTZ ^[b]	-9226.84	
I		$[\text{V}_{10}\text{O}_{28}]^{6-}$	B3LYP	6-31+G(d, p)	-11546.70
			M06	6-31+G(d, p)	-11545.28
			M06	cc-pVTZ ^[b]	-11544.14
	TBA cation ^[c]	M06-2X	6-31+G(d, p)	-684.94	
		M06-2X	cc-pVTZ ^[b]	-685.20	

[a] geometry optimization level;

[b] computed density level;

[c] Atomic coordinates from TBA cation of V6-C3 in chapter 2.

4.3 Results

4.3.1 Theoretical electron density maps

4.3.1.1 Electron density maps of V-O bonding in functionalized V6-C3 anion

The theoretical deformation density and Laplacian of total electron density for planes 1, 2 are presented in Figure 4.3, 4.4 respectively.

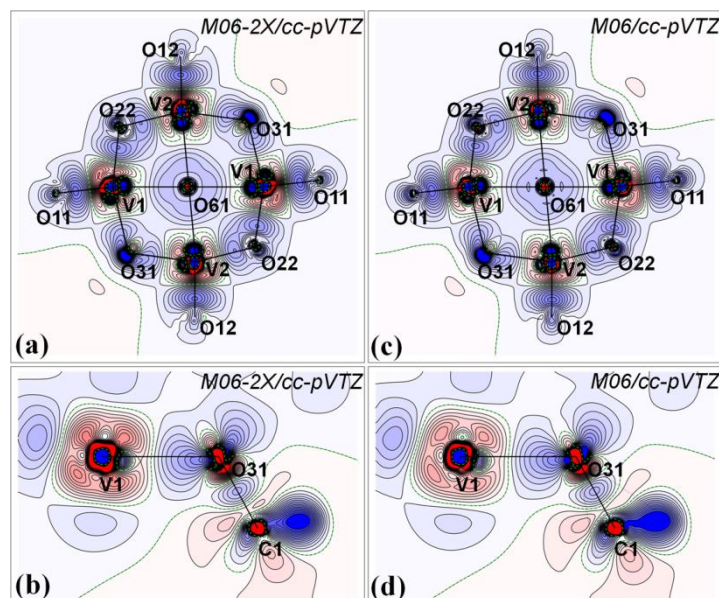


Figure 4.3. Theoretical 2D deformation electron density maps for plane 1, 2 defined in chapter 2. Contour intervals are $0.05 e\text{\AA}^{-3}$. Positive and negative contours are in blue and red respectively. The computational details are indicated.

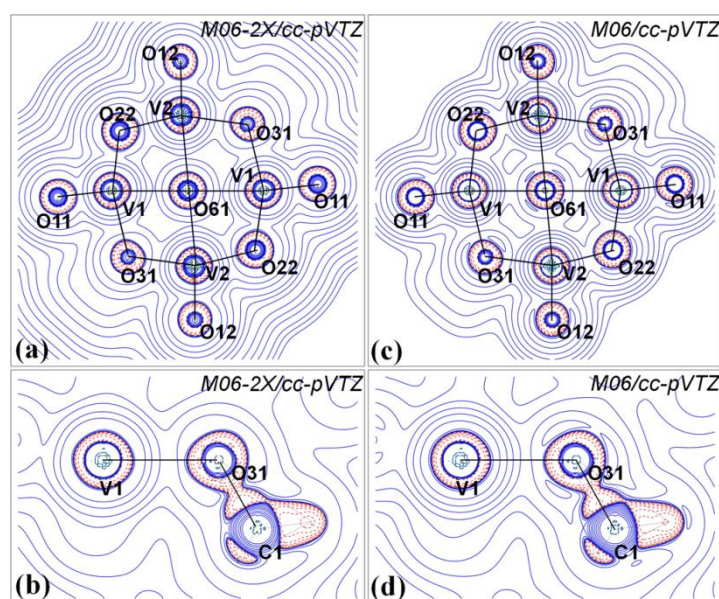


Figure 4.4. Theoretical 2D Laplacian of total electron density maps for plane 1, 2. Contour intervals are $\pm 2, 4, 8 \times 10^n e\text{\AA}^{-5}$ ($n = -1, 0, 1, 2$). The computational details are indicated.

4.3.1.2 Electron density maps of organic ligand and TBA cation

The theoretical deformation density and Laplacian of total electron density for plane 3, 4, 5 are presented in Figure 4.5, 4.6 respectively.

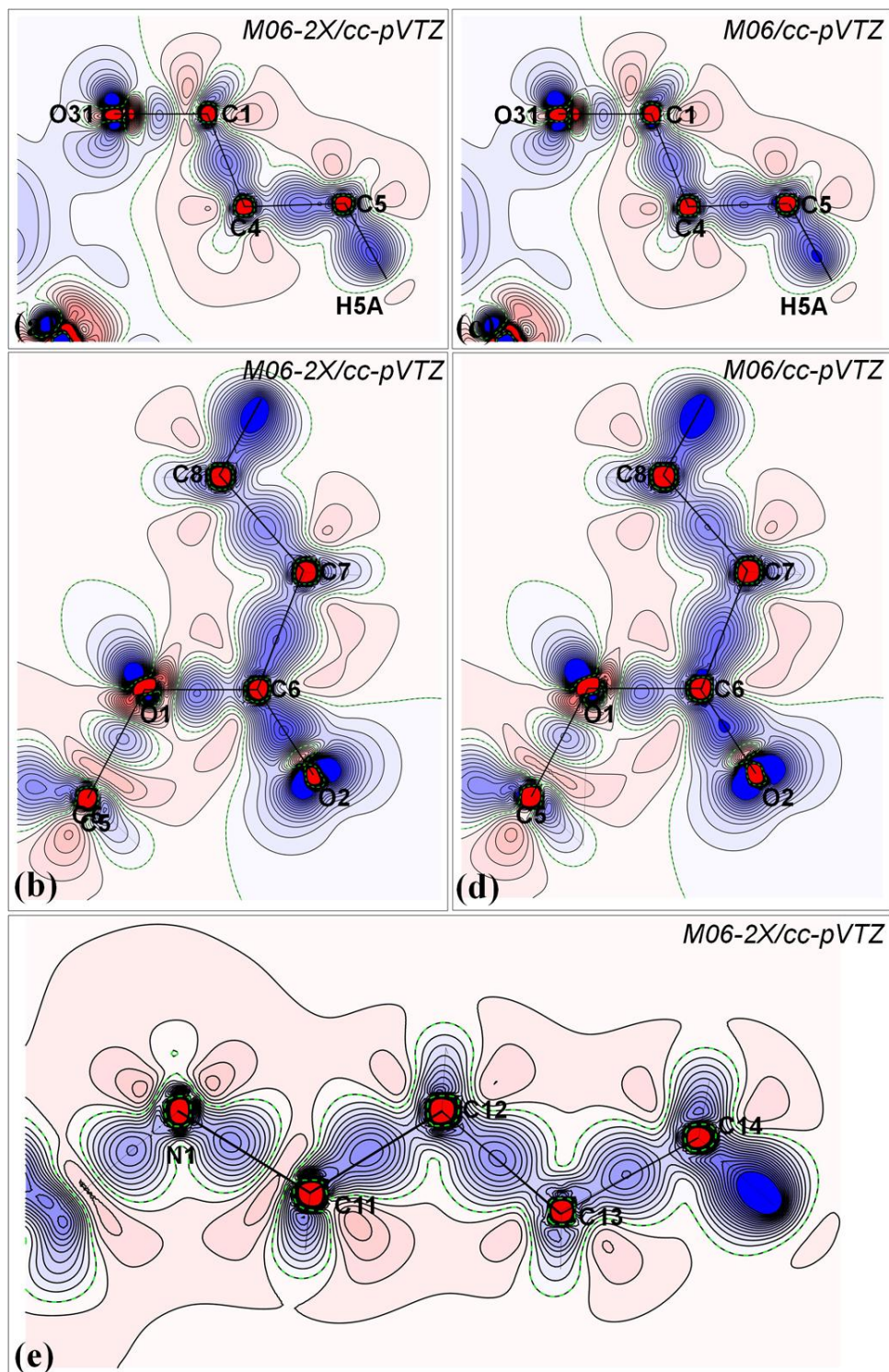


Figure 4.5. Theoretical 2D deformation electron density maps for plane 3, 4, 5 defined in chapter 2. Contour intervals are $0.05 \text{ e}\text{\AA}^{-3}$. Positive and negative contours are in blue and red.

The computational details are indicated.

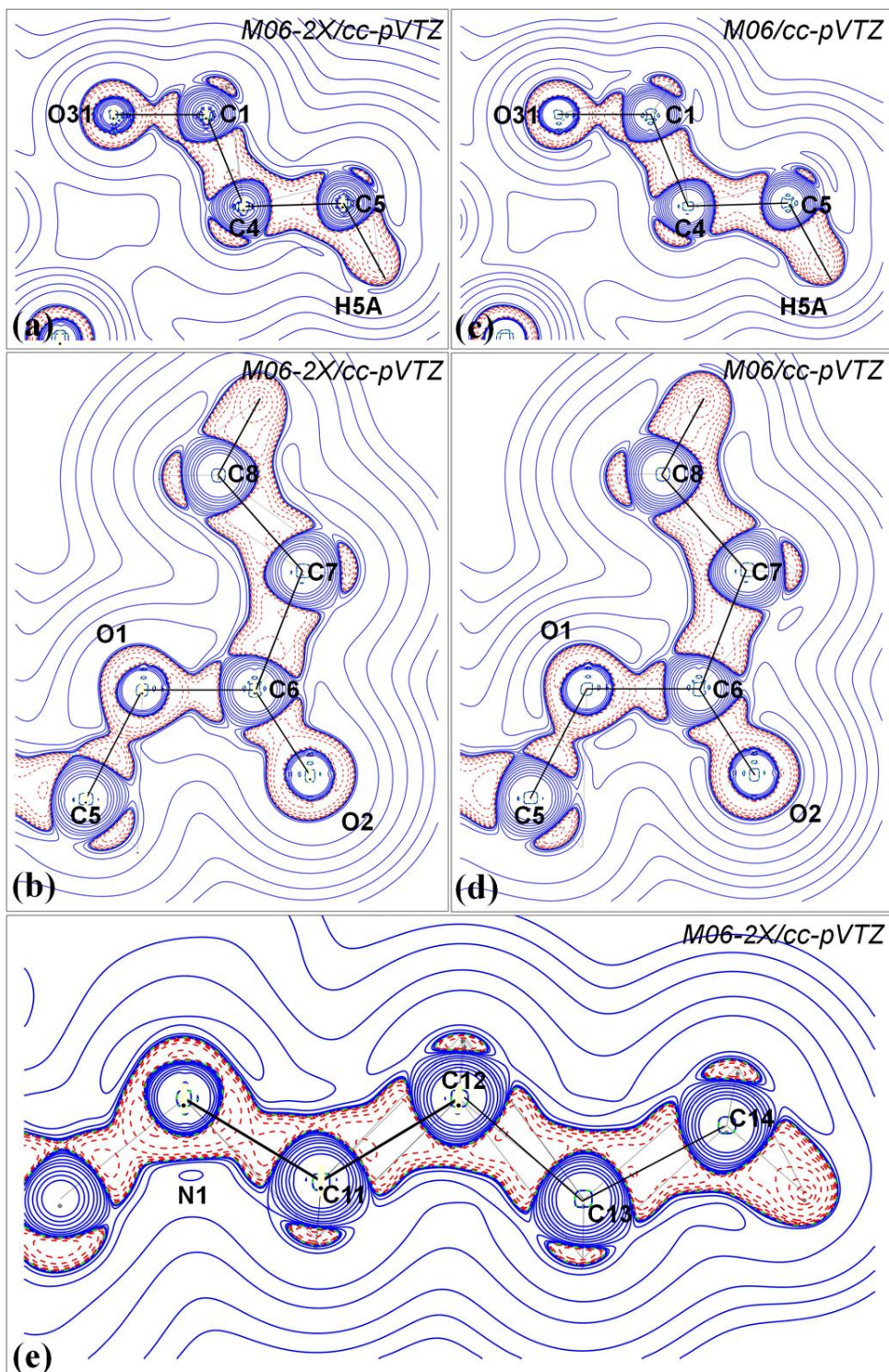


Figure 4.6. Theoretical 2D Laplacian of total electron density maps for plane 3, 4, 5 defined in chapter 2. Contour intervals are $\pm 2, 4, 8 \cdot 10^n \text{ e}\text{\AA}^{-5}$ ($n = -1, 0, 1, 2$). The computational details are indicated.

4.3.1.3 Electron density maps of V10 anion

The theoretical deformation density and Laplacian of total electron density for V10 anion are presented in Figure 4.7.

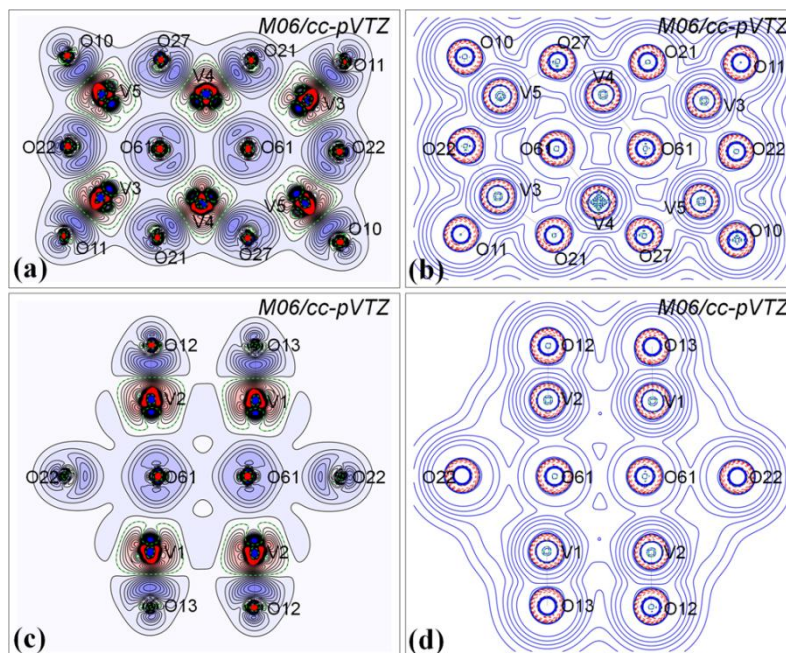


Figure 4.7. Theoretical 2D deformation electron density (contour intervals are $0.05 e\text{\AA}^{-3}$) and Laplacian of total electron density maps (Contour intervals are $\pm 2, 4, 8 \times 10^n e\text{\AA}^{-5}$ ($n = -1, 0, 1, 2$)) for horizontal and vertical-XZ plane in V10. The computational details are indicated.

4.3.2 Theoretical topological analysis

4.3.2.1 Theoretical topological parameters of functionalized V6 series

The theoretical topological parameters of: i) V-O in isolated $[\text{V6}]^{8-}$ are listed in Table 4.3; ii) V-O in $[\text{V6-C3}]^{2-}$ by M06/cc-pVTZ and M06-2X/cc-pVTZ are listed in Table 4.4, Table 4.6; iii) C-O and C-C bonds in $[\text{V6-C3}]^{2-}$ are listed in Table 4.5, 4.7. The theoretical topological parameters of other functionalized V6 mentioned in figure 2 are listed in Appendix.

4.3.2.2 Theoretical topological parameters of V10 anion

The theoretical topological parameters of V-O in isolated $[\text{V10}]^{6-}$ are listed in Table 4.8.

4.3.2.3 Theoretical topological parameters of TBA cation

The theoretical topological parameters of TBA cation are listed in Table 4.9.

Table 4.3. Theoretical topological analysis of charge density at (3,-1) bond critical point (BCP) for isolated $[V_6]^{8-}$ by M06/cc-pVTZ.

Type	Bond	d_{12}	$\rho(r_c)$	$\nabla^2\rho(r_c)$	λ_1	λ_2	λ_3	ϵ	$G(r_c)$	$V(r_c)$	$H(r_c)$
V-O1x	V1-O11	1.682	1.464	19.22	-10.45	-9.89	39.56	0.056	0.358	-0.516	-0.158
	V2-O12	1.682	1.464	19.22	-10.45	-9.89	39.56	0.056	0.358	-0.516	-0.158
	V3-O13	1.682	1.464	19.22	-10.45	-9.89	39.56	0.056	0.358	-0.516	-0.158
V-O2x	V1-O22	1.686	1.448	18.85	-10.33	-9.80	38.97	0.054	0.351	-0.507	-0.156
	V1-O23	1.686	1.448	18.85	-10.33	-9.80	38.97	0.054	0.351	-0.507	-0.156
	V2-O21	1.686	1.448	18.85	-10.33	-9.80	38.97	0.054	0.351	-0.507	-0.156
	V2-O22	1.730	1.258	17.94	-8.38	-8.26	34.58	0.015	0.299	-0.411	-0.113
	V3-O21	1.730	1.258	17.94	-8.38	-8.26	34.58	0.015	0.299	-0.411	-0.113
	V3-O23	1.730	1.258	17.94	-8.38	-8.26	34.58	0.015	0.299	-0.411	-0.113
	V1-O31	2.261	0.309	4.69	-1.44	-1.41	7.55	0.025	0.049	-0.050	-0.001
	V1-O33	2.261	0.309	4.69	-1.44	-1.41	7.55	0.025	0.049	-0.050	-0.001
	V2-O31	2.261	0.309	4.69	-1.44	-1.41	7.55	0.025	0.049	-0.050	-0.001
	V2-O32	2.301	0.277	4.18	-1.24	-1.20	6.62	0.037	0.043	-0.042	0.000
	V3-O32	2.301	0.277	4.18	-1.24	-1.20	6.62	0.037	0.043	-0.042	0.000
	V3-O33	2.301	0.277	4.18	-1.24	-1.20	6.62	0.037	0.043	-0.042	0.000
V-O6x	V1-O61	2.345	0.269	3.69	-1.10	-1.09	5.88	0.016	0.039	-0.039	-0.001
	V2-O61	2.345	0.269	3.69	-1.10	-1.09	5.88	0.016	0.039	-0.039	-0.001
	V3-O61	2.345	0.269	3.69	-1.10	-1.09	5.88	0.016	0.039	-0.039	-0.001

Table 4.4. Theoretical topological analysis of charge density at (3,-1) bond critical point (BCP) of V6 core in functionalized V6-C3 by M06/cc-pVTZ.

Type	Bond	d_{12}	$\rho(\mathbf{r}_c)$	$\nabla^2\rho(\mathbf{r}_c)$	λ_1	λ_2	λ_3	ϵ	$\mathbf{G}(\mathbf{r}_c)$	$\mathbf{V}(\mathbf{r}_c)$	$\mathbf{H}(\mathbf{r}_c)$
V-O1x	V1-O11	1.607	1.794	24.21	-12.64	-12.55	49.40	0.007	0.483	-0.715	-0.232
	V2-O12	1.609	1.783	23.99	-12.55	-12.45	48.98	0.008	0.478	-0.708	-0.229
	V3-O13	1.610	1.781	23.97	-12.52	-12.42	48.91	0.008	0.477	-0.706	-0.229
V-O2x	V1-O22	1.779	1.121	15.59	-7.53	-7.11	30.23	0.060	0.252	-0.342	-0.090
	V1-O23	1.784	1.109	15.39	-7.44	-7.05	29.88	0.055	0.248	-0.336	-0.088
	V2-O21	1.784	1.109	15.37	-7.42	-7.02	29.82	0.058	0.248	-0.336	-0.088
	V2-O22	1.856	0.913	12.68	-5.85	-5.81	24.33	0.007	0.190	-0.249	-0.059
	V3-O21	1.871	0.880	12.17	-5.58	-5.57	23.32	0.002	0.180	-0.235	-0.054
	V3-O23	1.874	0.875	12.05	-5.53	-5.51	23.09	0.002	0.179	-0.232	-0.054
V-O3x	V1-O31	1.993	0.632	9.42	-3.95	-3.70	17.08	0.067	0.121	-0.144	-0.023
	V1-O33	1.994	0.632	9.41	-3.95	-3.70	17.06	0.067	0.121	-0.143	-0.023
	V2-O31	2.000	0.622	9.27	-3.86	-3.63	16.77	0.065	0.118	-0.140	-0.022
	V2-O32	2.047	0.548	8.41	-3.29	-3.09	14.79	0.066	0.102	-0.116	-0.015
	V3-O32	2.048	0.544	8.40	-3.26	-3.06	14.72	0.067	0.101	-0.115	-0.014
	V3-O33	2.048	0.550	8.34	-3.30	-3.10	14.74	0.067	0.102	-0.117	-0.015
V-O6x	V1-O61	2.238	0.346	5.36	-1.56	-1.55	8.47	0.006	0.057	-0.059	-0.002
	V2-O61	2.240	0.344	5.33	-1.55	-1.54	8.43	0.005	0.057	-0.059	-0.002
	V3-O61	2.245	0.340	5.26	-1.52	-1.52	8.30	0.006	0.056	-0.058	-0.002

Table 4.5. Theoretical topological analysis of charge density at (3,-1) bond critical point (BCP) of organic ligand in functionalized V6-C3 by M06/cc-pVTZ.

Type	Bond	d_{12}	$\rho(r_c)$	$\nabla^2\rho(r_c)$	λ_1	λ_2	λ_3	ε	$G(r_c)$	$V(r_c)$	$H(r_c)$
Cx-O3x	C1-O31	1.424	1.712	-11.51	-11.36	-10.56	10.42	0.076	0.212	-0.544	-0.332
	C2-O32	1.427	1.705	-11.81	-11.29	-10.64	10.11	0.061	0.208	-0.539	-0.331
	C3-O33	1.427	1.708	-12.19	-11.33	-10.83	9.97	0.046	0.207	-0.540	-0.333
C-O	C5-O1	1.332	2.123	-13.25	-17.15	-16.58	20.48	0.035	0.326	-0.790	-0.464
	C6-O1	1.449	1.558	-7.02	-9.24	-8.60	10.82	0.075	0.201	-0.474	-0.274
	C6-O2	1.204	2.862	-8.02	-26.94	-24.29	43.22	0.109	0.632	-1.347	-0.715
C-C	C1-C4	1.534	1.678	-14.77	-12.18	-11.51	8.92	0.058	0.180	-0.513	-0.333
	C2-C4	1.534	1.678	-14.79	-12.13	-11.59	8.93	0.046	0.180	-0.513	-0.333
	C3-C4	1.537	1.667	-14.54	-12.04	-11.42	8.93	0.054	0.179	-0.508	-0.329
	C4-C5	1.525	1.694	-15.37	-12.05	-11.72	8.40	0.028	0.180	-0.520	-0.340
	C6-C7	1.507	1.778	-17.11	-13.52	-12.27	8.68	0.102	0.193	-0.563	-0.370
	C7-C8	1.511	1.686	-15.46	-11.78	-11.69	8.01	0.008	0.178	-0.516	-0.338

Table 4.6. Theoretical topological analysis of charge density at (3,-1) bond critical point (BCP) of V6 core in functionalized V6-C3 by M06-2X/cc-pVTZ.

Type	Bond	d_{12}	$\rho(r_c)$	$\nabla^2\rho(r_c)$	λ_1	λ_2	λ_3	ϵ	$G(r_c)$	$V(r_c)$	$H(r_c)$
V-O1x	V1-O11	1.607	1.842	21.71	-13.04	-12.91	47.66	0.010	0.480	-0.734	-0.255
	V2-O12	1.609	1.831	21.49	-12.94	-12.81	47.25	0.010	0.475	-0.727	-0.252
	V3-O13	1.610	1.828	21.47	-12.92	-12.79	47.18	0.010	0.474	-0.726	-0.251
V-O2x	V1-O22	1.779	1.161	13.59	-7.99	-7.62	29.19	0.049	0.247	-0.353	-0.106
	V1-O23	1.784	1.150	13.41	-7.90	-7.57	28.87	0.044	0.243	-0.347	-0.104
	V2-O21	1.784	1.149	13.40	-7.88	-7.52	28.79	0.047	0.243	-0.347	-0.104
	V2-O22	1.856	0.941	11.36	-6.20	-6.14	23.71	0.010	0.186	-0.255	-0.068
	V3-O21	1.871	0.907	10.94	-5.93	-5.86	22.73	0.013	0.177	-0.240	-0.063
	V3-O23	1.874	0.902	10.83	-5.87	-5.81	22.51	0.010	0.175	-0.238	-0.063
V-O3x	V1-O31	1.993	0.640	9.13	-4.11	-3.84	17.08	0.072	0.120	-0.145	-0.025
	V1-O33	1.994	0.640	9.11	-4.12	-3.84	17.06	0.072	0.120	-0.145	-0.025
	V2-O31	2.000	0.628	9.01	-4.02	-3.75	16.78	0.072	0.117	-0.141	-0.024
	V2-O32	2.048	0.551	8.30	-3.41	-3.19	14.90	0.071	0.102	-0.117	-0.015
	V3-O32	2.049	0.548	8.29	-3.38	-3.16	14.83	0.072	0.101	-0.116	-0.015
	V3-O33	2.048	0.554	8.22	-3.43	-3.20	14.84	0.072	0.101	-0.117	-0.016
V-O6x	V1-O61	2.238	0.344	5.61	-1.58	-1.57	8.76	0.006	0.059	-0.060	-0.001
	V2-O61	2.240	0.342	5.59	-1.57	-1.56	8.72	0.005	0.059	-0.059	-0.001
	V3-O61	2.245	0.338	5.51	-1.55	-1.54	8.59	0.006	0.058	-0.058	-0.001

Table 4.7. Theoretical topological analysis of charge density at (3,-1) bond critical point (BCP) of organic ligand in functionalized V6-C3 by M06-2X/cc - pVTZ.

Type	Bond	d_{12}	$\rho(\mathbf{r}_c)$	$\nabla^2\rho(\mathbf{r}_c)$	λ_1	λ_2	λ_3	ϵ	$\mathbf{G}(\mathbf{r}_c)$	$\mathbf{V}(\mathbf{r}_c)$	$\mathbf{H}(\mathbf{r}_c)$
Cx-O3x	C1-O31	1.424	1.698	-10.39	-10.78	-9.97	10.36	0.082	0.216	-0.540	-0.324
	C2-O32	1.427	1.691	-10.81	-10.73	-10.07	9.99	0.066	0.211	-0.535	-0.323
	C3-O33	1.427	1.695	-11.26	-10.80	-10.29	9.82	0.050	0.209	-0.535	-0.326
C-O	C5-O1	1.449	1.547	-5.40	-8.61	-8.02	11.24	0.073	0.209	-0.475	-0.265
	C6-O1	1.332	2.108	-10.96	-16.78	-16.67	22.49	0.006	0.337	-0.788	-0.451
	C6-O2	1.204	2.855	-3.98	-27.94	-25.52	49.47	0.095	0.657	-1.356	-0.698
C-C	C1-C4	1.534	1.667	-14.54	-11.87	-11.33	8.66	0.048	0.179	-0.508	-0.329
	C2-C4	1.534	1.667	-14.55	-11.84	-11.40	8.69	0.038	0.179	-0.508	-0.329
	C3-C4	1.537	1.656	-14.31	-11.75	-11.25	8.68	0.045	0.177	-0.503	-0.326
	C4-C5	1.525	1.680	-15.03	-11.74	-11.48	8.19	0.023	0.179	-0.514	-0.335
	C6-C7	1.511	1.675	-15.20	-11.54	-11.47	7.81	0.006	0.176	-0.510	-0.334
	C7-C8	1.507	1.765	-16.89	-13.16	-12.12	8.39	0.085	0.190	-0.556	-0.365

Table 4.8. Theoretical topological analysis of charge density at (3,-1) bond critical point (BCP) of isolated $[V10]^{6-}$ by M06-2X/cc-pVTZ.

Type	Bond	d_{12}	$\rho(r_c)$	$\nabla^2\rho(r_c)$	λ_1	λ_2	λ_3	ϵ	$G(r_c)$	$V(r_c)$	$H(r_c)$
V-O1x	V5 - O10	1.612	1.765	22.31	-12.90	-12.87	48.08	0.002	0.461	-0.691	-0.230
	V3 - O11	1.612	1.764	22.07	-12.91	-12.87	47.84	0.003	0.459	-0.690	-0.230
	V1 - O7	1.620	1.733	22.14	-12.53	-12.46	47.14	0.006	0.451	-0.672	-0.221
	V2 - O6	1.623	1.717	22.17	-12.39	-12.31	46.87	0.006	0.447	-0.663	-0.217
V-O2x	V4 - O18	1.685	1.440	20.31	-10.67	-9.88	40.86	0.081	0.359	-0.508	-0.148
	V4 - O13	1.707	1.350	19.92	-9.90	-9.11	38.93	0.088	0.334	-0.462	-0.128
	V1 - O15	1.814	0.994	16.36	-6.90	-6.54	29.80	0.054	0.231	-0.293	-0.061
	V2 - O16	1.814	0.994	16.37	-6.87	-6.51	29.74	0.055	0.231	-0.293	-0.061
	V2 - O17	1.825	0.963	15.97	-6.62	-6.30	28.88	0.051	0.222	-0.279	-0.057
	O14 - V23	1.829	0.952	15.78	-6.50	-6.16	28.43	0.055	0.219	-0.274	-0.055
	V1 - O12	1.834	0.942	15.61	-6.42	-6.10	28.13	0.052	0.216	-0.270	-0.054
	V3 - O14	1.851	0.894	15.15	-6.00	-5.75	26.91	0.044	0.204	-0.250	-0.046
	V3 - O17	1.872	0.852	14.29	-5.60	-5.42	25.31	0.033	0.190	-0.232	-0.042
	V5 - O15	1.881	0.832	14.01	-5.45	-5.25	24.71	0.037	0.185	-0.224	-0.039
	O12 - V21	1.888	0.818	13.75	-5.32	-5.15	24.21	0.033	0.180	-0.218	-0.038
	O16 - V23	1.892	0.806	13.66	-5.21	-5.05	23.92	0.032	0.178	-0.214	-0.036
	V3 - O13	2.020	0.551	9.92	-3.19	-3.16	16.27	0.007	0.113	-0.122	-0.010
	V5 - O18	2.070	0.479	8.64	-2.62	-2.60	13.86	0.007	0.095	-0.100	-0.005
V-O3x	O8 - V22	1.923	0.754	12.42	-4.77	-4.70	21.89	0.013	0.160	-0.192	-0.031
	V4 - O9	1.944	0.714	11.73	-4.45	-4.40	20.58	0.012	0.149	-0.177	-0.027

	V1 - O9	1.999	0.614	10.22	-3.70	-3.63	17.54	0.020	0.124	-0.141	-0.017
	V2 - O8	2.005	0.601	10.11	-3.59	-3.52	17.22	0.018	0.121	-0.137	-0.016
	V1 - O8	2.021	0.573	9.76	-3.36	-3.30	16.43	0.018	0.115	-0.128	-0.013
	V2 - O9	2.028	0.566	9.51	-3.31	-3.26	16.08	0.016	0.112	-0.125	-0.013
V-O6x	V4 - O37	2.078	0.490	8.72	-2.62	-2.59	13.93	0.011	0.097	-0.103	-0.006
	V4 - O38	2.158	0.396	6.94	-1.93	-1.89	10.76	0.019	0.073	-0.075	-0.001
	V2 - O38	2.242	0.325	5.53	-1.39	-1.39	8.32	0.001	0.057	-0.056	0.001
	V1 - O37	2.267	0.305	5.12	-1.26	-1.25	7.63	0.002	0.052	-0.051	0.001
	V23 - O38	2.294	0.289	4.66	-1.15	-1.11	6.91	0.035	0.047	-0.046	0.001
	V3 - O38	2.333	0.261	4.13	-0.96	-0.92	6.01	0.048	0.041	-0.040	0.002

Table 4.9. Theoretical topological analysis of charge density at (3,-1) bond critical point (BCP) of TBA cation by M06-2X/cc-pVTZ.

Type	Bond	d_{12}	$\rho(\mathbf{r}_c)$	$\nabla^2\rho(\mathbf{r}_c)$	λ_1	λ_2	λ_3	ϵ	$\mathbf{G}(\mathbf{r}_c)$	$\mathbf{V}(\mathbf{r}_c)$	$\mathbf{H}(\mathbf{r}_c)$
N-Cx1	N1-C11	1.524	1.527	-11.91	-9.45	-9.05	6.59	0.044	0.159	-0.441	-0.282
	N1-C21	1.520	1.544	-12.25	-9.68	-9.24	6.68	0.048	0.161	-0.449	-0.288
	N1-C31	1.523	1.531	-12.03	-9.50	-9.12	6.60	0.041	0.159	-0.443	-0.284
	N1-C41	1.518	1.544	-12.13	-9.57	-9.08	6.52	0.055	0.162	-0.450	-0.288
Cx1-Cx2	C11-C12	1.521	1.634	-14.10	-11.10	-10.89	7.89	0.019	0.172	-0.491	-0.319
	C21-C22	1.521	1.634	-14.04	-11.09	-10.95	8.00	0.013	0.173	-0.492	-0.319
	C31-C32	1.514	1.679	-15.04	-11.56	-11.35	7.87	0.019	0.179	-0.513	-0.335
	C41-C42	1.521	1.653	-14.45	-11.31	-11.04	7.90	0.025	0.175	-0.501	-0.325
Cx2-Cx3	C12-C13	1.520	1.661	-14.70	-11.41	-11.20	7.91	0.020	0.176	-0.504	-0.328
	C22-C23	1.526	1.626	-13.85	-10.99	-10.91	8.05	0.007	0.172	-0.488	-0.316
	C32-C33	1.522	1.659	-14.69	-11.40	-11.25	7.96	0.013	0.175	-0.503	-0.328
	C42-C43	1.527	1.622	-13.72	-10.95	-10.83	8.07	0.011	0.172	-0.486	-0.314
Cx3-Cx4	C13-C14	1.498	1.712	-15.75	-11.87	-11.62	7.74	0.021	0.183	-0.529	-0.346
	C23-C24	1.516	1.653	-14.40	-11.25	-11.13	7.98	0.011	0.176	-0.501	-0.325
	C33-C34	1.527	1.620	-13.69	-10.91	-10.82	8.05	0.009	0.172	-0.485	-0.314
	C43-C44	1.521	1.639	-14.05	-11.14	-10.99	8.09	0.013	0.174	-0.494	-0.320

4.3.2.4 Theoretical topological analysis of V-O bonds at BCP

For understanding the relationship between V-O distances and different topological properties from different V6 and V10 structures computed by two functionals, the following three graphs (figures 4.8, 4.9, 4.10) present the topological properties at the BCPs V-O bonds.

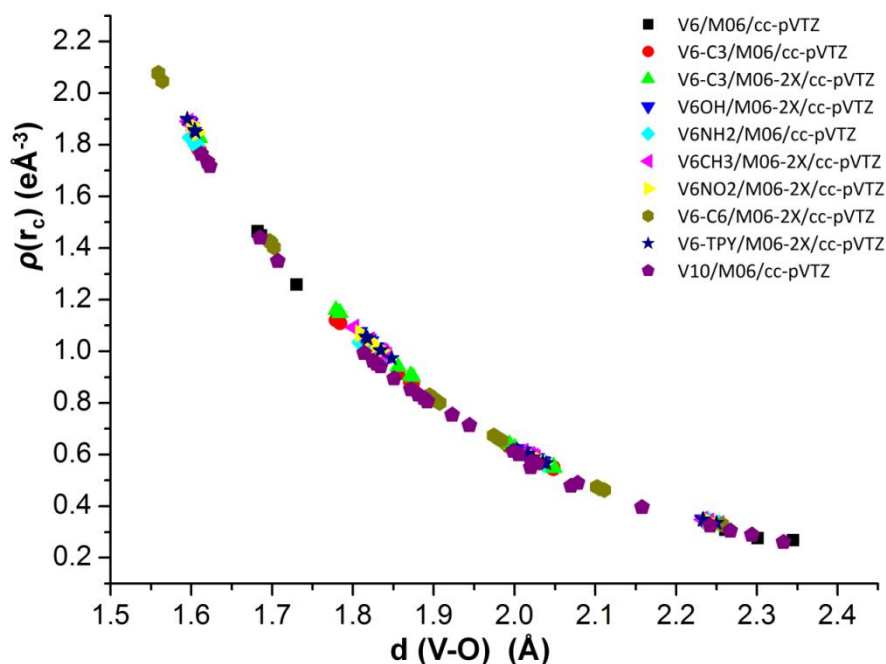


Figure 4.8. Behavior of $\rho(r_c)$ versus V-O interatomic distance in different calculation.

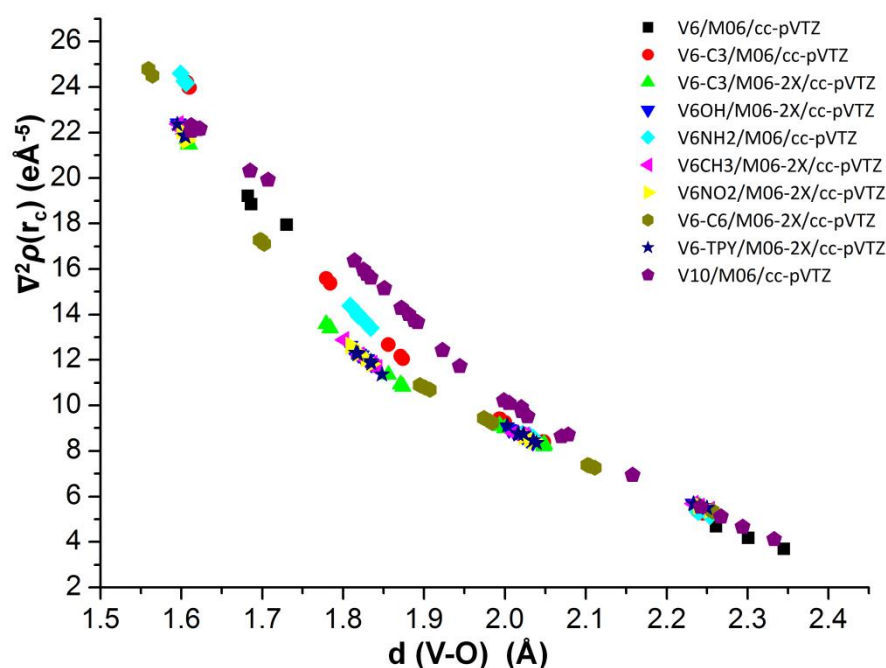


Figure 4.9. Behavior of $\nabla^2\rho(r_c)$ versus V-O interatomic distance in different calculation.

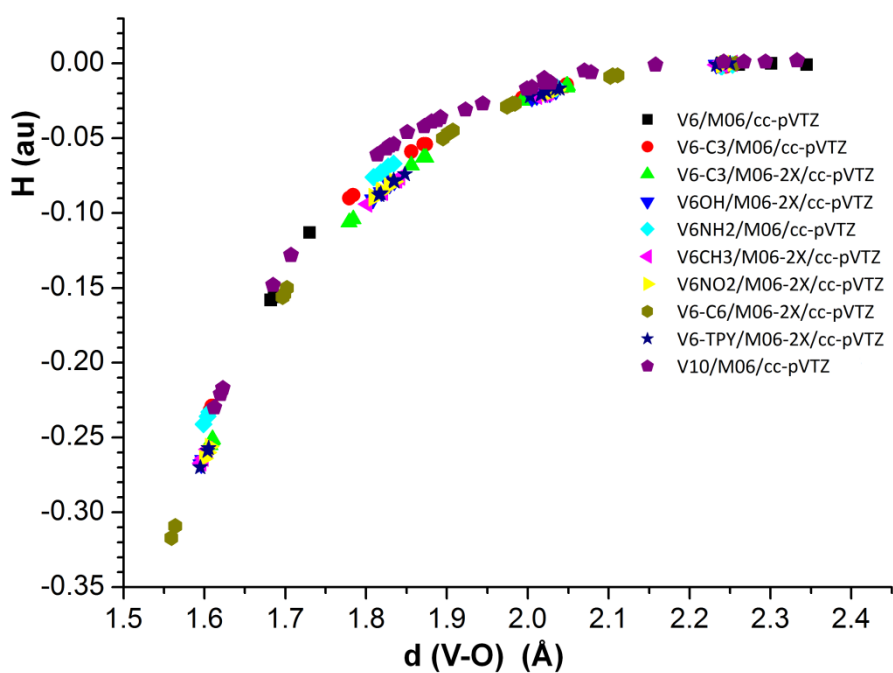


Figure 4.10. Behavior of $\rho(r_c)$ versus V-O interatomic distance in different calculations.

4.3.2 Theoretical AIM charges

4.3.2.1 Theoretical AIM charges for functionalized V6 series and V10 anion

The theoretical AIM charges of V and O atoms from functionalized V6 series and V10 anion are listed in Table 4.10. The summations of AIM charges for V6 core and organic ligands are also given.

4.3.2.2 Theoretical AIM charges for TBA cation

The theoretical AIM charges for TBA cation calculated from different basis sets are listed in Table 4.11.

Table 4.10. Theoretical AIM charge for different V6 and isolated V10 anion.

		<i>Isolated POV</i>		<i>Short functionalized V6 series</i>				<i>Long functionalized V6 series</i>			
Type	Atom	V6	V10	V6CH ₃	V6NH ₂	V6OH	V6NO ₂	V6-C3	V6-C3	V6-C6	V6-TPY
		m06	m06	m06-2X	m06	m06-2X	m06-2X	m06	m06-2X	m06-2X	m06-2X
		cc-pVTZ	cc-pVTZ	cc-pVTZ	cc-pVTZ	cc-pVTZ	cc-pVTZ	cc-pVTZ	cc-pVTZ	cc-pVTZ	cc-pVTZ
VII	V1			+2.480	+2.338	+2.481	+2.477	+2.333	+2.476	+2.470	+2.478
	V2			+2.482	+2.336	+2.481	+2.474	+2.333	+2.476	+2.463	+2.477
	V3			+2.483	+2.337	+2.482	+2.476	+2.337	+2.479	+2.466	+2.472
	<i>Average</i>	+2.311	+2.272	+2.482	+2.337	+2.482	+2.476	+2.234	+2.477	+2.466	+2.476
O1x	O11			-0.843	-0.818	-0.837	-0.822	-0.822	-0.843	-0.828	-0.840
	O12			-0.845	-0.821	-0.843	-0.831	-0.823	-0.845	-0.830	-0.838
	O13			-0.849	-0.826	-0.849	-0.835	-0.824	-0.846	-0.847	-0.816
	<i>Average</i>	-1.299	-0.899	-0.845	-0.822	-0.843	-0.829	-0.823	-0.845	-0.835	-0.831
O2x	O21			-1.068	-1.006	-1.068	-1.060	-0.999	-1.058	-1.048	-1.068
	O22			-1.069	-1.008	-1.070	-1.061	-1.000	-1.059	-1.048	-1.067
	O23			-1.071	-1.010	-1.072	-1.063	-1.002	-1.062	-1.050	-1.063
	<i>Average</i>	-1.070	-1.040	-1.069	-1.008	-1.070	-1.061	-1.000	-1.060	-1.049	-1.066
O3x	O31			-1.177	-1.138	-1.175	-1.187	-1.135	-1.189	-1.212	-1.192
	O32			-1.178	-1.141	-1.178	-1.188	-1.135	-1.189	-1.213	-1.191
	O33			-1.185	-1.153	-1.179	-1.195	-1.138	-1.192	-1.216	-1.183
	<i>Average</i>		-1.121	-1.180	-1.144	-1.177	-1.190	-1.136	-1.190	-1.214	-1.189
O6x	O61			-1.478	-1.365	-1.478	-1.477	-1.369	-1.478	-1.474	-1.481
	<i>Average</i>	-1.270	-1.329	-1.478	-1.365	-1.478	-1.477	-1.369	-1.478	-1.474	-1.481
V6 or V10 core		-8.000	-6.000	-5.182	-5.185	-5.156	-5.110	-5.119	-5.182	-5.261	-5.145
Organic ligand				+3.194	+3.182	+3.161	+3.113	+3.117	+3.194	+3.267	+3.156
functionalized V6		-8.000	-6.000	-1.998	-2.003	-1.995	-1.997	-2.002	-1.998	-1.994	-1.999

Table 4.11. Theoretical AIM charges in TBA cation by different basis sets.

Atom	M06-2X/cc-pVTZ	M06-2X/6-31+G(d, p)
N1	-0.984	-0.910
C11	0.551	0.546
C12	0.300	0.321
C13	0.525	0.574
C14	0.408	0.418
C21	0.669	0.638
C22	0.715	0.643
C23	0.606	0.536
C24	0.618	0.567
C31	0.797	0.758
C32	0.585	0.544
C33	0.423	0.433
C34	0.334	0.359
C41	0.821	0.771
C42	0.403	0.406
C43	0.294	0.311
C44	0.709	0.687
AIM charges of TBA	+1.000	+1.000

4.3.3 Theoretical *d*-orbital population of vanadium atoms

The theoretical *d*-orbital population of V atoms in V6-C3 are listed in Table 4.12.

Table 4.12. Theoretical *d*-orbital population of V atoms in V6-C3 by NBO analysis^[a]

Orbital	V1		V2		V3	
	$d(z^2)$	0.50985	17.77%	0.55942	19.52%	0.47660
$d(x^2-y^2)$	0.49523	17.26%	0.47938	16.73%	0.56541	19.75%
$d(xy)$	0.66952	23.34%	0.65251	22.77%	0.65792	22.98%
$d(xz)$	0.58506	20.39%	0.59694	20.83%	0.65877	23.01%
$d(yz)$	0.60924	21.24%	0.5774	20.15%	0.50483	17.63%
<i>d</i> orbital population	2.86890		2.86565		2.86353	

[a] Calculated by M06/cc-pVTZ.

4.3.4 Theoretical electrostatic potential

The theoretical electrostatic potentials are presented in the following section.

4.3.4.1 Theoretical EP of Isolated V6 and V10

Figure 4.11 presents the theoretical electrostatic potentials of isolated $[\text{V}_{10}\text{O}_{28}]^{6-}$ and $[\text{V}_6\text{O}_{19}]^{2-}$ anions mapped on the 3D isodensity surface ($0.007 \text{ e}\cdot\text{\AA}^{-3} / 0.001 \text{ a.u.}$).

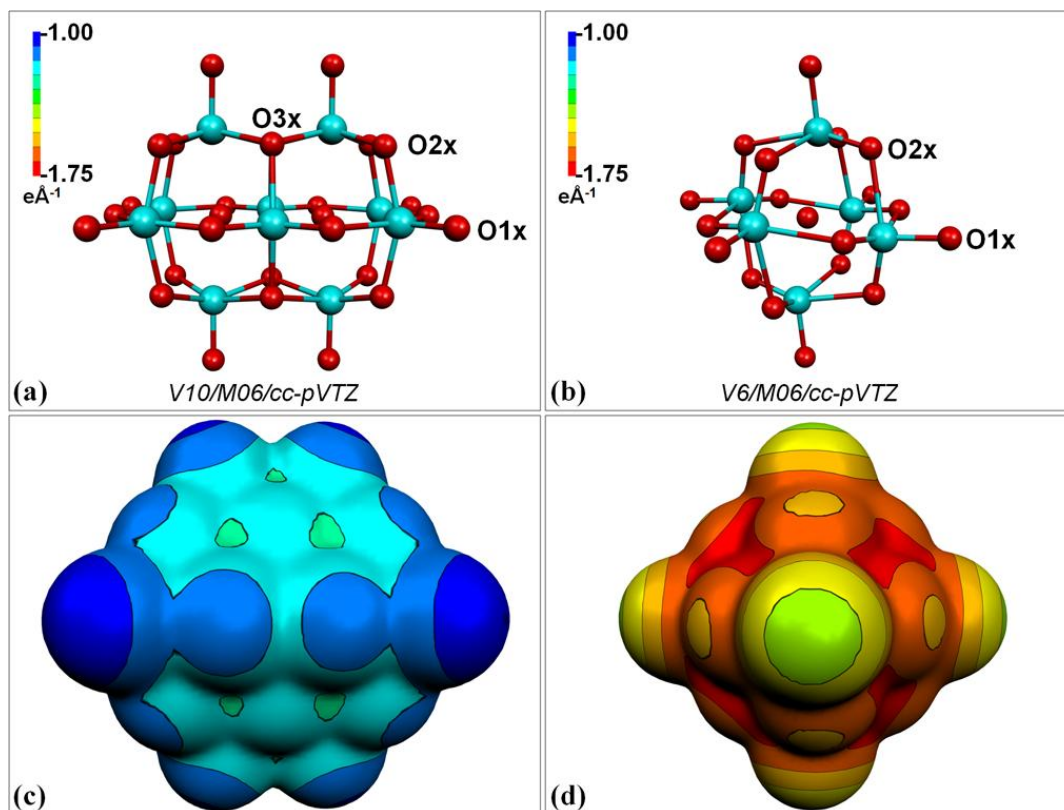


Figure 4.11. EP ($\text{e}\cdot\text{\AA}^{-1}$) mapped on isodensity surface ($0.007 \text{ e}\cdot\text{\AA}^{-3}$) for isolated $[\text{V}_{10}\text{O}_{28}]^{6-}$ (left column) and $[\text{V}_6\text{O}_{19}]^{2-}$ (right column). The computational details are indicated.

4.3.4.2 Theoretical electrostatic potential of functionalized V6-C3

Figure 4.12 presents the theoretical electrostatic potential of $[\text{V6-C3}]^{2-}$ mapped on the 3D isodensity surface ($0.007 \text{ e.}\text{\AA}^{-3} / 0.001 \text{ a.u.}$).

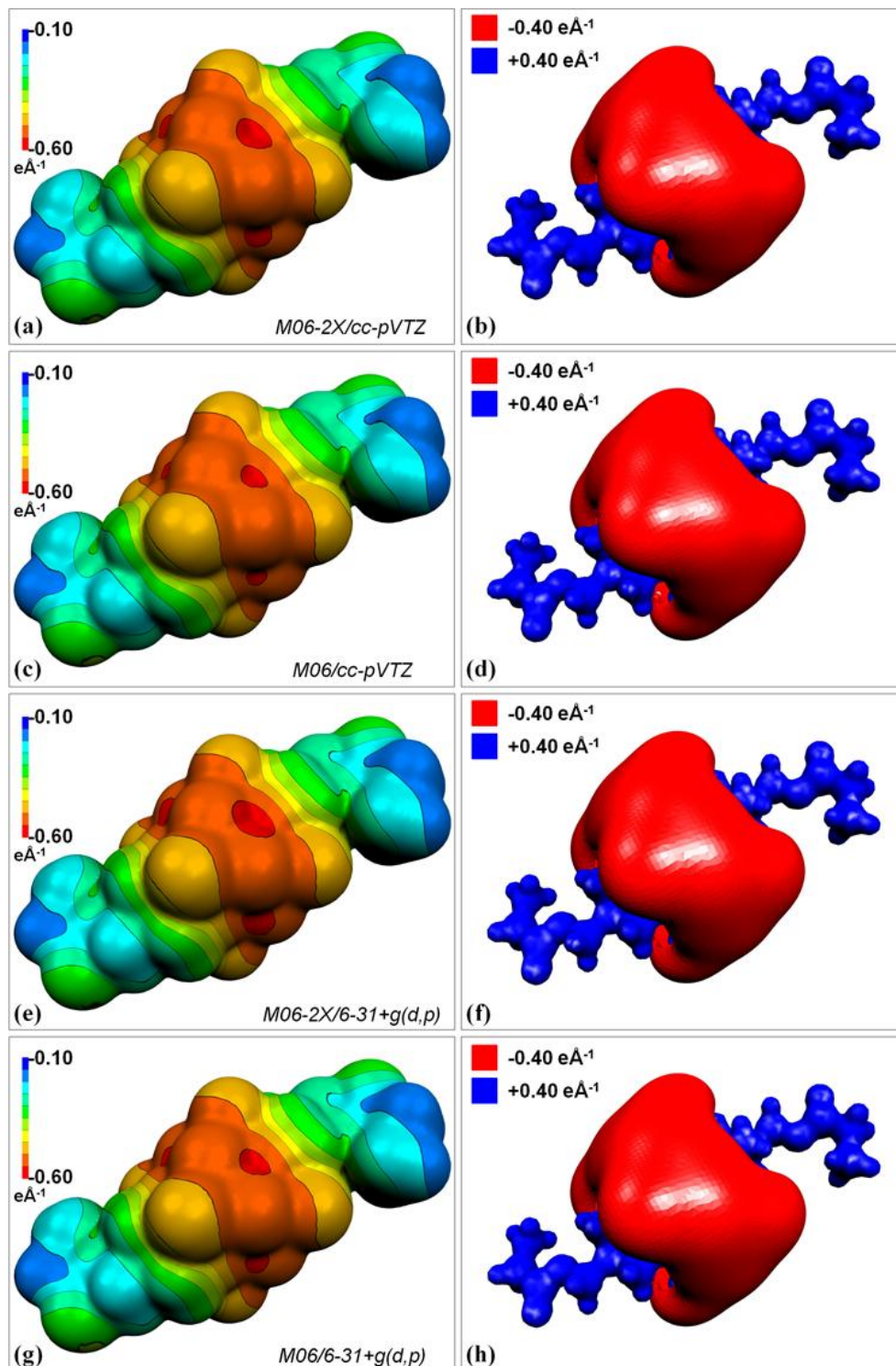


Figure 4.12. Theoretical EP distribution of $[\text{V6-C3}]^{2-}$ from different computations. EP ($\text{e.}\text{\AA}^{-1}$) mapped on isodensity surface ($0.007 \text{ e.}\text{\AA}^{-3}$) (left column); EP isovalue surface with cutoff $\pm 0.40 \text{ e.}\text{\AA}^{-1}$. The computational details are indicated.

4.3.4.3 Theoretical electrostatic potentials of short functionalized V6 series

Figure 4.13 presents the theoretical electrostatic potentials of short functionalized V6 series mapped on the 3D isodensity surface ($0.007 e \cdot \text{\AA}^{-3} / 0.001 \text{ a.u.}$).

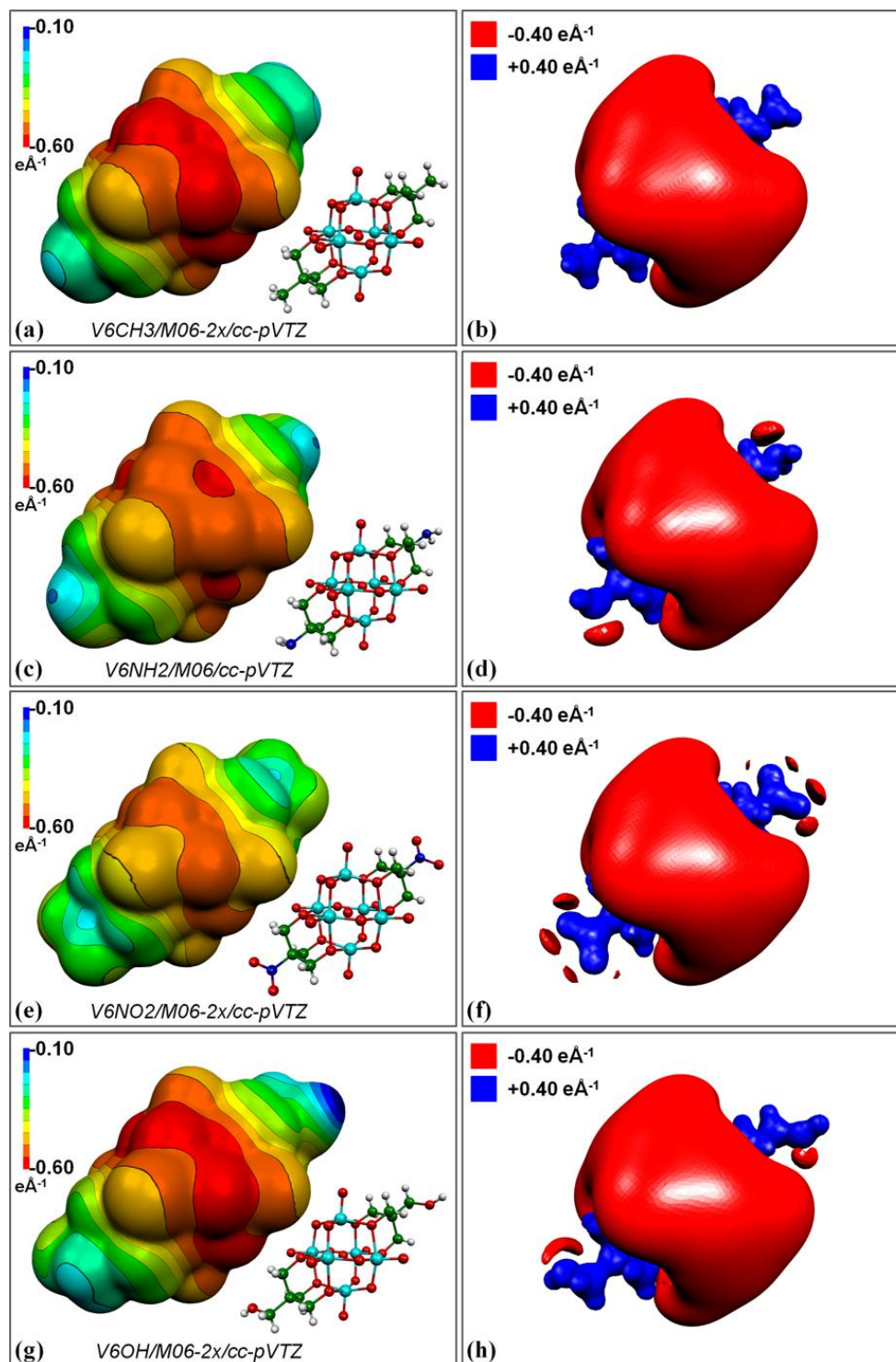


Figure 4.13. Theoretical EP distributions of short functionalized V6 series. EP ($e \cdot \text{\AA}^{-1}$) mapped on isodensity surface ($0.007 e \cdot \text{\AA}^{-3}$) (left column); EP isovalue surface with cutoff $\pm 0.40 e \cdot \text{\AA}^{-1}$. The corresponding structures are given. The computational details are indicated.

4.3.4.4 Theoretical electrostatic potentials of long functionalized V6 series

Figure 4.14 presents the theoretical electrostatic potentials of long functionalized V6 series mapped on the 3D isodensity surface ($0.007 \text{ e} \cdot \text{\AA}^{-3} / 0.001 \text{ a.u.}$).

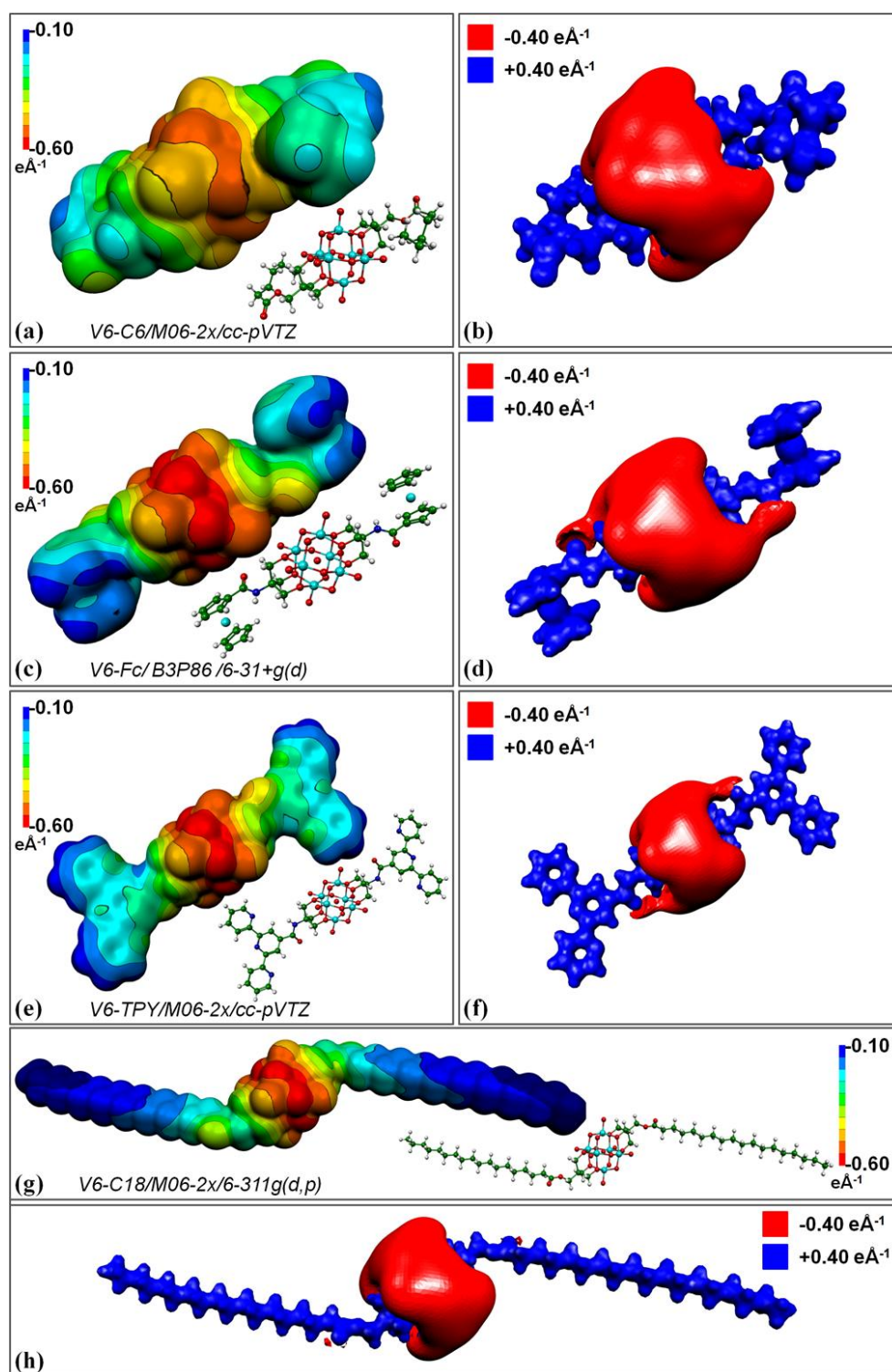


Figure 4.14. Theoretical EP distributions of long functionalized V6 series. EP ($\text{e} \cdot \text{\AA}^{-1}$) mapped on isodensity surface ($0.007 \text{ e} \cdot \text{\AA}^{-3}$) (left column); EP isovalue surface with cutoff $\pm 0.40 \text{ e} \cdot \text{\AA}^{-1}$. The corresponding structures are given. The computational details are indicated.

4.3.4.5 Theoretical electrostatic potential of TBA cation

Figure 4.15 presents the theoretical electrostatic potential of TBA cation mapped on the 3D isodensity surface ($0.007 \text{ e}\text{\AA}^{-3} / 0.001 \text{ a.u.}$).

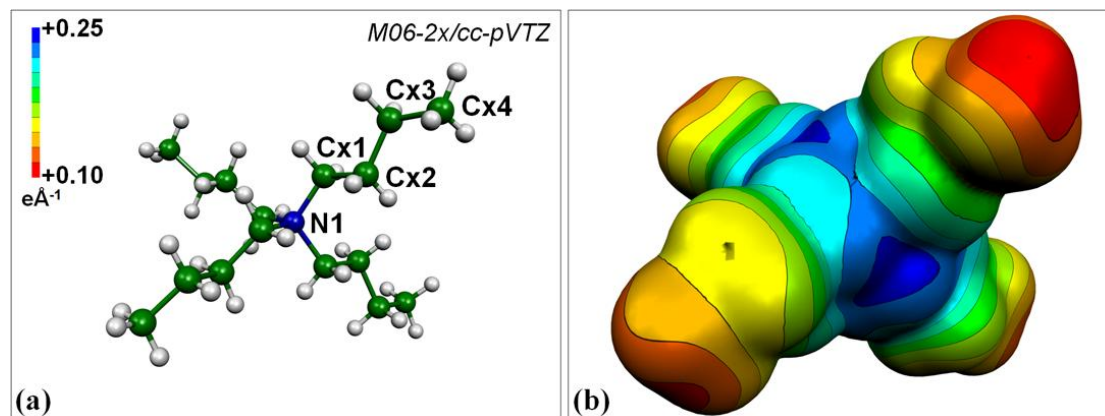


Figure 4.15. EP ($e.\text{\AA}^{-1}$) mapped on isodensity surface ($0.007 \text{ e}\text{\AA}^{-3}$) for TBA cation. The computational details are indicated.

4.4 Discussion and conclusion

After examination of the results, we have chosen M06/M06-2X [Zhao, 2008] as density functional and cc-pVTZ as the basis set for the computed density. The reasons are the following:

- (1) At the beginning of DFT calculation, one of the most important purpose was to investigate the non-covalent interaction between acceptors (O atoms from V6 core) and donors (C, O, N from organic ligand or cation). The M06 suite of density functionals are parametrized for non-covalent interactions.
- (2) M06/M06-2X are the hybrid functionals which parametrize the models involving transition metals, which is the case of the functionalized V6 series and V10.
- (3) For the basis sets, we have chosen cc-pVTZ as the basis set of computed density. cc-pVTZ is one of Dunning's correlation consistent basis sets [Dunning, 1989], including polarization functions. These basis sets have had redundant functions removed and have been rotated [Davidson, 1996] in order to increase computational efficiency.

Considering the mentioned reasons, we choose M06/cc-pVTZ for type **I** (isolate POVs), M06-2X/cc-pVTZ for type **II** (short functionalized V6 series) and for type **III**, (long functionalized V6 series). To evaluate the validation of the employed density

functional and basis set, we have performed the charge density analysis based on corresponding computed density from various DFT calculations.

- (1) Deformation density and Laplacian of total density maps for different defined planes in V6-C3 are shown in Figure 4.4- 4.7, generated from M06 and M06-2X functional with the same basis set, cc-pVTZ. There is no significant difference.
- (2) As shown in Figure 4.8 - 4.10, the topological properties, at BCPs at V-O bonds of functionalized V6 series, are well parametrized, and show high agreement even including the isolated V6 and V10 anions.
- (3) We try to employ different basis sets, 6-31+G(d, p)/cc-pVTZ to compute the density of $[V6-C3]^{2-}$ in Figure 4.12. The EP behaviours from different calculations remain in high agreement.
- (4) Based on M06/M06-2X functional, cc-pVTZ basis set, the atomic net charges are integrated for short and long functionalized V6 series by AIM theory. In Table 4.10, the AIM charge analysis reveals that: (i) the AIM charges of V atoms are in a narrow range, from +2.333 e to +2.483 e; (ii) summations of AIM charges for V6 core are maintained around -5.2 e though the organic ligands are chemically different.

To conclude, the employed density functional M06/M06-2X and basis set cc-pVTZ exhibit its good performance for theoretical charge density analysis.

5. GENERAL DISCUSSION

5.1 Introduction

In this work, we possess two sets of new experimental charge density on functionalized V6 compounds, one experimental charge density on V10 which is already published, ten sets of theoretical charge density on V6 and one set on theoretical charge density on V10. In the previous chapters, we have discussed the chemical bonding and reactivity based only on the experimental charge density of V6-C3.

Therefore the discussion is organized as follows:

In **section 5.2**, we will firstly establish differences and similarities between the three experimental charge density results and their corresponding theoretical ones in the case where the properties have been determined. For sake of clarity this section will be presented through three tables. The maps and the graphs are included in a small format, these Figures could be found in chapter 2, 3 or 4 in a bigger format. The conclusion of this section will validate the theoretical calculations properties per properties.

In **section 5.3**, we have compiled in a table the different results for each POV compound we will use in the next sections for discussing the chemical bonds and chemical reactivity.

In **section 5.4**, we will use all the results as defined in section 5.3 to reveal the electronic and topological properties of functionalized V6 and V10. The purpose of this section is to understand the charge density feature of V and O atoms in POVs, and the V-O chemical bonds, which will provide us important chemical information. Based on [Gatti, 2005], the topological parameters of the functionalized V6 and V10 will allow us to clearly characterize the different V-O1x, V-O2x, V-O3x, V-O6x. This characterisation expressed on a new graph will be compared to the behavior of the topological parameters of various metal-ligand (M-L) bonds retrieved from 49 papers leading to 252 different M-L bonds.

In **section 5.5**, based on the analysis of chemical reactivity of the existing functionalized POV, we propose a new insight on functionalization in POM/POV chemistry. We will establish that: i) the functionalization is very important for the stabilization of a pure inorganic POM or POV cluster; ii) the reasons why the organic ligand can functionalize and react with POM/POV anion; iii) the vicinity of some

oxygen atoms could be act as potential reaction sites. This section will give guidelines for POM/ POV synthesis.

In **section 5.6**, we will combine some chemical informations (EP, AIM, ISF) about chemical reactivity in order to understand the charge transfer behaviour in POM/POV-based charge transfer materials.

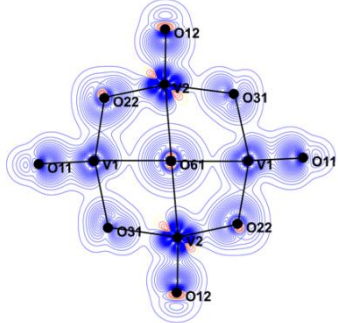
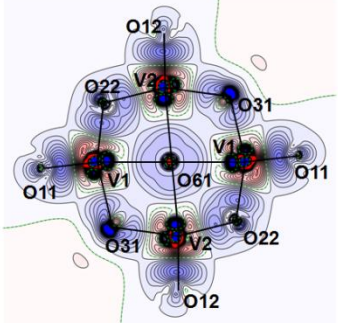
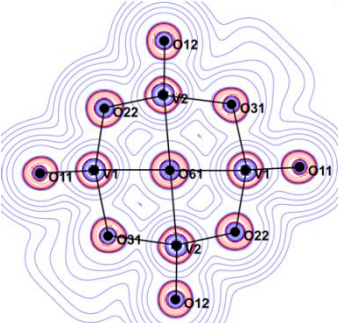
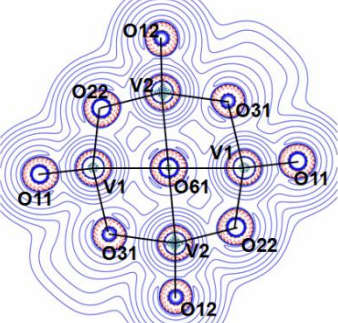
Finally, in **section 5.7**, we will present the preliminary bioactivity analysis of functionalized V6 compounds. For a better understanding of the bioactivity, we will make a statistical analysis from CSD in order to know the interaction sites of the compounds. We will also use the molecular interaction field (MIF) method (a part of a docking) to process a combined approach, developed for drug discovery in our group, to predict the interaction sites. This section will be useful for metal-drug design.

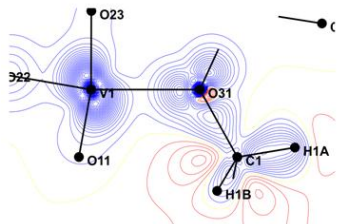
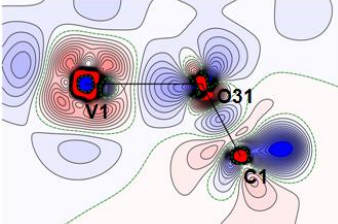
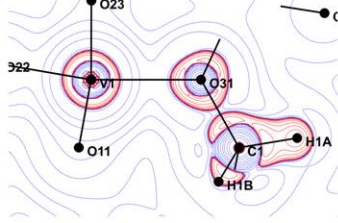
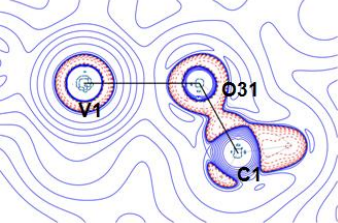
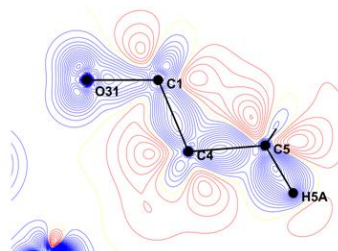
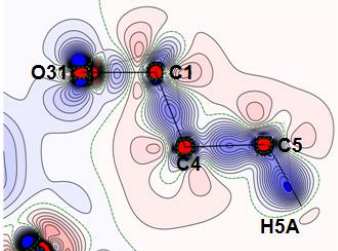
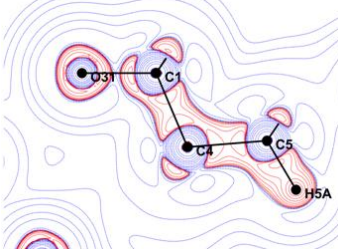
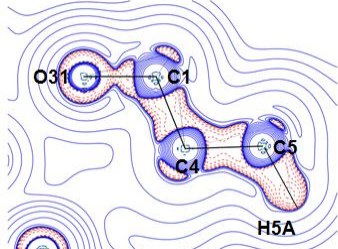
5.2 Similarities and differences in experimental and theoretical charge density of three POV compounds

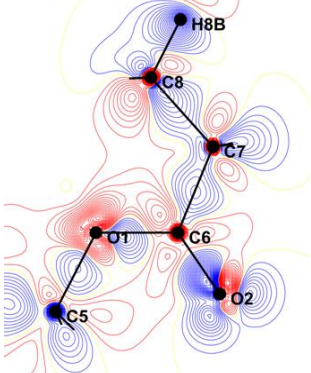
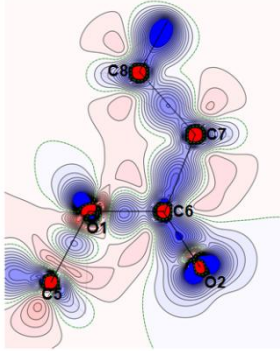
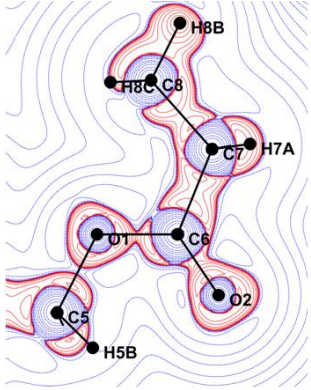
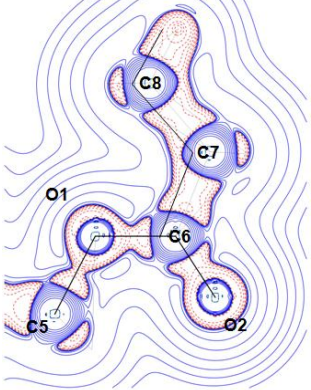
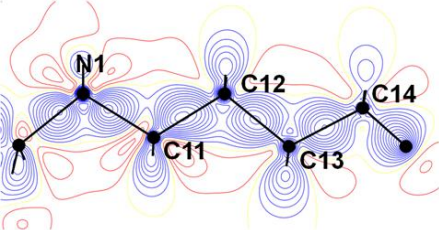
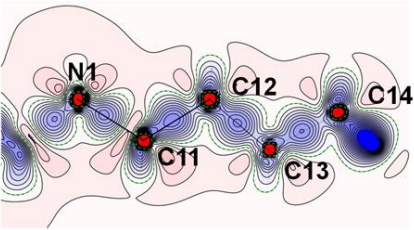
In the next three sections, we will summarized the similarities and differences observed for V6-C3, V6-OH and V10.

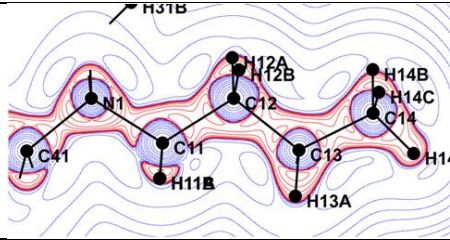
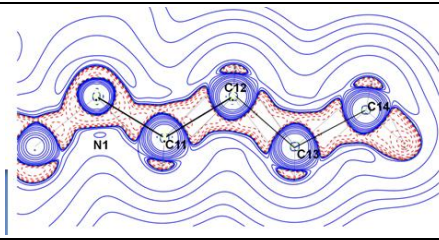
5.2.1 Functionalized V6-C3 anion

Table 5.1. Comparative summary of the experimental and theoretical V6-C3 results.

Charge density maps for V6-C3				
	Similarity	Difference	Experimental results	Theoretical results
Deformation density map, plane 1: V-O61-V	Similar around O atom	Different in the vicinity of V		
Laplacian of total density map, plane 1: V-O61-V	Similar			

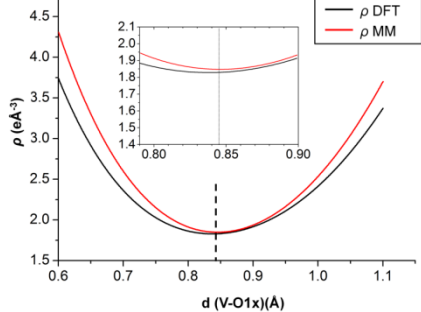
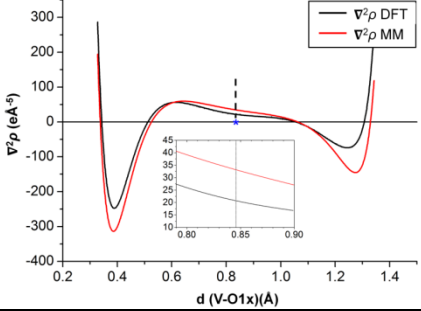
<p>Deformation density map, plane 2: V-O3x-C1</p>	<p>Similar around O atom</p>	<p>Different in the vicinity of V</p>		
<p>Laplacian of total density map, plane 2: V-O3x-C1</p>	<p>Similar</p>			
<p>Deformation density map, plane 3: V-O3x-C1</p>	<p>Similar</p>			
<p>Laplacian of total density map, plane 3: V-O3x-C1</p>	<p>Similar</p>			

<p>Deformation density map, plane 4: V-O3x-C1</p>		<p>Different density distribution in ester group</p>		
<p>Laplacian of total density map, plane 4: V-O3x-C1</p>	<p>Similar</p>			
<p>Deformation density map, plane 5: V-O3x-C1</p>	<p>Similar</p>			

Laplacian of total density map, plane 5: V-O3x-C1	Similar			
Short summary on experimental and theoretical charge density maps for V6-C3				
<p>(1) There are some differences in the density distribution around V atoms. The probable reason is based on the different models used for the V atom (in multipole model refinement (MM) ($4s^03d^3$) and DFT calculation ($4s^23d^3$)). The density around of V atoms in DFT is too concentrated, that make the AIM charge higher than in MM.</p> <p>(2) The density distribution around different type of O atoms is very similar. We notice that the O density is symmetrically distributed along the V-O bonds in DFT calculation, because there is no non-covalent interactions, which affect the density distribution.</p> <p>(3) The Laplacian density maps do not present any significant difference. The Laplacian of the total density around V atoms are almost spherical, while the Laplacian around O atoms depend on the chemical environment.</p> <p>(4) The density distributions from MM and DFT in the linkage (V6 core to organic ligand) and inside the TBA cation (plane 3, Figure 5.3) are quite similar.</p> <p>(5) There are different density behaviours at the ester group, in MM and DFT. The problem with the experimental density distribution in ester group is described in chapter 2. The static deformation density around C7, C8 is the same.</p> <p>(6) The Laplacian in the corresponding maps are similar, except the Laplacian of O1-C6 bond.</p>				

Topological analysis of BCPs for V-O bond

	Similarity	Difference	Experimental results	Theoretical results
$\rho(\mathbf{r}_c)$ vs d (V-O)	Excellent agreement			
$\nabla^2\rho(\mathbf{r}_c)$ vs d (V-O)	Similar, slightly higher absolute values for experimental than theoretical			
$H(\mathbf{r}_c)$ vs d (V-O)	Similar, higher absolute values for experimental than theoretical			

<p>Density $\rho(\mathbf{r})$ along the V-O1x bond path</p>	<p>Similar</p>		
<p>Laplacian of total density $\nabla^2\rho(\mathbf{r})$ along the V-O1x bond path</p>	<p>Similar</p>		
<p>Short summary on topological analysis of BCPs for V-O bond in V6-C3</p>			
<p>(1) Generally, the topological parameters of BCPs for V-O bond from MM and DFT calculation are in high agreement, especially the density $\rho(\mathbf{r}_c)$.</p> <p>(2) The absolute values the topological properties ($\rho(\mathbf{r}_c)$, $\nabla^2\rho(\mathbf{r}_c)$, $H(\mathbf{r}_c)$) are as the order: O1x > O2x > O3x > O6x.</p> <p>(3) The topological properties along the bond path can reveal the nature of the bonding. At BCP, we observe that the topological values are close. However, we found that at the other positions, the absolute density and Laplacian values of MM are higher than those from DFT calculation.</p>			

(4) The experimental Laplacian value is higher than from DFT calculation. That could be due to the fact that the propagation of the errors increased in the second derivatives.

(5) The topological properties from M06/cc-pVTZ and M06-2X/cc-pVTZ are quite similar.

AIM charge analysis in V6-C3

	Similarity	Difference	Experimental results	Theoretical results
AIM charge of V atom (Average values)		The charge of theoretical is more positive	+1.27 e	M06/cc-pVTZ: +2.33 e M06-2X/cc-pVTZ: +2.47 e
AIM charge of O atom (Average values)	The order of AIM charge of O atom type is same	The value	O1x (-0.74 e) > O2x (-0.94 e) > O3x (-1.04 e) > O6x (-1.09 e)	M06-2X/cc-pVTZ: O1x (-0.82 e) > O2x (-1.00 e) > O3x (-1.14 e) > O6x (-1.37 e) M06/cc-pVTZ O1x (-0.85 e) > O2x (-1.06 e) > O3x (-1.19 e) > O6x (-1.48 e)
AIM charges for V6 core	V6 core are high negative	AIM charge of MM is more negative than them of DFT	-9.76 e	-5.12 e (M06), -5.18 e (M06-2X)
AIM charges for OL		OL takes more positive charge in MM	+7.51 e	+3.12 (M06), + 3.19 e (M06-2X)

Short summary on AIM analysis of BCPs for V-O bond

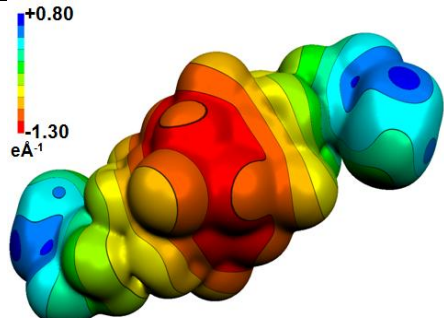
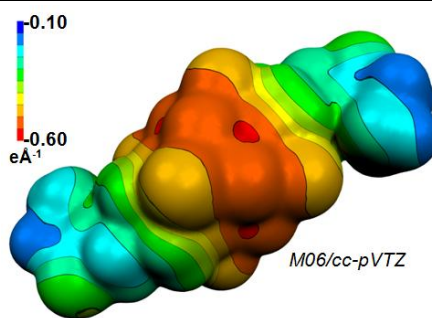
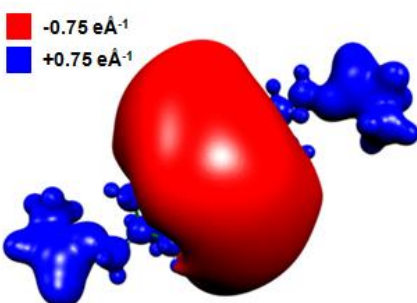
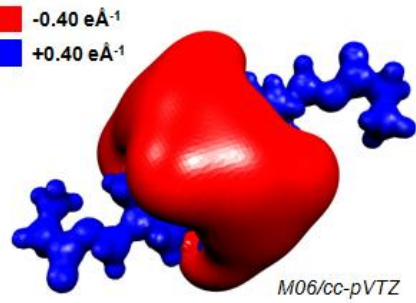
(1) The AIM charges of V atoms in experimental and theoretical charge density analysis are very different, due to the different models of V

employed in MM refinement and DFT calculation.

(2) The average AIM charges of different O atom types are in the order: O6x < O3x < O2x < O1x.

(3) The experimental and theoretical AIM charge analysis indicated that the V6 core takes a high negative charge, and OL part takes a positive one, which also illustrates that V6 core is a strong electron-reservoir.

Electrostatic potential in V6-C3

	Similarity	Difference	Experimental results	Theoretical results
EP mapped on molecular surface	Similar EP distribution for different	Experimental EP is higher than theoretical EP		
EP isovalue surface	High EP value distributed on V6 core			

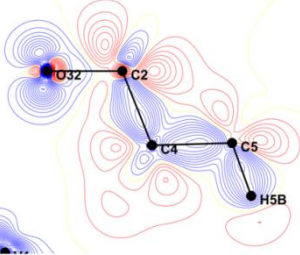
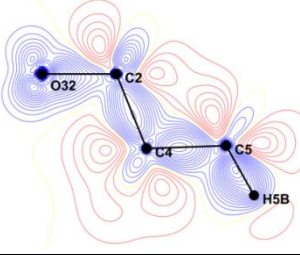
Short summary on electrostatic potential in [V6-C3]²⁻

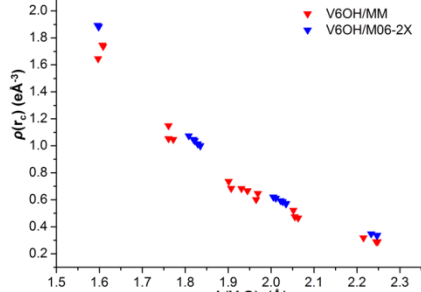
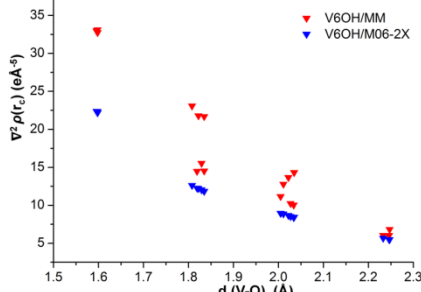
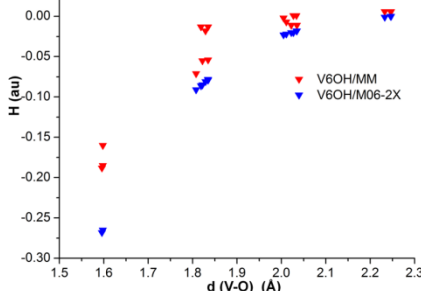
- (1) The most high EP value is in the vicinity of O2x which is both observed for experiment and theory.
- (2) The V6 core exhibits high EP value due to the fact that the V6 core concentrates a more negative charge, which corresponds to the nucleophilic molecular region. In contrary, the organic ligand is the electrophilic molecular region.

5.2.2 Functionalized V6OH anion

Table 5.2. Comparative summary of the experimental and theoretical V6-OH results except for the charge density maps which are compared with the experimental V6-C3 results.

Experimental charge density maps of V6OH and V6-C3				
	Similarity	Difference	Experimental results of V6OH	Experimental results of V6-C3
Deformation density map, plane 1: V-O61-V	Similar around O atom and vanadium atom	Negative density less pronounced in V6OH in agreement with the high residual density localized on vanadium		
Deformation density map, plane 2: V-O3x-C1	Similar around O atom			

Deformation density map, plane 3: V-O3x-C1	Similar			
Short summary on experimental charge density maps of V6OH and V6-C3				
<p>(1) From the density maps for V6OH, we can clearly observe that different types of O atoms show different density distributions. Such a behaviour is extremely similar with those observed in V6-C3.</p> <p>(2) For the O density distribution, we find that there are some differences between the two compounds, due to different H-bonding in the two compounds. The H bonds in V6OH are stronger than those in V6-C3. In organic ligand, plane 3, almost the same density distributions in the two V6 compounds.</p>				
Experimental and theoretical topological analysis of BCPs for V-O bond in V6OH				
	Similarity	Difference	Experimental results	Theoretical results

$\rho(\mathbf{r}_c)$ vs d (V-O)	High agreement		
$\nabla^2\rho(\mathbf{r}_c)$ vs d (V-O)		Similar, slightly higher absolute values for experimental than theoretical	
$H(\mathbf{r}_c)$ vs d (V-O)	Similar	Similar, slightly higher absolute values for experimental than theoretical Some discrepancies inside the experimental results	

Short summary on topological analysis of BCPs for V-O bond in V-OH

(1) The topological parameters of BCPs for V-O bond from MM and DFT calculation (M06-2X/cc-pVTZ) are in agreement, especially the

density $\rho(\mathbf{r}_c)$.

(2) V6-OH's topology curves reveal the same behavior: the absolute values of the topological properties ($\rho(\mathbf{r}_c)$, $\nabla^2\rho(\mathbf{r}_c)$, $H(\mathbf{r}_c)$) are in the order:
 $O1x > O2x > O3x > O6x$.

(3) The differences observed for a same distance in an experimental topological parameters is due to the H-bonds

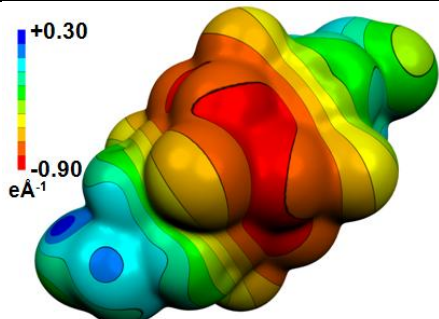
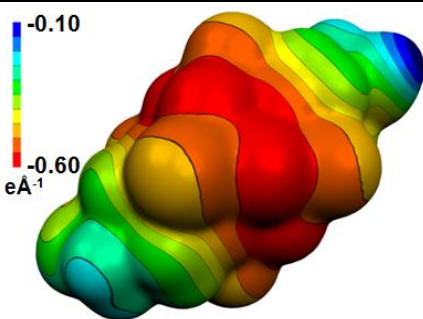
AIM charge analysis in V6OH

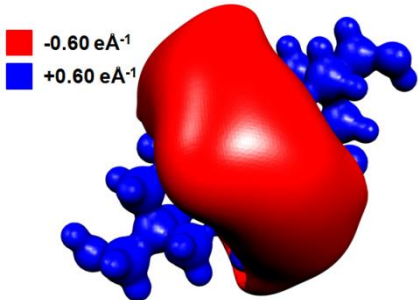
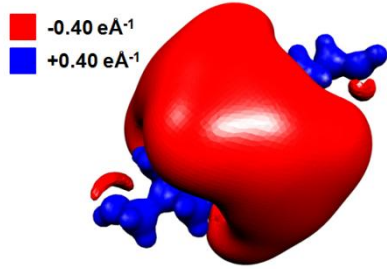
	Similarity	Difference	Experimental results	Theoretical results
AIM charge of V atom (Average values)		The theoretical charge is more positive	+1.75 e	M06-2X/cc-pVTZ: +2.48 e
AIM charge of O atom (Average values)		The theoretical charge is more negative	$O1x (-0.62 e) > O6x (-0.77 e) > O2x (-1.01 e) > O3x (-1.09 e)$	$O1x (-0.84 e) > O2x (-1.07 e) > O3x (-1.18 e) > O6x (-1.48 e)$
AIM charges for V6 core	V6 core is high negative	AIM charge of MM is slight more negative than from DFT	-4.96 e	-5.16 e (M06-2X)
AIM charges for OL		Organic ligand takes more positive charge in MM	+2.90 e	+ 3.16 e (M06-2X)

Short summary on AIM analysis of BCPs for V-O bond in V6OH

- (1) The average AIM charges of different O atom types are in the order: O6x < O3x < O2x < O1x.
- (2) The experimental and theoretical AIM charge analyses indicate that the V6 core takes a high negative charge, and OL part takes a positive one, which also illustrates that V6 core is a strong electron-reservoir.
- (3) The summations of AIM charges for V6 core and organic ligand from experiment and theory are quite similar.

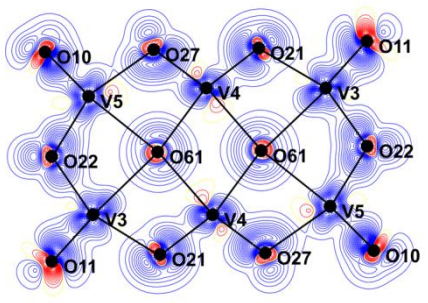
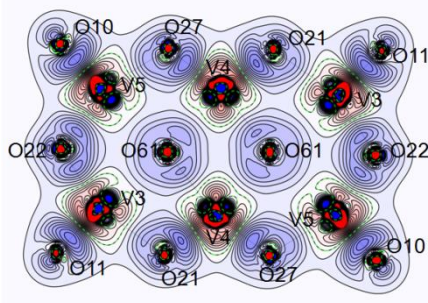
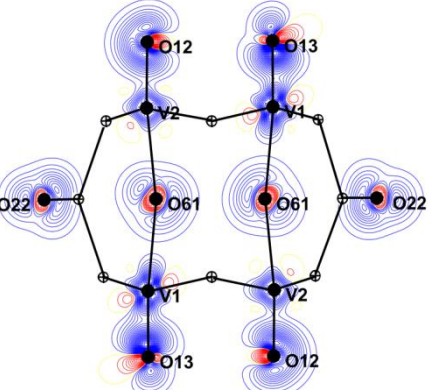
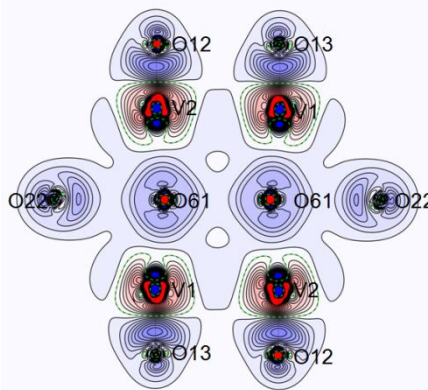
Electrostatic potential in V6OH

	Similarity	Difference	Experimental results	Theoretical results
EP mapped on molecular surface	Qualitatively similar	Experimental EP is higher than theoretical EP		

EP isovalue surface	High EP value distributed on V6 core			
Short summary on electrostatic potential of [V6OH]²⁻				
<p>(1) The most highest EP value is in the vicinity of O2x which is observed from both experiment and theory.</p> <p>(2) The V6 core exhibits high EP value due to more negative charge, which corresponds to nucleophilic molecular region. In contrary, the organic ligand is an electrophilic molecular region.</p> <p>(3) Generally, the experimental EP values are higher than theoretical ones.</p>				

5.2.3 V10 anion

Table 5.3. Comparative summary experimental and theoretical results of V10.

Charge density maps				
	Similarity	Difference	Experimental results	Theoretical results
Deformation density map for horizontal plane	Similar around O atom	Different in the vicinity of V		
Deformation density map for vertical-XZ plane	Similar around O atom	Different in the vicinity of V		

Topological analysis of BCPs for V-O bond in V10

	Similarity	Difference	Experimental results	Theoretical results
$\rho(\mathbf{r}_c)$ vs d (V-O)	Good agreement			
$\nabla^2\rho(\mathbf{r}_c)$ vs d (V-O)		Similar, slightly higher absolute values for experimental than theoretical		
$H(\mathbf{r}_c)$ vs d (V-O)	Excellent agreement			

Short summary on topological analysis of BCPs for V-O bond

- (1) The topological parameters of BCPs for V-O bond from MM and DFT calculations are in high agreement, especially the density $\rho(\mathbf{r}_c)$.
- (2) The absolute values of the topological properties ($\rho(\mathbf{r}_c)$, $\nabla^2\rho(\mathbf{r}_c)$, $H(\mathbf{r}_c)$) are in the order: O1x > O2x > O3x > O6x.
- (3) The experimental Laplacian values are higher than those obtained from DFT. See the explanation for V6-C3, Table 5.1.
- (4) The topological properties from M06/cc-pVTZ and M06/cc-pVTZ are quite similar. It indicates that M06-2X is well parameterized for V-O bonds.

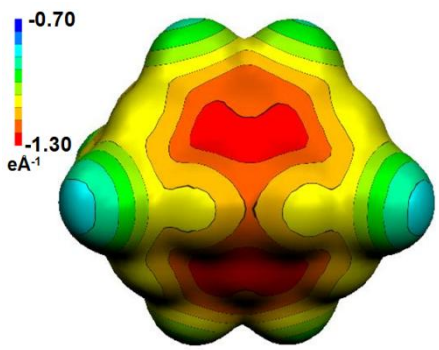
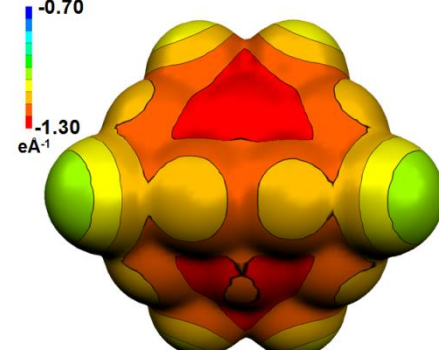
AIM charge analysis

	Similarity	Difference	Experimental results	Theoretical results
AIM charge of V atom (Average values)		The theoretical charge is more positive	+1.56 e	M06/cc-pVTZ: +2.27 e
AIM charge of O atom (Average values)		The theoretical charge is more negative	O1x (-0.64 e) > O6x (-0.72 e) > O2x (-0.81 e) > O3x (-0.90 e)	M06/cc-pVTZ: O1x (-0.89 e) > O2x (-1.04 e) > O3x (-1.21 e) > O6x (-1.33 e)

Short summary on AIM analysis of BCPs for V-O bond

(1) The theoretical AIM charges of O are in this order : $O1x > O2x > O3x > O6x$, which is also observed in V6-C3. The experimental AIM charges of O6x in V10 is not so much negative.

Electrostatic potential

	Similarity	Difference	Experimental results	Theoretical results
EP mapped on molecular surface		For each type of O atom, theoretical EP values are higher than experimental ones.		

Short summary on electrostatic potential of $[V10]^{8-}$

- (1) The EP values of O atoms are in the order: $O1x > O2x > O3x$.
- (2) The experimental and theoretical EP behaviour are in high agreement.

5.2.4 Conclusion

The three combined experimental and theoretical electron and electrostatic studies and the comparison made in the three previous sections allow us to make the following conclusions:

- (1) the experimental static deformation maps seems of better quality than the theoretical one due to the different treatments of the 4s population in the experimental or theoretical approach; the AIM charges of the oxygen atoms are influenced by the crystal packing, that explains some differences;
- (2) the summation of the experimental AIM charges belonging to the V6 core in V6-C3 (-9.76 e) is clearly more negative than the corresponding theoretical value (-5.12 e), while these values are almost the same for the V6-OH: -4.96 e from experience and -5.16 e from theory;
- (3) the EP values looks qualitatively the same. Quantitatively, the experimental EP is more negative than the theoretical ones. However, the EP values of V10 from experiment and theory are in high agreement, which indicates that the DFT can obtain more quantitative results of isolated V10 than that of functionalized V6 series;
- (4) the topological parameters are in excellent agreement, except that the experimental Laplacian is somewhat higher;
- (5) the other results are in excellent agreements.

These conclusions allow us to use all the results obtained in order to give some conclusions on the chemical bonding and reactivity.

5.3 A summary of charge density application in functionalized V6 compounds and decavanadate

Table 5.4 summarized the list of POV compound and specify results which will be used in the next chemical bonding, chemical reactivity discussions. Some simple semi-empirical calculations (Hirshfeld surface, Molecular Interaction Field) have been performed and will be added in the next sections. They have been mentioned in Table 5.4.

Table 5.4. List of POV compounds (ranked by theoretical energy order) and results, which will use in the next section for discussion (black symbol, •). The red symbol (•) means that the results exist but is not used in the next sections.

Compound		Crystallographic study			Ab initio calculations			Semi-empirical calculations		Properties	References ^[j]
Anion	Cation or Segment	Classical Single crystal	HR diffraction study	CSD statistical research	Method 1 ^[a]	Method 2 ^[b]	Other methods ^[c]	Hirshfeld surface ^[d]	MIF ^[e]	Bio-Activity ^{[f][g]}	
[V ₆ O ₁₉] ⁸⁻	-				•		•				Chapter 4
[V ₆ CH ₃] ²⁻	TBA										Chen, 1992b
	-					•	•	•	•		Chapter 4, 5
[V ₆ CH ₃] ²⁻	TBA			•						•	Chapter 5
	Na ⁺									•	Chapter 5
[V ₆ NH ₂] ²⁻	TBA	•		•							Chen, 1992b
	-				•		•	•	•		Chapter 4, 5
[V ₆ OH] ²⁻	TBA			•							Chen, 1992b
	Na ⁺ , H ₂ O	•	•	•							Chapter 3
	-					•	•	•	•		Chapter 4, 5
	TBA									•	Chapter 5
	Na ⁺ , H ₂ O									•	Chapter 5
[V ₆ NO ₂] ²⁻	TBA	•		•							Chen, 1992b
	-					•	•	•	•		Chapter 4, 5
	TBA									•	Chapter 5

[V6-C3] ²⁻	TBA	•									Wu, 2011
	TBA	•	•	•							Chapter 2
	-					•	•	•	•		Chapter 2, 4, 5
	TBA									•	Chapter 5
	H ⁺									•	Chapter 5
[V6-C6] ²⁻	TBA	•		•							Wu, 2011
	-					•	•				Chapter 4
[V6-C18] ²⁻	TBA	•		•							Wu, 2011
	-						•[h]	•	•		Chapter 4, 5
[V6-TPY] ²⁻	TBA	•		•							Santoni, 2011
	-					•	•	•	•		Chapter 4, 5
[V6-Fc] ²⁻	TBA, N(CH ₃) ₂ CHO	•		•			•[i]				Schulz, 2010
[V ₁₀ O ₂₈] ⁶⁻	-						•				Kempf, 1992
	[NH ₄] ⁺	•	•								Bognanović, 2007
	[NH ₄] ⁺									•	Krstić, 2009
	Na ⁺ , Cytosine	•	•								Bošnjaković, 2009
	Na ⁺ , Cytosine			•							Bošnjaković, 2011
	-					•		•			
All V6 ^[i]				•							Chapter 5

- [a]** Theoretical calculation by Gaussian/M06/cc-pVTZ;
- [b]** Theoretical calculation by Gaussian/M06-2X/cc-pVTZ;
- [c]** The other theoretical methods described in Table 4.1 of Chapter 4;
- [d]** Hirshfeld surface [Hirshfeld, 1976];
- [e]** MIF: Molecular interaction field, determined by Molecular Discovery-Grid [Cruciani, 2006];
- [f]** The tested V6 compounds are synthesis by Prof. Yongge Wei's group in Tsinghua University;
- [g]** Biological activity: in vitro inhibition on Na⁺/K⁺-ATPase tested by Dr. Danijela Krstić;
- [h]** Using the calculation way: Gaussian/M06-2X/6-311+G(d, p) for computer electrostatic potential;
- [i]** The cube files of total density and EP were kindly provided by Prof. Dr. Petr Stepnicka [Schulz, 2010], whose results are presented in Chapter 4 in a new way;
- [j]** Structures from tables 1.1 and A1.1 from which the hydrogen coordinates are available;
- [k]** References of the different results except the CSD statistical study presented in Chapter 5.

5.4 Electronic and topological properties of POV compounds

For a better understanding of electronic and topological properties of functionalized V6 series and V10, we have organized the charge density properties from “local” (electronic properties of O atoms or V atoms) to “non-local” (V-O bonding).

5.4.1 Charge density feature of V atom in POV structure

5.4.1.1 Atomic net charges

Table 5.5 lists the experimental and theoretical AIM charges of V atoms integrated for different {VO_x} (x = 1-6) compounds. Figure 5.1 represents the values found in the literature. We have decided to report on this graph the non-averaged values for the experimental charge density study and therefore highlights the wide range of the charge distribution of vanadium atom. This is the case for the (NH₄)V₁₀O₂₈·6H₂O for which the quality of the data was relatively poor. The experimental values obtained for V10, V6OH and V6-C3 are not too far, but in real disagreement with the theoretical ones.

Table 5.5. Experimental and theoretical AIM charge (e) of V atoms in all studied POV compounds and the other {VO_x} compounds.

Compound	V type	Experimental atomic net charge	Theoretical atomic net charge ^[e]
	{VO} ^[a]	-	+1.58
	{VO ₂ } ^[a]	-	+1.70
	{VO ₃ } ^[a]	-	+1.99
	{VO ₄ } ^[a]	-	+1.95
β -Na _x V ₂ O ₅ ^[b]	{VO ₅ }	+1.83 ^[f]	-
β -Na _x V ₂ O ₅ ^[b]	{VO ₆ }	+2.18 ^[f]	-
(NH ₄)V ₁₀ O ₂₈ ·6H ₂ O ^[c]		+1.6 - +2.0 ^[d]	-
V10		+1.56 ^[f]	+2.27
V6		-	+2.31
V6CH ₃		-	+2.48
V6NH ₂		-	+2.34

V6OH		+1.75 ^[f]	+2.48
V6NO₂			+2.48
V6-C3		+1.27 ^[f]	+2.23
V6-C6		-	+2.47
V6-TPY		-	+2.48

[a] Results from [Calatayud, 2001a]

[b] Results from [Ozerov, 2001]

[c] Results from [Bogdanovic, 2007]

[d] *k* charge is from *k* refinement, the different charge duo to the different chemical environment.

[e] Theoretical AIM charges obtained from AIMALL based on DFT calculation.

[f] Experimental AIM charges obtained from multipole refinement.

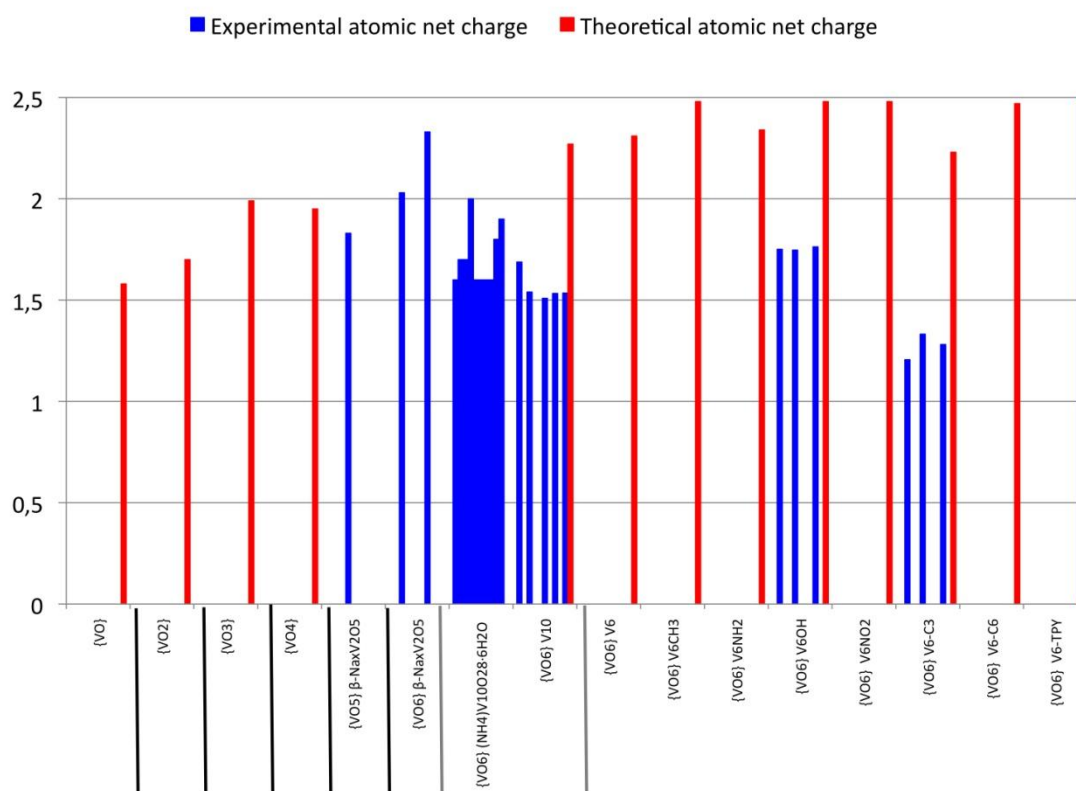


Figure 5.1. Experimental and theoretical (average) AIM charges for different POV compounds. References indicated in Table 5.5. Coordination sphere indicated in brace.

From Table 5.5, we can observe the atomic net charges of V atoms are followed in this order: {VO₆} > {VO₅} > {VO₄} > {VO₃} > {VO₂} > {VO}. Such observation indicates that the higher V coordination number is, the higher atomic net charges of V atoms are. This idea is very reasonable chemically speaking, the higher O connected to vanadium number is, the higher vanadium oxidation state is. This is

why isolated {VO6} does not exist; a high oxidation state of V atom induces an unstable {VO6}.

5.4.1.2 *d* orbital population

Due to the fact that V is an early transition metal, the determination of the *d* orbital populations of V atoms is very important to understand the electronic properties of V atoms in different chemical environments. However, such reported research is rare except the related result in vanadocene [Antipin, 1996] (Figure 5.2).

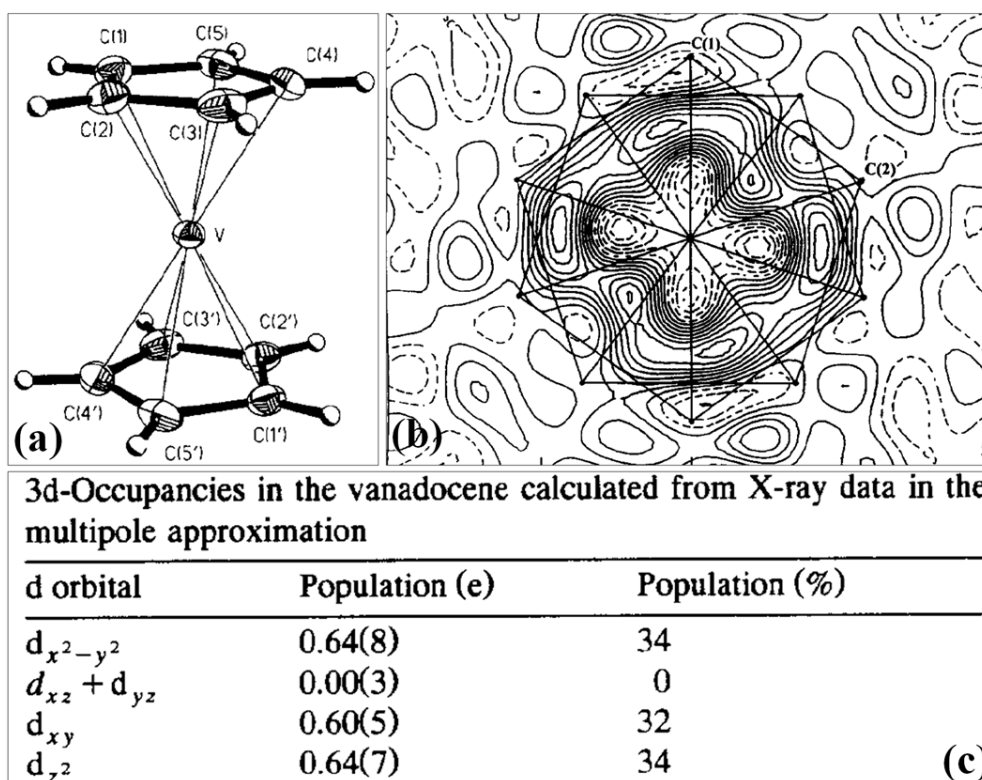


Figure 5.2. Experimental deformation density and *d* orbital population of V atom in vanadocene. (a) Structure of vanadocene; (b) Deformation density of V atom in the plane through V atom and parallel to Cp-ring plane; (c) *d* orbital population of V atom. The figure is produced from [Antipin, 1996].

The chemical environment of V atom in the vanadocene is totally different from those of functionalized V6 or V10. We can observe that the deformation density of V atom distributed symmetrically because the V atom localizes in the centrosymmetric position. In a plane parallel to the cyclopentadienyl, the density distribution is not too far from those observed for the functionalized V6-C3. However, Antipin *et al* [Antipin, 1996] find that only *d* orbital electrons populated in three directions due to the axial symmetry of the vanadocene molecule. In contrast, Farrugia *et al* [Farrugia,

2009a] have published an high resolution X-ray diffraction study of similar metallocene compounds, a ferrocene (Figure 5.3). We can observe that the populations of $d(xz)$ and $d(yz)$ are lower than others, but not equal to 0 due to non axial symmetry of the molecule around the Fe atom.

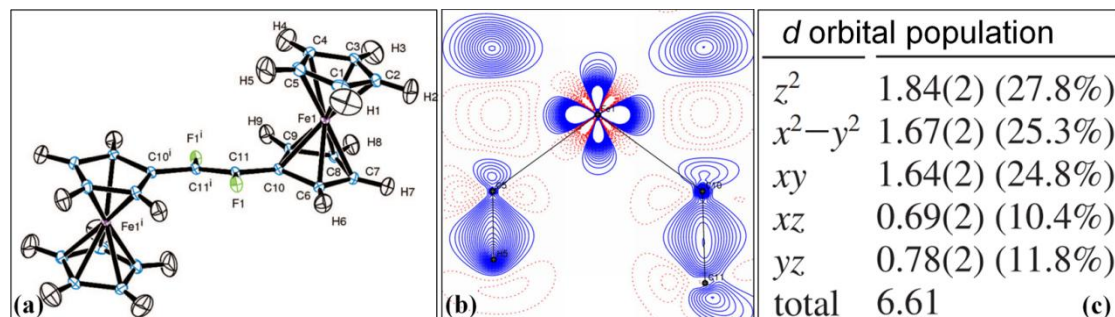


Figure 5.3. Experimental deformation density and d orbital population of Fe atom in ferrocene. (a) Structure of ferrocene; (b) Deformation density of Fe atom in the plane through V atom and parallel to Cp-ring plane; (c) d orbital population of V atom. The figure is produced from [Farrugia, 2009a].

In functionalized V6 series or V10, there are six O connections with V atom, as shown in Figure 5.4. We can observe that the density distribution is almost symmetrical, due to the chemical environment of V atoms. Table 5.6 lists the experimental and theoretical d orbital population of V atoms in POV compounds. We can conclude that:

- (1) The experimental d population occupy all the d orbitals. Due to the chemical environment of V atoms, the occupation percentages of each d orbital are in a relatively narrow range, e.g, 17.61% - 22.15% in V6OH; 16.80% -23.70% in V10. The results fit well with the deformation density distribution.
- (2) The theoretical d orbital populations of V atoms are in good agreement with the experimental ones;
- (3) Generally, for d block metals, the analysis of d orbital population can identify the density distribution and prove the quality of charge density refinement;
- (4) From Figure 5.4 b and d, we can observe that the experimental density distribution of V atoms in V6-C3 and V10 are similar; while in Figure 5.4 c, d, and f, the theoretical density distributions are similar, but too much concentrated;
- (5) For theoretical d orbital populations, the occupations is lower than the experimental ones, which leads to the higher positive AIM charges of V

atoms comparing with the experimental AIM charges.

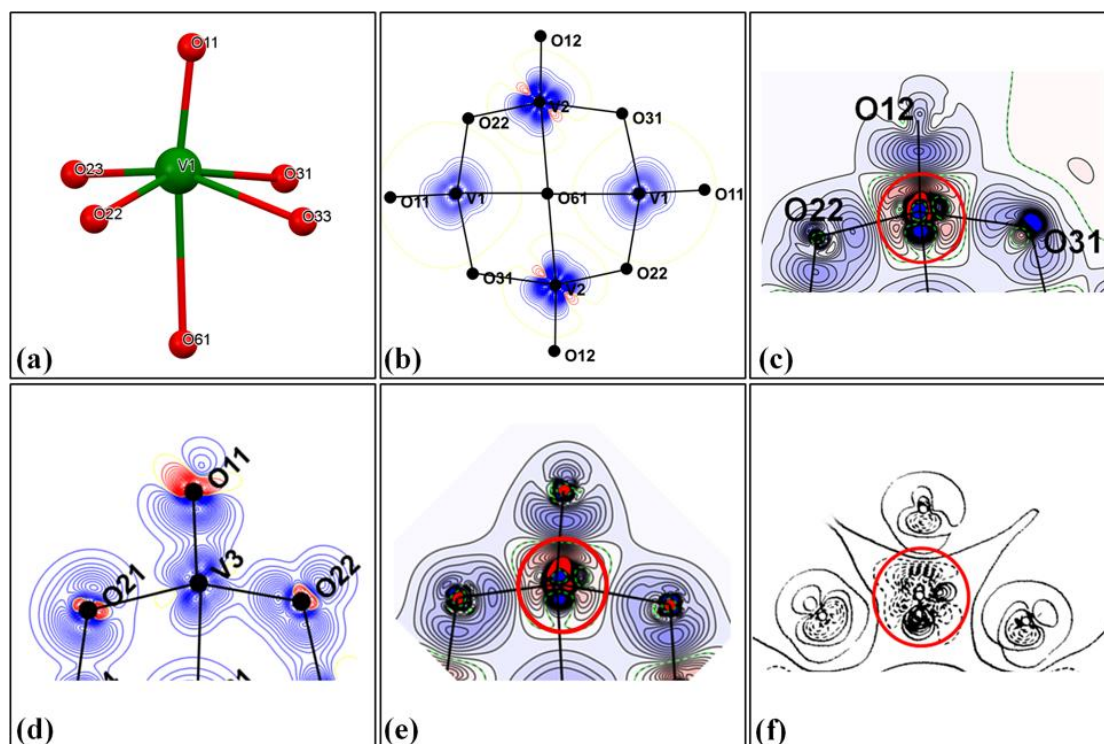


Figure 5.4. Experimental and theoretical deformation density of V atoms in POV. (a) The chemical environment; (b) experimental deformation density of V in V6-C3; (c) theoretical deformation density in V6-C3; (d) experimental deformation density in V10; (e) theoretical deformation density in V10; (f) theoretical deformation density in V10 from [Kempf, 1992].

Table 5.6. Experimental and theoretical determination of the *d* orbital (*e*) population of the vanadium in the V6-C3 and V10. In bold red the highest charge, in blue the lowest.

	V6-C3 by MM-1 ^[a]			V6-C3 by MM-2 ^[b]			V6-C3 by DFT			V6OH by MM-1			V10	
	V1	V2	V3	V1	V2	V3	V1	V2	V3	V1	V2	V3	V3	V5
<i>d</i> (<i>z</i> ²)	0.816	0.672	0.614	0.828	0.684	0.622	0.510	0.559	0.477	0.722	0.765	0.743	0.765	0.645
	22.83%	19.54%	17.85%	22.86%	19.64%	17.84%	17.77%	19.52%	16.64%	20.37%	21.73%	21.39%	23.70%	20.10%
<i>d</i> (<i>x</i> ² - <i>y</i> ²)	0.649	0.785	0.823	0.656	0.796	0.831	0.495	0.479	0.565	0.713	0.780	0.764	0.545	0.675
	18.15%	22.83%	23.93%	18.11%	22.85%	23.84%	17.26%	16.73%	19.75%	20.12%	22.15%	21.99%	16.80%	21.00%
<i>d</i> (<i>xy</i>)	0.543	0.753	0.720	0.553	0.775	0.727	0.670	0.653	0.658	0.721	0.688	0.668	0.599	0.619
	15.19%	21.90%	20.94%	15.27%	22.25%	20.85%	23.34%	22.77%	22.98%	20.34%	19.54%	19.23%	18.40%	19.10%
<i>d</i> (<i>xz</i>)	0.761	0.683	0.692	0.770	0.685	0.704	0.585	0.597	0.659	0.708	0.620	0.643	0.705	0.615
	21.29%	19.86%	20.12%	21.26%	19.67%	20.20%	20.39%	20.83%	23.01%	19.98%	17.61%	18.51%	21.80%	19.10%
<i>d</i> (<i>yz</i>)	0.806	0.546	0.590	0.815	0.543	0.602	0.609	0.577	0.505	0.680	0.667	0.656	0.625	0.664
	22.55%	15.88%	17.16%	22.50%	15.59%	17.27%	21.24%	20.15%	17.63%	19.19%	18.94%	18.88%	19.30%	20.70%
<i>d</i> orbital population	3.575	3.439	3.439	3.622	3.483	3.486	2.869	2.866	2.864	3.544	3.521	3.474	3.215	3.196

[a] MM-1: multipole refinement, strategy 1;

[b] MM-2: multipole refinement, strategy 2.

5.4.2 Charge density features of O atoms in POV structure

Table 5.7 lists the average AIM charges of different type of O atoms in POV compounds from experimental and theoretical charge density analyses.

Table 5.7. Experimental and theoretical AIM charge (e) of O atoms in all studied POV compounds.

	Compound	O1x	O2x	O3x	O6x
Experimental AIM charge from multipole refinement	V6-C3	-0.739	0.938	-1.040	-1.090
	V6OH	-0.615	-0.772	-1.012	-1.089
	V10	-0.644	-0.811	-0.896	-0.724
Theoretical AIM charge from DFT calculation	V10	-0.899	-1.040	-1.121	-1.329
	V6CH ₃	-0.845	-1.069	-1.180	-1.478
	V6NH ₂	-0.822	-1.008	-1.144	-1.365
	V6OH	-0.843	-1.070	-1.177	-1.478
	V6NO ₂	-0.829	-1.061	-1.190	-1.477
	V6-C3	-0.823	-1.000	-1.136	-1.369
	V6-C3	-0.845	-1.060	-1.190	-1.478
	V6-C6	-0.835	-1.049	-1.214	-1.474
Literature	V10 ^[a]	-0.870	-1.020	-	-1.510
	V6-TPY ^[b]	-0.550	-0.687	-0.740	-1.110

[a] AIM charge, from [Kempf, 1992]

[b] Natural charge, from [Schulz, 2010]

In § 2.4.2.2 and § 5.2, we have concluded that the average AIM charges of different types of O atoms are in the order: O6x < O3x < O2x < O1x. As presented in Table 5.7, we can observe that the experimental AIM charges of V6OH, and other theoretical AIM charge from DFT calculation or from literatures also show this behaviour, except the experimental AIM charge of O6x in V10 (in red in Table 5.2).

According to the oxygen valence, we propose that the atomic net charge of different O atoms in POV compounds are in the following order: O6x < O3x < O2x < O1x. To confirm the conjecture, we have found works on similar compound in the

literature. This order has already been observed in different theoretical calculations: the Mulliken charges deduced from *ab initio* SCF calculations in a V10 isolated anion, O6x (-1.27 e) < O3x (-1.04 e) < O2x (-0.90 e) < O1x (-0.65 e) [Kempf, 1992]; the charges from PACHA calculation for V10 isolated anion, O6x (-0.86 e) < O3x (-0.72 e) < O2x (-0.66 e) < O1x (-0.56 e) [Henry, 2002]; and also the natural charges by DFT calculation for a similar functionalized hexavanadate bearing two redox-active ferrocenyl groups at the end of organic ligand in the opposite sites reported by Schulz *et al.*, (Bu₄N)₂[FcC(O)NHC(CH₂O)₃V₆O₁₃(OCH₂)₃CNHC(O)Fc], O6x (-1.11 e) < O3x (-0.74 e) < O2x (-0.69 e) < O1x (-0.55 e) [Schulz, 2010] (Table 5.7). Additionally, Bridgeman *et al.* have also reported a similar trend in Mulliken charges and theoretical AIM charges for Lindqvist type POM cluster, [Mo₆O₁₉]²⁻ anion: O6x (-1.14 e, -1.37 e) < O2x (-0.69 e, -0.98 e) < O1x (-0.55 e, -0.82 e) [Bridgeman, 2003].

All the results enable us to consider that there is a relationship between the charge of O and the corresponding chemical environment. From the definition of O type in section 1.4.4, different O atoms connect with different number of V atoms *via* related type of V-O. Figure 5.5 displays the relationship between AIM charges of O atom and V-O distances. An excellent fit exists for the theoretical values (the green (V6-OH) and the orange line (V6-C3)). The experimental values display a larger discrepancy, but the trend, expressed by the blue and red curves remains the same.

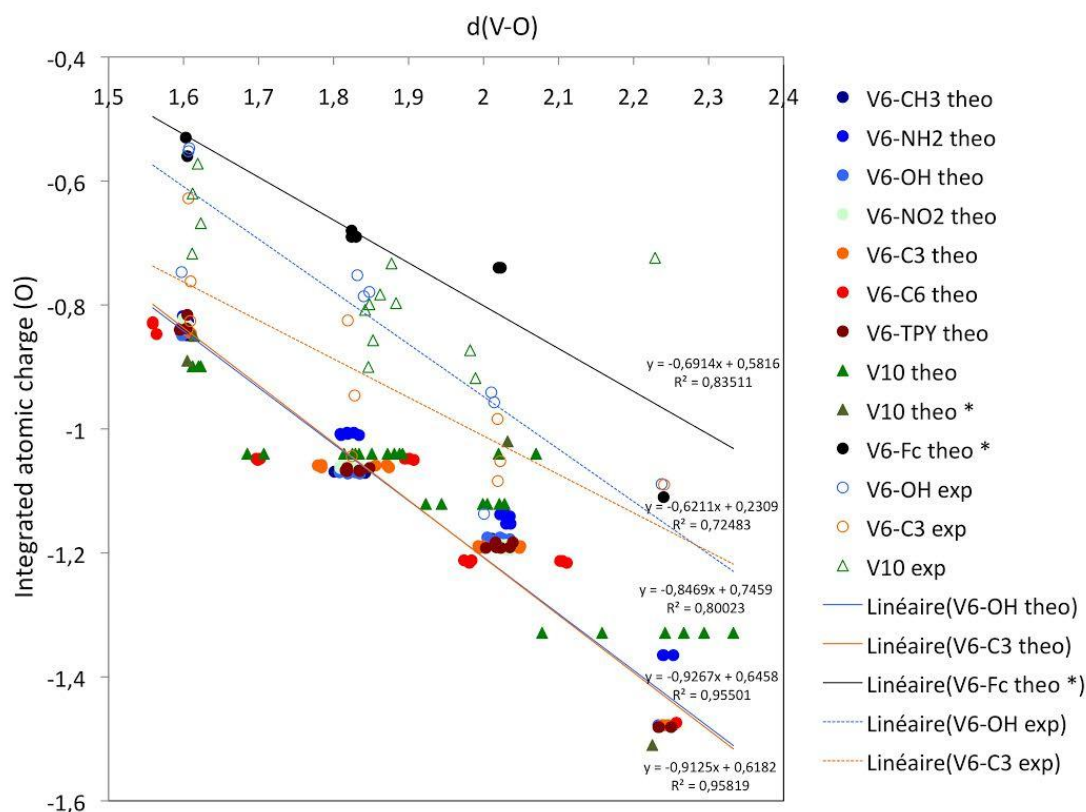


Figure 5.5. The relationship between AIM charges of O atoms and V-O distances

Generally, net atomic charges derived from experimental and theoretical densities are in good agreement, despite the fact that the theoretical calculations are based on an isolated molecule. Nevertheless, the AIM analysis gives a more rigorous definition of the charges of the atoms in molecules, thus provides a more reliable framework for comparison between molecules and between experiment and theory [Volkov, 2000].

We can conclude as follows:

- (1) In POV compounds, even POM compounds, the atomic net charges of O atoms are in the order : $O_{6x} < O_{3x} < O_{2x} < O_{1x}$;
- (2) Generally, the theoretical AIM charges are more negative than the experimental one. The probable reason is that the connected V atom have more positive AIM charges compared to experimental AIM charges of V atoms (+2.3e vs +1.3e);
- (3) The experimental and theoretical AIM charges of O show a good correlation with V-O distance, which can provide us some very useful predictable information for chemical bonding and chemical reactivity.

5.4.3 Chemical bonding in POV compounds

The chemical bonding of the V-O bonds can be described through the following tools:

- (1) Static deformation density (2D or 3D);
- (2) Laplacian maps (2D or 3D);
- (3) Topological parameters and their relationships;
- (4) Local source function.

The static deformation density maps are available in this work for only three compounds from both experiment and theory. The analysis could only be qualitative. Moreover, despite that these maps are at the origin of the charge density field, they depend on the reference (the promolecule). Therefore, we will not comment them more in this section, they have already been discussed for V6-C3, in § 2.4.2.1 (Figure 2.32).

The Laplacian maps have also been discussed in § 2.4.2.1 (Figure 2.32).

The local source function has been determined only for the experimental study of the V6-C3. The main conclusion are listed in § 2.4.2.1.

The topological parameters provide a useful tool and have been calculated for a series of functionalized V6. We will use these parameters to provide a classification of the V-O bonds. This will be presented in § 5.4.4.

5.4.4 Classification of V-O bonds based on topological parameters

In this work, we have the unique opportunity to carefully describe a M-L (M = vanadium, L = oxygen) bond based on a combined experimental and theoretical topological analysis. In fact, we have obtained the topological parameters of 202 V-O bonds determined from two experimental functionalized V6 (V6-C3 and V6-OH), seven theoretical functionalized V6 (V6CH₃, V6NH₂, V6OH, V6NO₂, V6-C3, V6-C6, V6-TPY), one experimental and one theoretical studies (V10). Gatti has summarized three classifications based on the topological parameters (Figure 1.8, § 1.2.8) [Gatti, 2005]. In the following section we will use these classifications to establish the nature of the vanadium – oxygen bonds.

The behavior of the different parameters are plotted in the Appendix, Figures A5.1 to A5.8. A small representation of these figures is given in Table 5.8, 5.9 and 5.10 according to the three classifications. A summary of these results is given in

tables 5.11, 5.12 and 5.13.

Considering the **first dichotomous classification** (Table 5.8), based on the sign of the $\nabla^2\rho(\mathbf{r}_c)$, there are height criteria, seven of which are accessible in our work (Table 5.11). It is clear that the character of a shared shell interaction decrease from V-O1x to V-O6x. Due to the behavior of the Laplacian ($\nabla^2\rho(\mathbf{r}_c) > 0$), some criteria of this classification indicate a closed shell interaction even though for V-O1x.

Considering the **second classification** (Table 5.9) based on the adimensional $|V(\mathbf{r}_c)| / G(\mathbf{r}_c) < 1$, one have to notice that we have had to define two new intermediate regions which have not been described by Gatti [Gatti, 2005]. The intermediate region n°2 (green square, Figure 5.6) corresponds to $\nabla^2\rho(\mathbf{r}_c) > 0$ and $H(\mathbf{r}_c) < 0$. This region has not been described initially by Gatti [Gatti, 2005]. All the V-O bonds belong to this region. That graph (Figure 5.6) is probably a pertinent way to describe such metal–organic bond (M-L). The V-O6x bonds are at the boundary between the intermediate region and the closed shell interaction. Hence, the softness degree of the closed shell interaction is too low than for usual closed shell interaction (Table 5.10).

Finally, the **third classification** based on the atomic valence shell and on both the local (bcp) and integral properties give quite clearly an open-shell character for the V-O1x bond as an open-shell character, while the other bonds present in this classification an intermediate or closed shell interaction, at least the open shell (metal-metal) can also be used.

In conclusion, the three classifications give for the V-O1x bond a pronounced character of shared-shell or open-shell, while the V-O6x is clearly of closed-shell type. The two other bonds V-O2x and V-O3x present an intermediate situation. This summarized in Table 5.14. According to these classifications the probably best representation of these M-L bonds is the graph of $\nabla^2\rho(\mathbf{r}_c)$ as a function of $H(\mathbf{r}_c)$ (Figure 5.6) where the V-O bonds are in the intermediate region corresponding to $\nabla^2\rho(\mathbf{r}_c) > 0$ and $H(\mathbf{r}_c) < 0$.

Another representation could be used to describe the chemical bond. It consists in the curve of the bond descriptor ($BD = H(\mathbf{r}_c) / \rho(\mathbf{r}_c)$) as a function of the adimensional ratio $V(\mathbf{r}_c) / G(\mathbf{r}_c)$ at the BCP. As far as we know, such a graph has only been published in the supplementary material by Wu *et al.* [Wu, 2011a] (Figure 5.7). Figure 5.8 represents our V6 data (experimental and theoretical) for the bonds contained in

the hexavanadate. According to the classification of Gatti [Gatti, 2005], if the $|V(\mathbf{r}_c)|/G(\mathbf{r}_c)$ adimensional ratio is greater than 2, it is a covalent bond; if the ratio is < 1 the bond is of closed-shell type (Figure 5.8). The correlation with the bond descriptor clearly put in evidence that the V-O bonds, even though the strongest one cannot be considered of the same type as a C-C or even a C-O bond. A polynomial function fits the theoretical values (Figure 5.9) with an excellent R ($> 98\%$). A zoom of this plot is given in Figure 5.10, where each V-Ox bond types are specified. This equation would describe the total energy density *per* electron as a function of the ratio of the potential energy over the kinetic energy for a specific M-L bond type.

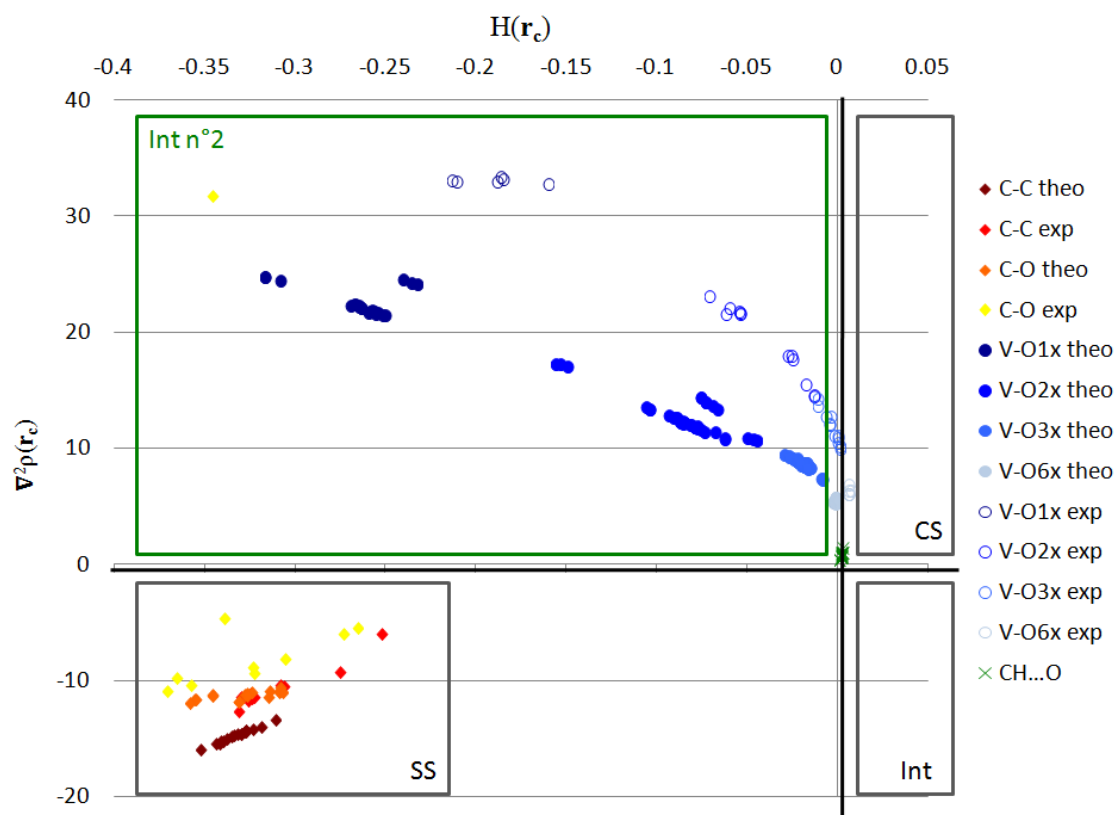


Figure 5.6. $\nabla^2\rho(\mathbf{r}_c)$ ($e\text{\AA}^{-5}$) as a function of $H(\mathbf{r}_c)$ (a.u.) for the V6 (experimental and theoretical). The grey squares represent the region defined by Gatti [Gatti, 2005]. The green square the new region, named intermediate n^2 .

Table 5.8. Dichotomous classification based on the sign of the $\nabla^2\rho(\mathbf{r}_c)$

Property	Shared-Shell (SS)	Inter-mediate (Int)	Closed-Shell (CS)	V-O1x	V-O2x	V-O3x	V-O6x	Figure
$\nabla^2\rho(\mathbf{r}_c)$	$\nabla^2\rho(\mathbf{r}_c) < 0$		$\nabla^2\rho(\mathbf{r}_c) > 0$	CS	CS	CS	CS	
Eigenvalue	$ \lambda_{1,2} / \lambda_3 > 1$		$ \lambda_{1,2} / \lambda_3 \ll 1$	SS	SS	SS	CS	
VSCC	Continuous		Atom-like	CS	CS	CS	CS	

$\rho(\mathbf{r}_c)$	Large		Small	SS	Int	CS	CS	
Energy lowering	By accumulating in the interatomic regions		$V(\mathbf{r})$ dominating separately localized within the boundaries of interacting atoms					No information
Energy components								
$2G(\mathbf{r}_c)/V(\mathbf{r}_c)$	$\frac{2G(\mathbf{r}_c)}{ V(\mathbf{r}_c) } < 1$		$2G(\mathbf{r}_c)/ V(\mathbf{r}_c) > 1$	CS	CS	CS	CS	

$G(\mathbf{r}_c) / \rho(\mathbf{r}_c)$	$G(\mathbf{r}_c) / \rho(\mathbf{r}_c) < 1$		$G(\mathbf{r}_c) / \rho(\mathbf{r}_c) > 1$	SS	SS	SS	SS	
$H(\mathbf{r}_c)$	$H(\mathbf{r}_c) < 0$		$H(\mathbf{r}_c)$ any value	SS	SS	CS	CS	

Table 5.9. Classification based on the adimensional $|V(\mathbf{r}_c)| / G(\mathbf{r}_c) < 1$.

Property	Shared-Shell (SS)	Intermediate (Int)	Closed-Shell (CS)	V-O1x	V-O2x	V-O3x	V-O6x	Figure
$ V(\mathbf{r}_c) / G(\mathbf{r}_c)$	$ V(\mathbf{r}_c) / G(\mathbf{r}_c) > 2$	$1 > V(\mathbf{r}_c) / G(\mathbf{r}_c) > 2$	$ V(\mathbf{r}_c) / G(\mathbf{r}_c) < 1$	Int	Int	Int	CS	
$\nabla^2\rho(\mathbf{r}_c) = f(H(\mathbf{r}_c))$	$H(\mathbf{r}_c) < 0$ & $\nabla^2\rho(\mathbf{r}_c) < 0$	$H(\mathbf{r}_c) < 0$ & $\nabla^2\rho(\mathbf{r}_c) > 0$	$(H(\mathbf{r}_c)) > 0$ & $\nabla^2\rho(\mathbf{r}_c) > 0$	Int (2)	Int (2)	Int (2)	Int (2)	

<p>Bond descriptor (BD) Covalency degree (CD) Softness degree (SD) $H(\mathbf{r}_c) / \rho(\mathbf{r}_c)$</p>	<p>BD = CD large and negative</p>	<p>BD \approx CD negative and smaller in magnitude than for SS</p>	<p>BD \approx SD positive and large</p>	<p>SS</p>	<p>Int</p>	<p>Int</p>	<p>Int (3)</p>	
---	--	--	---	-----------	------------	------------	----------------	--

Table 5.10. Classification based on the atomic valence shell and on both the local (bcp) and integral properties

Property	Light atoms			Metal-Metal		V-O1x	V-O2x	V-O3x	V-O6x	Figure
According to [Gatti, 2005]	Open-shell (covalent bonds); e.g. C-C, C-H, B-B	Intermediate interactions (polar bonds, donor-acceptor bonds; e.g. C-O, H ₃ B-CO	Closed-shell (ionic bonds, HBs, van der Waals interactions; e.g. LiF, H...O, Ne...Ne	Open-shell (e.g. Co-Co)	Donor acceptor (e.g. Co-As)					
According to [Cole, 2013]	Covalent	Polar shared	Ionic							
$\rho(\mathbf{r}_c)$	Large	Large	Small	Small	Small	Large	Int.	Int.	Int.	

$\nabla^2\rho(\mathbf{r}_e)$	$\ll 0$	Any value	> 0	≈ 0	> 0	> 0	> 0	> 0	≈ 0	
$G(\mathbf{r}_e)/\rho(\mathbf{r}_e)$	< 1	≥ 1	≥ 1	< 1	≈ 1	< 1	< 1	< 1	< 1	
$H(\mathbf{r}_e)/\rho(\mathbf{r}_e)$	$\ll 0$	$\ll 0$	> 0	< 0	< 0	$\ll 0$	< 0	< 0	≈ 0	

Table 5.11. Classification 1 (dichotomous classification based on the sign of the $\nabla^2\rho(\mathbf{r}_c)$), number of criteria fitted by each bond types.

	SS	Int	CS
V-O1x	4		3
V-O2x	3	1	3
V-O3x	2		5
V-O6x	1		6

Table 5.12. Classification 2 (classification based on the adimensional $|V(\mathbf{r}_c)|/G(\mathbf{r}_c) < 1$) number of criteria fitted by each bond types. Intermediate (1) = intermediate as defined by Gatti ($H(\mathbf{r}_c) > 0$, $\nabla^2\rho(\mathbf{r}_c) > 0$). Intermediate (2) = ($H(\mathbf{r}_c) < 0$, $\nabla^2\rho(\mathbf{r}_c) > 0$); Intermediate (3) = ($H \approx 0$, $\nabla^2\rho(\mathbf{r}_c) \approx 0$).

	SS	Int (1)	Int (2)	Int (3)	CS
V-O1x	1	1	1		
V-O2x		2	1		
V-O3x		2	1		
V-O6x			1	1	1

Table 5.13. Classification 3, (classification based on the atomic valence shell and on both the local (bcp) and integral properties) number of criteria fitted by each bond types.

	OS	Int	CS	OS (M-M)	Donor-acceptor
V-O1x	3	1	1		1
V-O2x		1	1	2	1
V-O3x		1	1	2	1
V-O6x		1	1	2	1

Table 5.14. Summary of the characterization via the three classifications.

	Classification 1	Classification 2	Classification 3
V-O1x	Int	Shared Shell	Open Shell
V-O2x	Int	Int (1)	Open Shell (M-M)
V-O3x	Int	Int (1)	Open Shell (M-M)
V-O6x	Closed Shell	Int (3) Closed Shell	Open Shell (M-M)

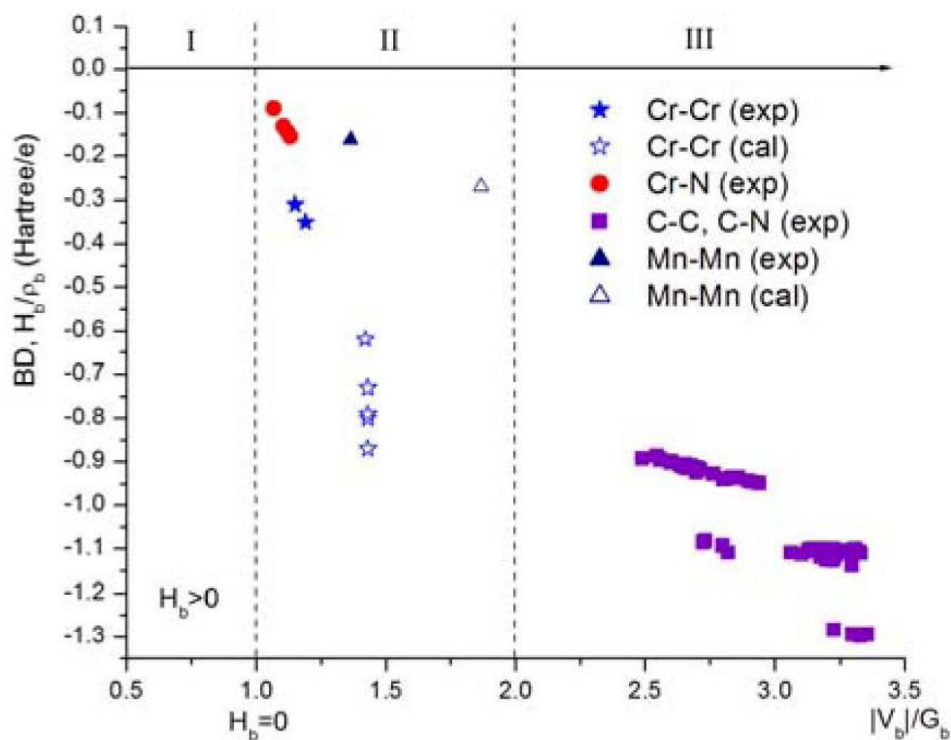


Figure 5.7. $V(r_c)/G(r_c)$ as a function of $H(r_c)/\rho(r_c)$ (a.u.) for some bonds. Reproduce from [Wu, 2011].

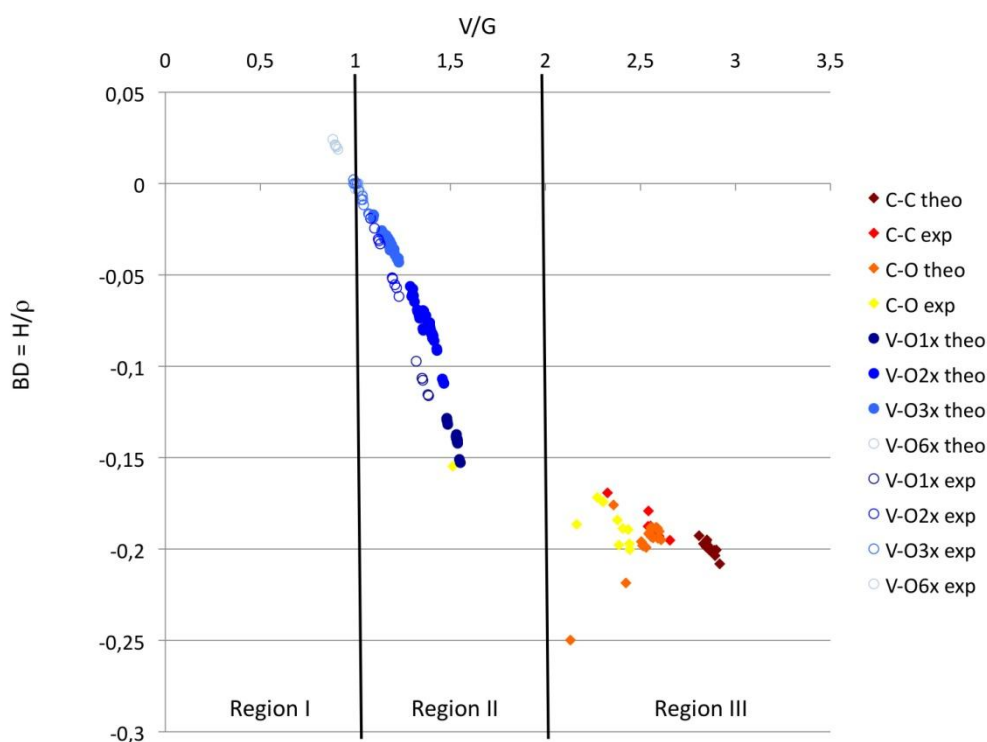


Figure 5.8. $V(r_c)/G(r_c)$ as a function of $H(r_c)/\rho(r_c)$ (a.u.) for the V6 (experimental and theoretical). Region I as closed-shell (CS), II as transit closed-shell and III as shared-shell (SS) interactions.

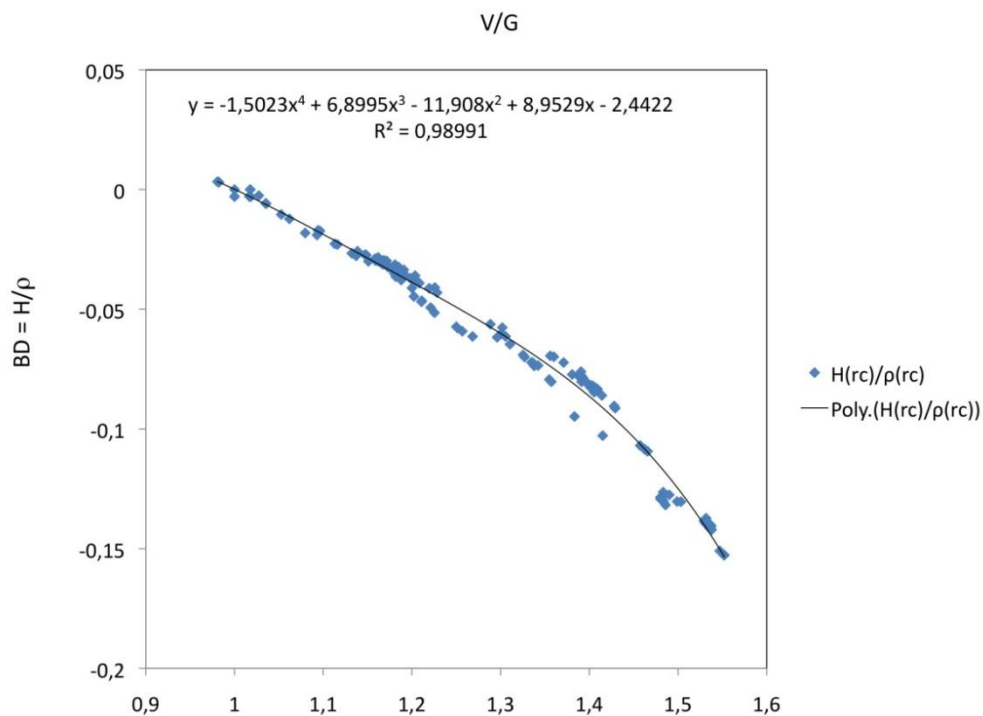


Figure 5.9. $V(r_c) / G(r_c)$ as a function of $H(r_c) / \rho(r_c)$ (a.u.) for all the V-O bond (theoretical).
Fit with a polynomial equation.

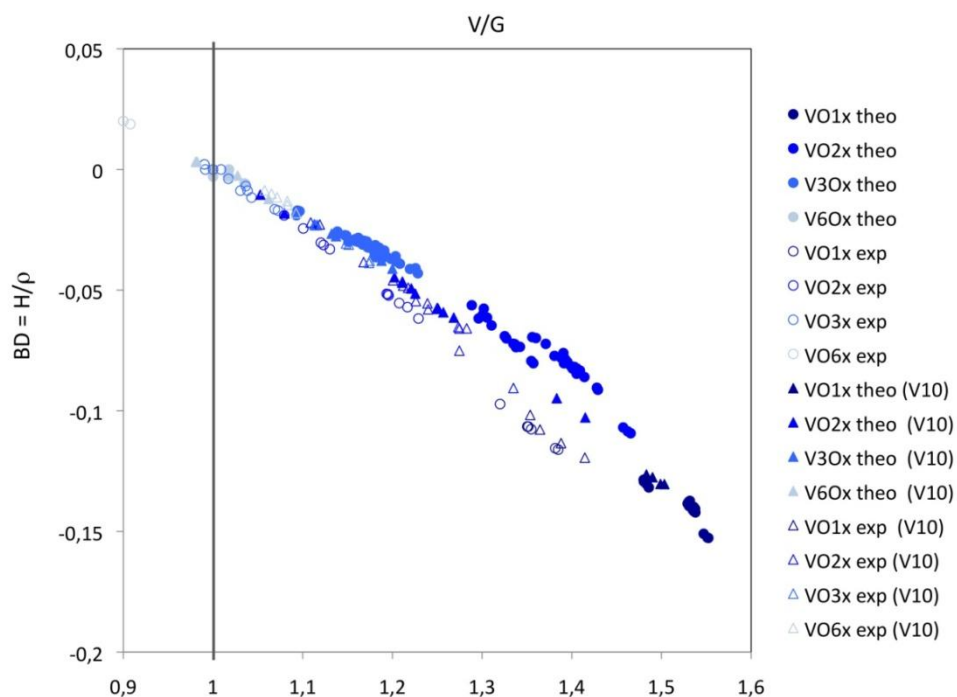


Figure 5.10. $V(r_c) / G(r_c)$ as a function of $H(r_c) / \rho(r_c)$ (a.u.) for all the V-O bond (experimental and theoretical). Limit between region I and II is indicated.

In order to examine if our curves (Figure 5.9) fit other metal-ligand bonds, we have retrieved from the literature the topology parameters ($\nabla^2\rho(\mathbf{r}_e)$ and $\rho(\mathbf{r}_e)$) determined after an experimental charge density study, for a large series of M-L bonds different from the V-O bonds. Figure 5.11a represents the position of these data compared with the V-O bonds, distributed by the ligand (O, N, S, B, Cl, H) while a decomposition by the metal is given in Figure 5.11b.

It is interesting to notice that the points which are closest to the strongest V-O bond belong mainly to the oxo bonds (Table 5.15). This result has appeared through a careful examination of the database containing actually 252 different bonds. That clearly means that the use of our graph (V/G, H/ ρ) to classify M-L bonds is pertinent. For these strongest bonds the energy potential dominates (>1.5), while the total energy density normalized by the density is quite low (-0.14 a.u.).

The dispersion of the (V/G, H/ ρ) from the curve we have determined for the V-O bond is greater as far as we are far from the V/G = 1, that means $H \approx 0$. The region where $H \approx 0$ is indicated inside the red lines (Figure 5.12, dashed lines).

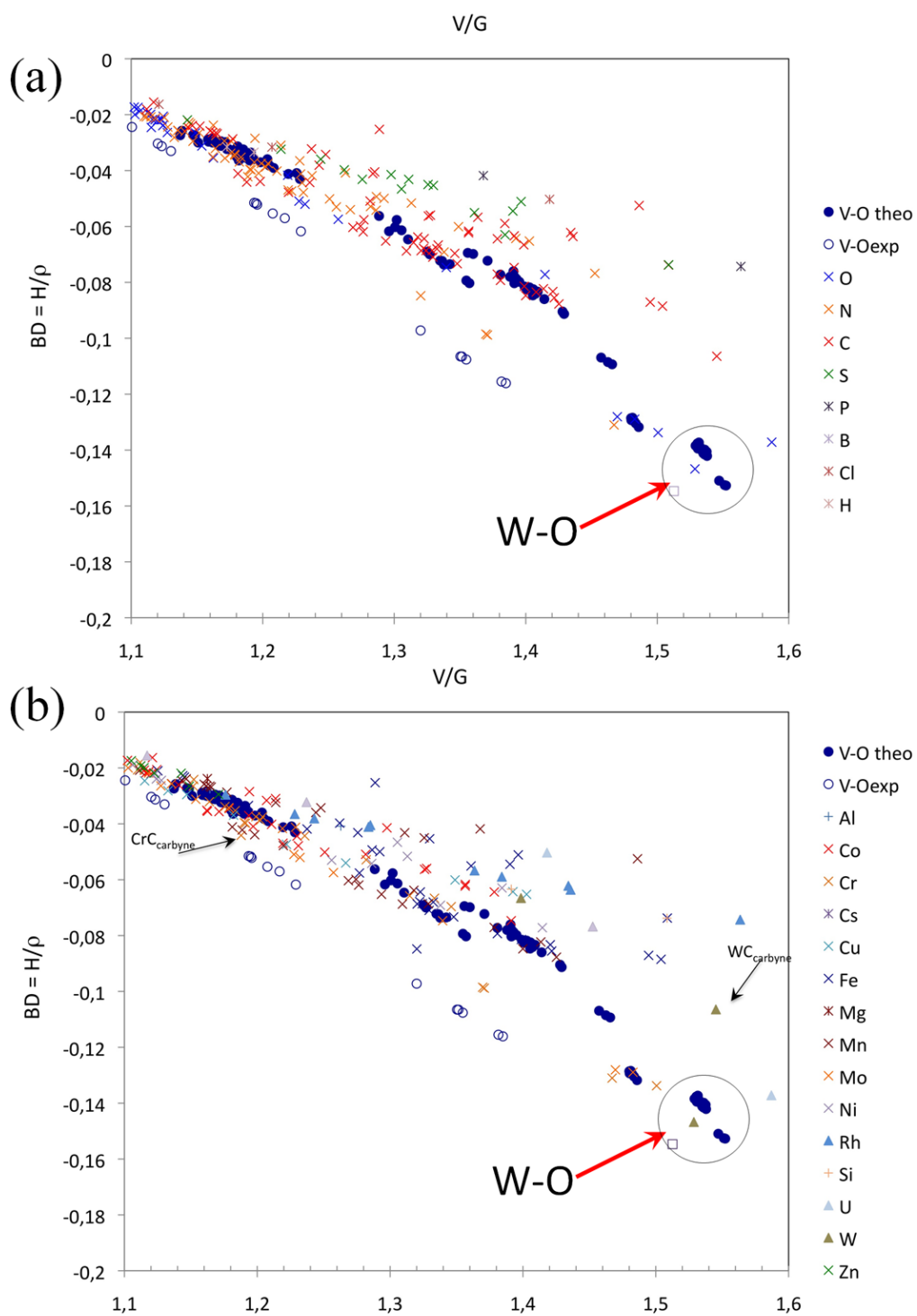
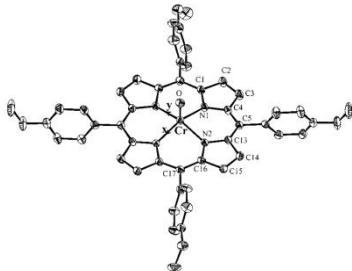
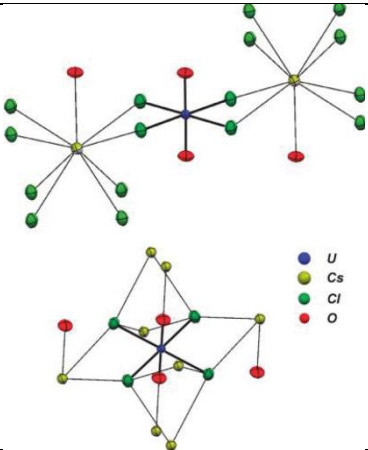
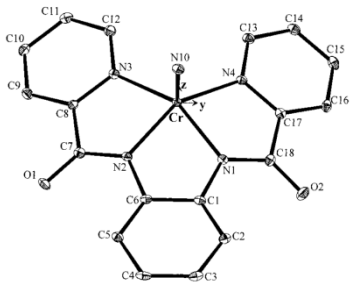


Figure 5.11. $V(r_c)/G(r_c)$ as a function of $H(r_c)/\rho(r_c)$ (a.u.) for all the V-O bonds (theoretical and experimental). (a) M-L data ranked by ligand; (b) M-L data ranked by metal. V-O1x are indicated by a circle.

Table 5.15. Compound possessing the closest couple (V/G , H/ρ) with those of $V-O1x$.

Bond type	V/G , H/ρ	Compounds	references
Cr-O (Oxo)	(1,50 ; -0,13)		Wang, 2000
W-O (Oxo)	(1,53 ; -0,15)	From theory	Wang, 2014
U-O	(1,59 ; -0,14)		Zhurov, 2011
Mo-O (Oxo)	(1,61 ; -0,16)	From theory	Wang, 2014
Cr-N (nitrido)	(1,71 ; -0,17)		Wang, 2000

We have also compared the M-L topological values on the simple plot as presented in Figure 5.6. The results are given in Figure 5.13. All, the M-L bonds remains in the same part of the graph ($\nabla^2\rho(\mathbf{r}_c) > 0$, $H(\mathbf{r}_c) < 0$), similar to those observe for the V-O bonds. This figure $\nabla^2\rho(\mathbf{r}_c) = f(\rho(\mathbf{r}_c))$ exhibits a larger dispersion for the M-L bond than the previous one.

In brief, we have been able to use the three classifications defined by Gatti [Gatti, 2005] to characterize the V-O bonds (Table 5.14 and Figure 5.6. Furthermore, we have used a new representation $H/\rho/ = f(V/G)$ which could provide a new descriptor of the metal-ligand bond.

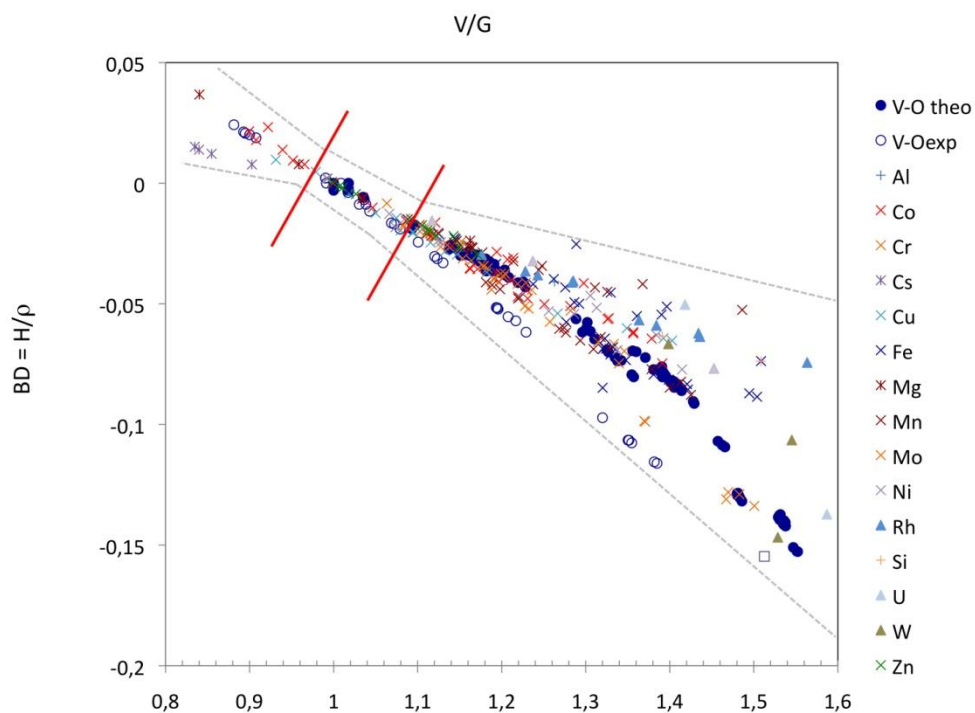


Figure 5.12. $V(r_c) / G(r_c)$ as a function of $H(r_c) / \rho(r_c)$ (a.u.) for all the V-O bond (theoretical and experimental). Symbol (x) concerns 3d metal involved in metal-ligand bonds.

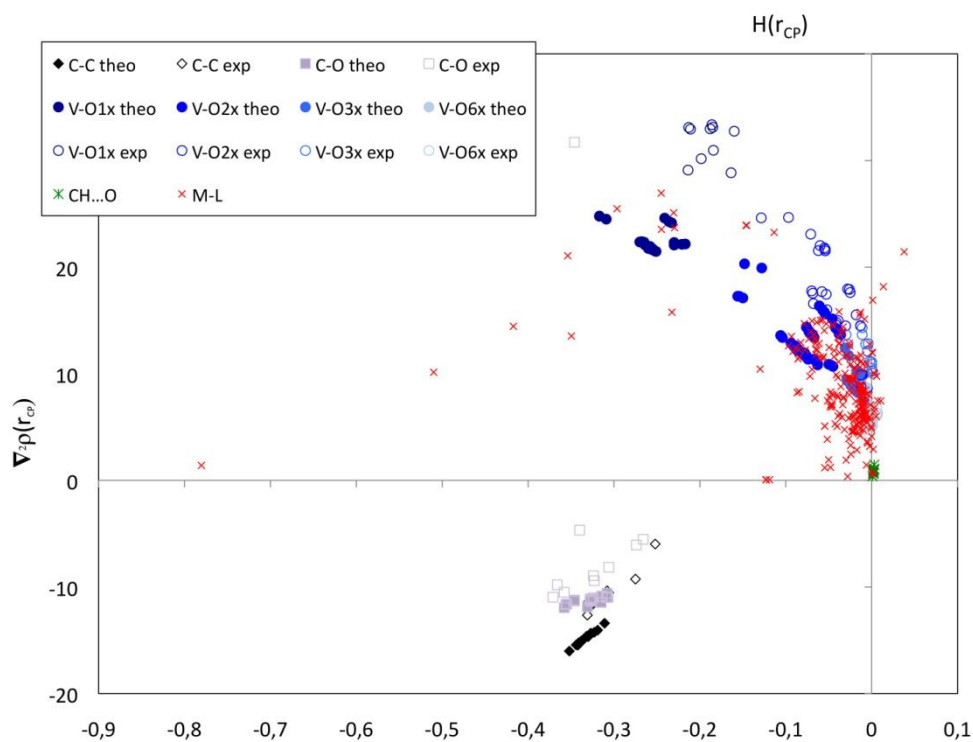


Figure 5.13. $\nabla^2\rho(r_c)$ ($e.\text{\AA}^{-5}$) as a function of $H(r_c)$ (a.u.) for the V6 (experimental and theoretical), V10 (experimental and theoretical) and all metal-ligand (red cross).

5.5 A better understanding of functionalization behavior by charge density analysis

In section 1.3.3, we have described the POM-based organic-inorganic hybrids. For class II, we call it organo-functionalized POMs. In the past 30 years, various organo-functionalized POMs have been synthesized and applied in various fields.

Organically functionalized POMs, *i.e.*, species where one or some oxo or $\{\text{Mo}_x\}^{n+}$ groups have been replaced with organic functional groups, have been extensively studied and now form the largest subclass of POM derivatives [Gouzerh, 1998]. Due to the “adding-value” of functionalized POMs, such classes of hybrid materials have received intense attention with their unique structures and potential novel properties. The functionalization of POMs or POVs are important, because:

- (1) Functionalization may result in the activation of surface {O-M-O} groups of POMs, thus giving more chances to be modified;
- (2) Functionalization can conduce to the stabilization of otherwise labile POM frameworks in the derivatives, providing novel building blocks for the assembly of larger systems;
- (3) The functionalized POMs are of special interest as model compounds for investigating the chemical reactions and properties;
- (4) The functionalized POMs can probably provide multifunctional oxidation or acidification catalysts that display selective recognition of substrates, thus higher selectivity, and might develop targeting of POMs in antiviral and anticancer chemotherapy.

However, the reasons listed above are from the chemist point of view, there is no direct experimental evidence to prove these assertions. Herein, there is a chance to understand the functionalization behavior by charge density analysis. We proposed, to utilize the chemical reactivity knowledge as a feasible way to reveal the functionalization behavior.

In particular, the functionalized hexavanadate (V6) and functionalized hexamolybdate (Mo6) are two important series as shown in Figure 5.14.

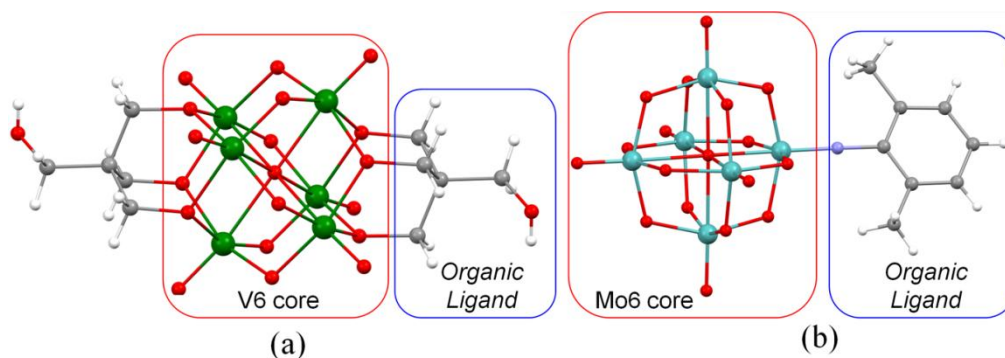


Figure 5.14. Functionalized V6 and Mo6. (a) $[V_6OH]^{2-}$; (b) $[Mo_6O_{18}(NC_6H_3(CH_3)_2)]^{2-}$

5.5.1 Functionalized hexavanadate

The synthesis process of V6OH has been described in § 3.2.1. For this reaction, we need to mention that the real reactant is $[V_{10}O_{28}]^{6-}$, which is described in [Chen, 1990]. In the solution, the reaction condition, $[V_{10}O_{28}]^{6-}$ can be transformed as $[V_6O_{19}]^{8-}$, which is not stable. The hydroxy derivative, like $R-C(CH_2OH)_3$, $R= CH_3$, NO_2 , OH , NH_2 , provides a useful precursor for condensation reactions coupling hexavanadate (V6) cores and for functionalization process. Based on the charge density analysis, we can illustrate such process as:

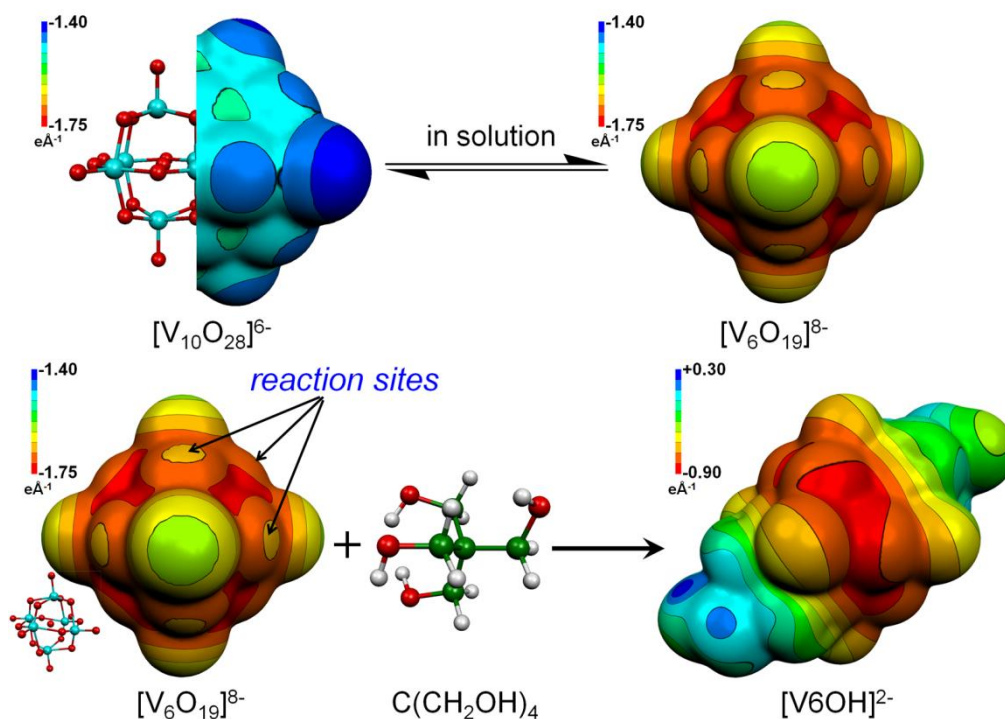


Figure 5.15. Functionalization process depicted by electrostatic potential.

From Figure 5.15, we can observe that:

- (1) The $[\text{V}_6\text{O}_{19}]^{8-}$ is extremely negatively charged, which makes itself not stable. Until now, a pure $[\text{V}_6\text{O}_{19}]^{8-}$ cannot be isolated;
- (2) The high negative charge of $[\text{V}_6\text{O}_{19}]^{8-}$ leads to a high electrostatic potential value $[-1.75 \text{ e}\text{\AA}^{-1}; -1.40 \text{ e}\text{\AA}^{-1}]$ in the vicinity of O atoms on the molecular surface. According to the EP distribution, we have established that the preferential reaction sites are O2x atoms, the bridged O atoms in §2.4.6.1;
- (3) The hydroxy derivative, like $\text{C}(\text{CH}_2\text{OH})_4$, have a potential to react with $[\text{V}_6\text{O}_{19}]^{8-}$ via a condensation reactions;
- (4) After the reaction, the functionalized V6 compound, V6OH, is obtained and characterized by single crystal X-ray diffraction experiment. The reason that a crystalline V6OH can be obtained, is that the functionalization process decreases the charges, and consequently the EP values decrease from $[-1.75 \text{ e}\text{\AA}^{-1}; -1.40 \text{ e}\text{\AA}^{-1}]$ to $[-0.90 \text{ e}\text{\AA}^{-1}; +0.30 \text{ e}\text{\AA}^{-1}]$. In other word, the functionalization enables the stabilization of V6 core.

In summary, we have used electrostatic potential to prove that the functionalization can stabilize the labile POV and generate a new POV cluster acting as a building block. The functionalized V6 compounds with a functional group, like –OH, NH_2 , can be used as a POV precursor reacted with other reactants, which has been described in section 2.2.1. Electrostatic potential can provide a meaningful chemical information to predict and explain the functionalization behaviour. In advance, EP can recognize the reaction sites, which could be a powerful tool to design a new series of functionalized POVs *via* a controllable synthesis.

5.5.2 Functionalized hexamolybdate

Inspired by the description of functionalization process in functionalized V6, we think that we can use EP to understand the functionalization behaviour. Unlike isolated $[\text{V}_6\text{O}_{19}]^{8-}$, the isolated Lindqvist type hexamolybdate, $[\text{Mo}_6\text{O}_{19}]^{2-}$ (Mo6), bearing only -2 e charge, which induces that it can be easily prepared and crystallized [Allcock, 1973]. The classification of O atoms in Mo6 is same with V6 (Figure 5.16). Furthermore, the description of the V-O bonds as shown (Figure 5.11 and Table 5.15) that the Mo-O (oxo) possess similar strength.

For the $[\text{Mo}_6\text{O}_{19}]^{2-}$, these terminal molybdyl groups ($\text{Mo}\equiv\text{O}$) are reactive enough for the terminal oxygen atoms to be directly replaced by various nitrogenous species,

for example, diazenido [Hsieh, 1983], diazoalkyl [Kwen, 1999], and imido groups [Du, 1992]. In the case of imido derivatives of the hexamolybdate, so far, the most important method is *DCC-dehydrating protocol*, developed by Wei *et.al* [Wei, 2001]. This method is used to functionalize $[\text{Mo}_6\text{O}_{19}]^{2-}$ in order to obtain a series of functionalized hexamolybdate, organoimido derivatives of the hexamolybdate.

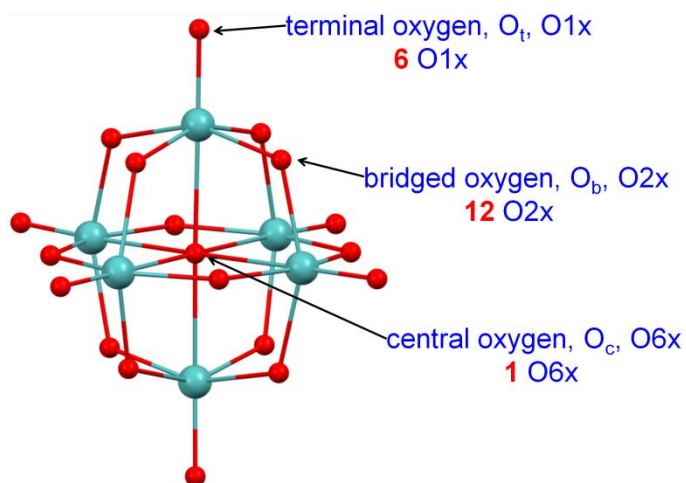
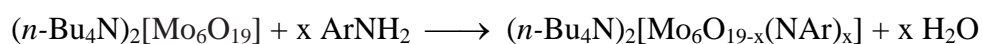


Figure 5. 16. Structure of $[\text{Mo}_6\text{O}_{19}]^{2-}$, [Allcock, 1973].

With this approach, the six terminal oxo, O1x (in certain case, some bridging-oxo groups, O2x) in the hexamolybdate cluster can be partially or completely substituted with organoimido ligands (Figure 5.17).



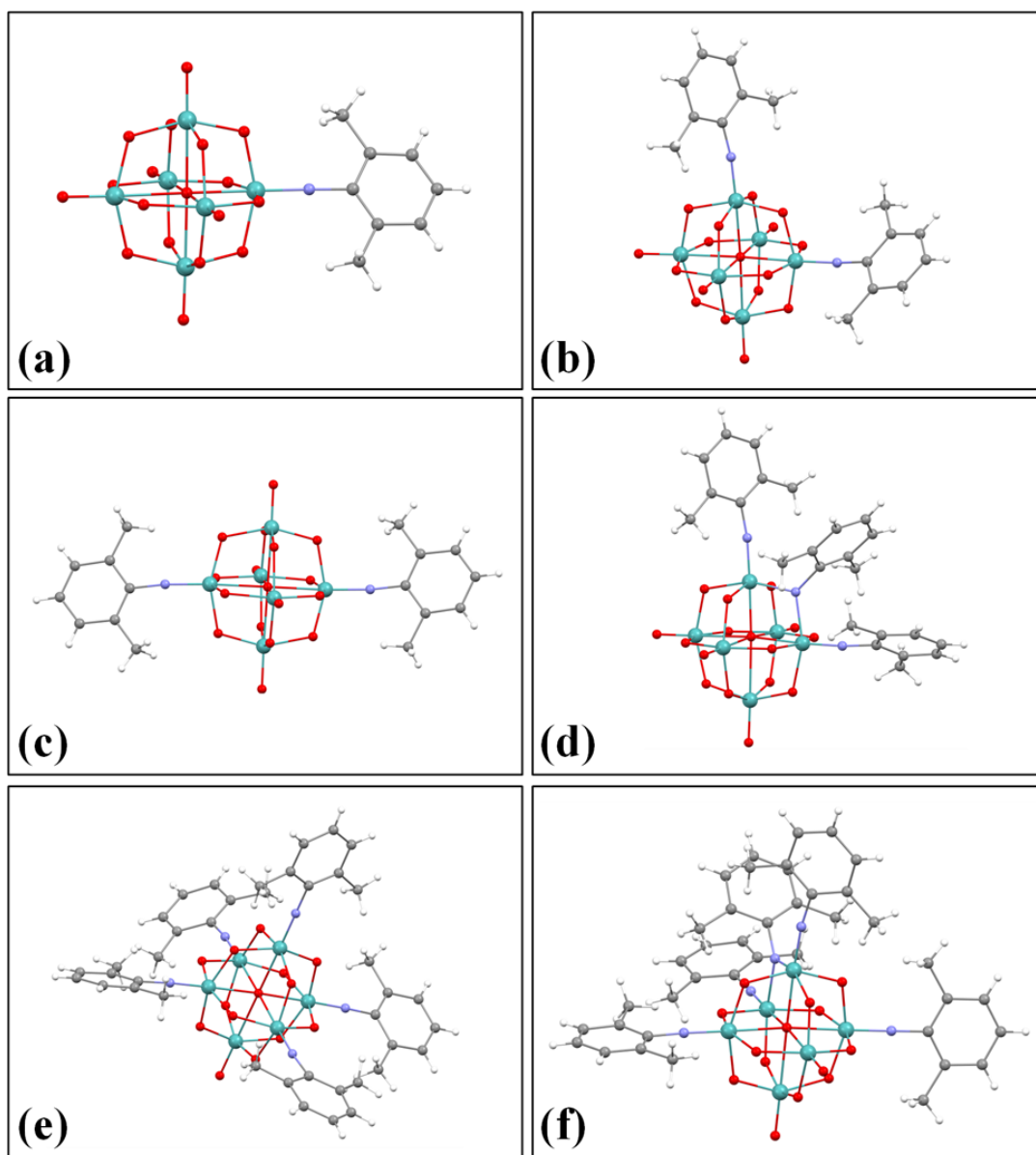


Figure 5.17. Functionalized hexamolybdate, organoimido derivatives of the hexamolybdate. (a) monosubstituted derivative, **Mo6-1**, CSD Cifcode: QIYLIT, [Wei, 200]; (b) cis-disubstituted derivative, **Mo6-2-cis**, CSD Cifcode: LULHUV, [Xu, 2002]; (c) trans-disubstituted derivative, **Mo6-2-trans**, CSD Cifcode: NAZBAS, [Xia, 2005]; (d) trisubstituted derivative, **Mo6-3**, CSD Cifcode: TIYGUE, [Hao, 2008]; (e) pentasubstituted derivatives I, **Mo6-5-I**, CSD Cifcode: TIYHAL, [Hao, 2008]; (f) pentasubstituted derivatives II, **Mo6-5-II**, CSD Cifcode: TIYHAL, [Hao, 2008].

There is no information about experimental charge density analysis of this series of functionalized Mo6. Therefore, we have performed DFT calculations on a series of functionalized Mo6 in order to understand their chemical reactivity in comparison with the functionalized V6 chemical reactivity. All the DFT calculations are performed by Gaussian 09 [Frisch, 2010] with B3LYP functional and LanL2DZ basis

set [Dunning, 1977].

The functionalization behaviour in Mo6 core is different with V6 core. Above all, we would like to explain why the functionalization occurs at O1x. To understand the EP distribution of isolated $[\text{Mo}_6\text{O}_{19}]^{2-}$, the precursor cluster of functionalized Mo6, can provide us some useful information. The electrostatic potential of isolated $[\text{Mo}_6\text{O}_{19}]^{2-}$ is presented in Figure 5.18 b. We can observe that the highest EP is in the vicinity of O2x, which is similar with V6 cluster. While we found that the EP values of O1x and O2x are very close (O1x: $0.404 \text{ e}\text{\AA}^{-1}$; O2x: $0.438 \text{ e}\text{\AA}^{-1}$).

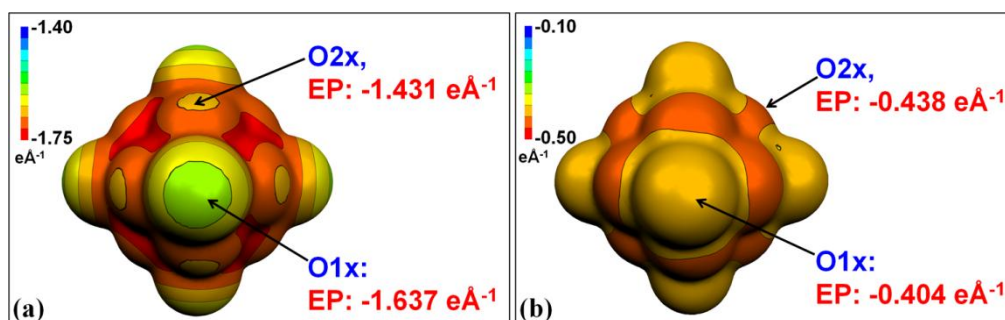


Figure 5.18. Electrostatic potential ($\text{e}\text{\AA}^{-1}$) mapped on molecular surface ($0.001 \text{ e}\text{\AA}^{-3}$). (a) isolated $[\text{V}_6\text{O}_{19}]^{8-}$; (b) isolated $[\text{Mo}_6\text{O}_{19}]^{2-}$.

The functionalization in the series is a substitution reaction, the electron effect and steric effects need to be considered at the same time. Obviously, the steric effect of Mo-O2x-Mo group is stronger than that of Mo-O1x group. Therefore, the undifferentiated EP distributions on the molecular surface enable that the preferential reaction sites are the O1x.

We mentioned above that there are different substituting degrees of functionalized Mo6. Using the two structure descriptors, atomic net charges and EP, can reveal the functionalization behaviors. The Mulliken charges of the compounds are listed in Table 5.16, and the electrostatic potentials of **Mo6-1**, **Mo6-2-cis**, **Mo6-2-trans**, **Mo6-3** are presented in Figure 5.19.

Table 5.16. Mulliken charges of functionalized hexamolybdates. The compound numbering is defined in Figure 5.17.

Atom type	Mo6	Mo6-1	Mo6-2- <i>cis</i>	Mo6-2- <i>trans</i>	Mo6-3	Mo6-5- I	Mo6-5- II
Mo	1.424	1.442	1.437	1.452	1.468	1.485	1.483
	1.424	1.404	1.418	1.452	1.463	1.483	1.456
	1.424	1.403	1.410	1.408	1.420	1.477	1.456
	1.424	1.403	1.408	1.408	1.413	1.464	1.454
	1.424	1.402	1.406	1.398	1.397	1.435	1.425
	1.424	1.392	1.399	1.398	1.386	1.426	1.425
Average	1.424	1.408	1.413	1.419	1.425	1.462	1.450
O1x	-0.429	-0.395	-0.401	-0.415	-0.399	-0.436	-0.431
	-0.429	-0.406	-0.408	-0.415	-0.407		-0.433
	-0.429	-0.406	-0.409	-0.417	-0.407		
	-0.429	-0.406	-0.409	-0.417	-0.410		
	-0.429	-0.410					
	-0.429						
Average	-0.429	-0.405	-0.407	-0.416	-0.406	-0.436	-0.432
O2x	-0.598	-0.607	-0.614	-0.609	-0.619	-0.623	-0.618
	-0.598	-0.609	-0.616	-0.616	-0.621	-0.623	-0.625
	-0.598	-0.610	-0.617	-0.617	-0.629	-0.635	-0.637
	-0.598	-0.620	-0.622	-0.622	-0.646	-0.642	-0.668
	-0.601	-0.606	-0.613	-0.609	-0.615	-0.623	-0.595
	-0.601	-0.608	-0.614	-0.610	-0.620	-0.623	-0.621
	-0.601	-0.609	-0.617	-0.617	-0.621	-0.635	-0.633
	-0.601	-0.615	-0.620	-0.617	-0.640	-0.640	-0.667
	-0.613	-0.608	-0.614	-0.610	-0.620	-0.623	-0.619
	-0.613	-0.609	-0.617	-0.616	-0.621	-0.625	-0.630
	-0.613	-0.613	-0.620	-0.617	-0.638	-0.639	-0.640
	-0.613	-0.620	-0.628	-0.622		-0.649	
Average	-0.604	-0.611	-0.618	-0.615	-0.626	-0.632	-0.632
O6x	-0.725	-0.754	-0.746	-0.749	-0.742	-0.728	-0.728
Average	-0.725	-0.754	-0.746	-0.749	-0.742	-0.728	-0.728
N		-0.558	-0.565	-0.567	-0.564	-0.584	-0.565
			-0.568	-0.567	-0.557	-0.588	-0.574
					-0.825	-0.592	-0.583
						-0.595	-0.591
Average	-	-0.558	-0.566	-0.567	-0.649	-0.591	-0.626
Mo6 Core	-2.000	-2.224	-2.439	-2.412	-2.652	-2.931	-2.972

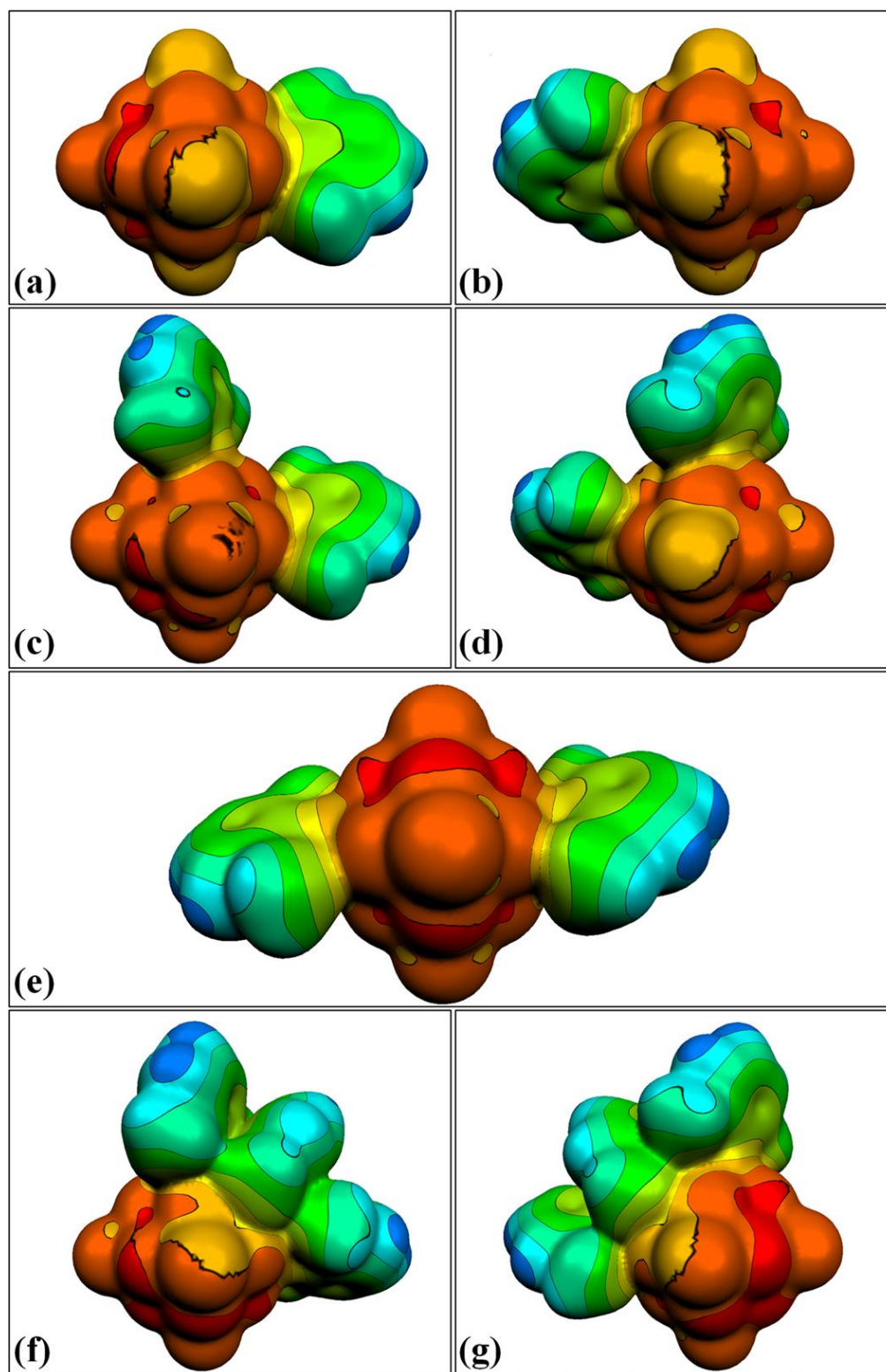


Figure 5.19. Electrostatic potential of functionalized hexamolybdate ($e\text{\AA}^{-1}$) mapped on molecular surface ($0.001 e\text{\AA}^{-3}$). The color scale is from red ($-0.50 e\text{\AA}^{-1}$) to blue ($-0.10 e\text{\AA}^{-1}$). (a) (b) monosubstituted derivative, **Mo6-1**; (c) (d) cis-disubstituted derivative, **Mo6-2-cis**; (e) trans-disubstituted derivative, **Mo6-2-trans**; (f) (g) trisubstituted derivative, **Mo6-3**.

We can describe the functionalization behaviours as follows:

- (1) The isolated $[\text{Mo}_6\text{O}_{19}]^{2-}$ is stable, because it takes less negative charge, and displays low EP distribution;
- (2) The most preferential reaction sites are the O1x due to the weak steric effect and adequate EP values;
- (3) Generally, the most negative EP distributions on the molecular surfaces of the isolated $[\text{Mo}_6\text{O}_{19}]^{2-}$ and functionalized Mo6 are in the vicinity of O2x;
- (4) From the Figure 5.19, we can observe that the functionalized Mo6 with different substituting degrees have different EP values. As the number of substituent groups increases, the EP value decreases. This is because the more organic parts, the Mo6 core can obtain more negative charges. From the Table 5.16, we notice that the Mo6 core absolute charges increase as the number of substituent groups increases (from -2 e to -2.97 e);
- (5) Due to the strong steric effect of O2x, it is hard to functionalize the Mo6 cluster at O2x position. When the two neighbouring O1x atoms are replaced by organic ligand, the Mo-O2x bond distances increased, leading to the activation of O2x is, which is in agreement with the conclusion from Wei *et al* [Hao, 2008]. Based on the conclusion in section 5.4.2, the longer distance M-O bond is , the more negative charge of O atom is (in *Mo6-2-cis*, O2x: -0.628 e). Hence, affected by the functionalization of two neighbouring O1x atoms, the electron density and EP distribution become higher. As the number of substituent groups increases, O2x is more activated (*i.e.*, possess a higher charge), which can be observed from the Table 5.16. The average charges of O2x increase from Mo6-1 (mono-functionalization) to Mo6-5 (penta-functionalization) compound;
- (6) As the number of substituent groups increase, the more negative charges of Mo6 core takes, the higher EP distribution around O2x is. In the later case, the chemists could synthesize functionalized Mo6 with a large number of substituent groups. However, as such number increasing, the O2x is less accessible, the steric effects becoming stronger and stronger. It is almost impossible to functionalize all the O2x, though the charges are low.

To conclude, in this section, we describe the functionalization behaviours in functionalized V6 series and functionalized Mo6 series. The structure descriptors,

atomic net charges and electrostatic potential, are the useful tools to understand the functionalization behaviours.

- (1) We can predict the probable reaction sites;
- (2) We can observe the different charge density distribution after different functionalization ways;
- (3) Based on the chemical information, especially, the information about chemical reactivity, we can design some new functionalized V6 or Mo series, which is called controllable synthesis;
- (4) This way can be extended to the other fields, e.g., organometallic chemistry and drug discovery, we can design the organometallic complexes with high stereoselectivity for the asymmetric reaction.

5.6 Charge density analysis of charge transfer behavior and fluorescence in POM/POV-based material

5.6.1 POM/POV-based charge transfer material

Charge transfer materials have attracted increasing attentions in recent years due to their roles in the fields of semiconductors [Zhu, 2009], solar cells [Zhao, 2012], metal organic frameworks (MOFs) [Miyasaka, 2013], fluorescent materials [Grabowski, 2003], and catalysts [Akimov, 2013], [Sadakane, 1998]. According to Mulliken's theory [Mulliken, 1952; Orgel, 1957; Mulliken, 1962; Mulliken, 1964], charge transfer (CT) system (Figure 5.20) is formed by an electron donor (D) and an electron acceptor (A), D and A could be two different molecules or ions, leading to intermolecular CT, or separate moieties within a large molecule, leading to intramolecular charge transfer (ICT) [Grabowski, 2003].

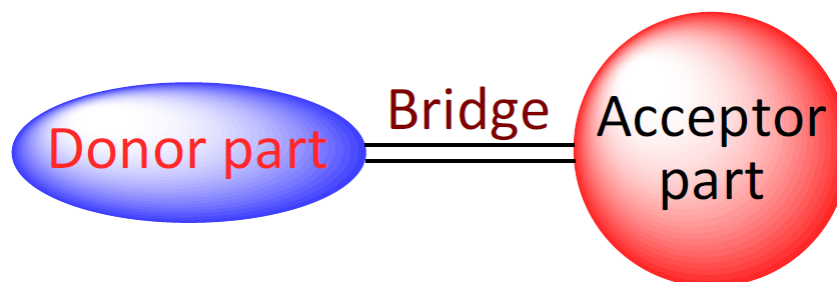


Figure 5.20. Schematic representation of charge transfer system and charge transfer interaction.

POMs are well-known electron acceptors in CT materials prepared with organic donors, which is based on the ability of POMs to act as electron reservoirs [Yamase, 1998; Coronado, 2005]. The synergistic combination of POM acceptors and organic donors gives to the CT materials some important potential properties (Figure 5.21). For example, the CT materials containing the spherical POM acceptors (Lindqvist-type $[\text{Mo}_6\text{O}_{19}]^{2-}$, Keggin-type $[\text{SiMo}_{12}\text{O}_{40}]^{4-}$) and planar arene donors exhibit unique structures, potential nonlinear optical and ferromagnetic properties [Maguerès, 2000]. Different POMs acceptors connecting with ferrocenyl donors have exhibited various spectroscopic properties and broad CT bands [Veya, 1995; Stark, 1995; Kang, 2004; Xu, 2010; Niu, 2010]. TTF-POMs CT materials show semiconductor properties and have a potential application in semiconductor devices [Coronado, 2005; Tsunashima, 2012; Li, 2011].

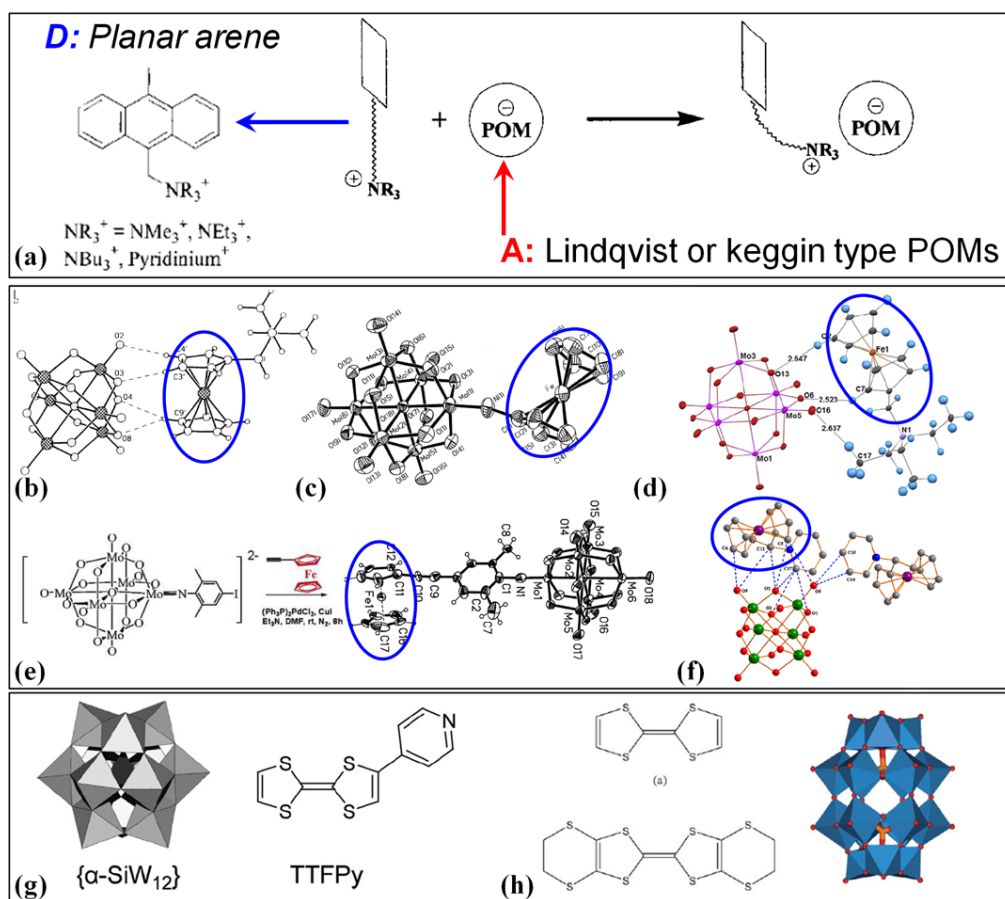


Figure 5.21. POM-based charge transfer materials. (a) planar arene donor [Maguerès, 2000]; (b) (c) (d) (e) (f) ferrocenyl donors [Veya, 1995; Stark, 1995; Xu, 2010; Kang, 2004; Niu, 2010]; (g) (h) TTF donor, TTF = tetrathiafulvalene [Tsunashima, 2012; Li, 2011].

Obviously, there are two types of POM-based charge transfer materials: i) POM-based intermolecular charge transfer materials for which the interaction between

organic donor and POM acceptors is non-covalent; ii) POM-based intramolecular charge transfer materials for which the D and A parts are covalently bonded. Hence, to understand the charge transfer behaviours in POM-based materials, it is necessary to prove that the POM electron acceptors are the electron reservoirs. In other word, the characterization of POM cluster possessing the ability of reserving the electrons could reveal the charge transfer behaviours. Therefore, some questions arise:

- (1) Which amount of negative charge can POM take?
- (2) If POM part takes a high negative charge, how it will looks like?
- (3) How does POM part obtain the negative charge?

However, up to now, the most widely methods used for the experimental CT behavior description are various spectroscopic characterizations, which only give indirect experimental evidences [Re, 2003; Benson-Smith, 2007].

A better knowledge of the experimental atomic charge distribution is needed for a more precise description of CT compounds. These results would be used as a direct evidence of CT behavior. It has been established that accurate charge density and electrostatic properties can give precise information on the CT behavior especially in the following aspects: i) the regions where the electrostatic potential are negative / positive give an idea of the D and A groups, ii) the atomic net charges of the different groups determine the amount of the charge transferred between D and A [Ortmann, 1992; Gikas, 2005; Meindl, 20009; Jiang, 2011; Kotova, 2011]. Therefore, charge density analysis on functionalized V6 clusters would be a promising approach to understand their CT behavior.

If we consider the questions listed above from a charge density point of view, which are the structure descriptors which can identify such behaviours? The answers are:

- (1) The determination of the POM atomic net charges can figure out the charge distribution of D and A parts;
- (2) The electrostatic potential can recognize different the nucleophilic / electrophilic molecular regions;
- (3) The source function as a topological indicator can reveal how the charge is transferred from D to A.

The chemical information about atomic net charges, EP and source function have been presented and discussed in the previous chapters for functionalized V6-C3 (§ 2.4.6). In this section, we will try to understand their consequences on the CT

behavior in functionalized POVs and POMs.

1. POV-based charge transfer materials:

In functionalized V6 series, the V6 core acts as the POV electron acceptor, while the organic ligands are the electron donors, which constitute an intramolecular charge transfer (ICT) system (Figure 5.22).

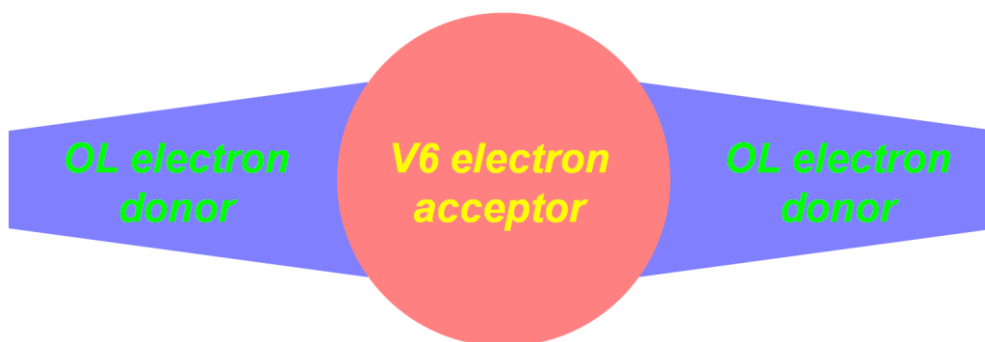


Figure 5.22. Functionalized V6 based intramolecular charge transfer system.

The three structure descriptors mentioned above are presented in Figure 5.23.

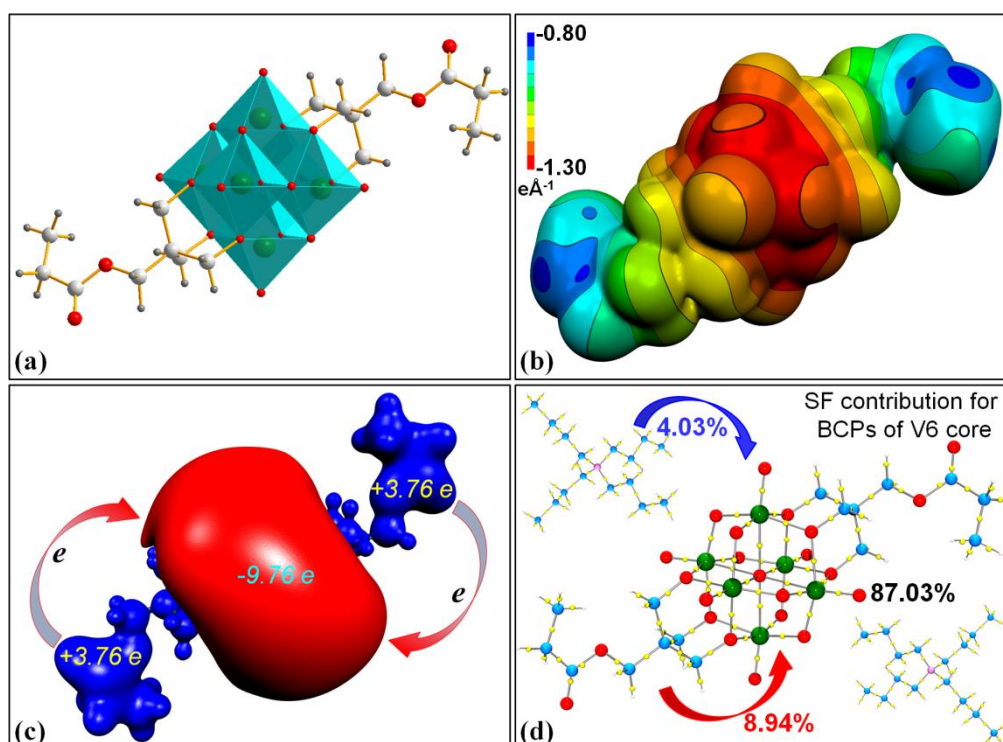


Figure 5.23. Description of charge transfer behavior based on experimental evidences in functionalized V6. (a) The octahedral structure of $[V6-C3]^{2-}$; (b) EP mapped on molecular surface ($0.001 e\text{\AA}^{-3}$); (c) EP isovalue surface (cutoff $\pm 0.75 e\text{\AA}^{-1}$). The AIM charges of D and A are indicated; (d) Source function contribution to BCPs of D (V6 core) from three parts of crystalline V6-C3.

We describe the CT behavior as follows:

- (1) For functionalized $[V6-C3]^{2-}$, there is an intramolecular charge transfer between V6 core and organic ligand. We can observe such behavior from AIM charge distributions in POV acceptor and OL donors (Figure 5.23 c);
- (2) We can observe that POV acceptor concentrates the most negative charge (Figure 5.23 b);
- (3) The EP distribution, especially the isovalue EP surface, distinctly exhibits the D and A parts (Figure 5.23 c);
- (4) The SF contribution to the BCPs in POV acceptor reveals that there are 12.97 % electron density at BCPs from OL donors and TBA cations (Figure 5.23 d).

In brief, the three structure descriptors enable us to understand that the V6 core is a strong electron reservoir, which could reserve much negative charge from OL donor. This is a direct evidence from the experimental charge density determination.

In advance, from a theoretical point of view, only two structure descriptors are available the EP and the AIM charges. Qualitatively, we have observed that these values differ significantly from the experimental values but still comparable inside the series. According to the charges belonging to the V6 core, the trend from the best electron reservoir in the series is the following: $V6-C6 > V6NH_2 > V6-C3 > V6CH_3 > V6OH > V6NO_2$.

2. POM-based charge transfer materials:

The charge transfer behavior of functionalized Mo6 is similar to that of functionalized V6. Actually, the evidences from theoretical charge density analysis have been presented in § 5.5.2. Using those results in Figure 5.18, 5.19 and Table 5.16, combined with the isovalue EP surface in Figure 5.24, as the established method for describing CT behavior in functionalized V6, we can also observe that the CT behavior occurs in functionalized POMs.

- (1) The Mulliken charges of Mo6 electron acceptor in different functionalized POM series are from -2.00 e to -2.97 e (Table 5.16), which reveals that POM electron acceptor have the ability of reserving electron;
- (2) We also notice that the negative EP surface of POM is expanded more and more as the number of substituent groups increases.

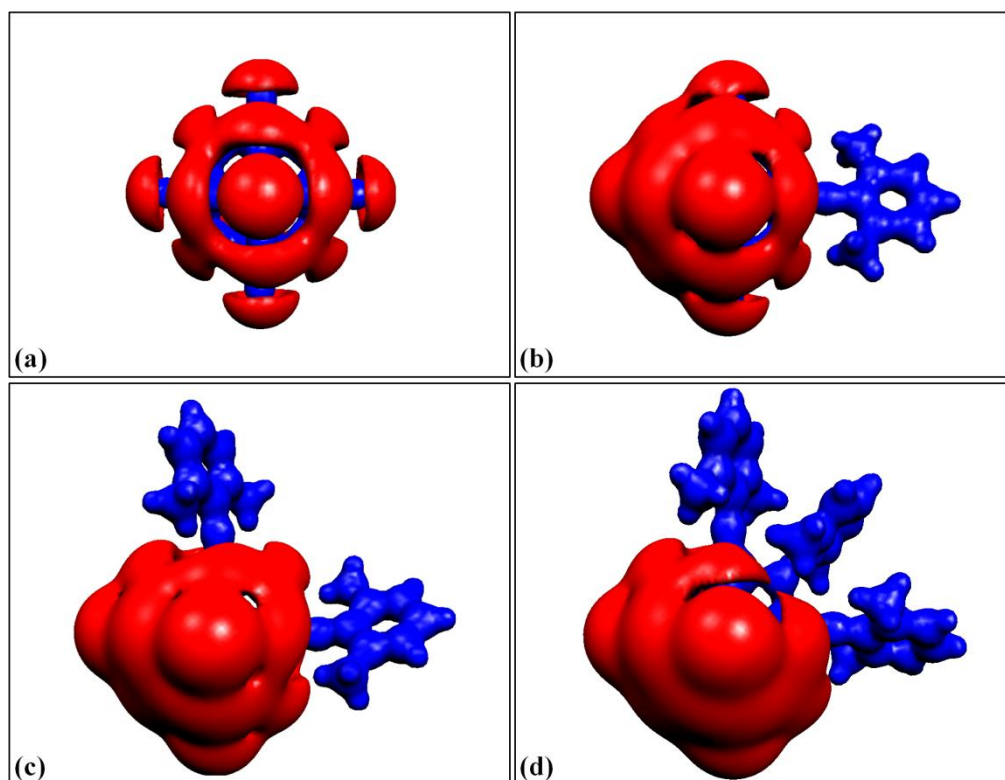


Figure 5.24. EP isovalue surfaces (cutoff $\pm 0.40 e \text{ \AA}^{-1}$) of Mo6 cluster and functionalized Mo6 series. (a) isolated Mo6 cluster; (b) monosubstituted derivative, **Mo6-1**; (c) cis-disubstituted derivative, **Mo6-2-cis**; (d) trisubstituted derivative, **Mo6-3**.

5.6.2 POV-based fluorescent material

POMs and POVs have long been considered as the luminescence quenchers [Anderson, 2004]. However, a few examples have shown that the POV/POM-based materials exhibit fluorescence. Especially the POV-based materials give the blue luminescent emission in solution [Yamase, 1994; Chen, 2005; Chen, 2009; Ma, 2011]. The oxide-to-vanadium charge transfer and intervalence charge transfer could be the probable reasons. Two examples are presented in Figure 5.25.

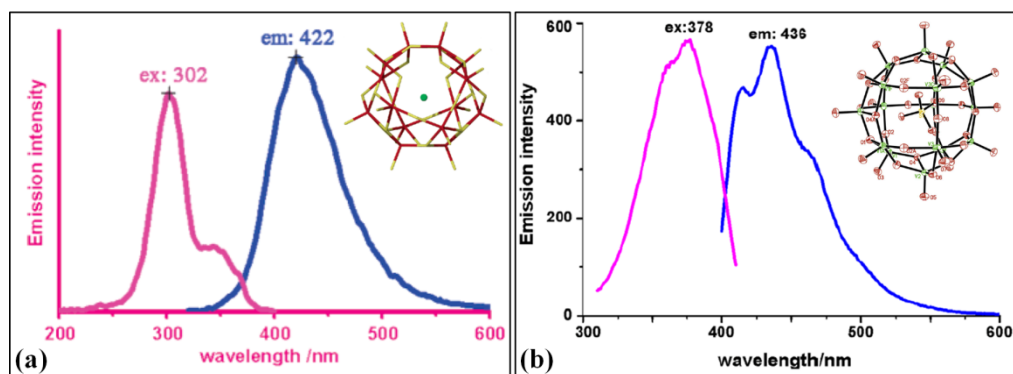


Figure 5.25. Luminescence excitation (ex) and emission (em) spectrums of POV compounds in aqueous solution. (a) $[Et_4N]_5[V_{14}O_{36}Cl]$, [Chen, 2005]; (b) $(Me_2NH_2)_4[H_6V_{16}O_{42}(SO_4)]$, [Chen, 2009].

Recently, Prof. Yongge Wei (Department of Chemistry, University of Tsinghua, Beijing, China) firstly found that the functionalized V6 with hydrophobic groups shows unexpected blue luminescence, probably due to the ligand-to-metal charge transfer (LMCT), which might inspire a new mechanism for fluorescence emission [Yin, 2011; Wu, 2011; Li, 2011]. However, understanding such a CT behavior and fluorescence mechanism of these functionalized hexavanadates is still a formidable challenge.

In order to better understand the luminescent emission in functionalized V6 series. We have tested luminescence spectrum for several functionalized V6 compounds with different cations and different length as shown in Figure 5.26.

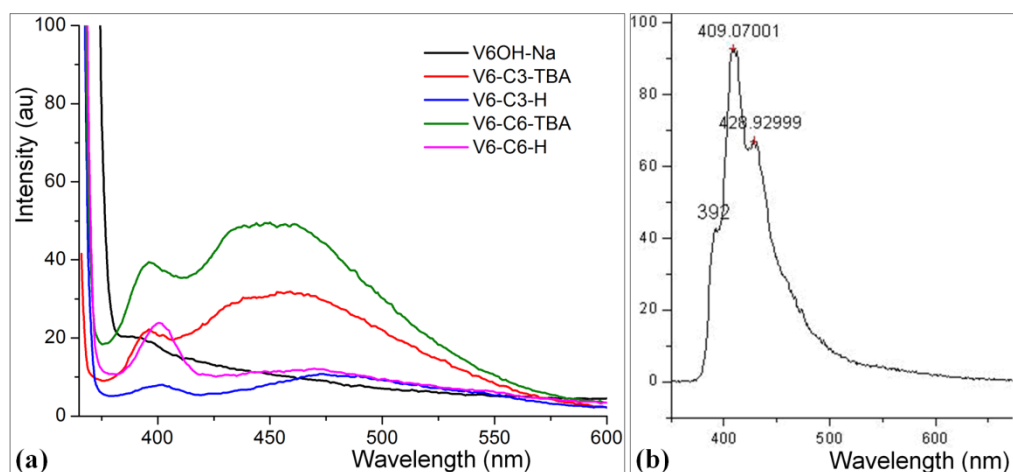


Figure 5.26. Luminescence emission spectrums of POV compounds in aqueous solution. (a) Functionalized V6 series excited at 340 nm (Tested by Dr. Kun Chen in Prof. Wei's group); (b) V6-C18-H excited at 335 nm [Yin, 2011].

As Prof. Wei suggests, the excitation with light of wavelengths between 300–420

nm can trigger such blue luminescence. No emission is observed if the wavelength of the light is below 300 nm. In this case, the wavelength 335 – 340 nm is chosen to excite the luminescence emission. From Figure 5.25, we can observed:

- (1) Certainly due to the fact that the chain of V6-C18 is too long, which show different luminescence emission compared to the other functionalized V6 series;
- (2) Functionalized V6-C18-H emits blue luminescence with peaks at 392 nm, 409 nm, and 429 nm (Figure 5.25 b);
- (3) Generally, the other functionalized V6 series emit a blue luminescence with peaks at two positions. The first ones are similar, pecking around 400nm. For the functionalized V6 bearing TBA cation, V6-C6-TBA and V6-C6-TBA have higher peaks at 460 nm. When the TBA cations are replaced by protons, it gives a broad, but week emission at 475 nm. Such behaviors are because the protons associated with the bridge oxygen ligands;
- (4) We also observed that the longer length of the organic moieties is, the stronger emissions of the functionalized (V6-C3: 31 au; V6-C6: 49 au; V6-C18: 93 au);
- (5) As for V6OH-Na, we cannot observe the luminescence emission.

Through experimental charge density analysis of V6-C3-TBA (chapter 2) and V6OH-Na (chapter 3), we find that there are different AIM charges distribution between V6 core and organic ligands (Table 5.17).

Table 5.17. AIM charge (*e*) distribution in V6-C3-TBA and V6OH-Na.

	V6-C3-TBA	V6OH-Na
V6 core	-9.76	-4.96
Organic ligand	+7.51	+2.90

In order to understand the charge transfer behaviours related to the fluorescent properties, we have plotted the HOMO and LUMO for the [V6OH]²⁻, [V6-C3]²⁻, [V6-C6]²⁻ (Figure 2.26). The HOMO of V6-OH and V6-C3 cover spatially the same extension i.e. the V6 core while the V6-C6 is spread over the OL. The extension of the LUMO is a little bit greater for V6-C6 than for the two others compounds. These observations could be correlated with the luminescent spectra behaviours.

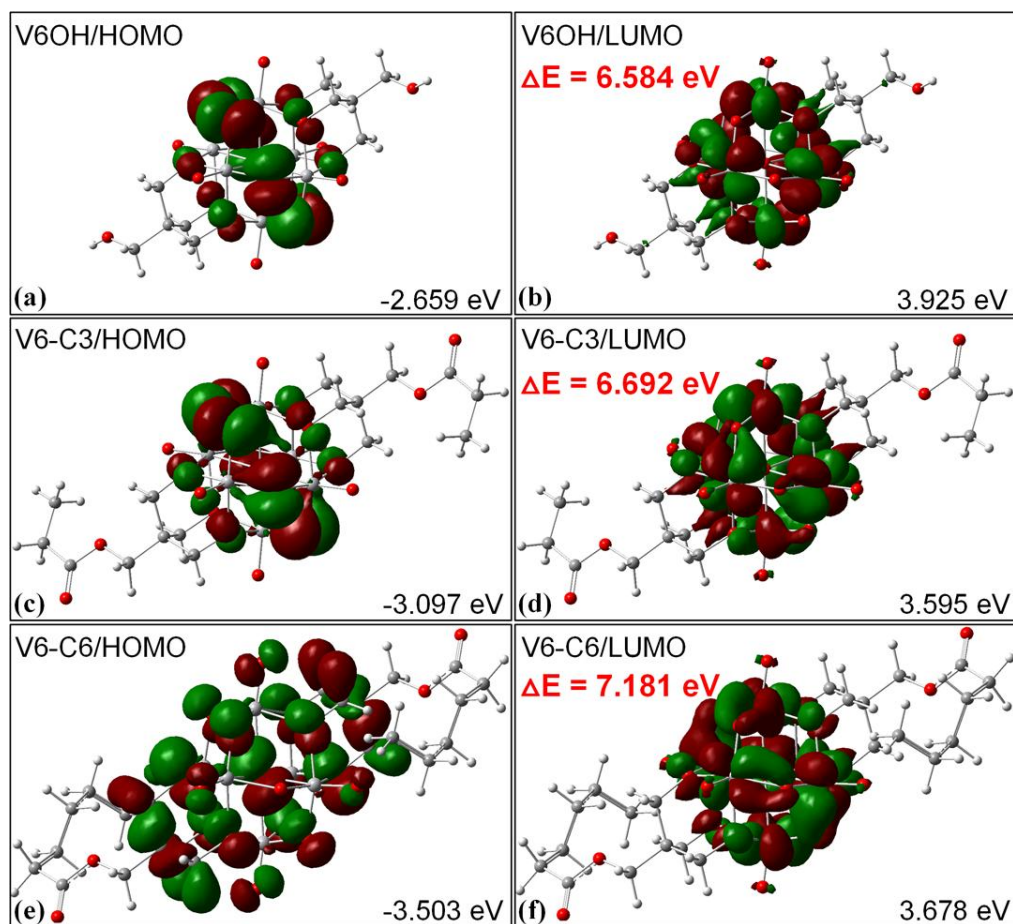


Figure 5.26. HOMO and LUMO for V6-OH, V6-C3 and V6-V6.

To conclude:

- (1) The different cations can affect the fluorescence emission behaviours;
- (2) The longer length of organic ligand is, the stronger emission the functionalized V6 has;
- (3) According to the HOMO/LUMO of the ground state, we suggest that the charge transfer involved the V6 core;
- (4) Moreover, a correlation could be done between the spatial expansion of the HOMO and the best luminescent properties;
- (5) The AIM charge analysis could be a possible tool to explain the fluorescent properties based on the different AIM charge distributions of crystalline functionalized V6 compounds. Despite the fact that the experimental and theoretical AIM charges are not quantitatively in agreement, both methods express the same trend, exhibiting a correlation between the highest values of the charges carried by the V6 core and the best luminescent properties.

5.7 Toward a better understanding of biological activity

5.7.1 Biological activity of functionalized V6 and V10 compounds

5.7.1.1 Biological activity of V10 – A state of arts

Interest in the interaction of vanadate oxoanions with biological systems has increased since it has been demonstrated to have a variety of physiological effects acting either as a phosphate analogue in the monomeric form (H_2VO_4^-) [Cantley,1977] or through oligomeric (dimeric (V2), tetrameric (V4) and decameric i.e. decavanadate (V10) species which interact with many biomolecules with various and versatile activity (enzymes inhibitor or activator). Ten years ago, data indicate spermicidal and anti-HIV activity of vanadium compounds [D’Cruz, 2003] and the use of these compounds for the treatment of diabetes [Heinemann, 2003; Sakurai, 2004; Yang, 2004] as well as the prevention of animal carcinogens [Kanna, 2004; Molinuevo, 2004]. It was reported that decavanadate is the major protein-bound species of vanadium and that V10 has a stronger effect on various enzymes, when compared to other vanadate oligomers [Aureliano, 2005]. V10 studies include also the possibility of its use as a tool in the understanding of the transducing chemical energy into conformational energy for Ca^{2+} transport by Ca^{2+} -ATPase [Stokes, 2005] as well as molecular mechanism of muscle contraction [Tiago, 2004]. Inhibitions of several ATPases such as P-type ATPases, ABC-ATPases and ribonucleases by decavanadate suggest that V10 interactions with these proteins are probably favored by the existence of an ATP binding site [Pezza, 2002; Messmore, 2000]. The exceptional biological activity has been reviewed more recently by Aureliano *et al* [Aureliano, 2009; Aureliano, 2014]. Figure 5.27 summarizes the putative cellular target and processs of V10.

Na^+/K^+ -ATPase (sodium pump) and plasma membrane Ca^{2+} -ATPase (PMCA)-calcium pump belong to the P-type ATPase family, the members of which are able to utilize the energy of ATP to transport ions against their electrochemical gradient across membrane and strongly inhibited by nanomolar concentration of orthovanadate (V4) [Cantley,1977]. Na^+/K^+ -ATPase is a cell membrane located enzyme that establishes and maintains the high internal K^+ and low internal Na^+ concentrations, characteristic and essential for normal cellular activities of most animal cells [Vasilets, 1993; Rodriguez de Lores Arnaiz, 1995]. The activity of this enzyme is very sensitive

to the presence of some metal ions and organic compounds of various structures, especially some drugs and pesticides [Krstić, 2004; Krstić, 2005; Blasiak,1995]. Plasma membrane Ca^{2+} -ATPase is a fine tuner of cytosolic calcium concentration in excitable cells, while the calcium pump is the sole system responsible for extrusion of calcium ions outside nonexcitable cells [Zylinska, 2000]. The ecto-adenosine triphosphatase (ecto-ATPase) represents an integral membrane protein that, in the presence of divalent cations (Ca^{2+} or Mg^{2+}), hydrolyses extracellular nucleotides because of the outward orientation of its active site [Nagy, 1986]. By hydrolysing ATP to ADP, ecto-ATPase represents the major inactivating agent in purine-triphosphate signalling [Horvat, 2006].

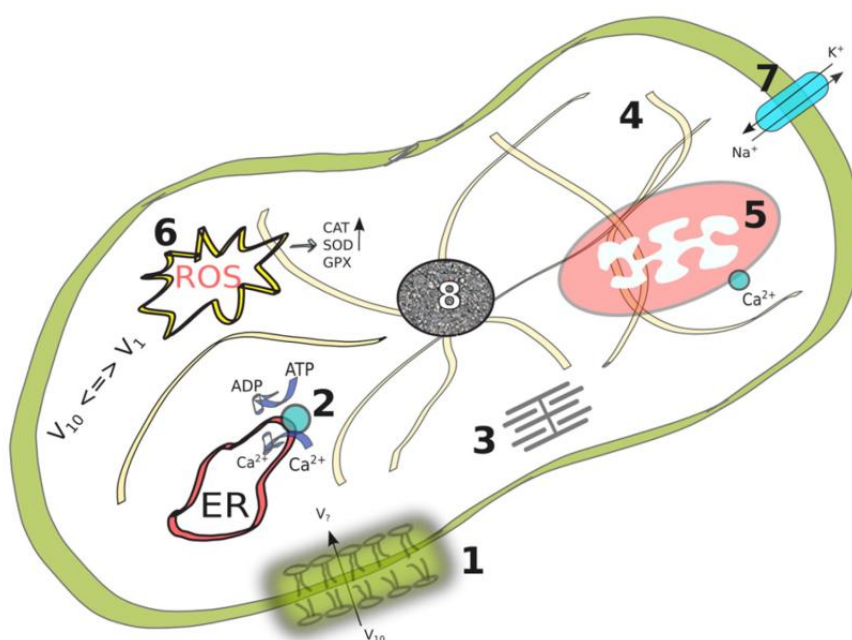


Figure 5.27. Putative cellular targets and processes affected by V10. (1) membrane; 2) calcium pumps in sarco or endoplasmic reticulum (ER) membrane; 3) contractile system; 4) actin cytoskeleton structure and function; 5) mitochondria bioenergetics; 6) reactive oxygen species changes and antioxidants responses and 7) cytoplasmic membrane E1E2 pumps; 8) V10 interactions with DNA have, to our knowledge, not yet been explored (reprinted from [Aureliano, 2014]).

The investigation of the *in vitro* effect of ammonium decavanadate, $(\text{NH}_4)_6\text{V}_{10}\text{O}_{28}\cdot 5\text{H}_2\text{O}$ on Na^+/K^+ -ATPase (sodium pump), plasma membrane Ca^{2+} -ATPase (PMCA)-calcium pump and ecto-ATPase (Mg^{2+} -ATPase) activity, using rat synaptic plasma membrane (SPM) as a model system was undertaken by Krstić *et al* [Krstić, 2009], while the commercial porcine cerebral cortex Na^+/K^+ -ATPase served

as a reference. In addition, extensive kinetic studies of porcine cerebral cortex Na^+/K^+ -ATPase were undertaken to determine the nature of enzyme inhibition by decavanadate. These enzymes were chosen because of their key role in normal functioning most cells of higher eukaryotic organisms [Scheiner-Bobis, 2002] as well as pivotal roles in cancer cell migration [Lefranc, 2008] and, on the other hand, known influence of decavanadate on nucleotide dependent enzymes [Boyd, 1985; Pezza, 2002; Aureliano, 2000; Aureliano, 2005]. The main result of this study could be summarized as follows:

- (1) the obtained dose-dependent inhibition of PMCA and sodium pump by decavanadate, as well as kinetic analysis, is in agreement with previously reported findings that decameric vanadate species block the active side of P-type ATPases and consequently affect phosphorylation step in the enzyme cycle of P-type ATPases (sodium and calcium pumps) [Stokes, 2005];
- (2) this mechanism could not be responsible for obtained ecto-ATPase inhibition (a member of E-NTPDases) and probably occurs via different mechanism resulting in less sensitivity compared to P-type ATPases (sodium and calcium pumps).

Table 5.18. Inhibition parameters of the ATPases inhibition by of ammonium V10 obtained by fitting the experimental points by sigmoidal function and Hill analysis

	IC ₅₀ (mol/l)
Na^+/K^+ -ATPase	4.79×10^{-7}
Ca^{2+} -ATPase	4.68×10^{-8}
Mg^{2+} -ATPase	1.58×10^{-4}
Commercial Na^+/K^+ -ATPase	1.71×10^{-6}

5.7.1.2 Biological activities of functionalized V6 series – new tests

If the V10 anion has already exhibited attractive biological properties, no report have been published on the potential bioactivity of functionalized V6 compounds. In the context of a bilateral project CNRS – MSEP, France – Serbia, the biological activity against Na^+/K^+ -ATPase of some functionalized V6 compounds have been studied at the Faculty of Medicine, University of Belgrade by Dr. Danijela Krstić and Pr. Vesna Vasić. The compounds sent to Serbia have been listed in Appendix (Table A5.1 and Figure A5.9). Eight of them have been tested (Table 5.19).

Stock solutions (0.1 mol/L) of **1**, **2**, **3**, **5**, and **8** were prepared by dissolving the solid compounds in DMSO, while **4**, **6** and **7** stock solutions were prepared in water. Working solutions were prepared daily by diluting (with water) the stock solutions to desired concentrations (as needed), shortly before use.

The standard assay medium for investigation of Na⁺/K⁺-ATPase activity contained (in mmol/L): 50 Tris-HCl (pH 7.4), 100 NaCl, 20 KCl, 5 MgCl₂, 2 ATP and 290 mg/L commercially available porcine cerebral cortex proteins in a final volume of 200 μL. After preincubation for 10 min at 37°C in the absence (control) or in the presence of the appropriate concentration of the investigated V₆ compounds, the reaction was initiated by addition of ATP and stopped after 20 min by adding 22 μl ice cold of 3 mol/L HClO₄ and immediate cooling on ice. Final DMSO volume fraction in the incubation medium did not exceed 1%. The inorganic phosphore (Pi) liberated from the hydrolysis of ATP was determined by a modified spectrophotometric method [Vasić, 1999]. The spectrophotometric measurements were performed on the UV-Vis spectrophotometer (Perkin Elmer Lambda 35). The results are expressed as mean percentage enzyme activity compared to the corresponding control value ± the standard error of the mean (SEM) of two independent experiments done in triplicate (Table 5.19).

The influence of the eight functionalized V₆ compounds (Table 5.19) on commercial porcine cerebral cortex Na⁺/K⁺-ATPase activity was investigated by *in vitro* exposure to the enzyme in the concentration range from 1 × 10⁻⁹ to 1 × 10⁻³ mol/L. The results show that increasing concentrations of the investigated compounds induce inhibition of enzymatic activity in a concentration-dependent manner in all cases (Figure 5.28). Experimentally obtained dependence of the enzyme activity, expressed as a percentage of the control value (obtained without inhibitor), on inhibitor concentration fits a sigmoidal function (Figure 5.28). The inhibition parameters (IC₅₀ values), defined as the concentration of investigated compound with capability to inhibit 50% of the enzyme after given exposure time, were determined using the sigmoidal fit and summarized in Table 5.19. The obtained results demonstrate that the inhibitory effect on Na⁺/K⁺-ATPase activity was rated as compound [V6NO₂][TBA]₂ > [V6OH][TBA]₂ > [V6CH₃][Na]₂ > [V6-C3][TBA]₂ > [V6CH₃][TBA]₂ > [V6-C3][H]₂ > [V6-C5d][TBA]₂ > [V6OH][Na]₂. Actually, the most potent inhibitor is compound [V6NO₂][TBA]₂ (IC₅₀ = (1.8 ± 0.5) × 10⁻⁵ mol/l), while the compounds [V6OH][TBA]₂, [V6CH₃][Na]₂, [V6-C3][TBA]₂ and

[V6CH₃][TBA]₂ are several times weaker inhibitors of Na⁺/K⁺-ATPase, which induced half of maximal enzyme activity (control) at the concentrations (in mol/L) of: $(2.9 \pm 0.3) \times 10^{-5}$; $(4.6 \pm 0.3) \times 10^{-5}$; $(5.5 \pm 0.3) \times 10^{-5}$; $(7.6 \pm 0.5) \times 10^{-5}$, respectively. The enzyme is significantly less sensitive toward hexavanadate [V6OH][Na]₂, *i.e.* half of maximal enzyme inhibition was not reached at the highest investigated concentration 1×10^{-3} mol/L.

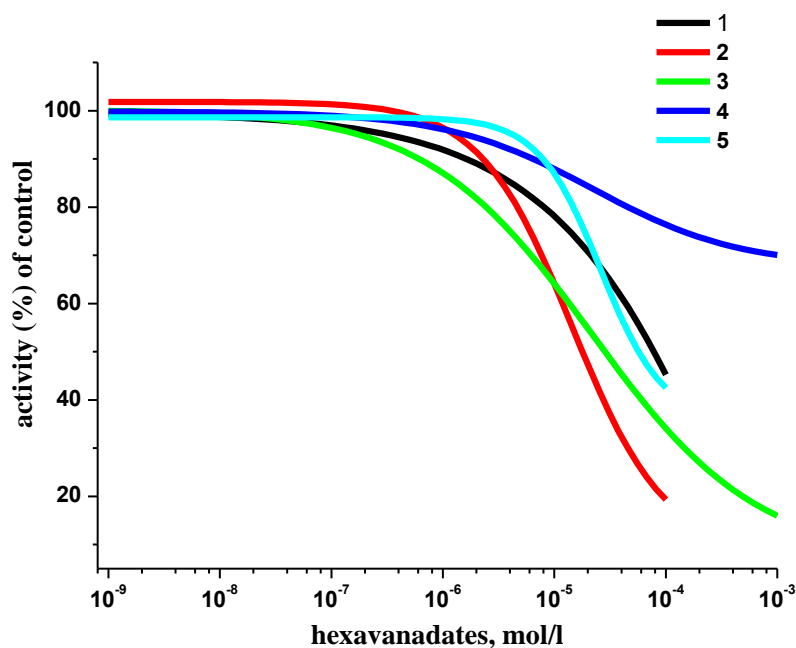


Figure 5.28. The concentration-dependent inhibition of purified porcine cerebral cortex Na⁺/K⁺-ATPase by functionalized hexavanadates for a selection of five of the eight compound tested.

The obtained results (Figure 5.28 and Table 5.19) are in agreement with previously reported concentration-dependent inhibitory effect of polyoxovanadates on synaptic plasma membrane and purified porcine cerebral cortex Na⁺/K⁺-ATPase as well as several nucleotide-dependent enzymes [Boyd, 1985; Aureliano, 2000]. However, decavanadate was approximately ten times more potent inhibitor [Krstic, 2009] of the purified enzyme compared with investigated hexavanadates ([V6NO₂][TBA]₂, [V6OH][TBA]₂, [V6CH₃][Na]₂, [V6-C3][TBA]₂, [V6CH₃][TBA]₂, [V6-C3][H]₂).

In order, to understand these results, we have to answer to these two questions:

- (1) How could we explain the interaction between V6 compounds and Na⁺/K⁺-ATPase?
- (2) How could we explain why V6NO₂ seems a better inhibitor than the others

functionalized V6 compounds?

Generally, the main key-factors, which could be implied in the answer of these questions are:

- (1) the size of the inhibitor (consistent with the enzyme pocket);
- (2) the EP express by the inhibitor (in complementary with the EP express by enzyme pocket);
- (3) the possibility of the inhibitor to built hydrogen bonds or non-covalent interactions with the amino acids of the enzyme.

In our case, the inhibitor is the functionalized V6, the counter ion is necessary to stabilize the V6, but in solution the functionalized V6 is supposed to be isolated. Figure 5.29 represents the inhibition results under an histogram, where the counter ion is indicated. From these results, it is difficult to conclude on the influence of the counter ion.

The size of the V6 series could be modeled by the size of the V6 as defined in chapter 4, Figure 4.2. Figure 5.29 represents the behavior of this length function of the energy of stabilization as determined by the *ab initio* calculation. There is a correlation between these two quantities, as indicated by the blue line. The relationship between the inhibition activity and the length of the functionalized V6 is depicted in Figure 5.30b. The trend is less marked, but obviously, a smaller size seems to be a character for a better inhibitor.

Table 5.19. Inhibition parameters of the ATPases inhibition by a series of functionalized V6 obtained by fitting the experimental points by sigmoidal function and Hill analysis.

Number	Compound	Structure	IC ₅₀ , mol/L
1	[V6CH ₃]- [TBA] ₂		7.6×10^{-5}
2	[V6NO ₂]- [TBA] ₂		1.8×10^{-5}
3	[V6OH]- [TBA] ₂		2.9×10^{-5}
4	[V6OH]- [Na] ₂		$> 10^{-3}$
5	[V6-C3]- [TBA] ₂		5.5×10^{-5}
6	[V6CH ₃]- [Na] ₂		4.6×10^{-5}
7	[V6-C3]- [H] ₂		1.1×10^{-4}
8	[V6-C5d]- [TBA] ₂		1.5×10^{-4}

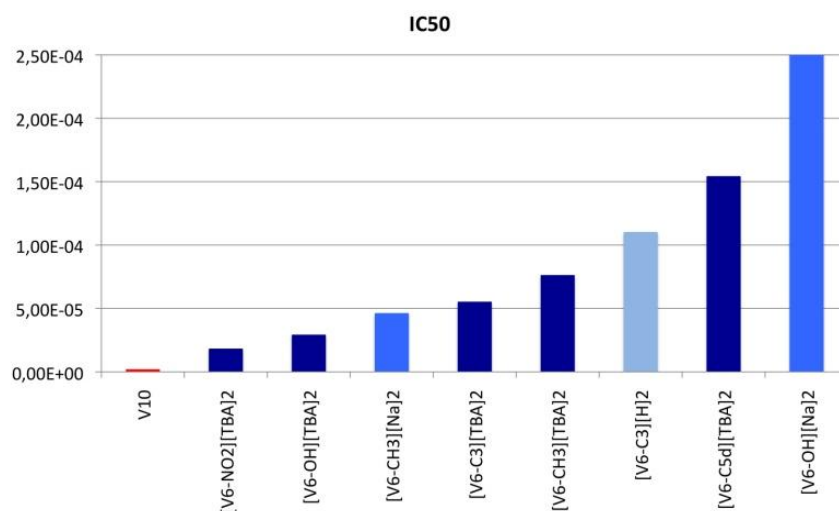


Figure 5.29. IC₅₀ (in different blue color, according the cation) mol/L.

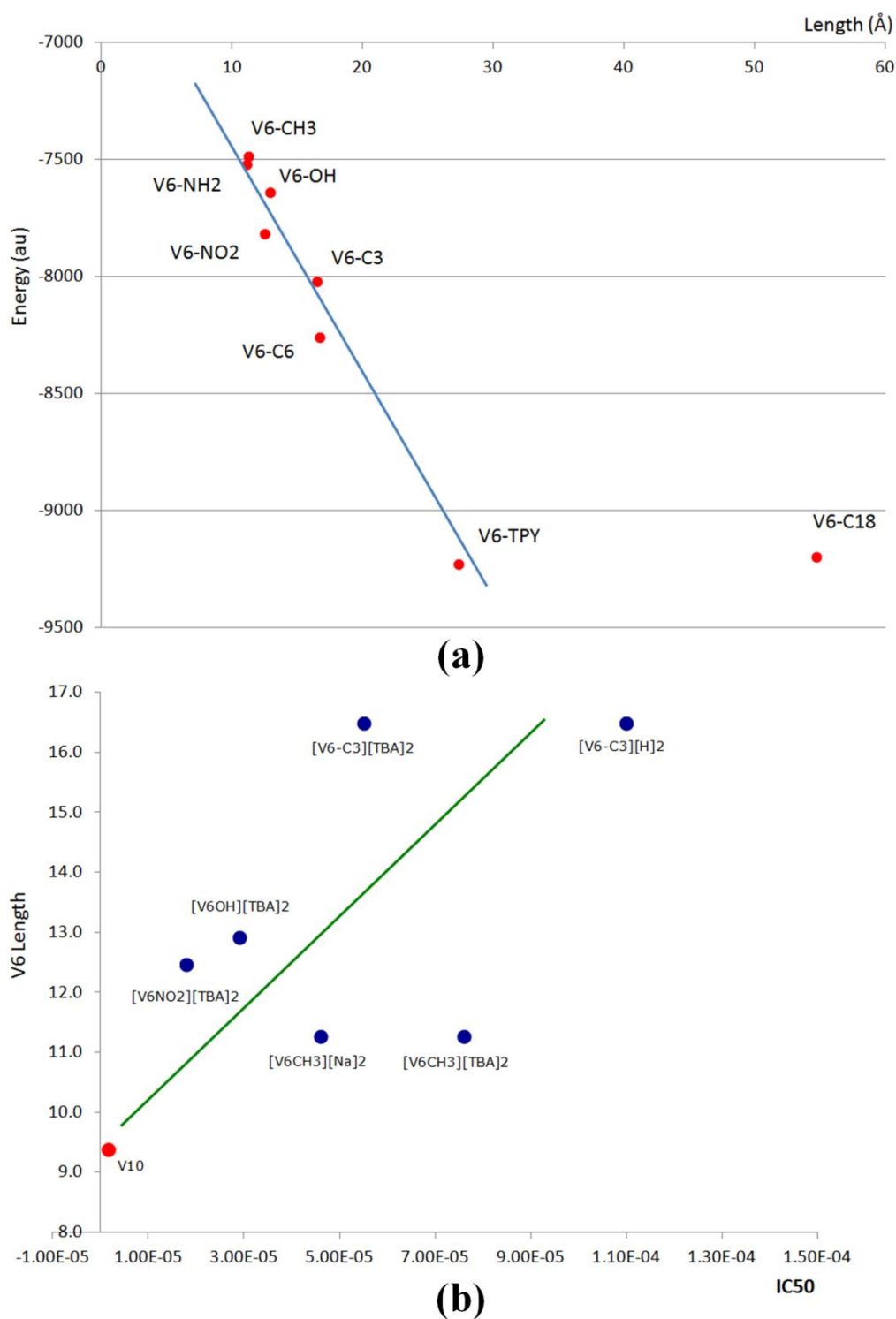


Figure 5.30. Behavior of the energy of the V6 functionalized. (a) energy (au) function of the length (Å); (b) length (Å) function of the inhibition activity (mol/L).

The EP values at the molecular surface of the functionalized V6 series have been determined and plotted (figures 4.12, 4.13 and 4.14). Figure 5.31 represents the evolution of the EP minimum, the EP maximum and the difference between these two values. Clearly, a very negative value (V10) implies a better inhibition. Nevertheless,

it is difficult to understand the inhibitor behavior inside the functionalized V6 series from these EP values. The qualitative observation of the EP (Figure 4.12, 4.13 and 4.14) indicates that the V6NO₂, and in a less extent the V6OH presents additional negative regions. This could be the reason why these compounds could be good inhibitors.

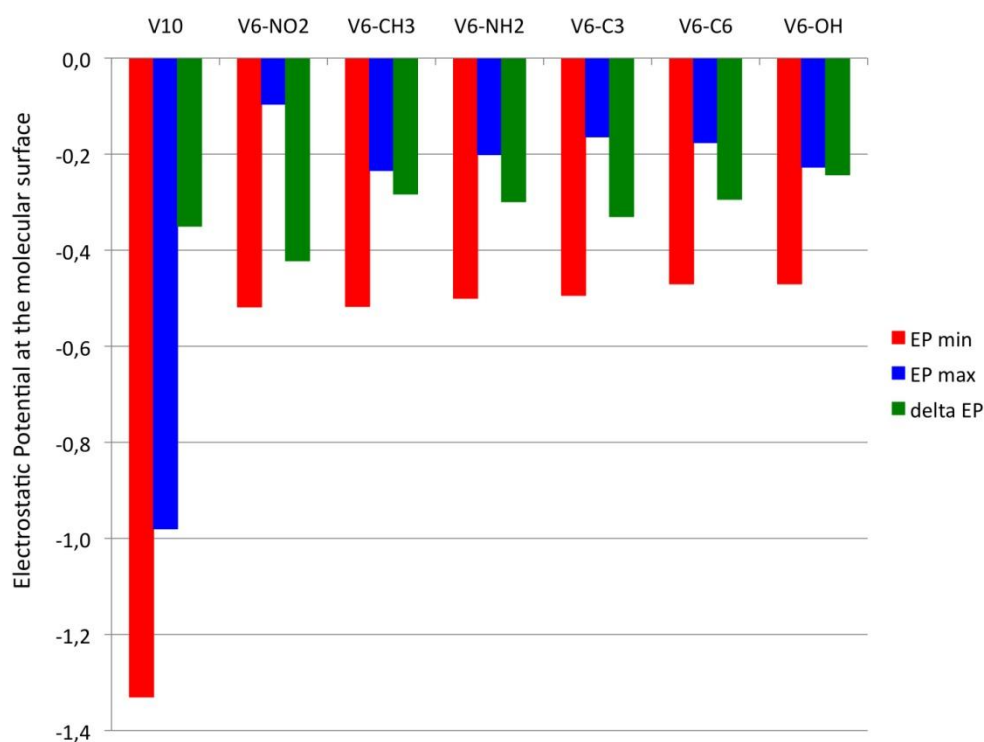


Figure 5.31. Theoretical EP values ($e\text{\AA}^{-1}$) at the molecular surface for V10 and for the functionalized V6 series.

Ziegler *et al* [Ziegler, 2009] demonstrated by *ab initio* electron density calculation and biochemical investigations, that an increasing positive charge on the vanadyl group increases the inhibition potency of the vanadyl complex on alkaline phosphatase (Figure 5.32). The explanations of the functionalized V6 different bioactivities have to be searched inside the possibility of interaction with the enzyme. That means the possibility of V6 core to built hydrogen bonds, and the possibility of functionalized V6 to have complementary electrostatic potential interactions with the interaction enzyme pocket site. Following the work of Ziegler [Ziegler, 2009], the charges belonging to the V-O group have been explored (Figure 5.32 a, b). We observe that the most charged V-O1x bond belongs to V6NO₂. The specific behavior of V6NO₂ is clearer when calculating the average Mulliken charges over the three bonds (V-O1x, V-O2x and V-O3x), shown in Figure 5.32 c. Our results are in

agreement with those of Ziegler where the more positive V-O bonds allows the complex to bind more tightly to the enzyme [Ziegler, 2009].

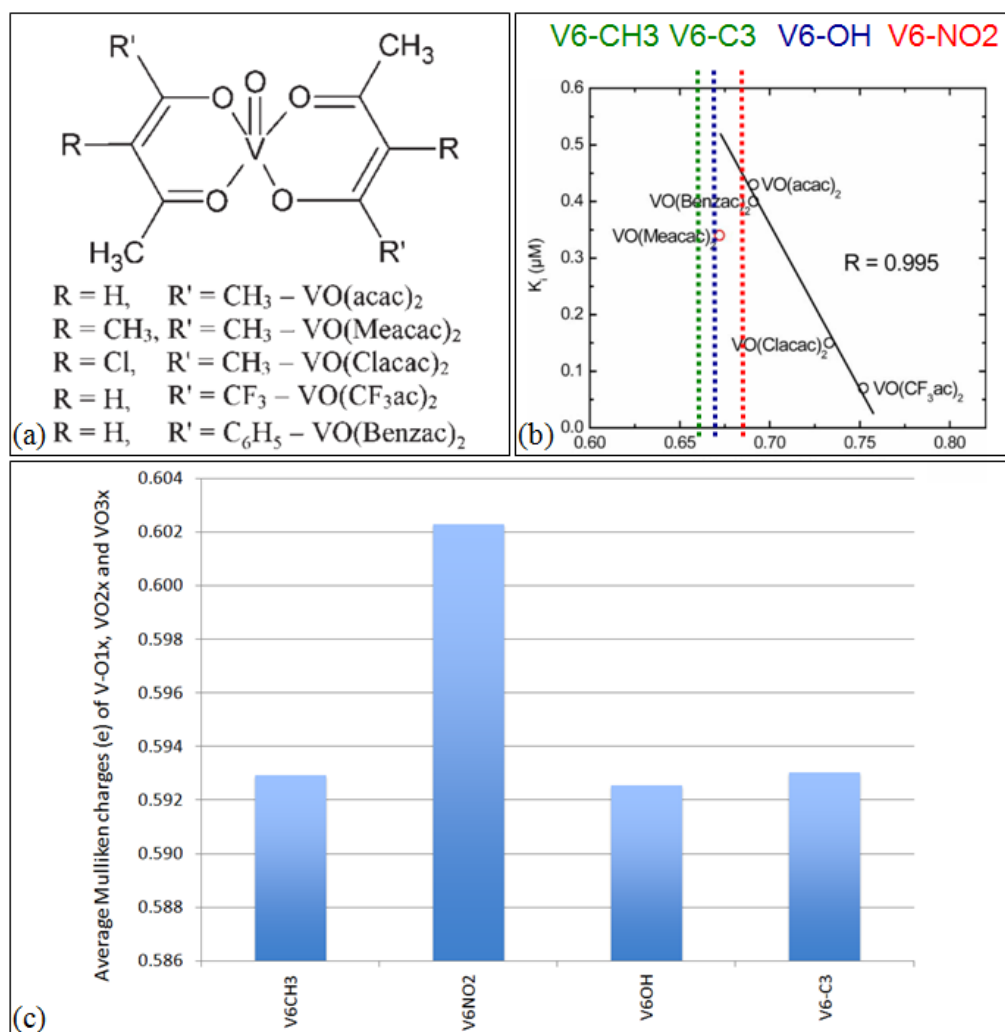


Figure 5.32. Mulliken charges of VO group charges. (a) Chemical structures of substituted VO(diketone)₂ complexes (acac = acetylacetonato); (b) Correlation of K_i (mM) for VO(diketone)₂ complexes in aqueous solution with the calculated Mulliken charges of the VO group in atomic units. The charges of V6 series of the V-O1x bond are reported on the plot; (c) Average Mulliken charges of the V-O1x, V-O2x and V-O3x for functionalized V6 series. (a) and (b) are reproduced from [Ziegler, 2009].

Holtz *et al*, [Holtz, 1999] has studied the co-crystallization of alkaline phosphatase complexed with vanadate. They have established the binding site where the vanadate ligand is a modified serine as shown on Figure 5.33. Previously reported protein structures show that V10 is bonded via hydrogen bond with acid phosphatase [Felts, 2006] and tyrosine kinase [Bae, 2008]. In these two protein structures, V10 anion is linked to enzymes through the amino acids: histidine (His), lysine (Lys),

asparagines (Asp), arginine (Arg), which are with positive charges or polar chains.

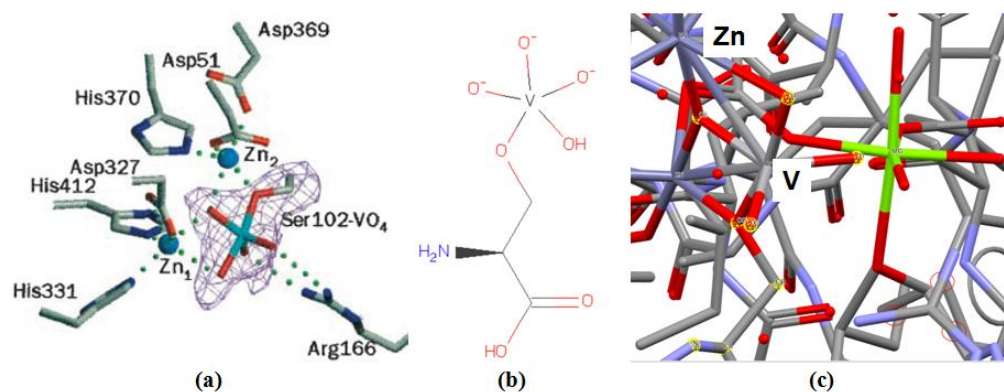


Figure 5.33. Co-crystallization of alkaline phosphatase complexed with vanadate [PDB code: 1B8J]. (a) binding sites; (b) serine-102-VO₄ modified; (c) a Mercury view of the binding site with the Zn, V and Mg complex. Reproduced from [Holtz, 1999].

5.7.2 CSD statistical research on non-covalent interactions of functionalized V6 anion

As a consequence of the previous section, it is necessary to better understand the possibility of non-covalent interactions that the functionalized V6 could have. Therefore, we have undertaken a CSD statistical research on the non covalent interactions within the V6 core. A similar work have been done by Bosnjakovic-Pavlovic *et al* for V10 [Bosnjakovic-Pavlovic, 2011].

The CSD data was searched for compounds containing hexavanadate anion (Table 1.1, in chapter 1) and hexavanadate based compounds where more than six oxygen atoms are bridged with organic ligands (Appendix, Table A1.1). Some of these compounds are protonated (PAGSOF, PAGESUL, PAGTAS, KURBOO, KURBUU, see Table 1.1, chapter 1). In order to avoid low quality of crystal structure, the R factor was required to be less than 10%. We have searched the C-H...O noncovalent interactions for 24 structures, depending of the oxygen type O1x and O2x. There is a few of C-H...O3x which have not been reported in the following graph. For each interaction, we have calculated the C-H...O distance and angle. The searching results contain 138 interactions, which are shorter than the sum of van der Waals radii. These weak interactions reveal an usual behavior as depicted in Figure 5.34 and in Appendix, Figure A5.10.

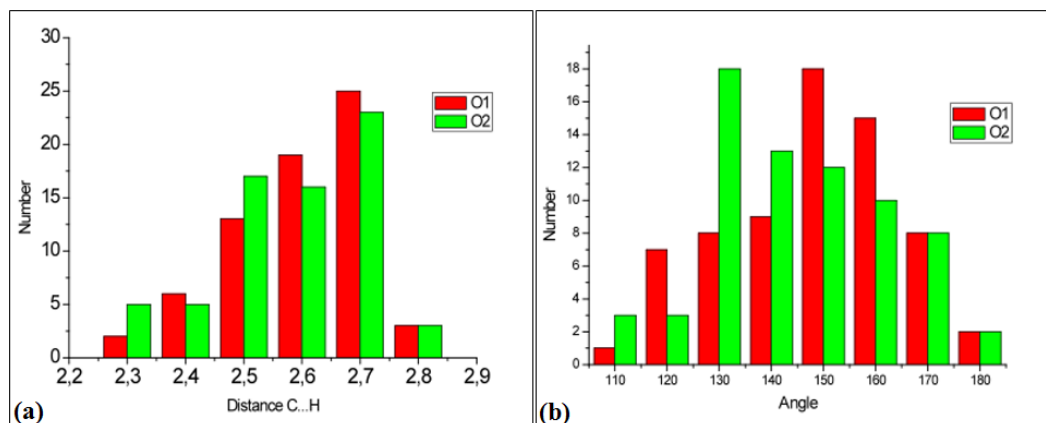


Figure 5.34. Number of non-covalent interactions within the functionalized V6 compounds according to (a) the distances $CH\cdots O$ (Å); (b) the angle $CH\cdots O$ (°).

More interesting, the hydrogen atoms belonging to the V6 core or to the organic ligand are bridged with O2x atoms from V6 core. Oxygen atom O1x is never connected with organic ligands. Therefore the main protonation sites for the protonated hexavanadate anion is oxygen atom O2x and the main atoms for connection with organic parts is O2x. These results suggest that O2x atoms are more reactive than O1x atoms. The protonation / basic sites of hexavanadate core have been identified as the doubly bridging oxygen atoms (O2x), establishing these as more nucleophilic / basic than the single bridging oxygen atoms (O1x). That observation is clearly coherent with the observation made in chapter 2, § 2.4.6.1, Figure 2.43 where the most accessible region is inside the triangle O2x – O2x – O3x. The different theoretical EP values in the functionalized V6 series located in the vicinity of this triangle have already been presented in Figure 5.34. The V6NO₂ exhibits the most negative EP.

The interactions between the organic ligand and the rest of the crystal for the compounds of Table 1.1 have been studied (see Appendix, Table A 5.2). The number of interactions where organic ligand (OL) acts as donor is 18 through 12 CH...O, 4 NH...O, 1 CH...N and 1 NO...Cl, while OL acts as acceptor 19 times through 14 CH...O, 4 NH...O and 2 CH...N. From this small series of functionalized V6 compounds, mainly those containing NO₂ or OH group, it is difficult to give insight in the understanding of the biological activities.

In that study, we have clearly demonstrated that the V6 core built non covalent interactions through O2x. This coherent with the fact, that the EP values is the most negative in the vicinity of the triangle O2x – O2x – O3x.

5.7.3 A combined approach to predict the interaction sites of functionalized V6 compounds: experimental/theoretical electrostatic potential, crystallographic statistical analysis, molecular interaction field determination

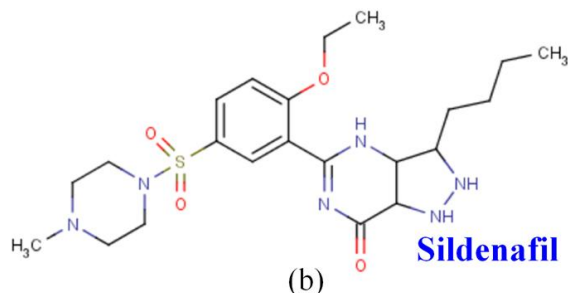
The description of a molecule and its influence on the surroundings is a useful information to explain and understand the chemical reactions and chemico-biological interactions. Depending on the different fields, there are several ways to define the interaction force of a molecule with a protein or a receptor, such as lipophilicity, polarizability, electronic properties, steric interactions and so on.

In crystallography and related fields, a better understanding of the interaction between a protein and a small molecule is taken into account as two following ways:

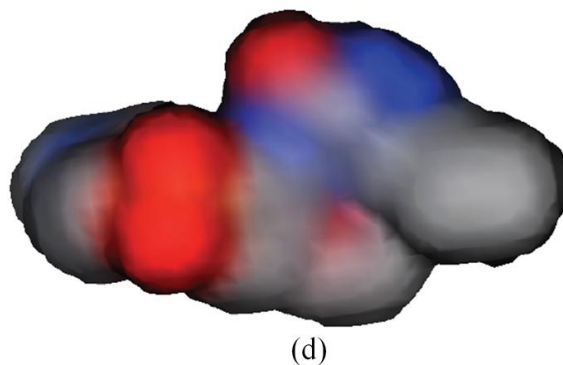
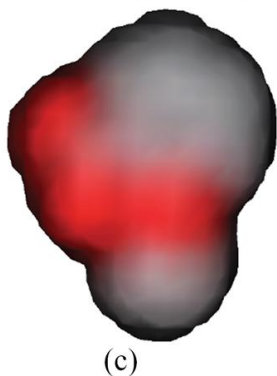
- (1) experimentally, when it is possible, with the determination on the co-crystal structure of targeted protein and small molecule;
- (2) theoretically, with the molecular docking of the inhibitor against the biological target.

However, it is difficult to obtain a high quality co-crystal of a membrane protein and a small molecule. From charge density analysis, we try to extract some useful information to know the potential interaction sites or regions, which could non-covalently interact with the other molecules or protein. This is “so-called” chemical reactivity, which is what we “think” about it. In parallel, how does a protein “think” about a small molecule? Figure 5.35 represents the different understandings of a molecule from different views.

What a chemist sees:



What a crystallographer sees:



What a protein sees:

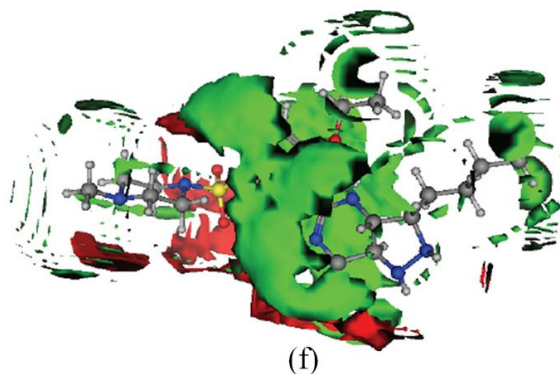
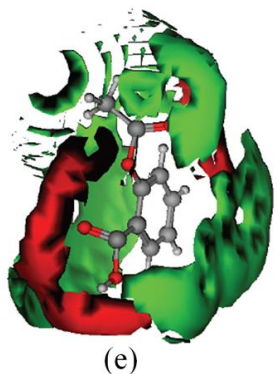


Figure 5.35. structure characteristics in different fields. (a)(b)chemical structures of aspirin and sildenafil; (c) (d) electrostatic potentials; (e) (f) interaction surfaces.

In this section, we propose a combined approach to predict the interaction sites to understand the bioactivity of functionalized V6 series involving experimental/theoretical electrostatic potential, crystallographic statistical analysis, molecular interaction field (MIF) determination. This combined approach has been worked through the help of an innovation project S7/S8 in Ecole Centrale Paris (Master 1 level) as shown in Figure 5.36.

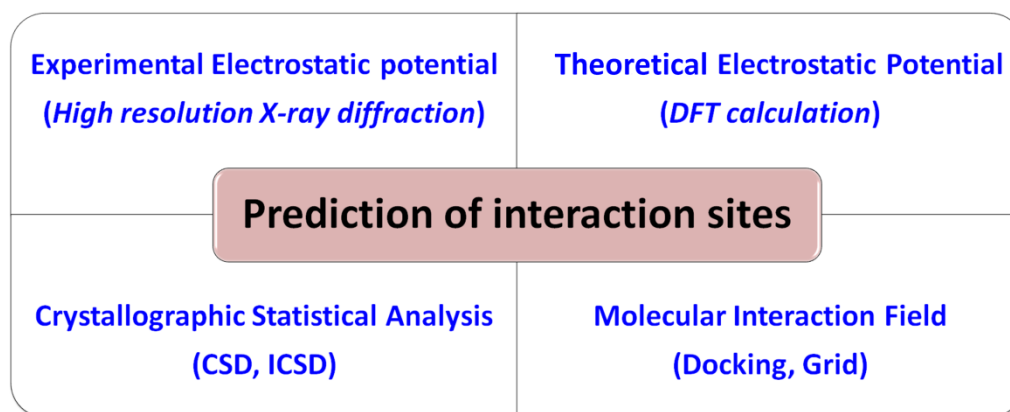


Figure 5.36. A combined approach to predict the interaction sites

We have describe the methodologies for experimental/theoretical EP in chapter 2-4, and the crystallographic statistical analysis based on CSD searching in § 5.7.2. The methodology of molecular interaction field (MIF), developed by Molecular Discovery Limited [GRID - VERSION 22], is based on the determination of the molecular interaction field (MIF) [Cruciani, 2006].

The GRID code allows the user to determine the preferential interaction site of a probe (H₂O, OH, NH, CH₃, metal,...) with a target (the drug or the inhibitor) as shown in Figure 5.37. The interaction of the probe group with the target is computed at sample positions (the grid points) distributed throughout and around the molecule. With the probe at each GRID point in turn, the total interaction energy is calculated from:

$$\sum E = E_{LJ} + E_Q + E_{HB} + S \quad (5.1)$$

in which $\sum E$ indicates pairwise energy summation between the probe at its grid point and every appropriate atom of the target (including predicted water molecules), and S is the appropriate entropic term at the grid point (Figure 5.37).

The E_{LJ} term in Eq. (5.1) is the well-known “Lennard-Jones energy”, and is computed as the sum of two terms:

$$E_{LJ} = \frac{A}{d^{12}} - \frac{B}{d^6} \quad (5.2)$$

the interacting atoms are a distance d apart, and the energy variables A and B are calculated from the Van der Waals radius, polarizability and effective number of electrons of the atoms ($E_{LJ} = E_{VDWR}$).

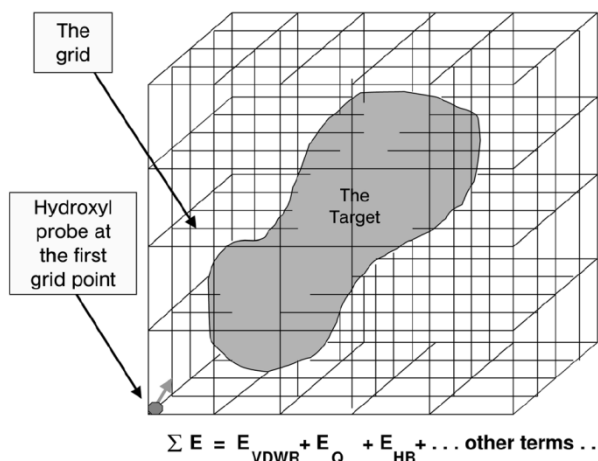


Figure 5.37. The target and probe in GRID computation. The total interaction energy is indicated.

The electrostatic term, E_Q , is computed as:

$$E_Q = p \times q \times K \times \left[\frac{1}{d} + \frac{M-W}{M+W} \times \frac{1}{\text{SQRT}(d \times d + 4 \times P \times Q)} \right] \times \frac{1}{M} \quad (5.3)$$

where p and q are the electrostatic charges on the Probe group and the pairwise Target atom, and K is a combination of geometrical factors and natural constants. The macromolecular target and the surrounding water have dielectrics of M and W respectively, and the depth of the charges p and q in the target phase is P and Q . For small molecules the Target phase is effectively absent, and P and Q are both zero.

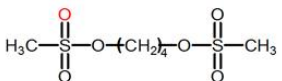
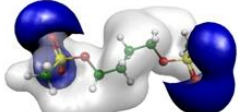
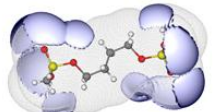
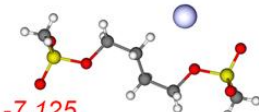
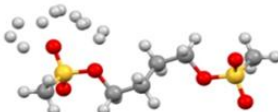
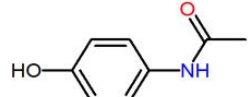
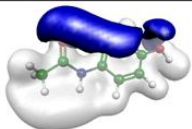
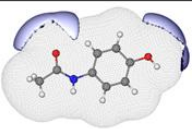
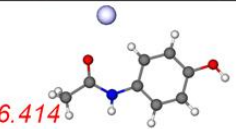
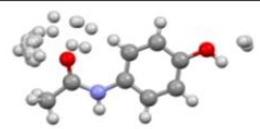
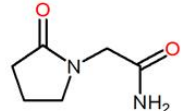
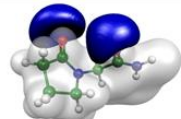

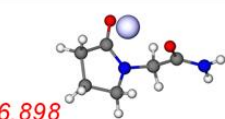

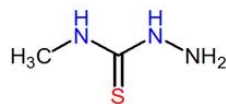

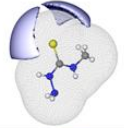
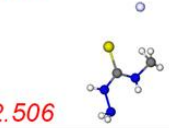

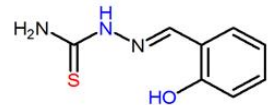
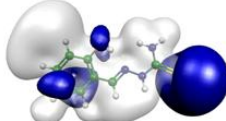
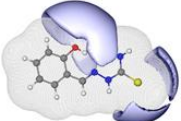
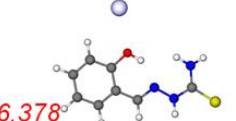
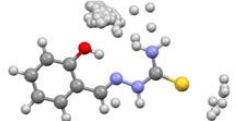
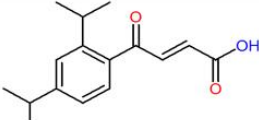
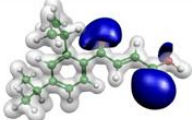
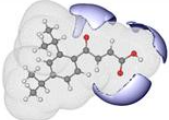
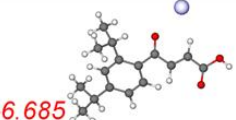
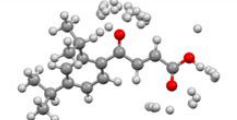
The standard hydrogen bond interaction is computed from:

$$E_{HB} = \left[\frac{C}{d^8} - \frac{D}{d^6} \right] \times [f(U, U', U'', \dots)] \times [f'Q] \quad (5.4)$$

where f and f' are functions; U, U', U'' etc are angles and distances defining the geometrical arrangement of the atoms engaged in hydrogen bonding and their neighbours; and Q depends on the charges of the interacting atoms. Energy variables C and D are computed from the hydrogen bond radii.

In the context, we have performed the related research on the six drug molecules (Table 5.20).

Table 5.20. Combined approach to study the interaction sites of six drug molecules.

Compound	Formula	Experimental EP (Crystallography)	Theoretical interaction field (with probe H ₂ O)*	Theoretical favorable site (Min energy, kcal/mol)	Crystallographic statistical analysis (CSD)
Busulfan [Ghermani, 2004]				 -7.125	
Paracetamol [Bouhmaida, 2009]				 -6.414	
Piracetam [Chambrier, 2011]				 -6.898	
MeTSC [Novakovic, 2007]				 -2.506	
SalTSC [Francuski, 2011]				 -6.378	
Keto Acid [Drakulic, 2005]				 -6.685	

The actual version of GRID is still not parameterized for vanadium atom despite our multiple interactions with the team of Pr. G. Cruciani, University of Perugia, Italy. As preliminary results, we have replaced the vanadium atoms by iron atoms. Table 5.21 gives the MIF surfaces (probe H₂O of the different V6 species). The observations of the MIF surfaces compared to the EP surfaces are the following:

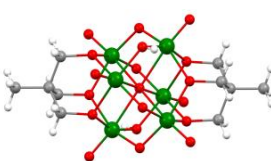
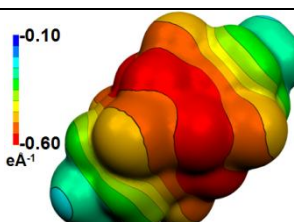
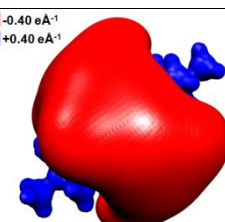
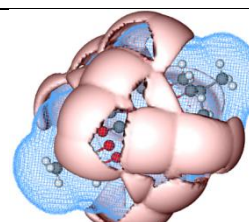
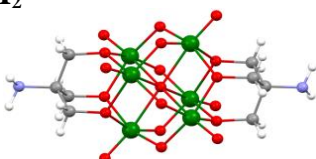
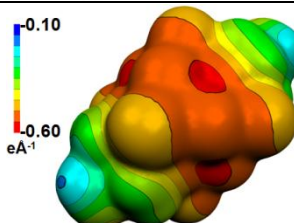
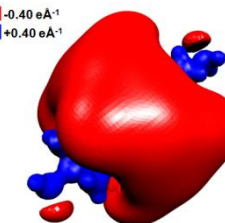
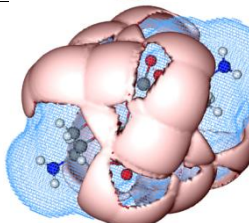
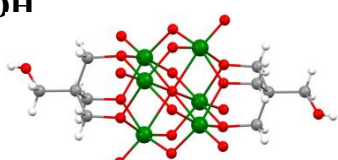
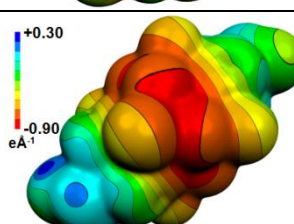
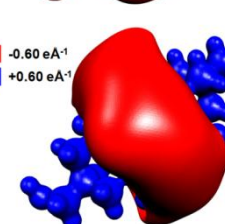
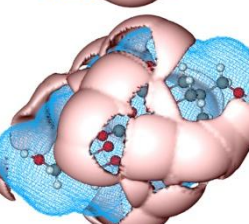
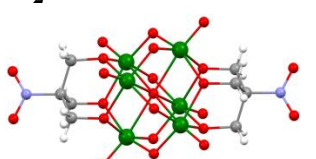
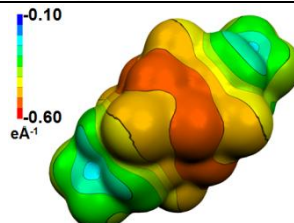
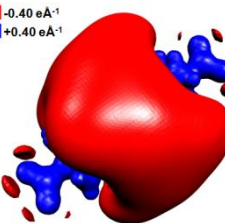
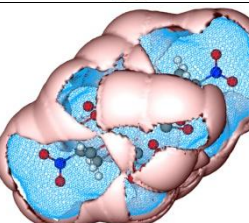
- (1) The MIF iso-energy surface (± 5.0 kcal/mol) describes a quite similar surface with the EP iso-value surfaces in each V6 compounds;
- (2) The extent of the MIF iso-surface is slightly greater than the EP values (for the chosen iso-surface chosen) because the former is the interaction energy surface, and the latter is the potential surface. Between these two surfaces, there are the interactions between functionalized V6 and the probe;
- (3) The larger MIF iso-surface concerns the V6NO₂ compound. That would be in agreement with that the V6NO₂ is a slightly better inhibitor than the other functionalized V6 compounds.

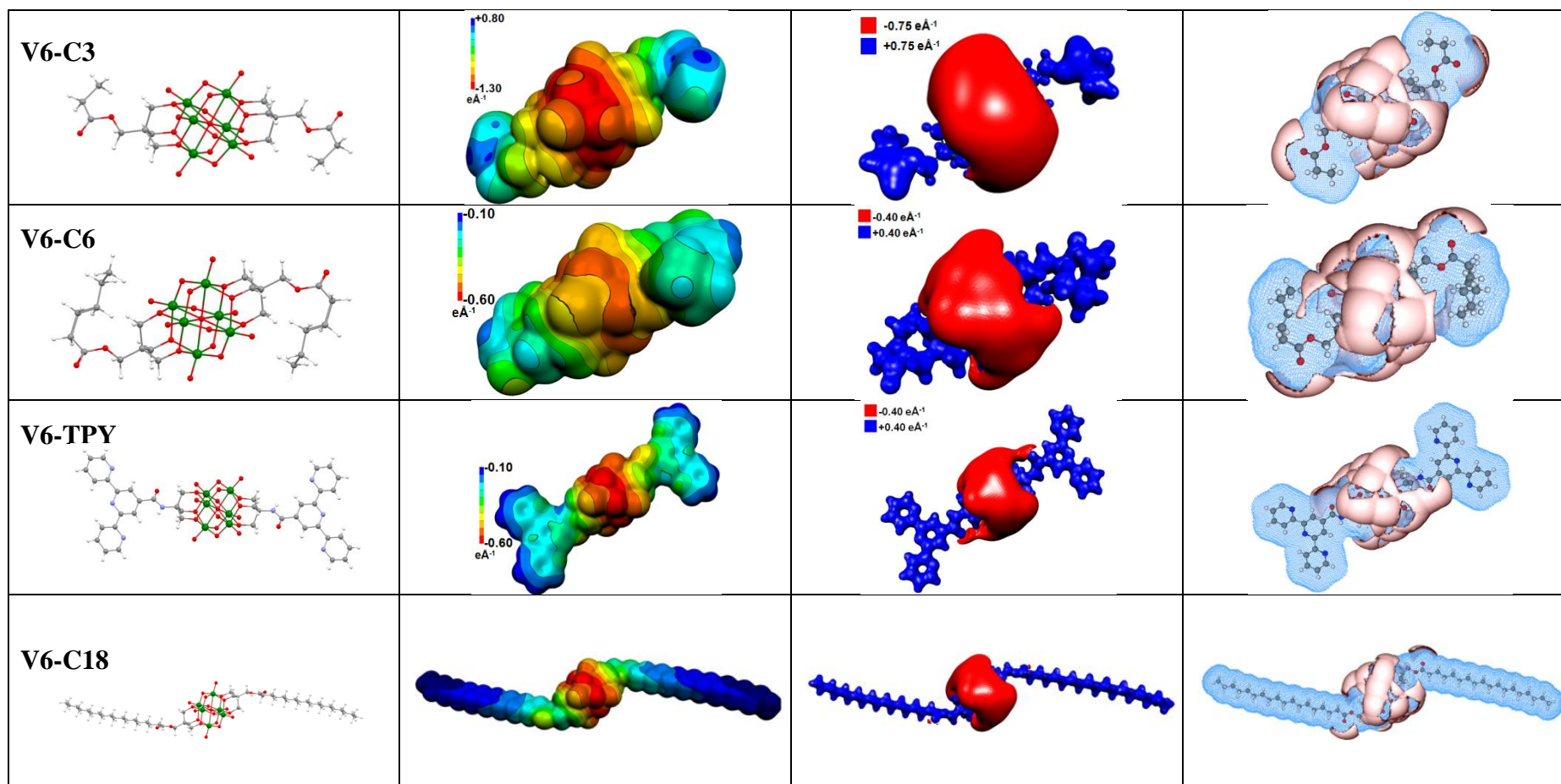
In conclusion on the inhibition test of the V6 functionalized series we can assert the following:

- (1) V10 is a better inhibitor than the V6 functionalized. This is in agreement with the following observations:
 - i) The negative minimum EP value of V10 is stronger than those of the functionalized V6 compounds, which indicates that there are more potential interaction sites for V10;
 - ii) The size of V10 is smaller than the functionalized V6, which indicates that V10 can access to the binding site in receptor easily.
- (2) The interactions between POV and ATPase could be done:
 - i) *Via* the non covalent interactions built with / from the V6 core (where the nucleophilic affinity takes place) preferentially in the triangle O2x - O2x - O3x according to the EP values and the CSD statistical study;
 - ii) *Via* the non covalent interactions built with / from the organic ligand (where the electrophilic affinity takes place) according to the EP values and to the CSD statistical study.

- (3) The reasons why the V_6NO_2 seems to be the better inhibitor is in agreement with:
- i) The size of the different V_6 in the series (the smaller size is, the better inhibitor is); the size of V_6NO_2 is relatively small;
 - ii) The negative EP minimum (the more negative EP is, the better inhibitor is);
 - iii) The average Mulliken V-O bond charge (the higher Mulliken bond charge is, the better inhibitor is);
 - iv) The extent of the EP iso-surface (the more extended the EP iso-surface is, the better inhibitor is);
 - v) The extent of the MIF iso-surface (the more extended the MIF iso-surface is, the better inhibitor is).

Table 5.21. Combined approach to study the interaction sites of functionalized V6 compounds.

Structure	EP	EP isovalue surface	MIF surface (± 5.0 kcal/mol)
V6CH₃ 			
V6NH₂ 			
V6OH 			
V6NO₂ 			



CONCLUSION AND PERSPECTIVES

Very often, the main purpose of undertaking a charge density (CD) analysis (either experimental or theoretical) is to shed some light on the chemical bonding or chemical reactivity of the studied system. As described in the beginning of the manuscript, charge density analysis can be applied in many fields of chemistry, as well as materials and biomolecular sciences. In my three years PhD period, I learned which chemical informations can be obtained from CD analysis and how to use them to understand other physical and chemical properties.

The experimental and theoretical charge density analysis of functionalized hexavanadate series and decavanadate have been extensively described in the previous chapters. The specific conclusions concerning the chemical bonding and chemical reactivity of the targeted POV compounds are highlighted in the corresponding sections. In this manuscript, the CD analysis of POV compounds could contribute to:

- (1) Crystallography of POM/POV compounds.** We have established the charge density refinement methodology for functionalized V₆ series and decavanadate. This methodology can be also extended to the other POV and POM compounds.
- (2) Understanding of POV/POM structures.** The CD analysis provides us full of chemical information about the POV/POM structures involving electronic, topological, and electrostatic properties, which enable us to better understand the chemical bonding and chemical reactivity of these compounds.
- (3) Functionalization.** We have firstly depicted the functionalization behaviors in functionalized hexavanadate and functionalized hexamolybdate.
- (4) Synthetic chemistry.** The established method for understanding functionalization behaviors can also guide us to design and synthesize new POM/POM compounds with special applications in a more controllable way. Such an established method can be also extended to the other fields, *e.g.*, organometallic chemistry and drug discovery, we can design the organometallic complexes with high stereoselectivity for the asymmetric reaction.

- (5) **POV/POM-based materials.** From the view of CD analysis, we have proposed some promising methods and explanations to understand the charge transfer and fluorescence/luminescence behaviors.
- (6) **M-L bonding features.** Based on the topological parameters of various M-L containing V-O bonds and various other M-L bonds, the classification of M-L bonds are described for understanding the M-L bonding features.
- (7) **Non covalent interaction and biological chemistry.** We have proposed a combined approach to predict the interaction sites in order to understand the bioactivity of functionalized V6 series based on experimental/theoretical electrostatic potential, crystallographic statistical analysis, and molecular interaction field (MIF) determination.

Nevertheless, different works have to be done in the future:

- (1) **New way for theoretical charge density analysis.** Due to different density distributions around V atom, different AIM charge of V atoms and different EP value of functionalized V6 anions from experiment and theory, we plan to perform the theoretical charge density analysis in a new way: to compute the theoretical structure factors, and refine the structure with the same strategy of the experimental one.
- (2) **Experimental charge analysis of other functionalized V6 compounds.** In the previous study [Yin, 2011], it was said that the protonated functionalized V6 compounds exhibits stronger luminescence emission than the unprotonated one. We would like to perform an experimental charge analysis of these compounds to understand the luminescence behavior at the atomic level.
- (3) **Experimental charge analysis of functionalized hexamolybdate.** Through the theoretical charge density analysis of it, we find some very interesting results. The experimental charge analysis of this compound could provide reliable information about its electronic and electrostatic properties despite there are some difficulties to perform charge density studies on *4d* metal compounds.
- (4) **Experimental charge analysis of functionalized V6-C3 by synchrotron X-ray diffraction.** We have collected the diffraction data at synchrotron SOLEIL. We will analyze the data in the near future.

(5) Experimental and theoretical charge density analysis on new POV cage compounds. A collaboration with Prof. Hayashi Yoshihito from Kanazawa University (Japan) for determination of charge density of V18 compounds.

LIST OF ABBREVIATIONS

AIM	Atoms-In-Molecule
BCP	Bond critical point
CD	Charge density
CT	Charge transfer
DFT	Density functional theory
ED	Electron density
EP	Electrostatic potential
IAM	Independent atom model
ISF	Integrated local source
LS	Local source
MM	Multipole model
MM-1	Multipole refinement by refinement strategy 1
MM-2	Multipole refinement by refinement strategy 2
Mo6	Hexamolybdate
OL	Organic ligand
POM	Polyoxometalate
POV	Polyoxovanadate
SF	Source function
TBA	Tetrabutylammonium
V6	Hexavanadate
V10	Decavanadate
V6-C3	Functionalized V6-C3
[V6-C3]²⁻	Functionalized V6-C3 anion
V6OH	Functionalized V6OH with -OH terminal group
VSCC	Valence shell charge concentration
κ	Contraction/expansion coefficient of spherical valence density
κ'	Contraction/expansion coefficient of aspherical valence density
κ-1	Kappa refinement by refinement strategy 1
κ-2	Kappa refinement by refinement strategy 2

REFERENCE

A

- [**Akimov, 2013**] Akimov, A. V.; Neukirch, A. J.; Prezhdo, O. V. *Chem. Rev.* **2013**, *113*, 4496–4565.
- [**Allain, 2008**] Allain, C.; Favette, S.; Chamoreau, L-M.; Vaissermann, J.; Ruhlmann, L.; Hasenknopf, B. *Eur. J. Inorg. Chem.* **2008**, 3433–3441.
- [**Allcock, 1973**] Allcock, H. R.; Bissell, E. C.; Shawl, E. T. *Inorg. Chem.* **1973**, *12*, 2963-2968.
- [**Altomare, 1993**] Altomare, A.; Cascarano, G.; Giacobazzo, C.; Guagliardi, A. *J. Appl. Crystallogr.* **1993**, *26*, 343–350.
- [**Anderson, 2004**] Anderson, T. M.; Neiwert, W. A.; Kirk, M. L.; Piccoli, P. M. B.; Schultz, A. J.; Koetzle, T. F.; Musaev, D. G.; Morokuma, K.; Cao, R.; Hill, C. L. *Science*, **2004**, *306*, 2074–2077.
- [**Antipin, 1996**] Antipin, M. Y.; Lyssenk, K.A.; Boese, R. *Journal of Organometallic Chemistry.* 1996, *508*, 259–262.
- [**Arfken, 1985**] *Mathematical methods for physicists.* Academic, Orlando, FL, **1985**.
- [**Aronica, 2008**] Aronica, C.; Chastanet, G.; Zueva, E.; Borshch, S. A.; Clemente-Juan, J. M.; Luneau, D. J. *Am. Chem. Soc.* **2008**, *130*, 2365–2371.
- [**Aureliano, 2000**] Aureliano, M. *J. Inorg. Biochem.* **2000**, *80*, 145–147.
- [**Aureliano, 2005**] Aureliano, M.; Gândara, R. M. C. *J. Inorg. Biochem.* **2005**, *99*, 979–985.
- [**Aureliano, 2009**] Aureliano, M. *Dalton Trans.*, **2009**, 9093–9100.
- [**Aureliano, 2014**] Aureliano, M.; André Ohlin, C. *Journal of Inorganic Biochemistry*, **2014**, *137*, 123–130.
- [**Augustyniak–Jablokow, 2005**] Augustyniak–Jablokow, M. A.; Borshch, S.; Daniel, C.; Hartl, H.; Yablokov, Y. V. *New J. Chem.* **2005**, *29*, 1064–1071.

B

- [**Bader, 1985**] Bader, R. F. W. *Atoms in molecules.* Acc. Chem. Res: **1985**, *18*.
- [**Bader, 1990**] Bader, R. F. W. *Atoms in molecules: A Quantum Theory.* Oxford University Press, New York. 1990.

- [Bader, 1991] Bader, R. F. W. *Chem. Rev.* **1991**, *91*, 893–928.
- [Bader, 1998a] Bader, R. F. W. *J. Phys. Chem. A.* **1998**, *102*, 7314–7323.
- [Bader, 1998b] Bader, R. F. W.; Gatti, C. *Chem. Phys. Lett.* **1998**, *287*, 233–238.
- [Bader, 2009] Bader, R. F. W. *J. Phys. Chem. A.* **2009**, *113*, 10391–10396.
- [Bae, 2009] Bae, J. H.; Lew, E.D.; Yuzawa, S.; Tome, F.; Lax, I.; Schlessinger, J. *Cell.* (Cambridge, Mass.). **2009**, *138*, 514–524.
- [Batchelor, 2010] Batchelor, L. J.; Shaw, R.; Markey, S. J.; Helliwell, M.; McInnes, E. J. L. *Chem. Eur. J.* **2010**, *16*, 5554–5557.
- [Becke, 1993] Becke, A. D. *J. Chem. Phys.* **1993**, *98*, 5648–5652.
- [Benson-Smith, 2007] Benson-Smith, J. J.; Goris, L.; Vandewal, K.; Haenen, K.; Manca, J. V.; Vanderzande, D.; Bradley, D. D. C.; Nelson, J. *Adv. Funct. Mater.* **2007**, *17*, 451–457.
- [Binning, 1990] Binning, R. C.; Curtiss, L. A. *J. Comp. Chem.* **1990**, *11*, 1206–1216.
- [Blasiak, 1995] Blasiak, J. *Z. Naturforsch.* **1995**, *50c*, 660–663.
- [Blessing, 1987] Blessing, R. H. *Crystallogr. Rev.* **1987**, *1*, 3–58.
- [Blessing, 1997] Blessing, R. H. *J. Appl. Crystallogr.* **1997**, *30*, 421–426.
- [Born, 1926] Born, M. *Z. Phys.* **1926**, *38*, 803.
- [Born, 1927] Born, M.; Oppenheimer, R. *Ann. Phys(Berlin).* **1927**, *389*, 457–484.
- [Bošnjaković-Pavlović, 2008] Electron and electrostatic properties of compounds containing a decavanadate anion from high resolution X-ray diffraction: toward a better understanding of chemical and biological properties of polyoxovanadates. PhD thesis. **2008**.
- [Bošnjaković-Pavlović, 2009] Bošnjaković-Pavlović, N.; Spasojević – de Biré A.; Tomaz, I.; Bouhaida, N.; Avecilla, F.; Mioc, U. B.; Pessoa, J. C.; Ghermani, N. E. *Inorg. Chem.* **2009**, *48*, 9742–9753.
- [Bošnjaković-Pavlović, 2010] Bošnjaković-Pavlović, N.; Spasojević – de Biré, A. *J. Phys. Chem.* **2010**, *114*, 10664–10675.
- [Bošnjaković-Pavlović, 2011] Bošnjaković-Pavlović, N.; Prévost, J.; Spasojević – de Biré A. *Cryst. Growth & Des.* **2011**, *11*, 3778–3789.
- [Boyd, 1985] Boyd, D.W.; Kustin, K.; Niwa, M. *Biochim. Biophys. Acta.* **1985**, *827*, 472–475.
- [Bradley, 1936] Bradley, A. J.; Illingworth, J. W. *Proc. R. Soc. Lond. A.* **1936**, *157*, 113–131.

[**Brechin, 2005**] Brechin, E. K. *Chem. Commun.* **2005**, 5141–5153.

[**Burnett, 1996**] Burnett, M. N.; Johnson, C. K. ORTEP III. Report ORNL-6895. Oak Ridge National Laboratory, Tennessee, USA, **1996**.

C

[**Calatayud, 2001a**] Calatayud, M.; Silvi, B.; Andres, J.; Beltran, A. *Chemical Physics Letters.* 2001, 333, 493–503.

[**Calatayud, 2001b**] Calatayud, M.; Andres, J.; Beltran, A.; Silvi, B. *Theoretical Chemistry Accounts.* **2001**, 105, 299–308.

[**Cantley, 1977**] Cantley, L. C.; Josephson, L.; Warner, R.; Yanacisawa, M.; Lechene, C.; Guidotti, G. *J. Biol. Chem.* **1977**, 252, 7421–7423.

[**Chen, 1990**] Chen, Q.; Zubieta, J. *Inorg. Chem.* **1990**, 29, 1456–1458.

[**Chen, 1992a**] Chen, Q.; Zubieta, J. *Inorg. Chim. Acta.* **1992**, 95, 198–200.

[**Chen, 1992b**] Chen, Q.; Goshorn, D. P.; Scholes, C. P.; Tan, X.; Zubieta, J. *J. Am. Chem. Soc.* **1992**, 114, 4667–4681.

[**Chen, 1993**] Chen, Q.; Zubieta, J. *J. Chem. Soc., Chem. Commun.* **1993**, 1180–1182

[**Chen, 2005**] Chen, L.; Jiang, F.; Lin, Z.; Zhou, Y.; Yue, C.; Hong, M. *J. Am. Chem. Soc.* **2005**, 127, 8588–8589.

[**Chen, 2009**] Chen, L.; Jiang, F.; Li, N.; Yan, C.; Xu, W.; Hong, M. *Inorg. Chem. Commun.* **2009**, 12, 219–222.

[**Coppens, 1985**] Coppens, P. *Coord. Chem. Rev.* **1985**, 65, 285–307.

[**Coppens, 1997**] Coppens, P. *X-ray charge densities and chemical bonding. IUCr texts on crystallography, vol 4.* International Union of Crystallography/Oxford University Press, Oxford: **1997**.

[**Coppens, 2004**] Coppens, P.; Volkov, A. *Acta. Crystallogr. A.* **2004**, 60, 357–364.

[**Coronado, 2005**] Coronado, E.; Gimenezsaiz, C.; Gomezgarcia, C. *Coord. Chem. Rev.* **2005**, 249, 1776–1796.

[**Cremer, 1984a**] Cremer, D.; Kraka, E. *Angew. Chem. Int. Ed. Engl.* **1984a**, 23, 627–628.

[**Cremer, 1984b**] Cremer, D.; Kraka, E. *Croat. Chem. Acta* **1984b**, 57, 1259–1281.

[**Cruciani, 2006**] Cruciani, G. *Molecular Interaction Fields: Applications in Drug Discovery and ADME Prediction.* Wiley, **2006**.

D

[**Daniel, 2005**] Daniel, C.; Hartl, H. *J. Am. Chem. Soc.* **2005**, *127*, 13978-13987.

[**Daniel, 2009**] Daniel, C.; Hartl, H. *J. Am. Chem. Soc.* **2009**, *131*, 5101-5114.

[**D’Cruz, 2003**] D’Cruz, O.J.; Dong, Y.; Uckun, F. M. *Biochem. Biophys. Res. Commun.* **2003**, *302*, 253-264.

[**Debye, 1915**] Debye, P. *Ann. Phys.* **1915**, *46*, 809-823.

[**Desiraju, 1989**] Desiraju, G. R. *Crystal engineering: the design of organic solids*. Elsevier, Amsterdam: **1989**.

[**Dolbecq, 2010**] Dolbecq, A.; Dumas, E.; Mayer, C. R.; Mialane, P. *Chem. Rev.* **2010**, *110*, 6009-6048.

[**Domae, 2009**] Domae, K.; Uchimura, D.; Koyama, Y.; Inami, S.; Hayashi, Y.; Isobe, K.; Kameda, H.; Shimoda, T. *Pure and Applied Chemistry*. **2009**, *81*, 1323-1330.

[**Domagała, 2008**] Domagała, S.; Jelsch, C. *J Appl Crystallogr.* **2008**, *41*, 1140-1149.

[**Du, 1992**] Du, Y.; Rheingold, A. L.; Maatta, E. A. *J. Am. Chem. Soc.* **1992**, *114*, 345-346.

[**Du, 2013**] Du, D. Y.; Yan, L. K.; Su, Z. M.; Li, S. L.; Lan, Y. Q.; Wang, E. B. *Coordination Chemistry Reviews*. **2013**, *257*, 702-717.

[**Dunning, 1977**] Dunning, J. T. H; Hay, P. J. *Modern Theoretical Chemistry*. Editor, Schaefer, H. F. **1977**, *3*, 1-28.

[**Dunning, 1989**] Dunning, T. H. *J. Chem. Phys.* **1989**, *90*, 1007-1023.

F

[**Farrugia, 1999**] Farrugia, L. J. *J. Appl. Crystallogr.* **1999**, *32*, 837-838.

[**Farrugia, 2003**] Farrugia, L. J.; Mallinson, P. R.; Stewart, B. *Acta. Cryst.* **2003**, *B59*, 234-247.

[**Farrugia, 2006**] Farrugia, L. J.; Evans, C.; Tegel, M. *J. Phys. Chem. A.* **2006**, *110*, 7952-7961.

[**Farrugia, 2009a**] Farrugia, L. J.; Evans, C.; Lentz, D.; Roemer, M. *J. Am. Chem. Soc.* **2009**, *131*, 1251-1268.

[**Farrugia, 2009b**] Farrugia, L. J.; Macchi, P. *J. Phys. Chem. A.* **2009**, *113*, 10058-10067.

[**Felts, 2006**] Felts, L. R.; Reilly, J.T.; Tanner, J.J. *J. Biol. Chem.* **2006**, *281*, 30289–30298.

[**Frisch, 2010**] Frisch, M. J.; Trucks, G. W.; Schlegel, H. B. ; Scuseria, G. E.; Robb, M. A.; Cheeseman, J. R.; Scalmani, G.; Barone, V.; Mennucci, B.; Petersson, G. A.; Nakatsuji, H.; Caricato, M.; Li, X. ; Hratchian, H. P.; Izmaylov, A. F.; Bloino, J.; Zheng, G.; Sonnenberg, J. L.; Hada, M.; Ehara, M.; Toyota, K.; Fukuda, R.; Hasegawa, J.; Ishida, M.; Nakajima, T.; Honda, Y.; Kitao, O.; Nakai, H.; Vreven, T.; Montgomery, J. A.; Peralta, J. E.; Ogliaro, F.; Bearpark, M.; Heyd, J. J.; Brothers, E.; Kudin, K. N.; Staroverov, V. N.; Keith, T.; Kobayashi, R.; Normand, J.; Raghavachari, K.; Rendell, A.; Burant, J. C.; Iyengar, S. S.; Tomasi, J. ; Cossi, M.; Rega, N.; Millam, J. M.; Klene, M.; Knox, J. E.; Cross, J. B.; Bakken, V.; Adamo, C.; Jaramillo, J.; Gomperts, R.; Stratmann, R. E.; Yazyev, O.; Austin, A. J.; Cammi, R.; Pomelli, C.; Ochterski, J. W.; Martin, R. L.; Morokuma, K.; Zakrzewski, V. G.; Voth, G. A.; Salvador, P.; Dannenberg, J. J.; Dapprich, S. ; Daniels, A. D.; Farkas, O.; Foresman, J. B.; Ortiz, J. V.; Cioslowski, J.; Fox, D. J. Gaussian, Inc., Wallingford CT, 2010.

[**Fux, 2012**] Fux, S.; Reiher, M. *Struct Bond.* **2012**, *147*, 99–142.

G

[**Gadre, 1999**] Gadre, S. R. *Topography of atomic and molecular scalar fields. In: Jerzy Leszczynski (ed) Computational chemistry: reviews of current trends, vol 4.* World Scientific, Singapore: **1999**.

[**Gatti, 2004**] Gatti, C.; Bertini, L. *Acta Crystallogr.* **2004**, *A60*, 438–449.

[**Gatti, 2005**] Gatti, C. *Z. Kristallogr.* **2005**, *220*, 399–457.

[**Gatti, 2007**] Gatti, C.; Lasi, D. *Faraday Discuss.* **2007**, *135*, 55–78.

[**Gatti, 2012**] Charge density analysis book. The Source Function Descriptor as a Tool to Extract Chemical Information from Theoretical and Experimental Electron Densities. *Struct. Bond.* **2012**, *147*, 193–286. Springer-Verlag Berlin Heidelberg.

[**Gatti, 2013**] Gatti, G. *Phys. Scr.* **2013**, *87* 048102.

[**Ghermani, 1993**] Ghermani, N.; Bouhaida, N.; Lecomte, C. *Acta Crystallogr.* **1993**, *A49*, 781–789.

[**Gikas, 2005**] Gikas, E.; Parissi-Poulou, M.; Kazanis, M.; Vavagiannis, A. *J. Mol. Struct. THEOCHEM.* **2005**, *724*, 135–142.

[**Grabowski, 2003**] Grabowski, Z. R.; Rotkiewicz, K.; Rettig, W. *Chem. Rev.*

2003, *103*, 3899–4032.

[**Gouzerh, 1998**] Gouzerh, P.; Proust, A. *Chem. Rev.* **1998**, *98*, 77–112.

[**Guillot, 2000**] Guillot, B.; Viry, L.; Guillot, R.; Lecomte, C.; Jelsch, C. *J. Appl. Crystallogr.* **2000**, *34*, 214–223.

H

[**Han, 2006**] Han, J. W.; Hardcastle, K. I.; Hill, C. L. *Eur. J. Inorg. Chem.* **2006**, 2598–2603.

[**Han, 2007**] Han, J. W.; Hill, C. L. *J. Am. Chem. Soc.* **2007**, *129*, 15094–15095.

[**Hansen&Coppens, 1978**] Hansen, N. K.; Coppens, P. *Acta Crystallogr.* **1978**, *A34*, 909–921.

[**Hayashi, 1991**] Hayashi, Y.; Ozawa, Y.; Isobe, K. *Inorg. Chem.* **1991**, *30*, 1025–1033.

[**Heinemann 2003**] Heinemann, G.; Fichtl, B.; Vogt, W. *Br. J. Clin. Pharmacol.* **2003**, *55*, 241–245.

[**Henry, 2002**] Henry, M. J. *Cluster Sci.* **2002**, *13*, 437–457.

[**Hill, 1998**] Hill, C. L. *Chem. Rev.* **1998**, *98*, 1–2.

[**Hill, 2006**] Hill, C. L.; Anderson, T. M.; Han, J. W.; Hillesheim, D. A.; Geletii, Y. V.; Okun, N. M.; Cao, R.; Botar, B.; Musaev, D. J.; Morokuma, K. *J. Mol. Catal. A: Chem.* **2006**, *251*, 234–238.

[**Hill, 2007**] Han, J. W.; Hill, C. L. A Coordination Network That Catalyzes O₂-Based Oxidations. *J. Am. Chem. Soc.* **2007**, *129*, 15094–15095.

[**Holladay, 1983**] Holladay, A.; Leung, P.; Coppens, P.; *Acta Cryst.* **1983**, *A39*, 377–387.

[**Horvat, 2006**] Horvat, A.; Orlić, T.; Banjac, A.; Momić, T.; Petrović, S.; Demajo, M. *Gen. Physiol. Biophys.* **2006**, *25*, 91–105.

[**Hsieh, 1983**] Hsieh, T.-C.; Zubieta, J. A. *Polyhedron.* **1986**, *5*, 1655–1657.

J

[**Janell, 2001**] Polyoxometalate Chemistry From Topology via Self-Assembly to Applications, pp Ribosomal Crystallography and Heteropolytungstates. **2001**, 391–415.

[**Jeannin, 1998**] Jeannin, Y. P. *Chem. Rev.* **1998**, *98*, 51–76.

[Jelsch, 2005] Jelsch, C.; Guillot, B.; Lagoutte, A.; Lecomte, C. *J. Appl. Crystallogr.* **2005**, *38*, 38–54.

[Jiang, 2011] Jiang, K.; Yang, Y.; Liu, Y.; Shi, D.; Sun, J. *Chem. Phys. Lett.* **2011**, *501*, 534–539.

K

[Kaminski, 2011] Kaminski, R.; Herbaczynska, B.; Srebro, M.; Pietrzykowski, A.; Michalak, A.; Jerzykiewicz, L.; Wozniak, K. *Phys. Chem. Chem. Phys.* **2011**, *13*, 10280–10284.

[Kang, 2004] Kang, J.; Nelson, J. A.; Lu, M.; Xie, B.; Peng, Z.; Powell, D. R. *Inorg. Chem.* **2004**, *43*, 6408–6413.

[Kanna, 2004] Kanna, P. S.; Mahendrakumar, C. B.; Indira, B. N.; Srivastawa, S.; Kalaiselvi, K.; Elayaraja, T.; Chatterjee, M. *Environ. Mol. Mutagen.* **2004**, *44*, 113–118.

[Keggin, 1933] Keggin, J. F. *Nature*, **1933**, *132*, 351.

[Keith, 2014] AIMALL (Version 14.11.23), Keith, T. A. TK Gristmill Software, Overland Park KS, USA, 2014 (aim.tkgristmill.com).

[Kempf, 1992] Kempf, J. Y.; Rohmer, M. M.; Poblet, J. M.; Bo, C.; Benard, M. *J. Am. Chem. Soc.* **1992**, *114*, 1136.

[Kessler, 2000] Kessler, V. G.; Seisenbaeva, G. A. *Inorganic Chemistry Communications* **2000**, 203–204.

[Khan, 1992] Khan, M. I.; Chen, Q.; Zubieta, J.; Goshorn, D. P. *Inorg. Chem.* **1992**, *31*(9), 1556–1558.

[Khan, 1993] Khan, M. I.; Chen, Q.; Hope, H.; Parkin, S.; O'Connor, C. J.; Zubieta, J. *Inorg. Chem.* **1993**, *32*(13), 2929–2937.

[Knoth, 1981] Knoth, W. H.; Harlow, R. L. *J. Am. Chem. Soc.* **1981**, *103*, 5265–4266.

[Kocher, 2004] Kocher, N.; Henn, J.; Gostevskii, B.; Kost, D.; Kalikhman, I.; Engels, B.; Stalke, D. *J. Am. Chem. Soc.* **2004**, *126*, 5563–5568.

[Kohout, 2004] Kohout, M. *Int J Quantum Chem.* **2004**, *97*, 651–658.

[Kohout, 2007] Kohout, M. *Faraday Discuss* **2007**, *135*, 43–54.

[Koritsanszky, 2001] Koritsanszky, T. S.; Coppens, P. *Chem. Rev.* **2001**, *101*, 1583–1628.

[**Kotova, 2011**] Kotova, O.; Lyssenko, K.; Rogachev, A.; Eliseeva, S.; Fedyanin, I.; Lepnev, L.; Pandey, L.; Burlov, A.; Garnovskii, A.; Vitukhnovsky, A.; Van der Auweraer, M.; Kuzmina, N. *J. Photochem. Photobiol. A*. **2011**, *218*, 117–129.

[**Krstić, 2004**] Krstić, D.; Krinulović, K.; Joksić, G.; Spasojević–Tišma, V.; Momić, T.; Vasić, V. *J. Enz. Inhib. Med. Chem.* **2004**, *19*, 409–415.

[**Krstić, 2005**] Krstić, D.; Krinulović, K.; Vasić, V. *J. Enz. Inhib. Med. Chem.* **2005**, *20*, 469–476.

[**Krstić, 2009**] Krstić, D.; Čolović, M.; Bošnjaković–Pavlović, N.; Spasojević–De Bire, A.; Vasić, V. *Gen. Physiol. Biophys.* **2009**, *28*, 302–308.

[**Kurki-Suonio, 1977**] Kurki-Suonio, K. *Isr. J. Chem.* **1977**, *16*, 115–123.

[**Kwen, 1999**] Kwen, H.; Young, V. G., Jr.; Maatta, E. A. *Angew. Chem. Int. Ed.* **1999**, *38*, 1145–1146.

L

[**Lecomte, 2001**] Lecomte, C.; Souhassou, M.; Pillet, S. *J. Mol. Struct.* **2003**, *647*, 53–64.

[**Lefranc, 2008**] Lefranc, F.; Mijatović, T.; Kondo, Y.; Sauvage, S.; Roland, I.; Krstić, D.; Vasić, V.; Gailly, P.; Kondo, S.; Blanco, G.; Kiss, R. *Neurosurgery*. **2008**, *62*, 211–222.

[**Leroy, 2008**] Leroy, F.; Miro, P.; Poblet, J. M.; Bo, C.; Avalos, J. B. *J. Phys. Chem. B*. **2008**, *112*, 8591.

[**Leusser, 2004**] Leusser, D.; Henn, J.; Kocher, N.; Engels, B.; Stalke, D. *J Am Chem Soc.* **2004**, *126*, 1781–1793.

[**Li, 2011**] Li, D.; Song, J.; Yin, P.; Simotwo, S.; Bassler, A. J.; Aung, Y.; Roberts, J. E.; Hardcastle, K. I.; Hill, C. L.; Liu, T. *J. Am. Chem. Soc.* **2011**, *133*, 14010–14016.

[**Li, 2011**] Li, Q.; Zhao, C.; Bond, A. M.; Boas, J. F.; Wedd, A. G.; Moubaraki, B.; Murray, K. S. *J. Mater. Chem.* **2011**, *21*, 5398–5407.

[**Long, 2003**] Long, D.-L.; Gerler, P. K.; Farrugia, L. J.; Cronin, L. *Angew.Chem.* **2003**, *115*, 4312–4315; *Angew. Chem. Int. Ed.* **2003**, *42*, 4180–4183.

[**Long, 2006**] Long, D.-L.; Cronin, L. *Chem. Eur. J.* **2006**, *12*, 3698–3706.

[**Long, 2010**] Long, D.-L.; Tsunashima, R.; Cronin, L. *Angew. Chem. Int. Ed.* **2010**, *49*, 1736–1758.

[Lu, 2012] Lu, T.; Chen, F. *Journal of Computational Chemistry*. **2012**, *33*, 580–592.

[Luis, 1998] Luis, P. A. L.; Martín-Zarza, P.; Sánchez, A.; Ruiz-Pérez, C.; Hernández-Molina, M. A.; Solans, X.; Gili, P. *Inorganica Chimica. Acta*, **1998**, *277*, 139–150.

M

[Ma, 2011] Ma, H.; Meng, X.; Sha, J.; Pang, H.; Wu, L. *Solid State Sci.* **2011**, *13*, 850–854.

[Macchi, 1999] Macchi P., Garlaschelli L., Martinengo S., Sironi A., *J. Am. Chem. Soc.* **1999**, *121*, 10428-10429.

[Macchi, 2007] Macchi, P.; Sironi, A. Interactions involving metals: from “chemical categories” to QTAIM, and backwards, chapter 13. *In: Matta CF, Boyd RJ (eds) The quantum theory of atoms in molecules: from solid state to DNA and drug design*. Wiley-VCH, Weinheim:2007.

[Maguerès, 2000] Maguerès, P. L.; Hubig, S. M.; Lindeman, S. V.; Veya, P.; Kochi, J. K. *J. Am. Chem. Soc.* **2000**, *122*, 10073–10082.

[Martin, 1982] Martin, M.; Rees, B.; Mitschler, A. *Acta Cryst.* **1982**, *B38*, 6–15.

[Matta, 2003] Matta, C. F.; Hernandez-Trujillo, J.; Tang, T.-H.; Bader, R. F. W. *Chem Eur J* **2003**, *9*, 1940–1951.

[Matta, 2007] Matta, C. F.; Boyd, R. J. *The quantum theory of atoms in molecules: from solid state to DNA and drug design*. Wiley-VCH, Weinheim: 2007.

[Meindl, 2009] Meindl, K.; Henn, J.; Kocher, N.; Leusser, D.; Zachariasse, K. A.; Sheldrick, G. M.; Koritsanszky, T.; Stalke, D. *J. Phys. Chem. A.* **2009**, *113*, 9684–9691.

[Messmore, 2000] Messmore, J. M.; Raines, R. T. *Biochem. Biophys.* **2000**, *381*, 25–30.

[Miyasaka, 2013] Miyasaka, H. *Acc. Chem. Res.* **2013**, *46*, 248–257.

[Molinuevo, 2004] Molinuevo, M. S.; Barrio, D. A.; Cortizo, A. M.; Etcheverry, S. B. *Cancer Chemother. Pharmacol.* **2004**, *53*, 163–172.

[Müller, 1995] Müller, A.; Krickemeyer, E.; Meyer, J.; Bogge, H.; Peters, F.; Plass, W.; Diemann, E.; Dillinger, S.; Nonnenbruch, F.; Randerath, M.; Menke, C. *Angew. Chem.* **1995**, *107*, 2293–2295; *Angew. Chem. Int. Ed. Engl.* **1995**, *34*, 2122–

2126.

[Müller, 1995] Müller, A.; Meyer, J.; Bogge, H.; Stammeler, A.; Botar, A. Z. *anorg. allg. Chem.* **1995**, *621*, 1818–1831.

[Müller, 1998] Müller, A.; Krickemeyer, E.; Bogge, H.; Schimidtmann, M.; Peters, F. *Angew. Chem.* **1998**, *110*, 3567–3571; *Angew. Chem. Int. Ed.* **1998**, *37*, 3359–3363.

[Müller, 2004] Müller, A.; Roy, S. *The Chemistry of Nanomaterials: Synthesis, Properties and Applications*. Wiley-VCH, Weinheim: **2004**.

[Mulliken, 1952] Mulliken, R. S. *J. Phys. Chem.* **1952**, *56*, 801–822.

[Mulliken, 1962] Mulliken, R. S.; Person, W. B. *Annu. Rev. Phys. Chem.* **1962**, *13*, 107–126.

[Mulliken, 1964] Mulliken, R. S. *J. Chim. Phys., Chim. Biol.* **1964**, *61*, 20–38.

N

[Nagy, 1986] Nagy, A. Eds. G. W. Kreutzberg, M. Reddington and H. Zimmermann. **1986**, 49–59.

[Nalwa, 1997] Nalwa, H. S. *Handbook of Organic Conductive Molecules and Polymers I–IV*, ed. Wiley, Chichester, 1997.

[Neier, 1995] Neier, R.; Trojanowski, C.; Mattes, R. *J. Chem. Soc. Dalton Trans.* **1995**, 2521–2528

[Niu, 2010] Niu, Y.; Ren, X.; Yin, B.; Wang, D.; Xue, G.; Hu, H.; Fu, F.; Wang, J. *J. Organomet. Chem.* **2010**, *695*, 1863–1868.

O

[Orgel, 1957] Orgel, L. E.; Mulliken, R. S. *J. Am. Chem. Soc.* **1957**, *79*, 4839–4846.

[Ortmann, 1992] Ortmann, I.; Werner, S.; Kruger, C.; Mohr, S.; Schaffner, K. *J. Am. Chem. Soc.* **1992**, *114*, 5048–5054.

[Overgaard, 2002] Overgaard, J.; Iversen, B. B.; Pali, S. P.; Timco, G. A.; Gerneleu, N. V.; Larsen, F. K. *Chem. Eur. J.* **2002**, *8*, 2775–2786.

[Ozerov, 2001] Ozerov, R. P.; Streltsov, V. A.; Sobolev, A. N.; Figgis, B. N.; Volkov, V. L. *Acta Cryst.* **2001**, *B57*, 244–250.

P

[Pathak, 1990] Pathak, R. K.; Gadre, S. R. *J Chem Phys.* **1990**, *93*, 1770–1773.

[Pearson, 1963] Pearson, R. G. *J. Am. Chem. Soc.* **1963**, *85*, 3533–3539.

[Perdew, 1986] Perdew, J. P. *Phys. Rev. B* **1986**, *33*, 8822–8824.

[Pezza, 2002] Pezza, R. J.; Villarreal, M. A.; Montich, G. G.; Argarana, C. E. *Nucleic Acids Res.* **2002**, *30*, 4700–4708.

[Pichon-Pesme, 1998] Pichon-Pesme, V.; Lecomte, C.; Lachekar, H. *J. Phys. Chem.* **1995**, *99*, 6242–6250.

[Piepenbrink, 2002] Piepenbrink, M.; Triller, M. U.; Gorman, N. H. J.; Krebs, B. *Angew. Chem. Int. Ed.* **2002**, *41*, 2523–2525.

[Pope, 1983] Pope, M. T. *Heteropoly and Isopoly Oxometalates*. Berlin: Springer; **1983**.

[Pope, 1991] Pope, M.T.; Müller, A. *Angew. Chem. Int. Ed. Engl.* **1991**, *30*, 34–48.

R

[Rassolov, 2001] Rassolov, V. A.; Ratner, M. A.; Pople, J. A.; Redfern, P. C.; Curtiss, L. A. *J. Comp. Chem.* **2001**, *22*, 976–984.

[Re, 2003] Re, R. E. D.; Kuehl, C. J.; Brown, M. G.; Rocha, R. C.; Bauer, E. D.; John, K. D.; Morris, D. E.; Shreve, A. P.; Sarrao, J. L. *Inorg. Chem.* **2003**, *42*, 5551–5559.

[Rees, 1976] Rees, B.; Mitschler, A. *J. Am. Chem. Soc.* **1976**, *98*, 7918–7924.

[Rodriguez de Lores Aranaiz, 1995] Rodriguez de Lores Aranaiz, G.; Pena, C. *Neurochem. Int.* **1995**, *27*, 319–327.

S

[Sabino, 2003] Sabino, J. R.; Coppens, P. *Acta Cryst.* **2003**, *A59*, 127–131.

[Sadakane, 1998] Sadakane, M.; Steckhan, E. *Chem. Rev.* **1998**, *98*, 219–237.

[Sagar, 1988] Sagar, R. P.; Ku, A. C. T.; Smith, V. H.; Simas, A. M. *J. Chem. Phys.* **1988**, *88*, 4367–4374.

[Sakurai 2004] Sakurai, H.; Inohara, T.; Adachi, Y.; Kawabe, K.; Yasui, H.; Takada, J. *Bioorg. Med. Chem. Lett.* **2004**, *14*, 1093–1096.

[Sanchez, 1999] Sanchez, C.; Ribot, F.; Lebeau, B. *J. Mater. Chem.* **1999**, *9*, 35–

44.

[**Santoni, 2012**] Santoni, M.-P.; Pal, A. K.; Hanan, G. S.; Tang, M.-C.; Venne, K.; Furtos, A.; M énard-Tremblay, P.; Malveaua, C.; Hasenknop, B. *Chem. Commun.* **2012**, 48, 200–202.

[**Scales, 2010**] Scales, E.; Sorace, L.; Dei, A.; Caneschi, A ; Muryn, C. A.; Collison, D.; McInnes, E. J. L. *Chemical Science*, **2010**, 1, 221–225.

[**Scheiner–Bobis, 2002**] Scheiner–Bobis, G. *Eur. J. Biochem.* **2002**, 269, 2424–2433.

[**Schulz, 2010**] Schulz, J.; Gyepes, R.; Cisarova, I; Stepnicka, P. *New J. Chem.* **2010**, 34, 2749–2756.

[**Sheldrick, 1997**] Sheldrick, G. M. SHELXS97 and SHELXL97: programs for crystal structure refinement; University of Gottingen: Gottingen, Germany, **1997**.

[**Sheldrick, 2003**] Sheldrick, G. SADABS (version 2.10): University of Göttingen, **2003**.

[**Sheldrick, 2008**] Sheldrick, G. M. *Acta Crystallogr.* **2008**, A64, 112–122.

[**Shi, 1988**] Shi, Z.; Boyd, R. J. *J. Chem. Phys.* **1988**, 88, 4375–4377.

[**Song, 2012**] Song, Y.-F.; Tsunashima, R. *Chem. Soc. Rev.* **2012**, 41, 7384–7402.

[**Spackman, 1986**] Spackman, M. A.; Maslen, E. N. *J. Phys. Chem.* **1986**, 90(10), 2020–2027.

[**Spackman, 1997**] Spackman, M.A. *Annu Rep Progr Chem C Phys Chem* **1997**, 94, 177–207.

[**Spackman, 2008**] Spackman, M.A.; McKinnon, J.J.; Jayatilaka, D. *Cryst. Eng. Comm.* **2008**, 10, 377–388.

[**Spackman, 2009**] Spackman, M. A.; Jayatilaka, D. *Cryst. Eng. Comm.* **2009**, 11, 19–32.

[**Spandl, 2003**] Spandl, J.; Daniel, C.; Brudgam, I.; Hartl, H. *Angew. Chem. Int. Ed.* **2003**, 42, 1163–1166.

[**Stark, 1995**] Stark, J. L.; Young, V. G.; Maatta, E. A. *Angew. Chem. Int. Ed. Engl.* **1995**, 34, 2547–2548.

[**Statoni, 2011**] Santoni, M.; Pal, A. K; Hanan, G. S; Proust, A.; Hasenknopf, B. *Inorg. Chem.* **2011**, 50, 6737–6745.

[**Stevens, 1979**] Stevens, E. D.; Coppens, P. *Acta Cryst.* 1979, A35, 536–539.

[**Stewart, 1980**] Stewart, R. F.; Feil, D. *Acta Crystallogr.* **1980**, A36, 503–509.

[**Stewart,1975**] Stewart, R. F.; Bentley, J.; Goodman, B. J. *Chem. Phys.* **1975**, 63,

3786–3793.

[**Stokes, 2005**] Stokes, D. L.; Delavoie, F.; Rice, W. J.; Champeil, P.; McIntosh, D.B.; Lacap ère, J. J. *J. Biol. Chem.* **2005**, *280*, 18063–18072.

[**Suss-Fink, 1998**] Suss-Fink, G.; Plasseraud, L.; Ferrand, V.; Stanislas, S.; Neels, A.; Stoeckli-Evans, H; Henry, M; Laurency, G; Roulet, R. *Polyhedron*.**1998**, *17*, 2817–2827.

T

[**Tiago, 2004**] Tiago, T.; Aureliano, M.; Guti érez–Merino, C. *Biochemistry*. **2004**, *43*, 5551–5561.

[**Tiana, 2010**] Tiana, D. Organometallic chemistry from the interacting quantum atoms approach, PhD thesis, University of Milano, **2010**.

[**Tsirelson ,1996**] Tsirelson, V. G.; Ozerov, R. P. Electron Density and Bonding in Crystals. **1996**.

[**Tsunashima, 2012**] Tsunashima, R.; Matsumoto, T.; Hoshino, N.; Niiho, W.; Kimura, M.; Kondo, K.; Suyama, Y.; Nishioka, Y.; Kawamata, J.; Noro, S.; Nakamura, T.; Akutagawa, T.; Ishiguro, K. *Dalton. Trans.* **2012**, *41*, 10060–10064.

V

[**Vasić, 1999**] Vasić, V.; Jovanović, D.; Krstić, D.; Nikezić, G.; Horvat, A.; Vujisić, L.; Nedeljković, N. *Toxicology Letters*. **1999**, *110*, 95–104.

[**Vasilets, 1993**] Vasilets, L. A.; Schwarz, W. *Biochim. Biophys. Acta*. **1993**, *1154*, 201–222.

[**Veya, 1995**] Veya, P. L.; Kochi, J. K. *J. Organomet. Chem.* **1995**, *488*, C4–C8.

[**Volkov, 2006**] Volkov, A.; Macchi, P; Farrugia, L. J.; Gatti, C.; Mallinson, P.; Richter, T.; Koritsanszky ,T. XD2006: a Computer Program Package for Multipole Refinement, Topological Analysis of Charge Densities and Evaluation of Intermolecular Energies from Experimental and Theoretical Structure Factors, **2006**.

W

[**Wang, 1976**] Wang, Y.; Blessing, R. H.; Ross, F. K.; Coppens, P. *Acta Cryst.* **1976**, *B32*, 572–578.

[**Wang, 2012**] Wang, Y. F; Weinstock, I. A. *Chem. Soc. Rev.*, **2012**, *41*, 7479–7496.

[Wang, 2013] Wang, Y. *J. Chin. Chem. Soc.* **2014**, *61*, 27–38.

[Wei, 2001] Wei, Y.; Xu, B.; Barnes, C. L.; Peng, Z. *J. Am. Chem. Soc.* **2001**, *123*, 4083–4084.

[Wu, 2011] Wu, P.; Xiao, Z.; Zhang, J.; Hao, J.; Chen, J.; Yin, P.; Wei, Y. *Chem. Commun.* **2011**, *47*, 5557–5559.

X

[Xia, 2005] Xia, Y.; Wei, Y. G.; Wang, Y.; Guo, H. Y. *Inorg. Chem.* **2005**, *44*, 9823–9828.

[Xu, 2002] Xu, L.; Lu, M.; Xu, B. B.; Wei, Y. G.; Peng, Z. H.; Powell, D. R. *Angew. Chem. Int. Ed.* **2002**, *41*, 4129–4132.

[Xu, 2010] Xu, H.; Zhang, L.; Li, Z.; Liu, X.; Hu, H.; Xue, G. *Solid State Sci.* **2010**, *12*, 1332–1336.

Y

[Yamase, 1994] Yamase, T.; Ohtaka, K. *J. Chem. Soc. Dalton Trans.* **1994**, *18*, 2599–2608.

[Yamase, 1998] Yamase, T. *Chem. Rev.* **1998**, *98*, 307–325.

[Yang, 2004] Yang, X. G.; Yang, X. D.; Yuan, L.; Wang, K.; Crans, D. C. *Pharm. Res.* **2004**, *21*, 1026–1033.

[Yin, 2011] Yin, P.; Wu, P.; Xiao, Z.; Li, D.; Bitterlich, E.; Zhang, J.; Cheng, P.; Vezenov, D. V.; Liu, T.; Wei, Y. *Angew. Chem. Int. Ed.* **2011**, *50*, 2521–2525.

[Yin, 2012] Yin, P.; Li, D.; Liu, T. *Chem Soc Rev.* **2012**, *41*, 7368–7383.

Z

[Zarychta, 2007] Zarychta, B.; Pichon-Pesme, V.; Guillot, B.; Lecomte, C.; Jelsch, C. *Acta Crystallogr A.* **2007**, *63*, 108–125.

[Zhao, 2008] Zhao, Y.; Truhlar, D. G. *Theor. Chem. Acc.*, **2008**, *120*, 215–41.

[Zhao, 2012] Zhao, Y.; Liang, W. *Chem. Soc. Rev.* **2012**, *41*, 1075–1087.

[Zhu, 2009] Zhu, X.; Yang, Q.; Muntwiler, M. *Acc. Chem. Res.* **2009**, *42*, 1779–1787.

[Ziegler, 2009] Ziegler, A.J.; Florian, J.; Ballicora, M. A.; Herlinger, A.W.; *J. Enzyme Inhib. Med. Chem.* **2009**, *24*, 22–28.

[Zylinska, 2000] Zylinska, L.; Soszynski, M. *Acta Biochim. Pol.* **2000**, *47*, 529–539.

APPENDIX

Table A1.1. The other functionalized V6 compounds.

Table A2.1. Atomic coordinates of functionalized V6-C3.

Table A2.2. Thermal displacement parameters of functionalized V6-C3.

Table A2.3. Selected bond angles in functionalized V6-C3.

Table A2.4. Bond distances in functionalized V6-C3.

Table A3.1. Atomic coordinates of functionalized V6OH.

Table A3.2. Thermal displacement parameters of functionalized V6OH.

Table A3.3. Selected Bond angles in functionalized V6OH.

Table A4.1. Theoretical results of the topological analysis of charge density at (3,-1) bond critical point (BCP) of V6 core in isolated V6 by M06/cc-pVTZ.

Table A4.2. Theoretical results of the topological analysis of charge density at (3,-1) bond critical point (BCP) in functionalized V6CH3 by M06-2X/cc-pVTZ.

Table A4.3. Theoretical results of the topological analysis of charge density at (3,-1) bond critical point (BCP) of V6 core in functionalized V6NH2 by M06/cc-pVTZ.

Table A4.4. Theoretical results of the topological analysis of charge density at (3,-1) bond critical point (BCP) of functionalized V6OH by M06-2X/cc-pVTZ.

Table A4.5. Theoretical results of the topological analysis of charge density at (3,-1) bond critical point (BCP) of functionalized V6NO2 by M06-2X/cc-pVTZ.

Table A4.6. Theoretical results of the topological analysis of charge density at (3,-1) bond critical point (BCP) of functionalized V6-C6 by M06-2X/cc-pVTZ.

Table A4.7. Theoretical results of the topological analysis of charge density at (3,-1) bond critical point (BCP) of functionalized V6-TPY by M06-2X/cc-pVTZ.

Table A4.8. Theoretical results of the topological analysis of charge density at (3,-1) bond critical point (BCP) of V10 by M06/cc-pVTZ.

Table A5.1. List of compounds sent in Faculty of Medicine, University of Belgrade for biological activity.

Table A5.2. Non covalent interaction in functionalized V6 series by CSD searching.

Figure A5.1. Compilation of the $\nabla^2\rho(\mathbf{r}_c)$ values determined in the functionalized V6 series.

Figure A5.2. Compilation of the abs (λ_1/λ_3) values determined in the functionalized V6 series.

Figure A5.3. Compilation of the $\nabla^2\rho(\mathbf{r}_c)$ values determined in the functionalized V6 series.

Figure A5.4. Compilation of the $2G(\mathbf{r}_c)/|V(\mathbf{r}_c)|$ values determined in the functionalized V6 series.

Figure A5.5. Compilation of the $G(\mathbf{r}_c)/\rho(\mathbf{r}_c)$ values determined in the functionalized V6 series.

Figure A5.6. Compilation of the $H(\mathbf{r}_c)$ values determined in the functionalized V6 series.

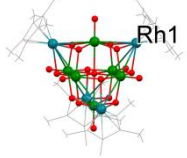
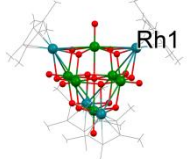
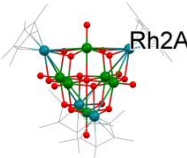
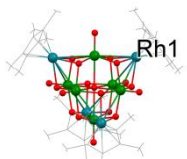
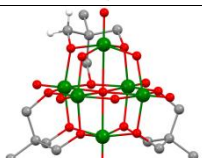
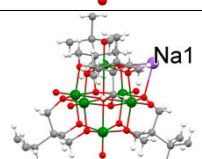
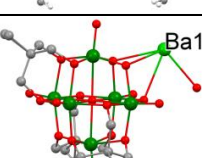
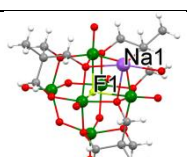
Figure A5.7. Compilation of the abs $|V(\mathbf{r}_c)| / G(\mathbf{r}_c)$ values determined in the functionalized V6 series.

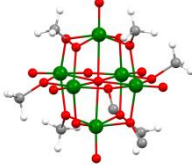

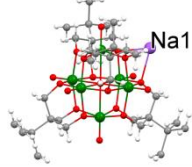
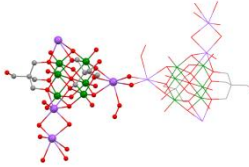
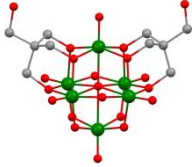
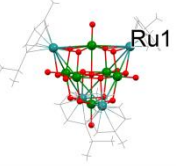
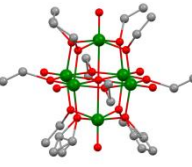
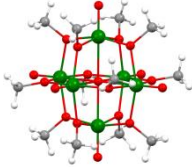


Figure A5.8. Behavior of $G(\mathbf{r}_c)$ as a function of $\nabla^2\rho(\mathbf{r}_c)$ as determined in the functionalized V6 series.

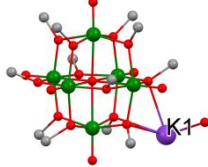

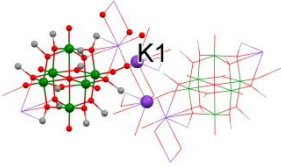

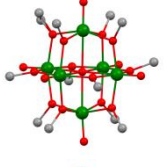
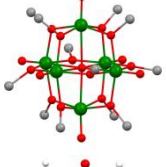
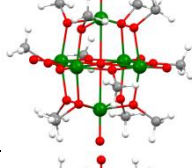
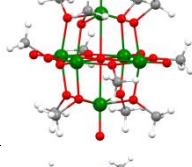
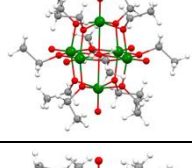
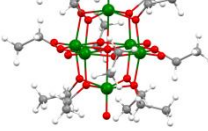
Figure A5.9. Photography of powder or crystals compounds sent in the Faculty of Medicine, University of Belgrade, for biological activity assay.

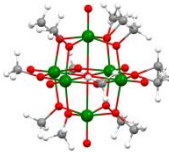

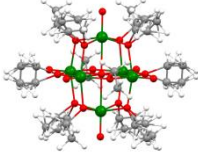
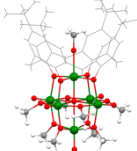
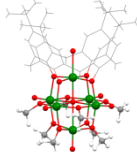
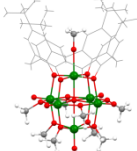
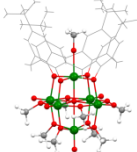

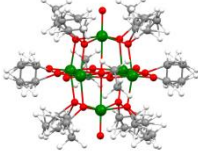
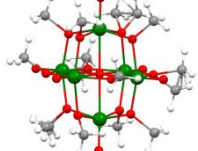
Figure A5.10. Distribution of distance and angle for CH O interaction according to the different type of oxygen atoms.

Table A1.1. The other functionalized V6 compounds.

CSD Refcode	Structure of functionalized hexavanadate	R factor	Cation or other segment	Reference
VALPUT		4.2	CH ₃ CN, CH ₃ CN, H ₂ O	Chae, 1989
VALPUT01		4.7	CH ₃ CN, H ₂ O	Hayashi, 1989
SIZROI		4.82	CH ₃ CN, H ₂ O	Hayashi, 1991
VALPUT11		4.6	CH ₃ CN, H ₂ O	Hayashi, 1991
JOXCII		4.1	(CH ₃) ₃ NH ⁺	Khan, 1992
JOXCOO		5.1	Na ⁺	Khan, 1992
HAHMEI		5.76	Ba ²⁺	Khan, 1993
HAHMIM	No crystal structure	0	Rb ²⁺	Khan, 1993
HAHMUY		3.71	Na ⁺ , H ₂ O	Khan, 1993

HEHNIR		5.68	Bu_4N^+	Hou, 1993
JOXCII10		4.1	$(\text{CH}_3)_3\text{NH}^+$	Khan, 1993
JOXCOO10		5.09	Na^+	Khan, 1993
ZEVLUH		6.7	Na^+ , H_2O	Müller, 1995
ZEVMAO		12.6	CH_6N_3^+ , H_2O	Müller, 1995
HIRMAW		3.66	H_2O	Suss-Fink, 1998
XADMEU		5.45	No	Kessler, 2000
MUXTAA		4.24	-	Spandl, 2003
MUXVUW		5.44	SbCl_6^- , CH_2Cl_2	Spandl, 2003
MUXTEE		7.36	Bu_4N^+ , CH_3OH	Spandl, 2003

MUXTII		5.68	K^+ , H_2O	Spandl, 2003
MUXTOO		4.37	Bu_4N^+	Spandl, 2003
MUXTUU		4.41	K^+ , H_2O	Spandl, 2003
MUXVAC		14.24	I^- , I_2	Spandl, 2003
MUXVEG		7.71	Br^- , Br_2	Spandl, 2003
MUXVIK		4.82	Br_3^-	Spandl, 2003
MUXTAA01		2.82	-	Augustyniak, 2005
MUXTAA02		2.82	-	Daniel, 2005
QAWDIC		3.36	$SbCl_6^-$	Daniel, 2005
QAWDOI		1.8	$SbCl_6^-$, CH_2Cl_2	Daniel, 2005

QAWDUO		3.59	SbCl_6^-	Daniel, 2005
XADMEU01		4.94	-	Daniel, 2005
XADMEU02		4	-	Daniel, 2005
NOBDAK		5.18	Et_4N^+	Aronica, 2008
NOBDEO		7.38	NH_4^+	Aronica, 2008
NOBDIS		5.04	$(\text{C}_2\text{H}_5)_3\text{NH}^+$	Aronica, 2008
NOBDOY		5.75	$\text{C}_5\text{H}_6\text{N}^+$	Aronica, 2008
XADMEU03		4.94	No	Augustyniak, 2008
XADMEU04		4	No	Augustyniak, 2008
FUSLEL		3.18	No	Daniel, 2009



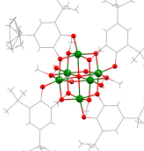
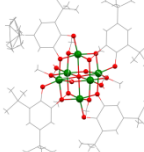



MUXVUW01		5.44	SbCl_6^- , CH_2Cl_2	Daniel, 2009
NABPAJ		6.61	Ph_4P^+	Domae, 2009
MUVLEV		5.5	CH_3OH	Scales, 2010
MUVLUL		7.24	CH_3OH , H_2O	Scales, 2010
TURWEJ		4.88	$\text{C}_3\text{H}_6\text{N}^+$, CH_3CN , H_2O	Batchelor, 2010
TURWIN		8.26	$\text{C}_3\text{H}_6\text{N}^+$, CH_3CN	Batchelor, 2010
ACIMEG		6.43	$[\text{Co}(\text{NCS})_4]^{2-}$, PhCH_3	Adach, 2012

Table A2.1: Atomic coordinates of functionalized V6-C3.

Atom	<i>x</i>	<i>y</i>	<i>z</i>	U_{eq}
V1	0.42450	-0.00405	0.38815	0.013892
V2	0.52194	-0.14972	0.48959	0.014056
V3	0.68140	0.03455	0.46368	0.014609
O61	0.50000	0.00000	0.50000	0.012251
O11	0.35181	-0.00264	0.31076	0.019175
O12	0.55501	-0.25605	0.48870	0.018933
O13	0.81955	0.04657	0.44311	0.020392
O21	0.62973	0.14708	0.47491	0.017578
O22	0.45129	-0.12694	0.40383	0.017505
O23	0.58211	0.01983	0.37847	0.017434
O31	0.60063	-0.12584	0.58853	0.013711
O32	0.68428	-0.10392	0.46728	0.014554
O33	0.73097	0.02083	0.56457	0.014452
O1	0.92408	-0.27352	0.58864	0.0232
O2	1.09243	-0.30892	0.66309	0.051106
C1	0.71659	-0.16753	0.61123	0.015735
C2	0.79573	-0.14704	0.49699	0.016806
C3	0.83954	-0.02902	0.58933	0.016926
C4	0.82253	-0.13065	0.57491	0.015528
C5	0.94229	-0.17839	0.60434	0.019371
C6	1.00548	-0.33116	0.62148	0.02831
C7	0.97689	-0.42827	0.60056	0.039432
C8	0.86183	-0.44325	0.54886	0.0505
N1	0.38065	-0.30994	0.27045	0.018396
C11	0.38224	-0.27700	0.19720	0.020862
C12	0.41506	-0.17778	0.18937	0.026557
C13	0.39489	-0.15223	0.11369	0.034832
C14	0.43152	-0.05709	0.09871	0.059196
C21	0.27822	-0.26102	0.30105	0.019479
C22	0.25064	-0.29516	0.37047	0.019555
C23	0.15011	-0.23548	0.39444	0.021107
C24	0.11232	-0.26658	0.46238	0.026185
C31	0.50315	-0.29058	0.31521	0.022056
C32	0.61850	-0.32588	0.28840	0.025119
C33	0.73099	-0.31864	0.34374	0.027007
C34	0.84694	-0.36001	0.32024	0.036392
C41	0.35921	-0.41132	0.26907	0.019562
C42	0.23324	-0.44419	0.23472	0.020661
C43	0.23048	-0.54750	0.23780	0.027173
C44	0.10761	-0.58655	0.20406	0.035699

Table A2.2. Thermal displacement parameters of functionalized V6-C3.

Atom	U ₁₁	U ₂₂	U ₃₃	U ₁₂	U ₁₂	U ₂₃
V1	0.013892	0.01858	0.01324	0.01010	-0.00091	0.00283
V2	0.014056	0.01773	0.00952	0.01470	-0.00122	0.00140
V3	0.014609	0.01600	0.01396	0.01471	0.00314	0.00515
O61	0.012251	0.01630	0.01011	0.01083	-0.00043	0.00360
O11	0.019175	0.02608	0.01953	0.01127	-0.00069	0.00018
O12	0.018933	0.02632	0.00988	0.02030	-0.00113	0.00205
O13	0.020392	0.01768	0.02305	0.02183	0.00507	0.00773
O21	0.017578	0.01821	0.01220	0.02248	0.00328	0.00331
O22	0.017505	0.02423	0.01269	0.01469	-0.00358	-0.00066
O23	0.017434	0.01925	0.02141	0.01266	0.00279	0.00587
O31	0.013711	0.01670	0.01199	0.01267	0.00040	0.00282
O32	0.014554	0.01691	0.01368	0.01354	0.00017	0.00379
O33	0.014452	0.01676	0.01242	0.01426	0.00040	0.00239
O1	0.0232	0.02401	0.01891	0.02561	0.00118	-0.00054
O2	0.051106	0.04466	0.04190	0.05729	-0.00002	-0.02753
C1	0.015735	0.01811	0.01432	0.01503	0.00200	0.00313
C2	0.016806	0.01926	0.01678	0.01505	0.00020	0.00479
C3	0.016926	0.01699	0.01564	0.01790	0.00039	0.00142
C4	0.015528	0.01684	0.01468	0.01533	0.00059	0.00312
C5	0.019371	0.01902	0.01948	0.01933	0.00092	0.00158
C6	0.02831	0.02951	0.02665	0.02799	0.00485	0.00106
C7	0.039432	0.05410	0.02301	0.04104	0.00520	0.00588
C8	0.0505	0.05964	0.02556	0.06258	-0.00642	-0.00522
N1	0.018396	0.02067	0.01948	0.01505	-0.00672	0.00246
C11	0.020862	0.02676	0.01954	0.01661	-0.00609	0.00413
C12	0.026557	0.03694	0.02140	0.02154	-0.00651	0.00469
C13	0.034832	0.05881	0.02323	0.02313	-0.00435	0.00799
C14	0.059196	0.10726	0.02899	0.04040	0.00165	0.00657
C21	0.019479	0.02150	0.02032	0.01675	-0.00489	0.00308
C22	0.019555	0.02121	0.02001	0.01777	-0.00419	0.00382
C23	0.021107	0.02051	0.02039	0.02338	-0.00257	0.00648
C24	0.026185	0.02455	0.03229	0.02323	-0.00320	0.00872
C31	0.022056	0.02107	0.02692	0.01812	-0.01078	0.00246
C32	0.025119	0.02062	0.03382	0.02063	-0.01181	0.00173
C33	0.027007	0.02338	0.03295	0.02383	-0.00760	0.00008
C34	0.036392	0.02314	0.04131	0.04222	-0.00906	-0.00465
C41	0.019562	0.02225	0.02000	0.01600	-0.00512	0.00102
C42	0.020661	0.02212	0.02089	0.01840	-0.00458	0.00068
C43	0.027173	0.02787	0.02189	0.03032	-0.00169	-0.00129
C44	0.035699	0.03338	0.03079	0.04047	-0.00506	-0.00395

Table A2.3: Bond angles (°) in functionalized V6-C3.

Bond	Angle	Bond	Angle	Bond	Angle
O61-V1-O33	76.87	O61-V2-O31	77.11	O32-V3-O61	76.70
O61-V1-O31	78.02	O32-V2-O61	77.91	O33-V3-O61	77.85
O61-V1-O22	80.39	O61-V2-O21	80.49	O23-V3-O61	80.32
O23-V1-O61	82.34	O61-V2-O22	81.96	O33-V3-O32	82.12
O33-V1-O31	82.41	O32-V2-O31	83.14	O61-V3-O21	82.24
O22-V1-O33	85.67	O31-V2-O21	85.19	O23-V3-O32	85.31
O23-V1-O31	89.79	O32-V2-O22	90.55	O33-V3-O21	91.01
O23-V1-O22	94.52	O22-V2-O21	93.44	O23-V3-O21	93.76
O11-V1-O33	95.84	O12-V2-O31	96.48	O32-V3-O13	96.26
O11-V1-O31	98.01	O12-V2-O32	97.16	O33-V3-O13	97.32
O11-V1-O22	102.49	O12-V2-O21	103.51	O23-V3-O13	103.40
O23-V1-O11	104.68	O12-V2-O22	104.22	O13-V3-O21	104.54

Table A2.4. Bond distances (Å) in functionalized V6-C3.

Bond	Distance	Bond	Distance
C1-H1A	1.09161	C22-H22B	1.09168
C1-H1B	1.09205	C23-H23B	1.09192
C2-H2A	1.09157	C23-H23A	1.09189
C2-H2B	1.09239	C24-H24A	1.05862
C3-H3A	1.09274	C24-H24C	1.05837
C3-H3B	1.09259	C24-H24B	1.05833
C5-H5A	1.09025	C31-H31A	1.09219
C5-H5B	1.09430	C31-H31B	1.09135
C7-H7A	1.09263	C32-H32A	1.09207
C7-H7B	1.09083	C32-H32B	1.09194
C8-H8A	1.06036	C33-H33A	1.09303
C8-H8B	1.05891	C33-H33B	1.09100
C8-H8C	1.05739	C34-H34A	1.06094
C11-H11A	1.09232	C34-H34C	1.05980
C11-H11B	1.09142	C34-H34B	1.05894
C12-H12B	1.09242	C41-H41B	1.09232
C12-H12A	1.09108	C41-H41A	1.09225
C13-H13B	1.09226	C42-H42A	1.09251
C13-H13A	1.09100	C42-H42B	1.09213
C14-H14C	1.05996	C43-H43A	1.09250
C14-H14B	1.05865	C43-H43B	1.09244
C14-H14A	1.05822	C44-H44B	1.05928
C21-H21A	1.09233	C44-H44A	1.05843
C21-H21B	1.09163	C44-H44C	1.05812
C22-H22A	1.09257		

Table A3.1: Atomic coordinates of functionalized V6OH.

Atom	<i>x</i>	<i>y</i>	<i>z</i>	U_{eq}
V1	0.22347	0.22285	0.14352	0.006578
V2	0.14113	0.21356	-0.16019	0.006734
V3	0.28873	0.07153	0.01202	0.006949
O61	0.25000	0.25000	0.00000	0.006741
O11	0.19434	0.19511	0.23080	0.011155
O12	0.06463	0.16675	-0.26910	0.011436
O13	0.31162	-0.05891	0.02926	0.012243
O21	0.37160	0.13982	0.15375	0.008702
O22	0.31244	0.26520	0.24632	0.008261
O23	0.31067	0.12628	-0.09167	0.008581
O31	0.13111	0.18076	-0.02001	0.007422
O32	0.18818	0.05619	-0.11643	0.007814
O33	0.25107	0.06882	0.12730	0.007484
C1	0.09474	0.08017	-0.02195	0.009044
C2	0.14858	-0.03833	-0.11337	0.009135
C3	0.20811	-0.02658	0.11805	0.008542
C4	0.13648	-0.02799	-0.00716	0.008035
C5	0.08823	-0.12514	-0.01439	0.010321
O6	0.11335	-0.23650	-0.01240	0.013171
NA1	0.50821	-0.09724	0.41515	0.018155
O1W	0.42788	-0.22269	0.26282	0.019012
O2W	0.47676	-0.17402	0.54425	0.021146
O3W	0.59701	-0.01991	0.61387	0.015016
O4W	0.50000	0.00670	0.25000	0.015601

Table A3.2: Thermal displacement parameters of functionalized V6OH

Atom	U ₁₁	U ₂₂	U ₃₃	U ₁₂	U ₁₂	U ₂₃
V1	0.00682	0.00778	0.00602	-0.00027	0.00406	0.00008
V2	0.00569	0.00782	0.00576	0.00055	0.00251	0.00020
V3	0.00702	0.00662	0.00798	0.00044	0.00458	0.00134
O61	0.00612	0.00743	0.00677	0.00005	0.00356	0.00071
O11	0.01342	0.01362	0.01094	0.00067	0.00954	-0.00016
O12	0.00734	0.01433	0.00898	-0.00066	0.00207	-0.00240
O13	0.01420	0.00868	0.01532	0.00140	0.00897	0.00305
O21	0.00705	0.00881	0.00898	0.00117	0.00353	0.00138
O22	0.00818	0.00988	0.00624	-0.00036	0.00360	-0.00103
O23	0.00963	0.00871	0.00955	0.00000	0.00660	0.00100
O31	0.00674	0.00810	0.00770	0.00037	0.00410	-0.00004
O32	0.00826	0.00797	0.00746	-0.00005	0.00443	-0.00034
O33	0.00771	0.00767	0.00733	0.00035	0.00425	0.00010
C1	0.00831	0.00902	0.01036	0.00071	0.00543	0.00014
C2	0.01056	0.00864	0.00874	-0.00093	0.00559	-0.00145
C3	0.00902	0.00808	0.00821	0.00119	0.00447	-0.00001
C4	0.00810	0.00808	0.00808	0.00032	0.00450	-0.00053
C5	0.01096	0.00956	0.01093	-0.00004	0.00627	-0.00188
O6	0.01677	0.00868	0.01255	0.00060	0.00699	-0.00021
NA1	0.01834	0.02449	0.01239	-0.00340	0.00884	-0.00709
O1W	0.01938	0.02269	0.01753	-0.00653	0.01168	-0.00852
O2W	0.01395	0.02596	0.02141	0.00858	0.00823	-0.00159
O3W	0.01406	0.01762	0.01304	0.00008	0.00715	-0.00468
O4W	0.01270	0.01424	0.02172	0.00000	0.01056	0.00000

Table A3.3: Bond angles (°) in functionalized V6OH.

Bond	Angle	Bond	Angle	Bond	Angle
O61-V1-O33	76.73	O61-V2-O31	77.23	O61-V3-O32	76.37
O61-V1-O31	78.58	O61-V2-O32	78.70	O61-V3-O33	78.77
O61-V1-O22	79.23	O61-V2-O21	80.75	O61-V3-O23	79.36
O61-V1-O23	82.00	O32-V2-O31	82.58	O32-V3-O33	82.57
O33-V1-O31	82.67	O61-V2-O22	83.65	O61-V3-O21	82.99
O33-V1-O22	83.54	O21-V2-O31	85.19	O32-V3-O23	83.08
O23-V1-O22	92.35	O22-V2-O32	92.72	O33-V3-O21	92.64
O23-V1-O31	93.43	O22-V2-O21	92.86	O23-V3-O21	94.10
O33-V1-O11	96.47	O12-V2-O31	94.44	O32-V3-O13	95.73
O11-V1-O31	99.48	O32-V2-O12	97.68	O33-V3-O13	99.07
O11-V1-O22	101.47	O12-V2-O21	101.51	O13-V3-O23	101.27
O23-V1-O11	104.80	O22-V2-O12	104.61	O13-V3-O21	104.88

Table A4.1. Theoretical results of the topological analysis of charge density at (3,-1) bond critical point (BCP) of isolated V6 by M06/cc-pVTZ.

Type	Bond	d_{12}	$\rho(\mathbf{r}_c)$	$\nabla^2\rho(\mathbf{r}_c)$	λ_1	λ_2	λ_3	ϵ	$\mathbf{G}(\mathbf{r}_c)$	$\mathbf{V}(\mathbf{r}_c)$	$\mathbf{H}(\mathbf{r}_c)$
V-O1x	V1-O11	1.682	1.464	19.22	-10.45	-9.89	39.56	0.056	0.358	-0.516	-0.158
	V2-O12	1.682	1.464	19.22	-10.45	-9.89	39.56	0.056	0.358	-0.516	-0.158
	V3-O13	1.682	1.464	19.22	-10.45	-9.89	39.56	0.056	0.358	-0.516	-0.158
V-O2x	V1-O22	1.686	1.448	18.85	-10.33	-9.80	38.97	0.054	0.351	-0.507	-0.156
	V1-O23	1.686	1.448	18.85	-10.33	-9.80	38.97	0.054	0.351	-0.507	-0.156
	V2-O21	1.686	1.448	18.85	-10.33	-9.80	38.97	0.054	0.351	-0.507	-0.156
	V2-O22	1.730	1.258	17.94	-8.38	-8.26	34.58	0.015	0.299	-0.411	-0.113
	V3-O21	1.730	1.258	17.94	-8.38	-8.26	34.58	0.015	0.299	-0.411	-0.113
	V3-O23	1.730	1.258	17.94	-8.38	-8.26	34.58	0.015	0.299	-0.411	-0.113
	V1-O31	2.261	0.309	4.69	-1.44	-1.41	7.55	0.025	0.049	-0.050	-0.001
	V1-O33	2.261	0.309	4.69	-1.44	-1.41	7.55	0.025	0.049	-0.050	-0.001
	V2-O31	2.261	0.309	4.69	-1.44	-1.41	7.55	0.025	0.049	-0.050	-0.001
	V2-O32	2.301	0.277	4.18	-1.24	-1.20	6.62	0.037	0.043	-0.042	0.000
	V3-O32	2.301	0.277	4.18	-1.24	-1.20	6.62	0.037	0.043	-0.042	0.000
	V3-O33	2.301	0.277	4.18	-1.24	-1.20	6.62	0.037	0.043	-0.042	0.000
V-O6x	V1-O61	2.345	0.269	3.69	-1.10	-1.09	5.88	0.016	0.039	-0.039	-0.001
	V2-O61	2.345	0.269	3.69	-1.10	-1.09	5.88	0.016	0.039	-0.039	-0.001
	V3-O61	2.345	0.269	3.69	-1.10	-1.09	5.88	0.016	0.039	-0.039	-0.001

Table A4.2. Theoretical results of the topological analysis of charge density at (3,-1) bond critical point (BCP) of functionalized V6CH3 by M06-2X/cc-pVTZ.

Type	Bond	d_{12}	$\rho(\mathbf{r}_c)$	$\nabla^2\rho(\mathbf{r}_c)$	λ_1	λ_2	λ_3	ε	$\mathbf{G}(\mathbf{r}_c)$	$\mathbf{V}(\mathbf{r}_c)$	$\mathbf{H}(\mathbf{r}_c)$
V-O1x	V1-O11	1.596	1.891	22.38	-13.51	-13.43	49.32	0.006	0.499	-0.766	-0.267
	V2-O12	1.599	1.879	22.16	-13.41	-13.32	48.89	0.006	0.494	-0.758	-0.264
	V3-O13	1.604	1.856	21.94	-13.18	-13.10	48.22	0.006	0.486	-0.744	-0.258
V-O2x	V1-O22	1.801	1.093	12.88	-7.43	-7.22	27.53	0.030	0.227	-0.321	-0.094
	V1-O23	1.820	1.043	12.21	-6.98	-6.82	26.02	0.023	0.212	-0.298	-0.086
	V2-O21	1.821	1.042	12.15	-7.01	-6.80	25.96	0.031	0.212	-0.297	-0.086
	V2-O22	1.836	1.000	11.84	-6.62	-6.52	24.98	0.016	0.201	-0.279	-0.078
	V3-O21	1.838	0.996	11.68	-6.61	-6.51	24.81	0.016	0.199	-0.277	-0.078
	V3-O23	1.842	0.984	11.66	-6.51	-6.43	24.61	0.013	0.197	-0.272	-0.076
V-O3x	V1-O31	2.011	0.612	8.79	-3.90	-3.64	16.32	0.072	0.113	-0.136	-0.022
	V1-O33	2.020	0.596	8.69	-3.77	-3.52	15.98	0.070	0.110	-0.131	-0.020
	V2-O31	2.024	0.587	8.68	-3.70	-3.44	15.83	0.073	0.109	-0.128	-0.019
	V2-O32	2.019	0.599	8.68	-3.79	-3.53	16.00	0.073	0.111	-0.131	-0.021
	V3-O32	2.026	0.586	8.60	-3.69	-3.43	15.72	0.075	0.108	-0.128	-0.019
	V3-O33	2.024	0.593	8.60	-3.74	-3.49	15.83	0.072	0.109	-0.129	-0.020
V-O6x	V1-O61	2.233	0.349	5.68	-1.62	-1.61	8.90	0.004	0.060	-0.061	-0.001
	V2-O61	2.241	0.341	5.56	-1.57	-1.56	8.68	0.005	0.058	-0.059	-0.001
	V3-O61	2.253	0.332	5.42	-1.50	-1.49	8.42	0.006	0.056	-0.057	0.000
Cx-O3x	C1-O31	1.436	1.659	-10.85	-10.34	-9.81	9.30	0.055	0.202	-0.516	-0.314
	C2-O32	1.443	1.639	-10.99	-10.16	-9.66	8.83	0.052	0.195	-0.505	-0.309
	C3-O33	1.444	1.632	-10.95	-10.07	-9.61	8.73	0.049	0.194	-0.501	-0.307
Cx-C4	C1-C4	1.527	1.700	-15.22	-12.18	-11.71	8.67	0.040	0.183	-0.524	-0.341
	C2-C4	1.528	1.693	-15.06	-12.11	-11.63	8.68	0.041	0.182	-0.521	-0.338
	C3-C4	1.532	1.680	-14.78	-11.98	-11.52	8.71	0.040	0.181	-0.515	-0.334

Table A4.3. Theoretical results of the topological analysis of charge density at (3,-1) bond critical point (BCP) of functionalized V6NH2 by M06/cc-pVTZ.

Type	Bond	d_{12}	$\rho(r_c)$	$\nabla^2\rho(r_c)$	λ_1	λ_2	λ_3	ε	$G(r_c)$	$V(r_c)$	$H(r_c)$
V-O1x	V1-O11	1.599	1.829	24.60	-12.98	-12.92	50.50	0.005	0.496	-0.737	-0.241
	V2-O12	1.604	1.809	24.27	-12.80	-12.74	49.81	0.005	0.488	-0.724	-0.236
	V3-O13	1.606	1.797	24.16	-12.67	-12.60	49.43	0.005	0.483	-0.716	-0.233
V-O2x	V1-O22	1.809	1.034	14.39	-6.81	-6.60	27.80	0.031	0.225	-0.302	-0.076
	V1-O23	1.810	1.032	14.35	-6.80	-6.61	27.76	0.029	0.225	-0.301	-0.076
	V2-O21	1.818	1.011	14.02	-6.64	-6.45	27.10	0.029	0.218	-0.291	-0.073
	V2-O22	1.819	1.009	13.94	-6.61	-6.42	26.97	0.029	0.217	-0.290	-0.073
	V3-O21	1.827	0.986	13.69	-6.41	-6.26	26.36	0.025	0.211	-0.280	-0.069
	V3-O23	1.834	0.970	13.41	-6.27	-6.14	25.82	0.023	0.206	-0.273	-0.067
V-O3x	V1-O31	2.022	0.589	8.76	-3.61	-3.37	15.74	0.069	0.110	-0.129	-0.019
	V1-O33	2.030	0.573	8.70	-3.49	-3.26	15.45	0.068	0.107	-0.124	-0.017
	V2-O31	2.029	0.576	8.67	-3.50	-3.28	15.45	0.069	0.107	-0.125	-0.017
	V2-O32	2.029	0.579	8.64	-3.53	-3.30	15.47	0.068	0.108	-0.126	-0.018
	V3-O32	2.035	0.567	8.57	-3.44	-3.22	15.22	0.068	0.106	-0.122	-0.017
	V3-O33	2.036	0.565	8.56	-3.42	-3.20	15.19	0.068	0.105	-0.122	-0.016
V-O6x	V1-O61	2.239	0.345	5.34	-1.56	-1.55	8.45	0.004	0.057	-0.059	-0.002
	V2-O61	2.240	0.344	5.33	-1.55	-1.54	8.42	0.005	0.057	-0.059	-0.002
	V3-O61	2.253	0.334	5.15	-1.48	-1.47	8.10	0.006	0.055	-0.056	-0.001
Cx-O3x	C1-O31	1.409	1.764	-11.31	-11.81	-11.23	11.73	0.051	0.229	-0.574	-0.346
	C2-O32	1.427	1.705	-11.87	-11.27	-10.69	10.09	0.054	0.208	-0.539	-0.331
	C3-O33	1.425	1.702	-11.23	-11.14	-10.59	10.50	0.053	0.211	-0.539	-0.328
Cx-C4	C1-C4	1.527	1.729	-16.01	-13.00	-12.07	9.07	0.078	0.186	-0.538	-0.352
	C2-C4	1.541	1.684	-14.88	-12.46	-11.63	9.21	0.071	0.181	-0.517	-0.335
	C3-C4	1.544	1.667	-14.63	-12.25	-11.49	9.11	0.067	0.178	-0.508	-0.330

Table A4.4. Theoretical results of the topological analysis of charge density at (3,-1) bond critical point (BCP) of functionalized V6OH by M06-2X/cc-pVTZ.

Type	Bond	d_{12}	$\rho(r_c)$	$\nabla^2\rho(r_c)$	λ_1	λ_2	λ_3	ϵ	$G(r_c)$	$V(r_c)$	$H(r_c)$
V-O1x	V1-O11	1.596	1.893	22.39	-13.52	-13.44	49.35	0.006	0.500	-0.768	-0.268
	V2-O12	1.598	1.885	22.34	-13.45	-13.37	49.16	0.006	0.497	-0.763	-0.265
	V3-O13	1.598	1.881	22.18	-13.43	-13.35	48.97	0.005	0.495	-0.760	-0.265
V-O2x	V1-O22	1.808	1.075	12.62	-7.26	-7.09	26.97	0.024	0.222	-0.312	-0.091
	V1-O23	1.819	1.048	12.27	-7.02	-6.85	26.14	0.026	0.214	-0.300	-0.086
	V2-O21	1.822	1.039	12.20	-6.96	-6.80	25.96	0.023	0.211	-0.296	-0.085
	V2-O22	1.829	1.015	12.04	-6.77	-6.65	25.45	0.017	0.205	-0.286	-0.081
	V3-O21	1.835	1.000	11.85	-6.65	-6.53	25.03	0.018	0.201	-0.279	-0.078
	V3-O23	1.835	1.002	11.83	-6.67	-6.56	25.06	0.018	0.201	-0.280	-0.079
V-O3x	V1-O31	2.005	0.621	8.96	-3.97	-3.70	16.63	0.075	0.116	-0.139	-0.023
	V1-O33	2.011	0.612	8.86	-3.90	-3.63	16.39	0.074	0.114	-0.136	-0.022
	V2-O31	2.022	0.594	8.67	-3.76	-3.50	15.93	0.074	0.110	-0.130	-0.020
	V2-O32	2.027	0.587	8.53	-3.69	-3.44	15.66	0.072	0.108	-0.128	-0.020
	V3-O32	2.035	0.571	8.44	-3.57	-3.33	15.33	0.073	0.105	-0.123	-0.018
	V3-O33	2.034	0.574	8.40	-3.59	-3.35	15.35	0.071	0.105	-0.124	-0.018
V-O6x	V1-O61	2.233	0.348	5.68	-1.61	-1.61	8.90	0.004	0.060	-0.061	-0.001
	V2-O61	2.247	0.336	5.50	-1.53	-1.52	8.55	0.007	0.057	-0.058	0.000
	V3-O61	2.246	0.337	5.50	-1.54	-1.53	8.56	0.004	0.057	-0.058	0.000
Cx-O3x	C1-O31	1.441	1.638	-10.59	-10.11	-9.53	9.05	0.062	0.198	-0.506	-0.308
	C2-O32	1.443	1.638	-10.94	-10.15	-9.61	8.82	0.056	0.195	-0.504	-0.309
	C3-O33	1.440	1.655	-11.45	-10.35	-9.86	8.77	0.050	0.197	-0.512	-0.315
Cx-C4	C1-C4	1.547	1.614	-13.40	-11.25	-10.79	8.65	0.043	0.172	-0.483	-0.311
	C2-C4	1.537	1.660	-14.34	-11.76	-11.31	8.73	0.039	0.178	-0.505	-0.327
	C3-C4	1.531	1.674	-14.62	-11.83	-11.44	8.64	0.034	0.180	-0.512	-0.332

Table A4.5. Theoretical results of the topological analysis of charge density at (3,-1) bond critical point (BCP) of functionalized V6NO2 by M06-2X/cc-pVTZ.

Type	Bond	d_{12}	$\rho(r_c)$	$\nabla^2\rho(r_c)$	λ_1	λ_2	λ_3	ε	$G(r_c)$	$V(r_c)$	$H(r_c)$
V-O1x	V1-O11	1.600	1.878	22.09	-13.33	-13.26	48.69	0.006	0.493	-0.758	-0.264
	V2-O12	1.604	1.859	21.75	-13.16	-13.09	48.00	0.006	0.485	-0.745	-0.260
	V3-O13	1.607	1.846	21.65	-13.04	-12.97	47.66	0.006	0.481	-0.737	-0.256
V-O2x	V1-O22	1.809	1.070	12.65	-7.22	-7.06	26.92	0.023	0.221	-0.311	-0.090
	V1-O23	1.809	1.068	12.62	-7.21	-7.05	26.88	0.022	0.220	-0.310	-0.089
	V2-O21	1.818	1.046	12.34	-7.04	-6.89	26.26	0.021	0.214	-0.300	-0.086
	V2-O22	1.819	1.043	12.28	-7.00	-6.85	26.13	0.022	0.213	-0.298	-0.085
	V3-O21	1.828	1.021	12.05	-6.80	-6.68	25.53	0.018	0.207	-0.288	-0.082
	V3-O23	1.835	1.004	11.83	-6.65	-6.54	25.02	0.017	0.202	-0.281	-0.079
V-O3x	V1-O31	2.023	0.591	8.62	-3.73	-3.48	15.83	0.073	0.109	-0.129	-0.020
	V1-O33	2.031	0.577	8.56	-3.62	-3.38	15.56	0.071	0.107	-0.125	-0.018
	V2-O31	2.030	0.579	8.53	-3.63	-3.37	15.54	0.075	0.107	-0.125	-0.018
	V2-O32	2.030	0.581	8.53	-3.65	-3.41	15.59	0.072	0.107	-0.126	-0.019
	V3-O32	2.036	0.567	8.48	-3.54	-3.30	15.32	0.073	0.105	-0.122	-0.017
	V3-O33	2.035	0.572	8.41	-3.57	-3.33	15.32	0.073	0.105	-0.123	-0.018
V-O6x	V1-O61	2.239	0.344	5.59	-1.58	-1.57	8.74	0.004	0.059	-0.060	-0.001
	V2-O61	2.240	0.342	5.58	-1.57	-1.56	8.72	0.005	0.059	-0.059	-0.001
	V3-O61	2.253	0.332	5.41	-1.50	-1.49	8.40	0.006	0.056	-0.057	0.000
Cx-O3x	C1-O31	1.425	1.702	-11.10	-10.91	-10.14	9.96	0.076	0.212	-0.540	-0.327
	C2-O32	1.409	1.766	-11.22	-11.64	-10.77	11.19	0.081	0.230	-0.576	-0.346
	C3-O33	1.427	1.699	-11.35	-10.92	-10.15	9.71	0.076	0.210	-0.537	-0.327
Cx-C4	C1-C4	1.541	1.636	-14.05	-11.66	-11.03	8.63	0.057	0.173	-0.493	-0.319
	C2-C4	1.544	1.647	-14.25	-11.82	-11.15	8.72	0.061	0.175	-0.498	-0.323
	C3-C4	1.528	1.700	-15.45	-12.37	-11.64	8.57	0.062	0.182	-0.523	-0.342

Table A4.6. Theoretical results of the topological analysis of charge density at (3,-1) bond critical point (BCP) of functionalized V6-C6 by M06-2X/cc-pVTZ.

Type	Bond	d_{12}	$\rho(r_c)$	$\nabla^2\rho(r_c)$	λ_1	λ_2	λ_3	ε	$G(r_c)$	$V(r_c)$	$H(r_c)$
V-O1x	V1-O11	1.559	2.078	24.79	-15.45	-15.21	55.46	0.016	0.575	-0.892	-0.317
	V2-O12	1.559	2.076	24.77	-15.45	-15.19	55.41	0.017	0.574	-0.891	-0.317
	V3-O13	1.564	2.047	24.50	-15.19	-14.96	54.65	0.016	0.563	-0.871	-0.309
V-O2x	V1-O22	1.697	1.427	17.27	-10.31	-9.66	37.25	0.067	0.335	-0.491	-0.156
	V1-O23	1.699	1.419	17.26	-10.25	-9.60	37.10	0.068	0.333	-0.487	-0.154
	V2-O21	1.702	1.403	17.11	-10.11	-9.48	36.70	0.066	0.328	-0.478	-0.150
	V2-O22	1.895	0.830	10.89	-5.38	-5.26	21.53	0.024	0.163	-0.212	-0.050
	V3-O21	1.901	0.815	10.79	-5.27	-5.13	21.19	0.026	0.159	-0.207	-0.047
	V3-O23	1.907	0.800	10.69	-5.15	-5.02	20.86	0.025	0.156	-0.201	-0.045
V-O3x	V1-O31	1.974	0.674	9.44	-4.37	-4.10	17.91	0.064	0.127	-0.156	-0.029
	V1-O33	1.981	0.660	9.31	-4.26	-4.00	17.57	0.065	0.124	-0.152	-0.027
	V2-O31	1.984	0.655	9.24	-4.22	-3.96	17.42	0.065	0.123	-0.150	-0.027
	V2-O32	2.102	0.474	7.39	-2.79	-2.62	12.81	0.064	0.086	-0.094	-0.009
	V3-O32	2.105	0.470	7.36	-2.76	-2.59	12.70	0.065	0.085	-0.093	-0.008
	V3-O33	2.111	0.463	7.27	-2.70	-2.54	12.51	0.063	0.083	-0.091	-0.008
V-O6x	V1-O61	2.257	0.331	5.36	-1.49	-1.48	8.33	0.007	0.056	-0.056	0.000
	V2-O61	2.257	0.331	5.35	-1.49	-1.48	8.33	0.008	0.056	-0.056	0.000
	V3-O61	2.257	0.331	5.33	-1.50	-1.48	8.30	0.007	0.056	-0.056	0.000
Cx-O3x	C1-O31	1.402	1.795	-11.66	-11.97	-11.71	12.01	0.022	0.235	-0.591	-0.356
	C2-O32	1.402	1.792	-11.58	-11.93	-11.66	12.01	0.022	0.235	-0.590	-0.355
	C3-O33	1.402	1.798	-11.94	-12.01	-11.77	11.84	0.020	0.234	-0.592	-0.358
Cx-C4	C1-C4	1.537	1.662	-14.40	-11.83	-11.38	8.81	0.040	0.178	-0.506	-0.328
	C2-C4	1.538	1.661	-14.38	-11.82	-11.37	8.81	0.039	0.178	-0.506	-0.327
	C3-C4	1.537	1.659	-14.33	-11.77	-11.36	8.79	0.036	0.178	-0.504	-0.327

Table A4.7. Theoretical results of the topological analysis of charge density at (3,-1) bond critical point (BCP) of functionalized V6-TPY by M06-2X/cc-pVTZ.

Type	Bond	d_{12}	$\rho(\mathbf{r}_c)$	$\nabla^2\rho(\mathbf{r}_c)$	λ_1	λ_2	λ_3	ϵ	$\mathbf{G}(\mathbf{r}_c)$	$\mathbf{V}(\mathbf{r}_c)$	$\mathbf{H}(\mathbf{r}_c)$
V-O1x	V1-O11	1.595	1.900	22.36	-13.56	-13.47	49.38	0.007	0.502	-0.772	-0.270
	V2-O12	1.604	1.857	21.86	-13.17	-13.09	48.12	0.006	0.486	-0.744	-0.259
	V3-O13	1.605	1.850	21.81	-13.09	-13.01	47.91	0.006	0.483	-0.740	-0.257
V-O2x	V1-O22	1.816	1.056	12.31	-7.08	-6.91	26.31	0.024	0.216	-0.304	-0.088
	V1-O23	1.818	1.049	12.28	-7.03	-6.85	26.15	0.026	0.214	-0.301	-0.087
	V2-O21	1.818	1.050	12.25	-7.04	-6.86	26.16	0.026	0.214	-0.301	-0.087
	V2-O22	1.834	1.003	11.95	-6.67	-6.56	25.18	0.017	0.202	-0.281	-0.078
	V3-O21	1.835	1.004	11.84	-6.67	-6.57	25.07	0.015	0.202	-0.281	-0.079
	V3-O23	1.848	0.973	11.36	-6.41	-6.30	24.07	0.019	0.192	-0.267	-0.074
V-O3x	V1-O31	2.003	0.619	9.13	-3.97	-3.70	16.80	0.075	0.117	-0.139	-0.022
	V1-O33	2.016	0.603	8.79	-3.82	-3.56	16.18	0.074	0.112	-0.133	-0.021
	V2-O31	2.023	0.588	8.75	-3.72	-3.47	15.94	0.073	0.110	-0.129	-0.019
	V2-O32	2.017	0.603	8.72	-3.82	-3.56	16.10	0.074	0.112	-0.133	-0.021
	V3-O32	2.035	0.570	8.47	-3.56	-3.32	15.35	0.073	0.105	-0.123	-0.017
	V3-O33	2.039	0.566	8.35	-3.53	-3.29	15.17	0.072	0.104	-0.121	-0.017
V-O6x	V1-O61	2.233	0.349	5.69	-1.62	-1.61	8.91	0.005	0.060	-0.061	-0.001
	V2-O61	2.234	0.347	5.66	-1.60	-1.60	8.86	0.004	0.060	-0.060	-0.001
	V3-O61	2.250	0.334	5.49	-1.52	-1.51	8.52	0.005	0.057	-0.057	0.000
Cx-O3x	C1-O31	1.427	1.692	-11.02	-10.81	-10.14	9.92	0.066	0.210	-0.534	-0.324
	C2-O32	1.425	1.701	-11.19	-10.90	-10.25	9.97	0.064	0.211	-0.539	-0.327
	C3-O33	1.427	1.707	-11.86	-11.00	-10.44	9.58	0.053	0.208	-0.540	-0.331
Cx-C4	C1-C4	1.540	1.667	-14.66	-12.15	-11.37	8.86	0.069	0.178	-0.508	-0.330
	C2-C4	1.532	1.694	-15.27	-12.44	-11.62	8.79	0.071	0.181	-0.521	-0.340
	C3-C4	1.530	1.706	-15.43	-12.46	-11.76	8.78	0.060	0.183	-0.527	-0.344

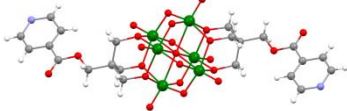
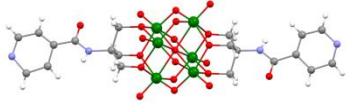

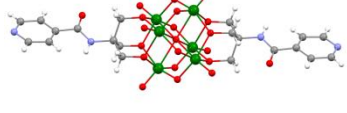

Table A4.8. Theoretical results of the topological analysis of charge density at (3,-1) bond critical point (BCP) of V10 by M06/cc-pVTZ.

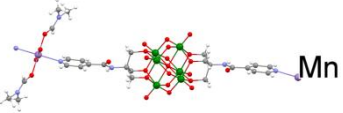
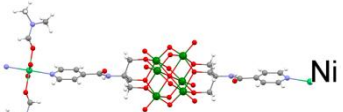
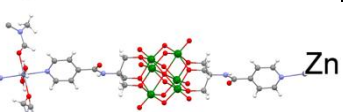
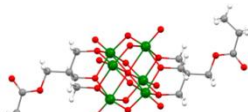
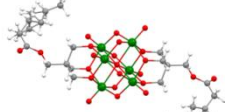
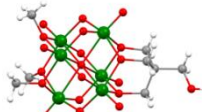
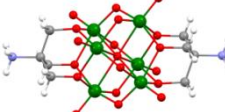
Type	Bond	d_{12}	$\rho(\mathbf{r}_c)$	$\nabla^2\rho(\mathbf{r}_c)$	λ_1	λ_2	λ_3	ε	$\mathbf{G}(\mathbf{r}_c)$	$\mathbf{V}(\mathbf{r}_c)$	$\mathbf{H}(\mathbf{r}_c)$
V-O1x	V5 - O10	1.612	1.765	22.31	-12.90	-12.87	48.08	0.002	0.461	-0.691	-0.230
	V3 - O11	1.612	1.764	22.07	-12.91	-12.87	47.84	0.003	0.459	-0.690	-0.230
	V1 - O7	1.620	1.733	22.14	-12.53	-12.46	47.14	0.006	0.451	-0.672	-0.221
	V2 - O6	1.623	1.717	22.17	-12.39	-12.31	46.87	0.006	0.447	-0.663	-0.217
V-O2x	V4 - O18	1.685	1.440	20.31	-10.67	-9.88	40.86	0.081	0.359	-0.508	-0.148
	V4 - O13	1.707	1.350	19.92	-9.90	-9.11	38.93	0.088	0.334	-0.462	-0.128
	V1 - O15	1.814	0.994	16.36	-6.90	-6.54	29.80	0.054	0.231	-0.293	-0.061
	V2 - O16	1.814	0.994	16.37	-6.87	-6.51	29.74	0.055	0.231	-0.293	-0.061
	V2 - O17	1.825	0.963	15.97	-6.62	-6.30	28.88	0.051	0.222	-0.279	-0.057
	O14 - V23	1.829	0.952	15.78	-6.50	-6.16	28.43	0.055	0.219	-0.274	-0.055
	V1 - O12	1.834	0.942	15.61	-6.42	-6.10	28.13	0.052	0.216	-0.270	-0.054
	V3 - O14	1.851	0.894	15.15	-6.00	-5.75	26.91	0.044	0.204	-0.250	-0.046
	V3 - O17	1.872	0.852	14.29	-5.60	-5.42	25.31	0.033	0.190	-0.232	-0.042
	V5 - O15	1.881	0.832	14.01	-5.45	-5.25	24.71	0.037	0.185	-0.224	-0.039
	O12 - V21	1.888	0.818	13.75	-5.32	-5.15	24.21	0.033	0.180	-0.218	-0.038
	O16 - V23	1.892	0.806	13.66	-5.21	-5.05	23.92	0.032	0.178	-0.214	-0.036
	V3 - O13	2.020	0.551	9.92	-3.19	-3.16	16.27	0.007	0.113	-0.122	-0.010
V5 - O18	2.070	0.479	8.64	-2.62	-2.60	13.86	0.007	0.095	-0.100	-0.005	
V-O3x	O8 - V22	1.923	0.754	12.42	-4.77	-4.70	21.89	0.013	0.160	-0.192	-0.031
	V4 - O9	1.944	0.714	11.73	-4.45	-4.40	20.58	0.012	0.149	-0.177	-0.027
	V1 - O9	1.999	0.614	10.22	-3.70	-3.63	17.54	0.020	0.124	-0.141	-0.017
	V2 - O8	2.005	0.601	10.11	-3.59	-3.52	17.22	0.018	0.121	-0.137	-0.016
	V1 - O8	2.021	0.573	9.76	-3.36	-3.30	16.43	0.018	0.115	-0.128	-0.013
	V2 - O9	2.028	0.566	9.51	-3.31	-3.26	16.08	0.016	0.112	-0.125	-0.013
V-O6x	V4 - O37	2.078	0.490	8.72	-2.62	-2.59	13.93	0.011	0.097	-0.103	-0.006
	V4 - O38	2.158	0.396	6.94	-1.93	-1.89	10.76	0.019	0.073	-0.075	-0.001
	V2 - O38	2.242	0.325	5.53	-1.39	-1.39	8.32	0.001	0.057	-0.056	0.001
	V1 - O37	2.267	0.305	5.12	-1.26	-1.25	7.63	0.002	0.052	-0.051	0.001
	V23 - O38	2.294	0.289	4.66	-1.15	-1.11	6.91	0.035	0.047	-0.046	0.001
	V3 - O38	2.333	0.261	4.13	-0.96	-0.92	6.01	0.048	0.041	-0.040	0.002

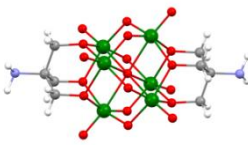
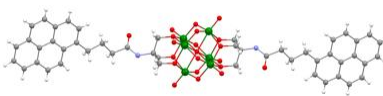
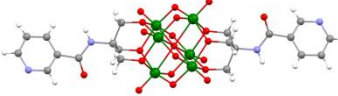
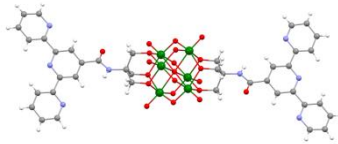
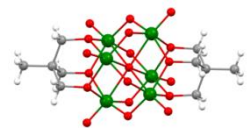
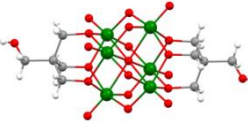
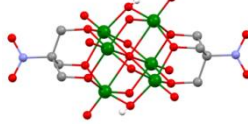
Table A5.1. List of compounds sent in Faculty of Medicine, University of Belgrade for biological activity.

No.	Compound	Formula	Structure
1	[V6CH3] [TBA] ₂	C42H90N2O19V6 1232.82	
2	[V6CH3] [Na] ₂	C10H18Na2O19V6 Mol. Wt.: 793.87	
3	[V6NO2] [TBA] ₂	C40H84N4O23V6 Mol. Wt.: 1294.76	
4	[V6OH] [TBA] ₂	C42H90N2O21V6 Mol. Wt.: 1264.81	
5	[V6OH] [Na] ₂	C10H18Na2O21V6 Mol. Wt.: 825.87	
6	[V6-C3] [TBA] ₂	C48H98N2O23V6 Mol. Wt.: 1376.94	
7	[V6-C3] [H] ₂	C16H28O23V6 Mol. Wt.: 894.03	
8	[V6-C5d] [TBA] ₂	C56H114N2O27V6 Mol. Wt.: 1553.15	
9	[V6-C6] [TBA] ₂	C58H122N2O23V6 Mol. Wt.: 1521.24	
10	[V6-C6] [H] ₂	C26H52O23V6 Mol. Wt.: 1038.33	
11	[V6-C12] [TBA] ₂	C69H143N2O23V6 Mol. Wt.: 1674.52	
12	[V6-C18] [TBA] ₂	C81H167N2O23V6 Mol. Wt.: 1842.84	
13	[Mo6O19] [TBA] ₂	C32H72Mo6N2O19 Mol. Wt.: 1364.56	

Table A5.2. Non covalent interaction in functionalized V6 series by CSD searching. The numbers of the different H-bonds are indicated.

Refcode	Structure of functionalized hexavanadate	Cation or other segment	OL						V6 Total (O1x/O2x)
			CH...O (14)	CH...N (2)	NH...O (4)	CH...O (12)	CH...N (1)	NO...Cl (1)	
EGEMUZ		Bu ₄ N ⁺	++						10(6/4)
EGENEK		Bu ₄ N ⁺ , CH ₃ CN, H ₂ O	+	+					7(2/5)
LOFVUY		Tb ²⁺ , (CH ₃) ₂ NCHO							6(3/3)
NEMDEP		Bu ₄ N ⁺ , N(CH ₃) ₂ CHO	+++			++	+		7(1/6)
NEMDIT		Co ²⁺ , N(CH ₃) ₂ CHO	++	+					8(7/1)

NEMDOZ		Mn^{2+} $\text{N}(\text{CH}_3)_2\text{CHO}$	+		+	+++			5(4/1)
NEMDUF		Ni^{2+} , $\text{N}(\text{CH}_3)_2\text{CHO}$			+	+++			5(4/1)
NEMFAN		Zn^{2+} , $\text{N}(\text{CH}_3)_2\text{CHO}$	+		+	++			9(5/4)
OQETOU		Bu_4N^+	+						6(3/3)
OQETUA		Bu_4N^+	+						6(1/5)
PELYIO		Bu_4N^+							8(1/7)
SAJWEH		CH_3SOCH_3							3(2/1)

SAJWIL		Bu_4N^+								6(3/3)
SAJWOR		Bu_4N^+ , $\text{N}(\text{CH}_3)_2\text{CHO}$, H_3O^+								3(2/1)
SAMMOK		Bu_4N^+ , $\text{N}(\text{CH}_3)_2\text{CHO}$	++		+	++				5(3/2)
UCOTEN		Bu_4N^+ , $\text{N}(\text{CH}_3)_2\text{CHO}$								4(2/2)
VERDEB10		Bu_4N^+								5(3/2)
VERDIF10		Bu_4N^+ , $\text{N}(\text{CH}_3)_2\text{CHO}$								4(1/3)
KURBOO		Bu_4N^+ , CH_2Cl_2							+	

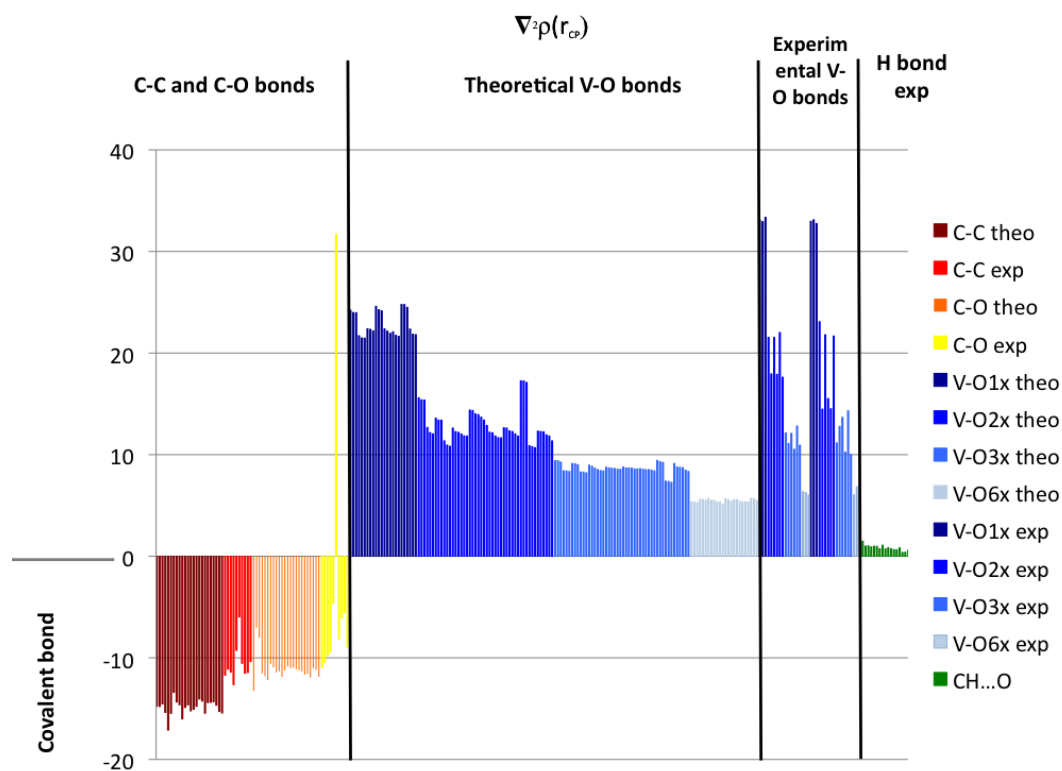


Figure A5.1. Compilation of the $\nabla^2\rho(r_c)$ values determined in the functionalized V6 series.

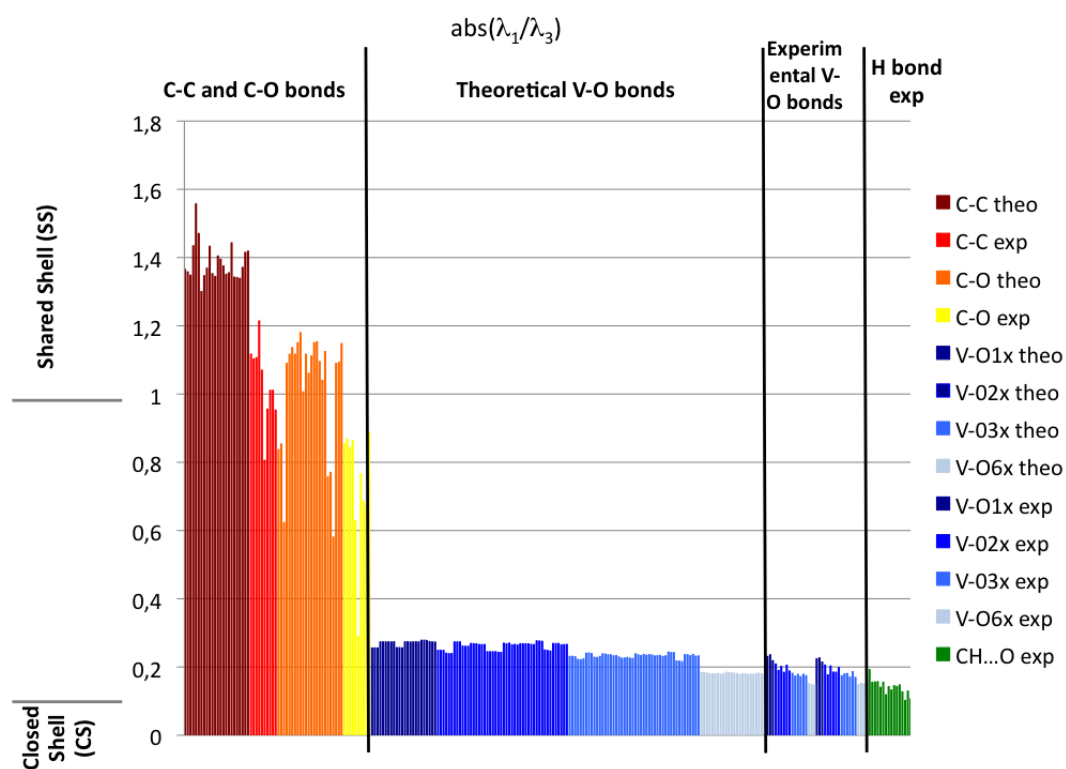


Figure A5.2. Compilation of the $\text{abs}(\lambda_1/\lambda_3)$ values determined in the functionalized V6 series.

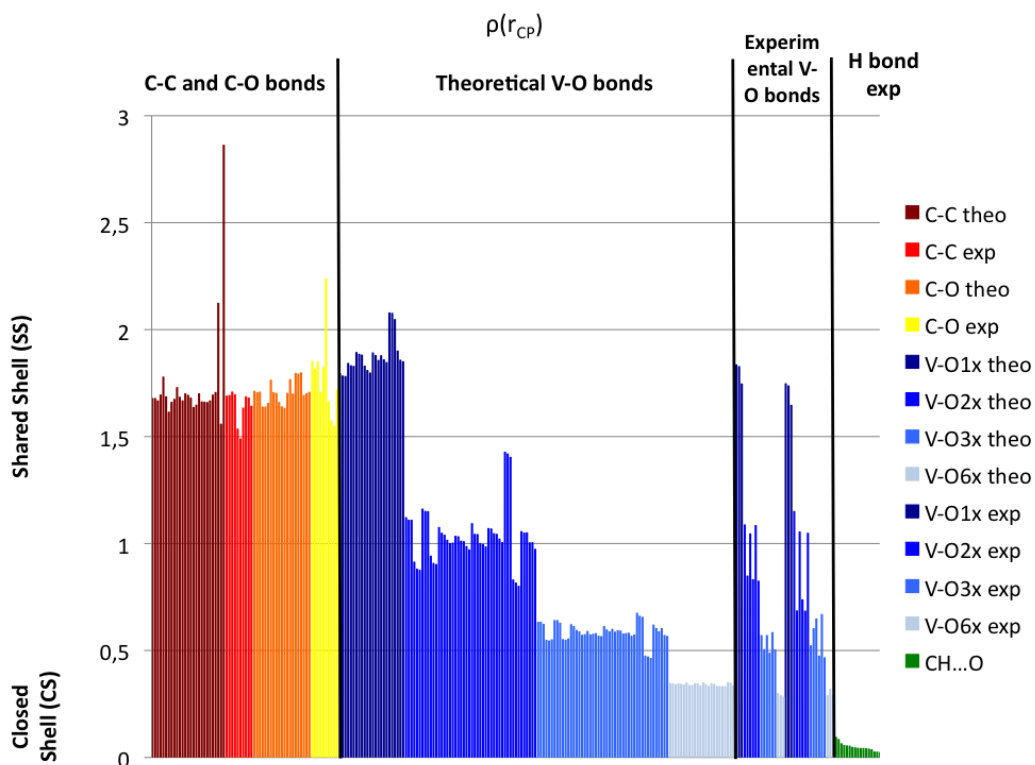


Figure A5.3. Compilation of the $\nabla^2\rho(r_c)$ values determined in the functionalized V6 series.

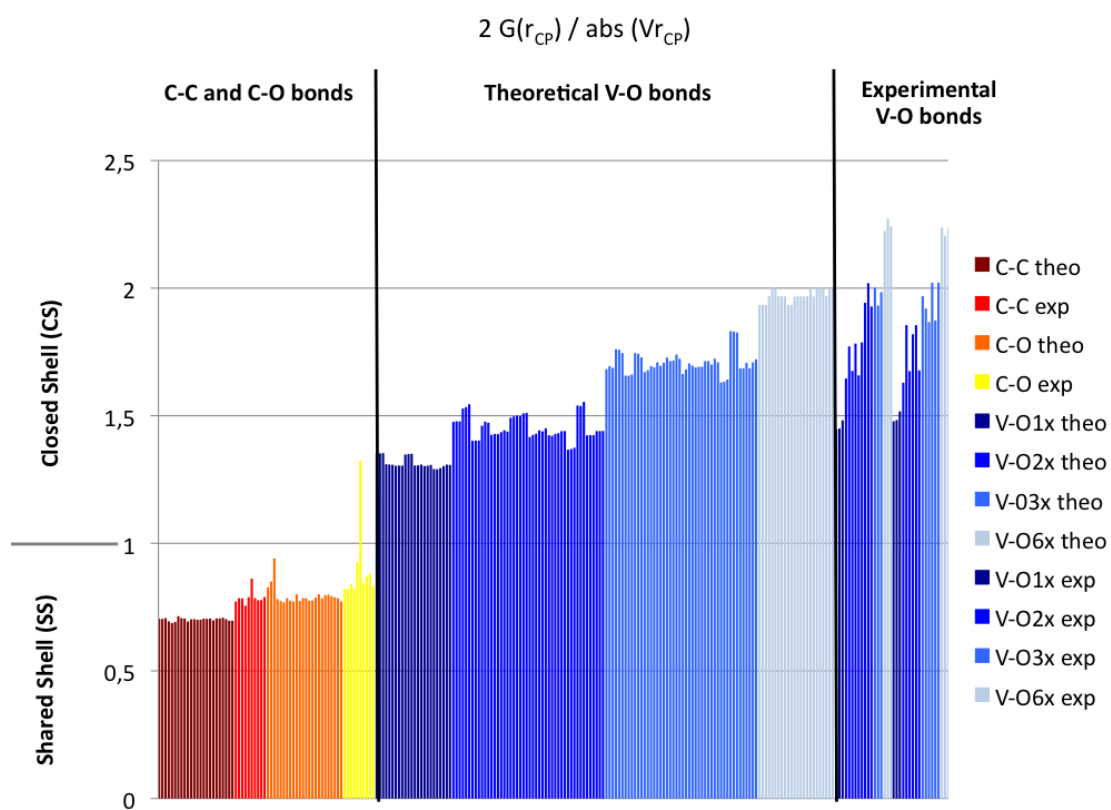


Figure A5.4. Compilation of the $2G(r_c)/|V(r_c)|$ values determined in the functionalized V6 series.

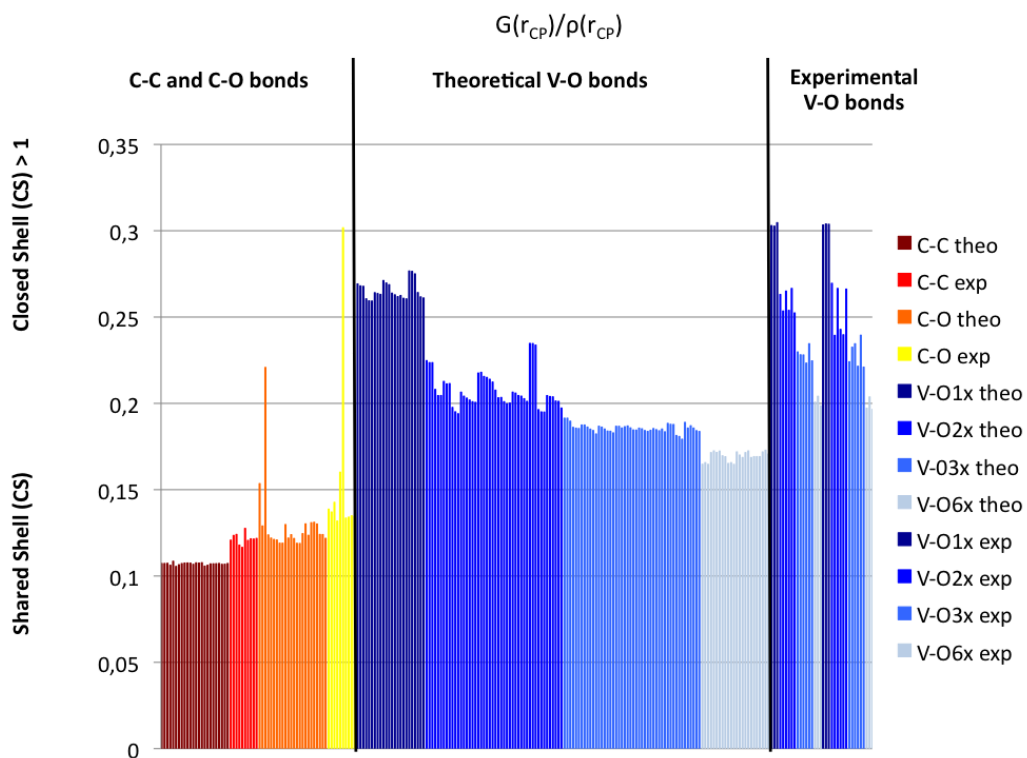


Figure A5.5. Compilation of the $G(r_c)/\rho(r_c)$ values determined in the functionalized V6 series.

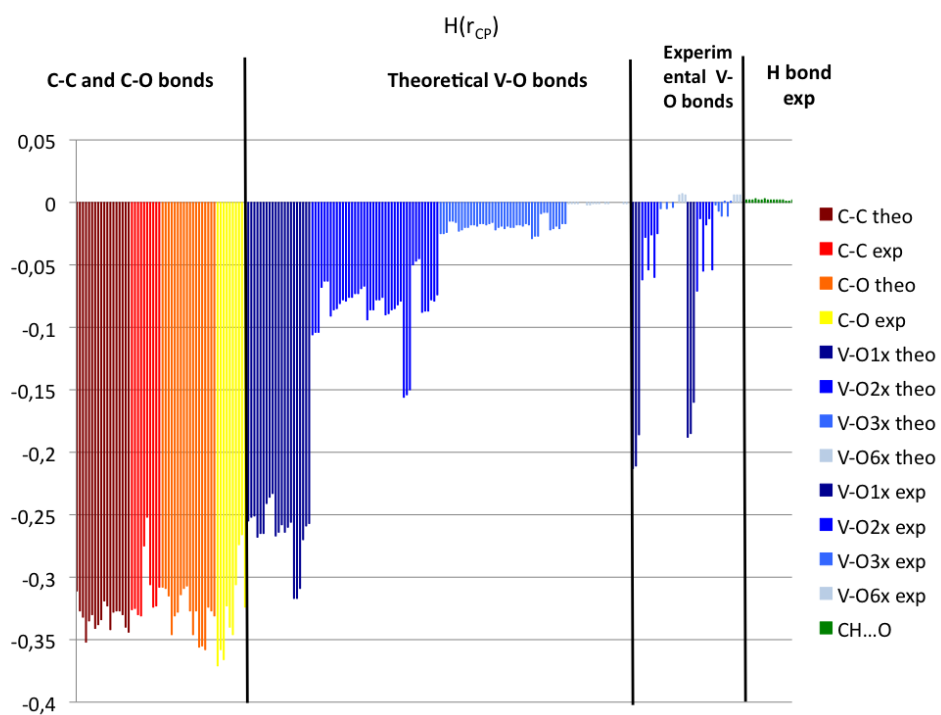


Figure A5.6. Compilation of the $H(r_c)$ values determined in the functionalized V6 series.

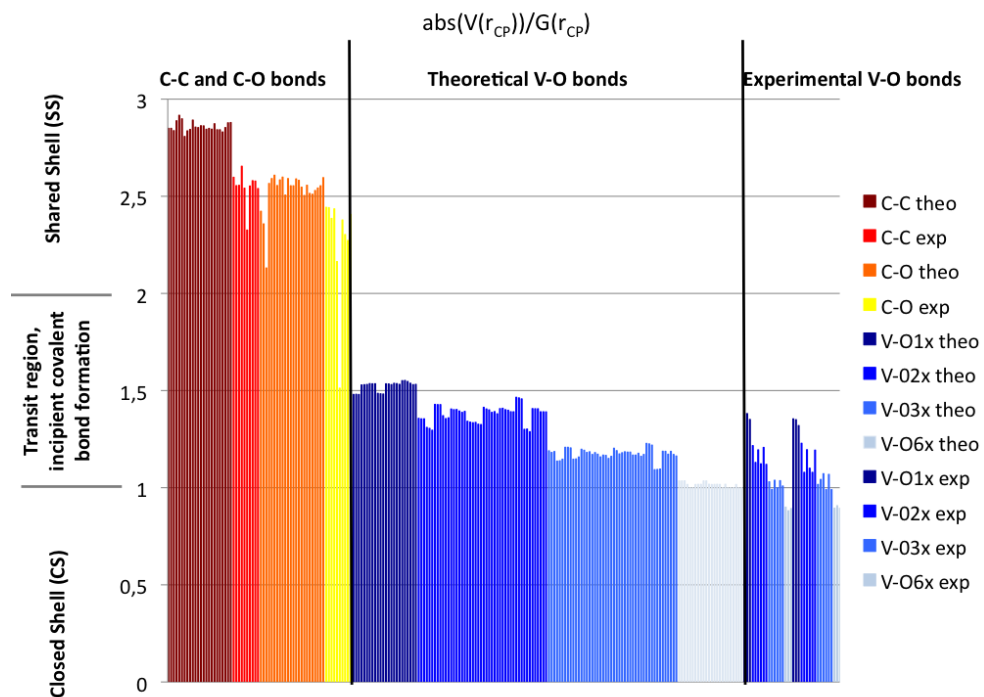


Figure A5.7. Compilation of the $\text{abs } |V(\mathbf{r}_c)| / G(\mathbf{r}_c)$ values determined in the functionalized V6 series.

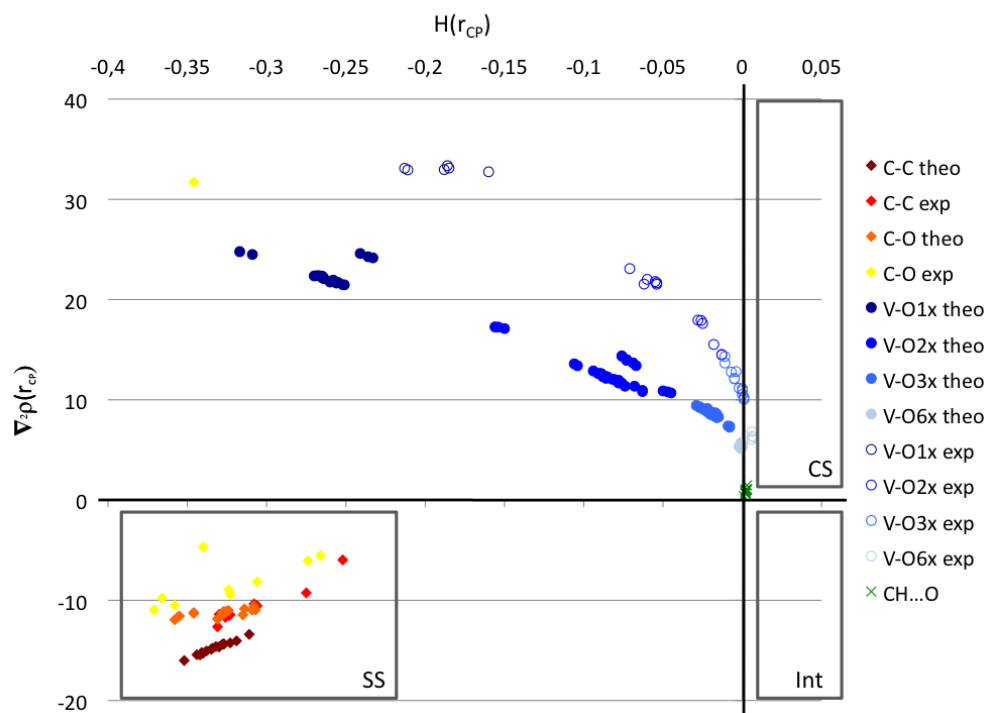


Figure A5.8. Behavior of $G(\mathbf{r}_c)$ as a function of $\nabla^2 \rho(\mathbf{r}_c)$ as determined in the functionalized V6 series.

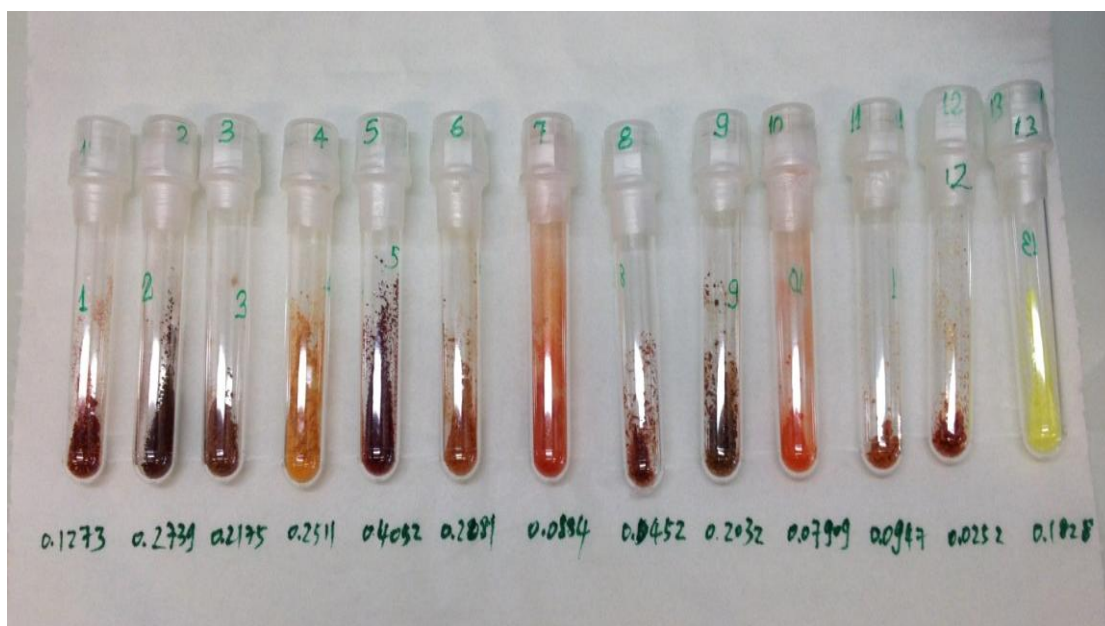


Figure A5.9. Photography of powder or crystals compounds sent in the Faculty of Medicine, University of Belgrade, for biological activity assay. (The number at the top of the tube is the corresponding number in table A5.1)

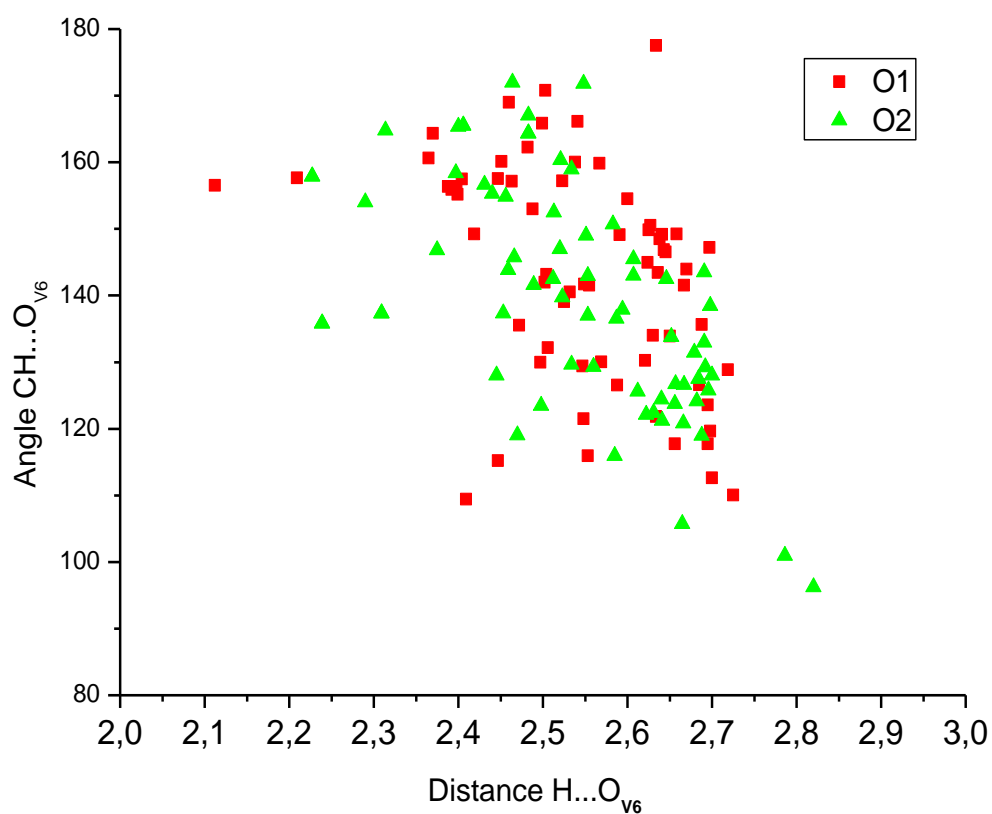


Figure A5.10. Distribution of distance and angle for CH O interaction according to the different type of oxygen atoms.

POSTER AND ORAL PRESENTATION

1. **X. XU**, N. BOŠNJAKOVIĆ-PAVLOVIĆ, D. KRSTIĆ, M. ČOLOVIĆ, V. VASIĆ, P. WU, Y. WEI, A. SPASOJEVIĆ – de BIRÉ. « *Crystal structures and Na⁺/K⁺ ATPase inhibition properties of functionalized hexavanadate: a new series with promising properties* », Serbian Crystallographic Meeting, Bela Crkva, Serbie, 31 May–2 June 2012. [Poster]
2. **X. XU**, A. CHITRE, T. DOUGLAS, R. JOHANSON, C-S LIM, T. NOMURA, Y. WANG, N. BOŠNJAKOVIĆ-PAVLOVIĆ, S. NOVAKOVIĆ, A. SPASOJEVIĆ – de BIRÉ. « *Prediction of interaction site of a drug. A combined approach using high resolution diffraction experiment, ab initio calculations, CSD analysis and molecular interaction field determination* », Serbian Crystallographic Meeting, Bela Crkva, Serbie, 31 May–2 June 2012. [Poster]
3. **X. XU**, A. CHITRE, T. DOUGLAS, R. JOHANSON, C-S LIM, T. NOMURA, Y. WANG, N. BOŠNJAKOVIĆ-PAVLOVIĆ, S. NOVAKOVIĆ, A. SPASOJEVIĆ – de BIRÉ. « *Prediction of interaction site of a drug. A combined approach using high resolution diffraction experiment, ab initio calculations, CSD analysis and molecular interaction field determination* », Rencontres Entreprises - Doctorants, Ecole Centrale Paris, 30 May 2013. [Poster]
4. **X. XU**, N. BOŠNJAKOVIĆ-PAVLOVIĆ, S. NOVAKOVIC, J-M. GILLET, Y. WEI, N-E. GHERMANI, A. SPASOJEVIĆ – de BIRÉ. « *Experimental and Theoretical Charge Density Study of a Functionalized Hexavanadate* », Serbian Crystallographic Meeting, Beograd, Serbie, 13-15 June 2013. [Oral presentation, 20 mins].
5. **X. XU**, N. BOŠNJAKOVIĆ-PAVLOVIĆ, S. NOVAKOVIC, J-M. GILLET, Y. WEI, N-E. GHERMANI, A. SPASOJEVIĆ – de BIRÉ. « *Experimental and Theoretical Charge Density Study of a Functionalized Hexavanadate* », 19th Colloque de Recherche Inter-Ecole Centrales. 24–27 June 2013. [Oral presentation, 15 mins].
6. **X. XU**, S. NOVAKOVIC, N. BOŠNJAKOVIĆ-PAVLOVIĆ, N-E. GHERMANI, Y. WEI, A. SPASOJEVIĆ – de BIRÉ. « *Experimental Electronic Properties of a Fluorescent Polyoxovanadate-Based Intramolecular Charge Transfer Hybrid. An High Resolution X-ray Diffraction Study* », 13th multidisciplinary symposium on theme of crystallography. Orsay, France, 13 March 2014. [Poster]
7. **X. XU**, S. NOVAKOVIC, N. BOŠNJAKOVIĆ-PAVLOVIĆ, N-E. GHERMANI, Y. WEI, A. SPASOJEVIĆ – de BIRÉ. « *Experimental Charge Density Study of a Fluorescent Polyoxovanadate-Based Charge Transfer Hybrid* », 9th International Vanadium Symposium., Padova, Italy, 29 June – 2 July 2014. [Oral presentation, 15mins]